UNIVERSITY OF
BIRMINGHAM

INVESTIGATION OF STRUCTURE AND PROPERTIES OF Li/Na ION CONDUCTING ELECTROLYTES AND ELECTRODE MATERIALS

by

IVAN TRUSSOV

A thesis submitted to
the University of Birmingham
for the degree of
DOCTOR OF PHILOSOPHY

School of Chemistry
College of Engineering and Physical Sciences
University of Birmingham
February 2019

Abstract

This thesis describes the synthesis, structure and properties of a range of materials to be used in Li/Na ion batteries. As potential solid electrolytes, Si/B doped lithium lanthanum titanium oxide (LLTO) perovskites, Na doped Nb/Ta/Zr-based garnets and mixed Na/K-Mg sulphates were studied. The oxoanion doped eldfellite material and mixed Na/K-Ti/V phosphates were studied as potential cathode materials. The silicon and boron doped LLTO perovskites were shown to have better sinterability but have a lower ionic conductivity. Na doped garnets demonstrated the ability to incorporate Na onto the La site with partial incorporation to the Li site as well, therefore blocking Li transport. New systems were reported for Na-Mg sulphates. The detailed X-ray diffraction study of $Na_2Mg_2(SO_4)_3$ highlights enormous complexities within the system. The thermal evolution of these phases was studied. The eldfellite $NaFe(SO_4)_2$ was demonstrated to be able to have 25% of sulphate replaced with hydrophosphate and selenate anions without degrading the structure. Mixed Na/K-Ti/V phosphates were shown to form two different structures: NASICON and langbeinite with unusual cell parameter changes.

Acknowledgements

At first, I would like to thank my supervisor Prof. Peter Slater for his support and guidance during this PhD work. Although far not every whacky idea was actually viable in this project I'm glad I was given enough help to maintain it well. I would also like to thank my second supervisor Dr. Adrian Wright for help in getting into neutron refinements.

A big thank to Dr. Jackie Deans for instrumental support and smooth running of the floor. My life would be much more difficult without her help during these years. I would like to thank Dr. Louise Male for her help and experience in single crystal diffraction she kindly shared with me.

Huge thanks to Abbey and Josh for being a very good company and making this time very enjoyable and memorable. Thanks to Lauren, Dan S., Kanika, Dean, Ashleigh, Ryan, George, Bo, Evin, Matt, Mark, Kiwi, Abu, Rachel, Asuza, Dan P., Beth for good time on the floor and all the British culture they taught me. A special thanks to "night shift" member Rebecca who made this shift much more fun and was brave enough to help me with proof reading.

I would also like to thank Dr. Ron Smith (ISIS) for neutron data collection at ISIS facility. Thanks to Prof. Frank Berry for the performance and analysis of Mössbauer data presented here. A big thanks to Dr. Alodia Orera and Dr. Maria Luisa Sanjuan (Instituto de Ciencia de Materiales de Aragón) for collection and analysis of variable temperature Raman data for this work.

Table of content

Chapter One

Introduction

Although the development of lithium batteries began in 1912, it was only in the 1970s that primary cells with a lithium anode started to be widely used. This advance provided the impetus for such power sources to firmly take their place as an integral part of portable equipment, and allowed the production of high voltage batteries with high specific capacity. There were, however, great difficulties in the creation of rechargeable lithium batteries that took more than 20 years to overcome. Even then the process occurring during their use ultimately caused safety issues, due to a violent reaction known as “ventilation with the release of fire”. An example of this phenomenon and its impact can be seen in Japan in 1991 where lithium batteries were being used as a power source in mobile phones for the first time. A number of users received facial injuries as a result of their device exploding during a call (when the current load was at its maximum) with the flames emanating from

the battery compartment. As a result of these incidents this type of Li anode battery was withdrawn from the market.

Many studies of Li batteries have shown that the problem is the reactivity of the lithium metal electrode. With the instability being inherent to the use of Li metal, the focus of research within the Li ion battery field moved to creating a cell with an electrode made of a lithium based compound. In such a system charging and discharging the battery are processes in which the lithium ions are transferred from one electrode to the other. On discharging the lithium ions deintercalate from the anode material and intercalate into that of the cathode (Figure 1). The charging process is the reverse. As no metallic lithium is present in the system this was known as a Li-ion or "rocking chair" battery. Although metallic lithium batteries provided the higher energy density, these newer lithium ion batteries were advantageous by being safer while having the correct mode of charging and discharging.

A revolution in the development of rechargeable lithium batteries led to the use of a new material for the anode. The well-known Japanese technology

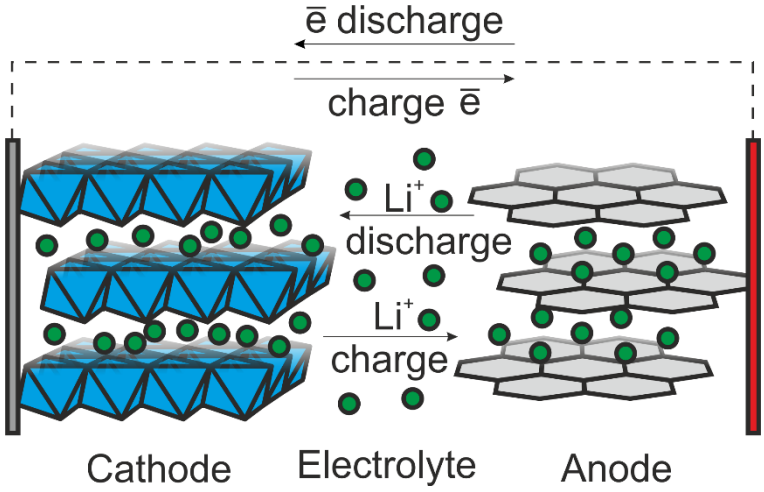

Figure 1. Schematic charge/discharge process in Li-ion cell. Li ions are green dots.

companies (Panasonic, Sanyo and Sony) developed a battery with a carbon based negative electrode: graphite, in particular, proved a convenient matrix for the intercalation of lithium ions. In order to achieve a sufficiently large voltage, $LiCoO_2$ was used as the active material for the cathode. First proposed as an electrode material by Goodenough et al.[1] $LiCoO_2$ has a potential of ~4V with respect to a lithium electrode. Thus, a lithium ion battery with a lithium cobalt oxide cathode and a graphite anode typically has an operating voltage above 3V.

Modern lithium ion batteries have high energy densities (100-180 Wh/kg and 250-400 Wh/l), and operating voltages (3.5-3.7 V). In a year, a Li-ion battery loses between 10-20% of the stored capacity through self-discharge: about 6.4% occurs in the first month with the rate significantly decreasing thereafter. Table 1 gives the Deutsche Bank 2008 comparison of the characteristics of several types of battery[2]. It is clear that the cost of producing lithium ion batteries was significantly lower already than that of nickel metal hydride batteries at this time. However, by 2016 the cost of Li-ion batteries has dropped to 200€/kWh[3] (from 350) and is predicted to fall further to 130€/kWh by 2020. The same report forecasts the energy density limit 300Wh/kg for lithium ion batteries to be reached in the near future.

Table 1. Characteristics and prices of batteries[2]

Batteries	Voltage	Specific Capacity	Self-discharge per month	Cycles	Price €/kWh
Ni-Cd	1,0-1,35V	40 Wh/kg	10%	1000-2000	200
Ni-MH	1,1V	71 Wh/kg	15%	1000-2000	600
Li-ion	3,5-3,7V	105-170 Wh/kg	4-6%	7000	350

There is no consensus regarding the status of the supply of materials for batteries particularly in relation to cobalt and lithium depletion[3,4]. However when any technology transits into the mass market, a large amount of resources will be required. For lithium-ion batteries the main difficulty of such a transition is the maintenance of balance between demand and supply of materials. A regular 60kWh Li-ion battery for an electric vehicle (~350km) contains 7.5kg of lithium, 65kg of transition metals, 55kg of carbon, 48kg of copper and 30kg of aluminium[5]. Such a large amount of valuable materials should not be withdrawn from the production cycle by directly disposing of the battery at the end of its life. Recycling such materials saves resources but requires an extra industrial loop and is therefore costly. Furthermore, recycling alone will not be sufficient to maintain the necessary supply of battery materials, given the large projected increase in Li-ion battery usage due to electric vehicles.

For these reasons new chemistry for batteries must be explored. Some of this resource problem could potentially be solved by replacing lithium with more earth abundant sodium[6]. The utilisation of sodium in rechargeable cells has been under investigation for some time but was significantly slowed by the major progress made with lithium ion batteries. Nowadays there has been renewed interest in sodium ion batteries due to the wide natural abundance of sodium. As such using sodium in combination with iron and manganese containing cathodes may be a cheap solution of the issues to supply and demand.

The chemistry for Na-ion and Li-ion batteries seems to be similar. However, the larger ion size and smaller polarisation causes the structure formation and

diffusion properties to be significantly different. Furthermore, the behaviour of the electrolyte changes as the simpler desolvation of Na ions[7] improves the charge transfer properties. Changing the alkali ion from lithium to sodium also enables the anode copper current collector to be replaced with cheaper aluminium as the latter does not form an alloy with sodium. In addition, some of the chemistries which are inactive for Li ion systems are active with the Na-ion. For example, Komaba et al. reported that lithium chromite ($LiCrO_2$) is passive in Li cells but sodium chromite ($NaCrO_2$) works in Na cells[8]. Further research is focused on studies of Na-air and Na-sulphur systems that are very different comparing to the Li[9,10]. One problem with Na-ion batteries is the inability of sodium ions to intercalate into layers of graphite, which requires an alternative anode, with a range of hard carbon being examined[11].

Cathode

With respect to the cathode of Li-ion batteries, reaching the current state of affairs has taken many years of constant development. Today a number of cathode materials are available for the mass production of lithium-ion batteries:

- Lithium cobalt oxide $LiCoO_2$ (LCO);
- Lithium manganese oxide $LiMn_2O_4$ (LMO);
- Lithium titanium oxide $Li_4Ti_5O_{12}$ (LTO);
- Lithium nickel manganese cobalt oxide $LiNi_{1-x-y}Mn_xCo_yO_2$ (NMC);
- Lithium nickel cobalt aluminium oxide $LiNi_{1-x-y}Co_xAl_yO_2$ (NCA);
- Lithium iron phosphate, $LiFePO_4$ (LFP).

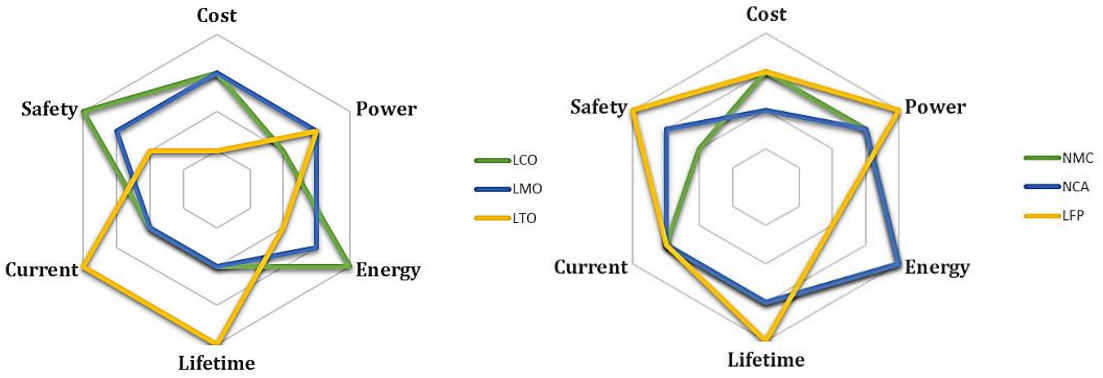

Figure 2. Comparison of different types of Li-ion batteries[3]

Different applications tend to use different chemistries to match the performance required. Figure 2 shows the comparison of these cathode materials.

Comprising from these characteristics LCO is commonly used for mobile electronics (phones, laptops), LMO and LFP is suitable for power tools and medical instruments, NCA and NMC are currently competing in electric vehicle industry, and LFP is far ahead in application requiring high thermal and chemical stability, i.e. safety.

Lithium cobalt oxide was first proposed as cathode material by Goodenough et al. in 1980[12]. Currently, it is the most studied cathode material for Li-ion batteries. The main advantages of this compound are a high voltage of the cell, high electronic conductivity, significant energy density and relatively simple manufacturing process. However, this material is not thermally stable, not environmentally friendly, expensive and pyrophoric when physically damaged. Currently there is no alternative for small, low consumption, high capacity appliances but LCO.

Lithium nickel manganese cobalt oxide (NMC) and lithium nickel cobalt aluminium oxide (NCA) show improved thermal and electrochemical behaviour in

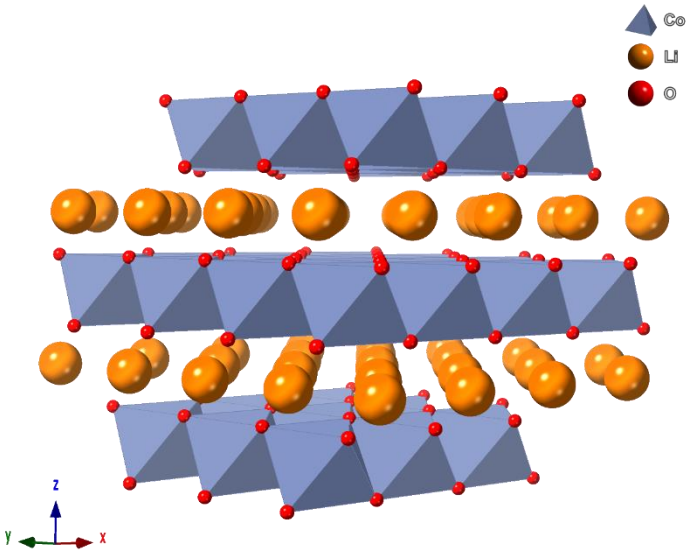

Figure 3. Structure of layered $LiCoO_2$

cells in comparison to LCO. Further improvement of these systems led to the appearance of Li-rich compositions, which have very attractive properties, and may potentially become the next generation of the cathode materials[13].

LCO, NMC and NCA have an ordered cation rock salt structure (Figure 3). The transition metals form layers consisting of edge sharing MO_6 octahedra. The nickel, aluminium, manganese and cobalt occupy random positions within the layer. These layers are separated by layers of Li in octahedral sites. In the case of Li-rich structures some of the lithium ions go into the transition metal site with the formation of a hole on the nearest oxygen site. This allows interlayer ion diffusion in addition to intralayer transport[14].

Lithium manganese oxide spinel (LMO) was first reported to have electrochemical activity suitable for Li-ion cells in 1984 by Goodenough et al.[15]. This compound has a 3D network of edge-sharing MnO_6 octahedra with a network of accompanying channels for Li ion transport. Lithium occupies tetrahedral sites

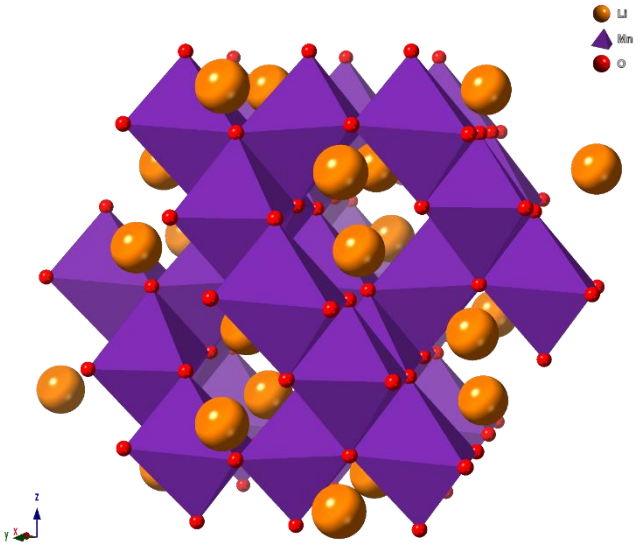

Figure 4. Structure of lithium manganese spinel $LiMn_2O_4$

within the channels (Figure 4)[16]. The main advantage of LMO system is that when the all Li is extracted, the residual phase remains stable in the λ-MnO_2 form[17]. This important property makes the compound very different from layered metal oxides which decompose at full discharge state and are thus no longer active. However, the complete extraction of Li requires very high voltages which are outside the stability window of most electrolytes used in cells[18]. Therefore, the actual capacity that can be achieved is only near 120mAh/g. Furthermore, at high voltages the presence of Mn^{3+} ions initiates disproportionation, with the material consequently decomposing[19]. As such, despite the fact that it is cheap and environment friendly, LMO materials are not as widely used as LCO, NMC, and NCA.

The electrochemical properties of lithium iron phosphate (LFP) were reported by Goodenough et al. in 1997[20]. LFP batteries are the third generation of lithium-ion batteries and are different from previous generations due to improvements in fire safety, specific capacity, rate of self-discharge and increased

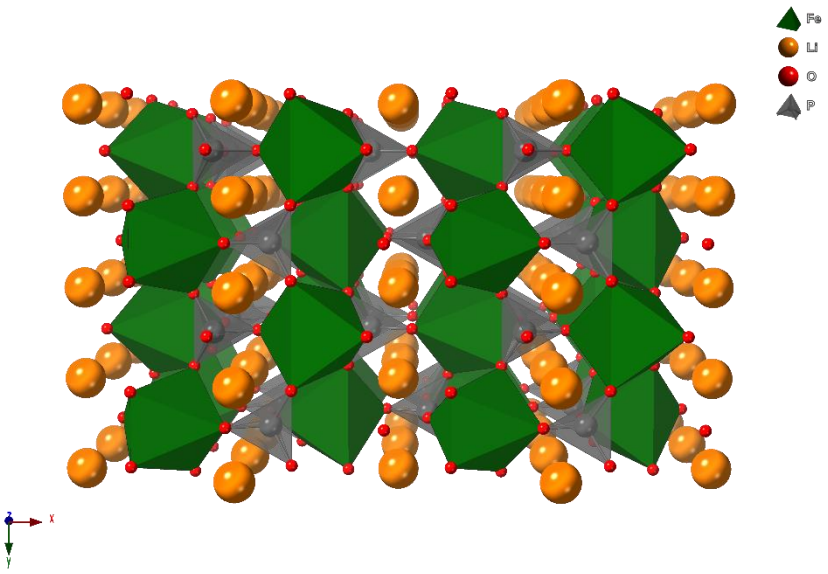

Figure 5. Structure of lithium iron phosphate $LiFePO_4$

number of charge-discharge cycles[21]. In comparison with LCO, LFP gives a lower operating voltage of 3.2-3.3 volts, but it is a very cheap, non-toxic and stable material, providing long duty cycle. Its main disadvantage is its very poor conductivity, which makes it challenging to realize its high theoretical capacity of 170 mAh/g. To improve conductivity, nanosized powder particles of LFP are coated with a carbon layer[22]. Partial replacement of iron with other transition metals (e.g. manganese or vanadium) was also reported to be beneficial to electrochemical performance[23,24]. The computational simulations have predicted that substituting a small percentage of the iron with lithium improve electrochemical characteristics[25,26], which was proved experimentally[27]. LFP is considered to be a good option for grid storage batteries and less beneficial for electric vehicles, due to giving a lower power density. However, following cases where cars with a LCO battery have caught fire, the Chinese government have forced electric bus manufacturers to change to using LFP batteries as they are much safer.

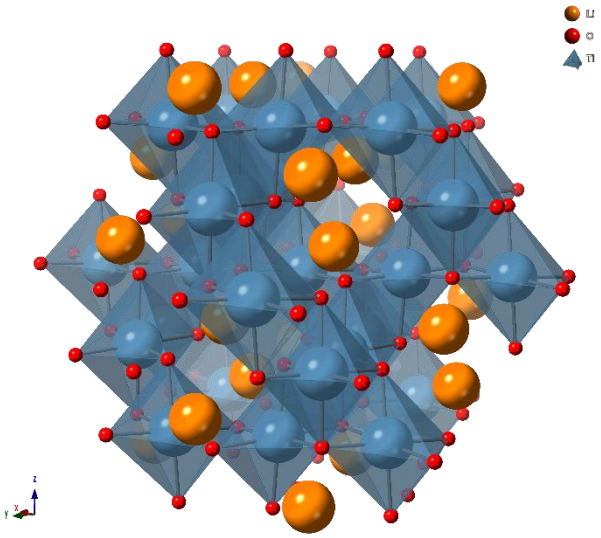

Figure 6. Structure of lithium titanium oxide $Li_4Ti_5O_{12}$

Lithium titanium oxide (LTO) is an interesting material. Having a relatively low potential vs Li (~1.5V), LTO can be utilised as cathode as well as anode[28], although the latter is more common. Therefore the direction of the processes happening depends on the potential of the opposite electrode: with a lithium electrode, LTO is a cathode; with a LCO electrode, LTO is an anode. This material has a spinel structure and is very similar to LMO. However, the octahedral transition metal site is partially occupied by lithium as well (Figure 6). When extra lithium intercalates into the structure, it forces the displacement of the tetrahedral lithium in to octahedral coordination, forming the rock-salt structure[29]. The high electronic resistance and low potential of LTO, however has inhibited its' widespread use. However, due to almost no major structural changes during intercalation/deintercalation processes, outstanding safety, stability and long cycle life, LTO is an excellent material for future devemopment[30].

There are many more materials that are promising options for cathodes of Li-ion batteries. As a result of the early stages of development, there are fewer materials available for the cathode of a Na-ion battery. For such battery systems to be commercially beneficial, the requirements are significantly different as the major application is likely to be in grid storage.

The structures of materials for Na-ion battery cathodes are very similar to those seen for Li-ion batteries with some variations. For example, different polymorphs of sodium transition metal oxides (similar to LCO) show electrochemical activity in cells (~3V), but undergo irreversible phase transitions, which causes quick degradation of the structure[31]. This kind of layered materials were used in Na cells by Sumitomo Kagaku company in Japan[32]. The sodium iron phosphate ($NaFePO_4$) exhibits the maricite structure (instead of the olivine structure exhibited by $LiFePO_4$) and therefore has problems with electrochemical behaviour due to slower diffusion of ions[33]. $Na_2FeP_2O_7$ has proved to be suitable for battery applications due to the structure having wide Na-ion migration pathways, which potentially allow large charge/discharge rates[34]. Sodium vanadyl phosphate is very similar to lithium analogue ($LiVOPO_4$), and has been shown to be promising for Na-ion batteries[35].

As highlighted in the above systems, a lot of research into Na ion cathode materials has examined systems containing polyanions, such as PO_4^{3-}, $P_2O_7^{4-}$, SO_4^{2-}. A significant step forward in the development of sulphate based cathodes for Na-ion batteries was achieved relatively recently[36]. Most of these materials are based on iron sulphate, but their chemistries can vary significantly.

Iron(III) sulphate, with a rhombohedral NASICON (Na Super Ionic Conductor) structure has been demonstrated to be able to intercalate Na[37]. Considering the very low manufacturing cost of this material and the high cell voltage, it has attracted a lot of attention as a potential cathode for Na-ion batteries. NASICON structures are famous for their high ionic conductivity and this feature aids their good electrochemical behaviour[38–44]. However due to the smaller size of sulphate units than phosphate, the diffusion of Na ions is significantly inhibited in NASICON sulphate systems[45]. Reliable reversible electrochemical performance of this material is therefore tricky to achieve.

Barpanda et al. reported that a non-stoichiometric alluaudite-type material[46], $Na_{2+2x}Fe_{2-x}(SO_4)_3$, can be reversibly charged/discharged, with a potential near 3.8V vs Na/Na^+. This is a monoclinic (C2/c) system consisting of edge sharing Fe_2O_{10} dimers connected by sulphate tetrahedra, where Na is distributed in the tunnels within the structure (Figure 7). Some of Na sites within the structure are

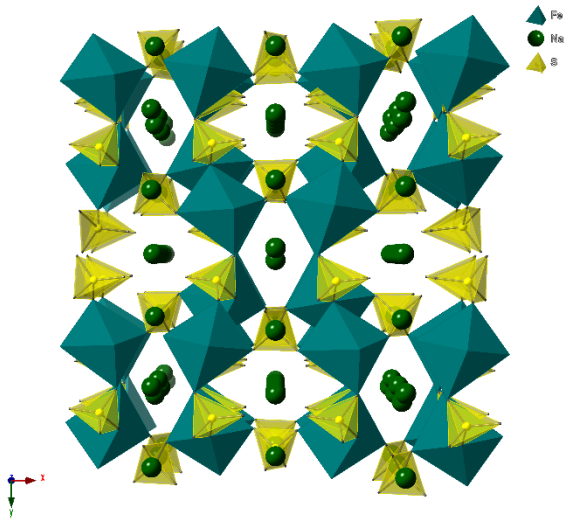

Figure 7. Alluaudite structure of $Na_{2.2}Fe_{1.8}(SO_4)_3$

inactive as they are fully occupied and therefore do not allow ion diffusion[47]. The room temperature conductivity of this material is rather low (~10^{-8}S/cm), which is comparable to NASICON materials[48] such as $Na_3V_2(PO_4)_3$. To improve electronic conductivity, extra processing is required, e.g. covering the material with carbon as for LFP. Similar derivatives of the materials with Co, Ni and Mn also have some electrochemical activity[49–51].

Bisulphate cathode materials with the kröhnkite[52], $Na_2Fe(SO_4)_2 \cdot 2H_2O$, and blöedite[53] structure, $Na_2Fe(SO_4)_2 \cdot 4H_2O$, were reported to have a potential ~3.3V vs Na/Na^+. These materials, however, undergo amorphization during charging cycles, leading to a loss of capacity. With care, it is possible to dehydrate these materials to synthesize $Na_2Fe(SO_4)_2$, which has some electrochemical activity and gives an average redox potential of 3.4 vs Na/Na^+.

Eldfellite is a mineral $NaFe(SO_4)_2$ that has been shown to be able to intercalate Na ions and was successfully utilised as a cathode material[54]. The structure consists of layers of FeO_6 octahedra connected by SO_4 units, separated by a layer of Na ions. A relatively insignificant volume change allows the reversible capacity of the material to be maintained on cycling. The activation energy of sodium ion migration was found to be approximately 0.6eV[55]. Banerjee et al. used DFT calculations to predict that this material can be improved by substitution of iron with other transition metal, such as vanadium or titanium[56].

Today the use of sulphate compounds in Na-ion batteries is preferable over the use of phosphates, as they are manufactured via cheap and sustainable approaches[36]. The high redox potential that is possible in some cases, also means

that they can even successfully compete with Li systems. However, the absence of extensive knowledge of such systems is slowing down their progress and transition into industry. Given the large diversity of structural features, sulphate compounds are a very interesting target for developing new battery material through understanding the relationship between structure and properties.

Electrolyte

The currently utilised electrolyte for a lithium (ion) battery has one very significant disadvantage – flammability. The replacement of this electrolyte with a ceramic ion conductive separators allows this problem to be excluded. Further, the issue of short circuiting due to cell fracture and formation of dendrites is resolved. This type of solid state electrolyte usually has high thermal stability, and with the rise of temperature, the conductivity of the ceramic electrolyte increases, making it favourable to use at elevated temperatures with molten electrodes[57].

Solid Li ion conductive electrolytes are currently divided into three main groups: phosphates, sulphides and oxides (crystalline or glass)[58].

Phosphates mainly include substances with the general formula $Li_{1+x}M1_yM2_z(PO_4)_3$, where M1 and M2 are germanium, titanium, zirconium or aluminium. These materials are good lithium ion-conductors, and adopt the NASICON structure. Currently, the phosphate that has the highest ionic conductivity at room temperature (5×10^{-3} S/cm) is the glass-ceramic with a general formula of

$Li_{1+x}Al_xGe_{2-x}(PO_4)_3$, where x = 0.5[59]. However, phosphate electrolytes often exhibit instability with respect to the electrodes.

Sulphide electrolytes are considered very promising for use in lithium-sulphur batteries, but the complexity of synthesis and of forming highly ordered structures leads to low diffusion rates during charge/discharge cycles.

One of the earliest and best representatives of oxide electrolytes remains lanthanum lithium titanate (LLTO). This has the highest bulk ionic conductivity stability for the oxide electrolytes. LLTO has a perovskite-type structure described by the general formula of ABO_3, where A is a large 12-coordinated cation located in the middle of the cubic unit cell, and B is small 6-coordinated cation located at the corners of the cell and linked via oxygen (Figure 8)[60]. In LLTO, the lanthanum ion shares the A site with a small amount of lithium, enabling Li ion conduction: this

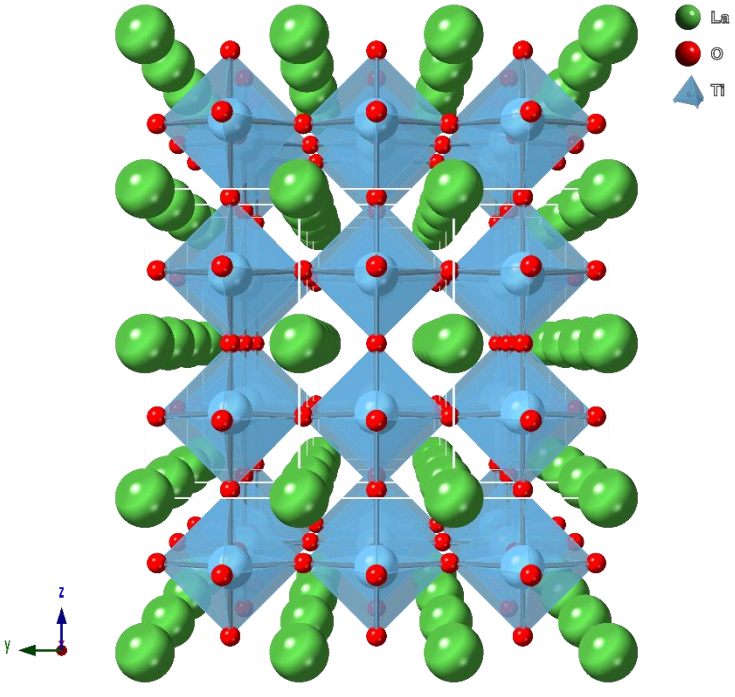

Figure 8. Crystal structure of LLTO

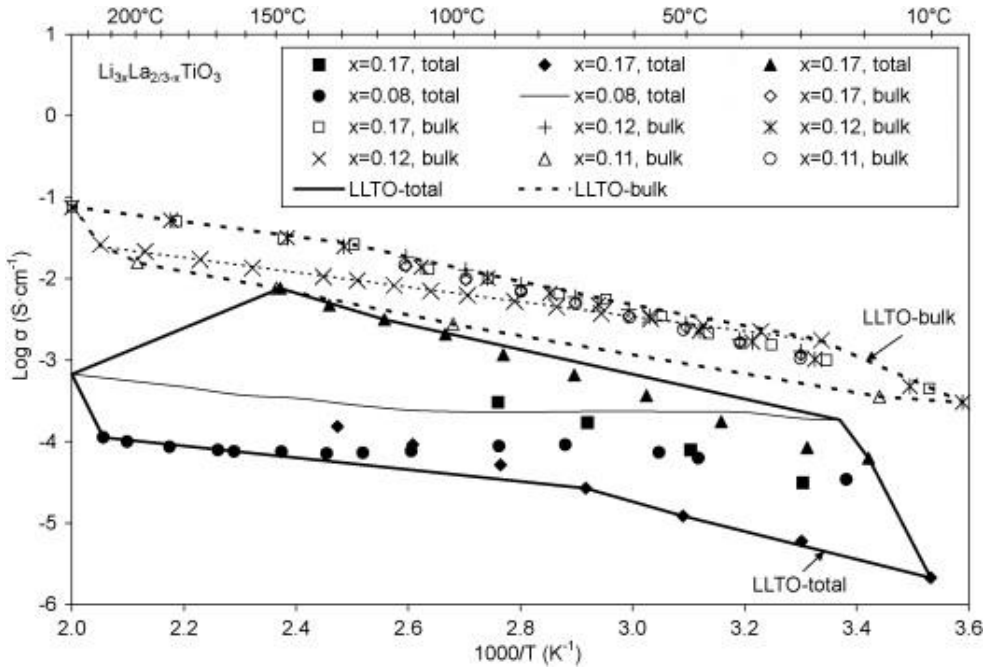

Figure 9. Conductivity of $La_{2/3-x}Li_{3x}TiO_3$ (LLTO) (used with permission)[198]

gives the general formula of $La_{2/3-x}Li_{3x}TiO_3$[61]. The maximum conductivity is on the order of 10^{-3} S/cm at room temperature[62–65].

The ratio of La to Li plays a key role in the transport of lithium ions. Increasing in the ratio to more than 1 leads to the formation of vacancies that remain neutrally charged. The maximum in the conductivity is observed when x = 0.125 (La/Li = 1.4) and the symmetry of system is tetragonal[66,67]. At lower lithium contents, the orthorhombic phase is formed. The tetragonal structure, which has a higher conductivity begins to form at x = 0.08[68]. Figure 9 shows the measured bulk conductivity of grains and the total conductivity for various compositions of LLTO. Distinguishing between bulk and total conductivity is very important as a large bulk grain conductivity with respect to that of grain boundaries shows that the transport of lithium ions is difficult at the grain surface. As well as the composition of the

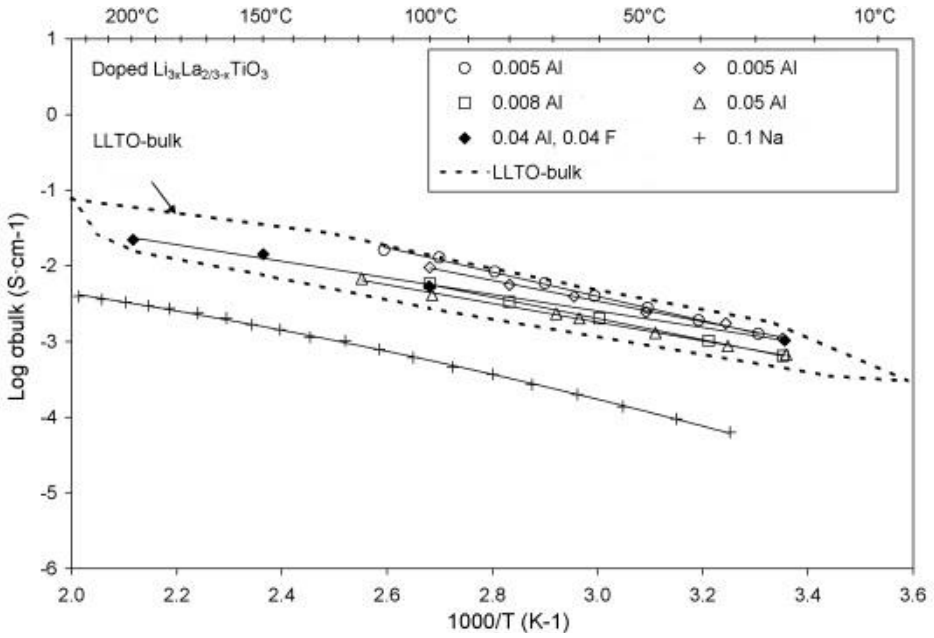

Figure 10. Bulk grain conductivity of LLTO with Al, Na and/or F additions (used with permission)[198]

interface, the size of the grain plays a crucial role in the conductivity of these systems. Considering that there are always grain boundaries in any working system, in practice, LLTO shows a maximum total (bulk and grain boundaries) conductivity around 10^{-4} S/cm at room temperature. Many approaches have been used to try to overcome this problem of a resistive grain boundaries - mostly related to the addition of interface enhancing compounds[69].

The influence of doping on the bulk conductivity of grains of LLTO is shown in Figure 10[65,70–72]. Substitution of small amounts of aluminium for titanium results in a higher conductivity. At the same time the addition of sodium, which replaces atoms in the A site, leads to a decrease in conductivity, while replacing some of the oxygen with fluorine does not have a significant effect on the conductivity . Other studies have shown that the addition of silica to $Li_{0.5}La_{0.5}TiO_3$ increases the overall

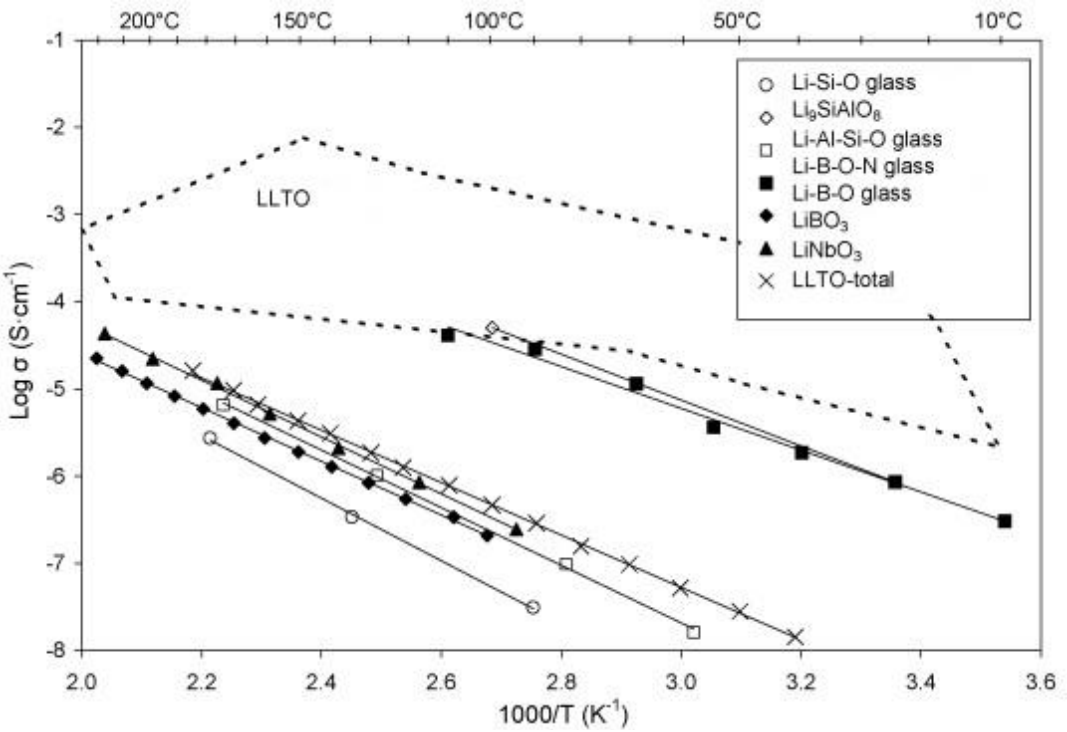

Figure 11. Conductivity of selection of oxide electrolytes (used with permission)[198]

conductivity, which may be due to its effect on diffusion of lithium ions at the grain boundaries[62].

The conductivities of some other oxides used as a solid electrolyte for lithium-ion batteries are shown in Figure 11[73–77]. The conductivity of lithium ions in $Li_3BO_{2.5}N_{0.5}$, Li_9SiAlO_8 and Li_4SiO_4 is close to the conductivity of LLTO, while other oxides tend to show lower li-ion diffusion. The high specific ionic resistance may prevent the use of these materials as the electrolyte for household batteries. However, materials with low conductivity may be used in thin film or high temperature batteries. Thus, $Li_3BO_{2.5}N_{0.5}$ with lower conductivity than LLTO under normal conditions, has been used in a thin film battery[75].

The other important member of oxide Li-ion conductors are the garnet materials. The classic garnets are based on orthosilicates $A^{II}_3B^{III}_2(SiO_4)_3$, where the A and B cation occupy eight and six coordinated cation sites respectively[78]. Garnets have been used in a very wide range of applications - from jewellery to laser generation. Garnets were first proposed as solid electrolytes by Thangadurai et al. in 2003[79]. The ionic transport in $Li_5La_3M_2O_{12}$ (M=Nb, Ta) was shown to be comparable to other ceramic Li-ion conductors. Even though the conductivity at room temperature for this material wasn't outstanding (10^{-6} S/cm), it revealed good stability against molten lithium.

The ideal Li-ion conductive garnet structure has a cubic symmetry with space group $Ia\bar{3}d$ (Figure 12). It consists of 6-coordinated octahedra ($Me1O_6$) linked by 8-coordinated square antiprisms ($Me2O_8$). This system forms a 3D

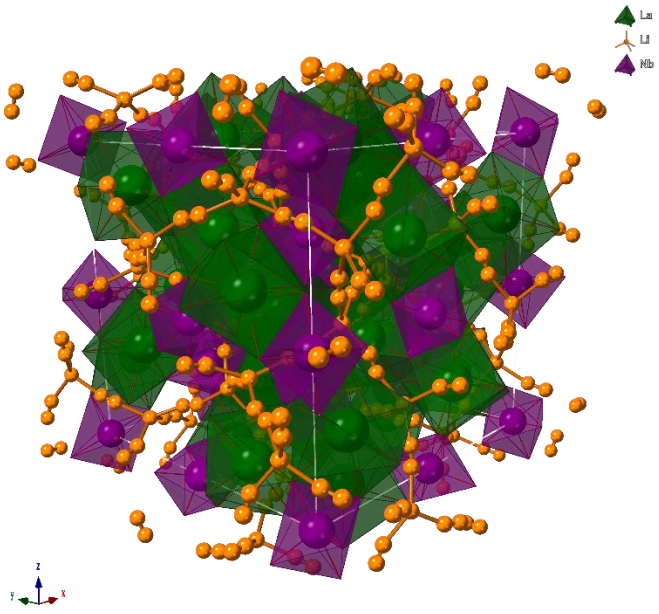

Figure 12. Crystal structure of garnet solid electrolyte. Lithium pathways are shown

structure with channels through the crystal lattice, in which there are two partially occupied Li sites. The first is tetrahedral, while the second is an interstitial distorted octahedral site. The occupancy of the Li site plays a key role in the Li-ion conduction. A fully occupied tetrahedral Li site was reported for $Ln_3Te_2Li_3O_{12}$ by O'Callaghan et al[80], but the Li-ion conductivity remains very low even at high temperatures (10^{-5} S/cm at 600^{o}C). In the same way, a fully occupied octahedral Li site was shown for tetragonal garnets, which are also very poor Li-ion conductors[81,82]. Interestingly, in 2007 Murugan et al. reported that the cubic garnet $Li_7La_3Zr_2O_{12}$ in which the Li sites are fully occupied, has a good conductivity about 10^{-4} S/cm at room temperature[83]. However, in this case the fully loaded with Li garnet (Li_7) should have a tetragonal crystal system[84], and it was later shown that the cubic garnet reported by Murugan actually arises from Al^{3+} incorporation on the Li site as result of reaction with the alumina crucible[85]. This aluminium incorporation causes a decrease in the overall Li content and creates vacancies, thereby promoting ionic conduction[86].

The fact that the conductivity of garnets can be improved by the introduction of more Li into the lattice inspired a wide range of doping studies on $Li_5La_3M_2O_{12}$ materials[87]. It has been shown that substitution of La(III) with divalent alkaline earth metals Ba(II)[88,89], Ca(II)[90,91], Sr(II)[89,91] in $Li_5La_3M_2O_{12}$ (M=Nb, Ta) leads to an improvement in the Li-ion conductivity due to an increase in the Li content. Ba and Sr substitution seems to be the most successful so far (Figure 13). Monovalent alkali metal substitution has also been reported: potassium doping was successfully applied to improve Li conductivity in the Nb based garnet[92]. Some improvement in the conductivity of $Li_7La_3Zr_2O_{12}$ was achieved by substituting of Zr

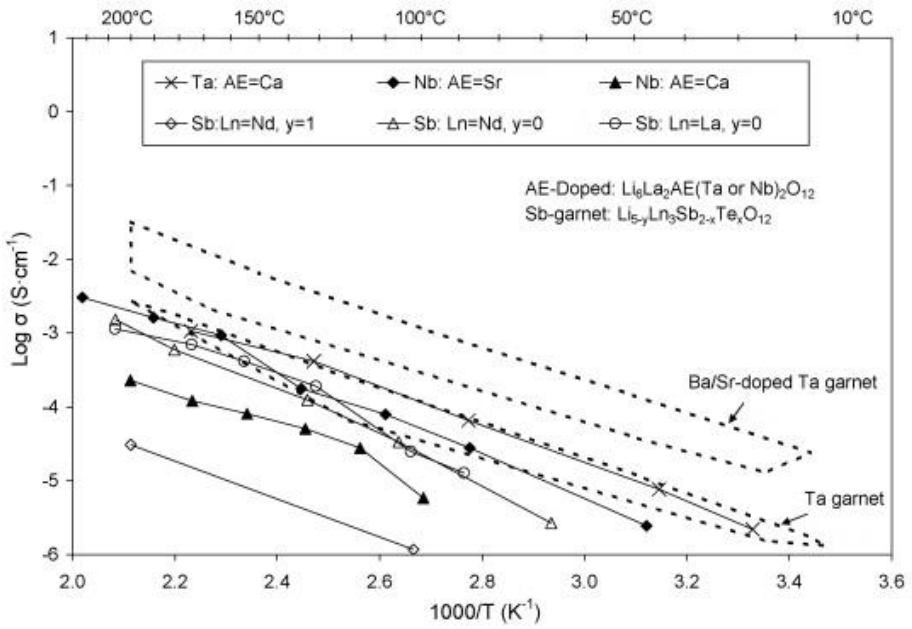

Figure 13. Conductivity of Garnet solid electrolytes (used with permission)[198]

with a low level of Nb[93], while $Li_{5+x}La_3A_{2-x}B_xO_{12}$ (A = Nb or Ta, B = Sc or Zr) showed good conductivity behaviour and stability towards metal lithium (for Ta).

Even though the first fast alkali ion conductors were reported for sodium[94], lithium-ion conductors are receiving the most attention from material scientists. This is related to the fact that the solid electrolytes may significantly enhance safety of Li-ion batteries, which is becoming more important when considering high power electric vehicle application. On the other hand, sodium-ion batteries are considered to be safer due to the higher stability of constituent compounds.

The most famous representative of Na-ion conductors is the NASICON structure[38,39]. The original compound studied consists of ZrO_6 octahedra linked via three PO_4/SiO_4 tetrahedra, forming the so-called NASICON lantern unit. These units form a rigid 3D framework in the lattice with trigonal symmetry. Interestingly,

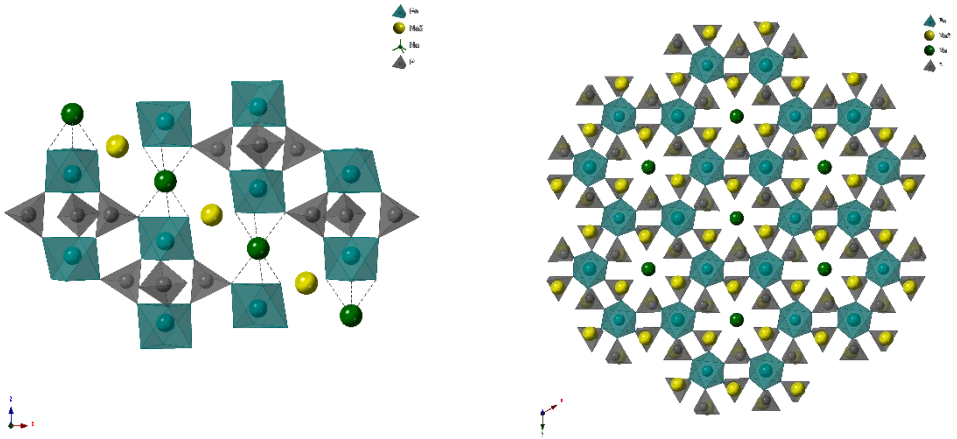

Figure 14. The structure of NASICON showing two different sites for sodium (green and yellow) in conducting channel and hexagonal array of groups in (0 0 1) plane

depending on composition, NASICON materials can exhibit rhombohedral, monoclinic or triclinic symmetry. There are two sites for the alkali metal: between the ZrO_6 octahedra in the vertical row and in an interstitial site between the tetrahedra (Figure 14). When sodium moves through the lattice, it jumps from one site to another. Therefore vacancies on these sites improve ionic conductivity of the material. It was shown that a change of the Na content significantly changes the conductivity[95] and thus can be achieved via partial replacement of the either framework metal or anion group[96]. Other anions (e.g. sulphate) may form NASICON structures as well, although there appears to be a specific relation between the cation and anion sizes required for NASICON to be formed.

Aims and objectives

The recent advances in Li/Na ion batteries revealed potential safety issues with current battery materials. Consequently, there is an increasing interest in the development of alternative electrode and electrolyte materials. This work contains a variety of different studies dedicated to the improvement of the behaviour of Na/Li cells. Doping strategies were utilised to create new phases which might exhibit better electrochemical performance and, subsequently, efficiency.

Work was carried out to research how doping silicon and boron oxides on to the B cation site influences the conductivity of lithium lanthanum titanium oxide electrolyte materials. This study follows the work done by Hancock et al. which showed the possibility of substituting oxyanions onto this site in the perovskite structures[97].

A study of doping Na onto the La site in the $Li_5La_3M_2O_{12}$ (M=Nb, Ta) garnet electrolyte was performed in the hope of increasing the amount of charge carriers (Li-ions) in the lattice and subsequently improve the conductivity. This strategy has been shown to be successful in the case of divalent metal substitution on the La site.

The promising electrochemical behaviour of Fe-alluaudites led to the investigation of potential Mg-alluaudites which might have high ionic conductivity. As such, a study of mixed alkali metal magnesium sulphates was designed, to try and form an alluaudite structure as observed for $Na_{2+2x}Fe_{2-x}(SO_4)_3$. Forming an alluaudite structure based on magnesium was unsuccessful. However this study led

to the discovery of a range of previously unknown structural frameworks very close in terms of composition.

Oxoanion doping of the promising cathode material $NaFe(SO_4)_2$ with eldfellite structure was performed in order to try and tailor the electrode potential. This approach has already been shown to be successful in previous studies of related systems by Driscoll et al.[98].

Work on a continuous range of Na-K for Ti/V phosphates was carried out to identify the stability regions of NASICON-langbeinite phases in the hope of finding potential new electrode materials for K/Na-ion batteries.

The experimental work for this thesis was done with a variety of techniques, as different studies required their own approaches. The main technique utilised, however, is X-ray diffraction as the first thing to study is always the crystal structure.

This work combines different findings that are sometimes quiet diverse from each other, as the work led to a range of interesting, somewhat tangential results.

Chapter Two

Experimental techniques

Synthetic routes

Solid state

One of the most common manufacturing processes for ceramic materials is the solid-state route. This method is very popular due to relative simplicity. Normally, no special equipment is required – just a crucible and a furnace. Reagents are mixed together and sintered at high temperature. However, due to the heterogeneous nature of the process, the rate of reaction highly depends on the contact surface area. Thus, to improve the reaction performance, reactants are ground together (e.g. using a pestle and mortar, ball-mill etc.) to allow even distribution of the chemicals over the entire reacting mass and to increase the contact surface area by minimizing the size of the reacting particles. Often the solid

mixture is pressed into pellet to decrease porosity, further increasing the contact surface area. For some systems, the product may start to form during this grinding stage. In this case, the process is called mechano-chemical activation. Normally, high-power ball milling is used to carry this process. Once the chemicals are mixed, the high temperature heat treatment is applied: the temperature used depends on the stability and melting point of the compounds. Often the reaction process takes a significant amount of time due to slow ion diffusion rates and requires intermediate regrinding to complete the formation of a single phase.

Dissolution-evaporation

If the melting point of product is too low or it decomposes at high temperatures, it is not possible to apply the very high temperature required in the solid-state reaction process. In this case, dissolution-precipitation method can be applied if the precursors are soluble. Once the reagents have dissolved in a suitable solvent (normally water), the solutions are mixed together. The mixed solution formed is subsequently evaporated on a hotplate with magnetic stirrer and dried. The precipitate can then be heated to ensure reaction to form the required phases. This method is especially good for solution stable salts like most of the sulphates studied in this work.

Single crystal growth

In this work single crystal studies have been used for structure solution. To grow the single crystals, a method of crystallisation from the melt was applied. A small amount of powder material is placed on a piece of gold foil and is heated above the melting point. The melt is then slowly cooled to room temperature at a rate 10^{o}C/hour. The cold mass is then crushed and small single crystals that are sufficient to conduct single crystal study extracted.

In some cases, the powders obtained via the dissolution-evaporation synthesis route (discussed above) with subsequent heat treatment can be used for the single crystal study as is. This is because small single crystals often appear in the powder mass and can be picked for use in the diffraction experiment.

Basic Crystallography

An ideal crystal structure can be expressed as a lattice consisting of an infinitely repeated stack of the same unique parallelepipeds (unit cell). This repetition represents the fundamental property of any crystal lattice – translational symmetry. Dimensions of the unit cell can be expressed as three vectors ($\vec{a}, \vec{b}, \vec{c}$) radiating from the same point, while the angles between the vectors can be assigned to α, β and γ (Figure 15): these six dimensions are called the unit cell parameters. Depending on the symmetry of the crystal lattice, it can be attributed to one of six crystal families or seven crystal systems (Table 2).

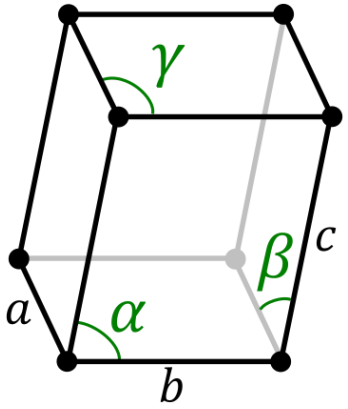

Figure 15. Crystal unit cell

A point group is a set of symmetry elements that leave at least one point in space fixed. Six symmetry elements are used to express the mutual positions of the atoms within the lattice: a centre of symmetry, a rotation axis, a mirror plane, a rotation-reflection axis, a screw axis and a glide plane. Rotational axes in crystallographic point groups can be 1, 2, 3, 4 and 6 order corresponding to 360^{o}, 180^{o}, 120^{o}, 90^{o} and 60^{o} angular intervals. Combining the different symmetry elements gives a total of 32 crystallographic point groups.

Depending on the centring within the lattice cell, there can be defined four types: primitive (P), body-centred (I), face-centred (F) and base-centred(C, A or B). The combination of the crystal systems with cell centring generates 14 different Bravais lattices.

The combination of the 14 Bravais lattices with the 32 crystallographic point groups generates 230 three-dimensional space groups. These space groups are used to fully describe any 3D crystal lattice.

Table 2. Crystal systems

Crystal family	Crystal system	Point groups	Cell parameters restrictions	No. of space groups	Bravais lattices
Triclinic (anortic), *a*	Triclinic	$1, \bar{1}$	a, b ,c α, β, γ	2	*aP*
Monoclinic, *m*	Monoclinic	$2, m,$ $2/m$	a, b, c α=β=90°, β (β >90°)	13	*mP* *mC (mA, mB, mI)*
Orthorhombic, *o*	Orthorhombic	$222, mm2,$ mmm	a, b, c α=β=γ=90°	59	*oP* *oC (oA, oB)* *oI* *oF*
Tetragonal, *t*	Tetragonal	$4, \bar{4}, 4/m,$ $422, 4mm,$ $\bar{4}2m,$ $4/mmm$	a=b, c α=β=γ=90°	68	*tP* *tI*
Hexagonal, *h*	Trigonal (hexagonal axes)	$3, \bar{3},$ $32, 3m,$ $\bar{3}m$	a=b, c α=β=90°, γ=120°	18	*hP*
	Trigonal (rhombohedral axes)		a=b=c α=β=γ	7	*hR*
	Hexagonal	$6, \bar{6}, 6/m,$ $622, 6mm,$ $\bar{6}2m,$ $6/mmm$	a=b, c α=β=90°, γ=120°	27	*hP*
Cubic, *c*	Cubic	$23, m\bar{3},$ $432, \bar{4}3m,$ $m\bar{3}m$	a=b=c α=β=γ=90°	36	*cP* *cI* *cF*

To describe lattice planes, rows or points, three integer Miller indices (h, k, l) are used. These are reciprocal coordinates of intercepts in fractions on the unit cell axis. Lattice planes are identified by regular parenthesis brackets, for example (102); to determine lattice rows square brackets are used: [102]; lattice points are defined without any brackets: 102. In every lattice, there are sets of repeating parallel planes crossing it at equal distance. This distance depends on the cell

parameters, and is known as the spacing of the planes or the interplanar distance, and is labelled by the letter d.

Diffraction

The typical d-spacing for any crystal lattice lies within 1-4 Å. X-rays, neutrons or electrons with a wavelength that is similar to the d-spacing can be scattered from the periodic array of atoms in the crystal cell. Let us assume that an incident monochromatic beam (S_0) of any kind is diffracted at an angle (θ) from adjacent planes with interplanar distance d_{hkl} (Figure 16). The difference in the path length between two waves passing through point A_1 and A_2 is BA_2+A_2C, and according to basic trigonometry equals $2d_{hkl}sin\theta$. Diffraction maxima are observed when there is a constructive interference between the diffracted beams, which only occurs when they are in phase. Therefore, the difference in path length between the

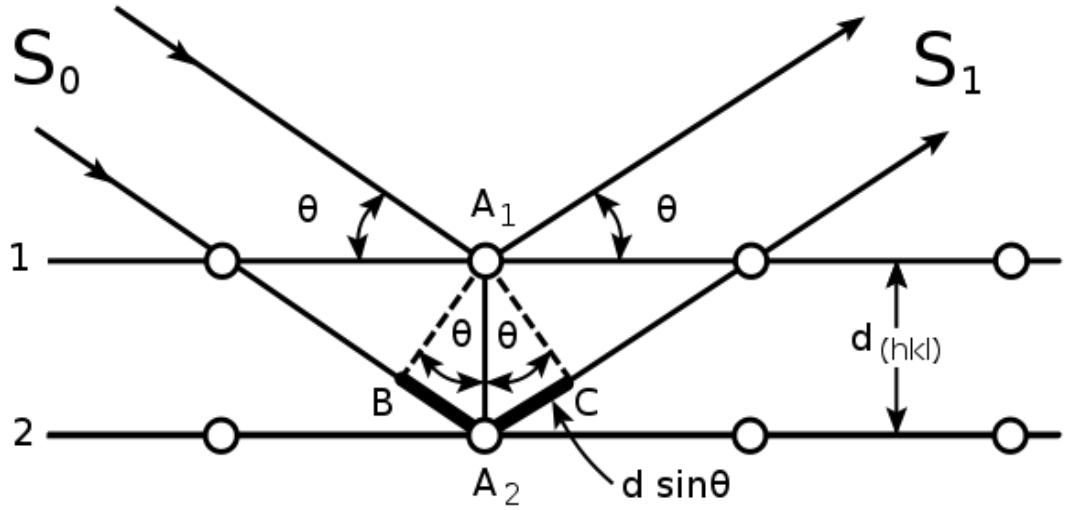

Figure 16. Diffraction of beam from a 2D-crystal

waves must be equal to an integer number of wavelengths. This condition is known as Bragg's Law:

$$n\lambda = 2d_{hkl}sin\theta$$

Since d spacing values are a function of the unit cell parameters (a, b, c, α, β and γ) and have a non-linear dependence it is quite difficult to work with direct-cell parameters. It is more convenient to use reciprocal-cell parameters (a^*, b^*, c^*, α^*, β^* and γ^*) and Miller indices (h, k, l). This way Bragg's Law can be written:

$$\frac{4\sin^2\theta}{\lambda^2} = \frac{n^2}{{d_{hkl}}^2}$$

$$= h^2a^{*2} + k^2b^{*2} + l^2c^{*2} + 2hka^*b^*\cos\gamma^* + 2hla^*c^*\cos\beta^* + 2klb^*c^*\cos\alpha^*$$

To calculate direct-space cell parameters these equations are used:

$$a = \frac{b^*c^*\sin\alpha^*}{V^*}$$

$$b = \frac{a^*c^*\sin\beta^*}{V^*}$$

$$c = \frac{a^*b^*\sin\gamma^*}{V^*}$$

$$\cos\alpha = \frac{\cos\beta^*\cos\gamma^* - \cos\alpha^*}{\sin\beta^*\sin\gamma^*}$$

$$\cos\beta = \frac{\cos\alpha^*\cos\gamma^* - \cos\beta^*}{\sin\alpha^*\sin\gamma^*}$$

$$\cos\gamma = \frac{\cos\alpha^*\cos\beta^* - \cos\gamma^*}{\sin\alpha^*\sin\beta^*}$$

$$V^* = a^*b^*c^*\sqrt{1 - \cos^2\alpha^* - \cos^2\beta^* - \cos^2\gamma^* + 2\cos\alpha^*\cos\beta^*\cos\gamma^*}$$

With an increase in the cell symmetry, these equations become much simpler. Remembering that:

$$\sin 90° = 1$$

$$\cos 90° = 0$$

Equations for an orthogonal cell turn into:

$$a = \frac{1}{a^*}$$

$$b = \frac{1}{b^*}$$

$$c = \frac{1}{c^*}$$

This mathematical approach is the basis of the interpretation for all diffraction experiments.

In order to calculate other parameters in the cell, the real-space metric (g_{ij}) tensor is often used. This is the matrix comprised of the scalar products of the crystal lattice basis vectors:

$$g_{ij} = \begin{pmatrix} |\vec{a}||\vec{a}| \cos 0° & |\vec{a}|\left|\vec{b}\right| \cos \gamma & |\vec{a}||\vec{c}| \cos \beta \\ |\vec{a}|\left|\vec{b}\right| \cos \gamma & \left|\vec{b}\right|\left|\vec{b}\right| \cos 0° & \left|\vec{b}\right||\vec{c}| \cos \alpha \\ |\vec{a}||\vec{c}| \cos \beta & \left|\vec{b}\right||\vec{c}| \cos \alpha & |\vec{c}||\vec{c}| \cos 0° \end{pmatrix}$$

X-ray diffraction

X-ray Diffraction (XRD) is a technique where X-rays are used to study the crystal structure of mono- and poly- crystalline materials. In the case of single crystal XRD, the information obtained is very accurate but only absolutely relevant for the current crystal. In powder XRD, the information obtained is an average and is a superposition of information from all the crystals present in the powder.

Normally diffraction patterns are unique for different crystalline materials and can be used for phase identification. The International Centre for Diffraction Data (ICDD) collects and systemises diffraction patterns (Powder Diffraction Files – PDF) for known crystalline materials. Today the ICDD PDF database is successfully used for phase analysis in many fields.

X-radiation is a form of electromagnetic radiation that typically has a wavelength from 0.01Å to 1000Å. The conditional border between soft and hard X-rays lies near 2Å (6 keV). The most commonly used wavelengths for diffraction experiments are in the range 0.7∼1.7 Å. In this case, all diffraction maxima will be located in measurable θ angles.

There are several ways to generate X-rays. The most common in laboratory practice is generation in an X-ray tube. This is a vacuum vessel with two electrodes

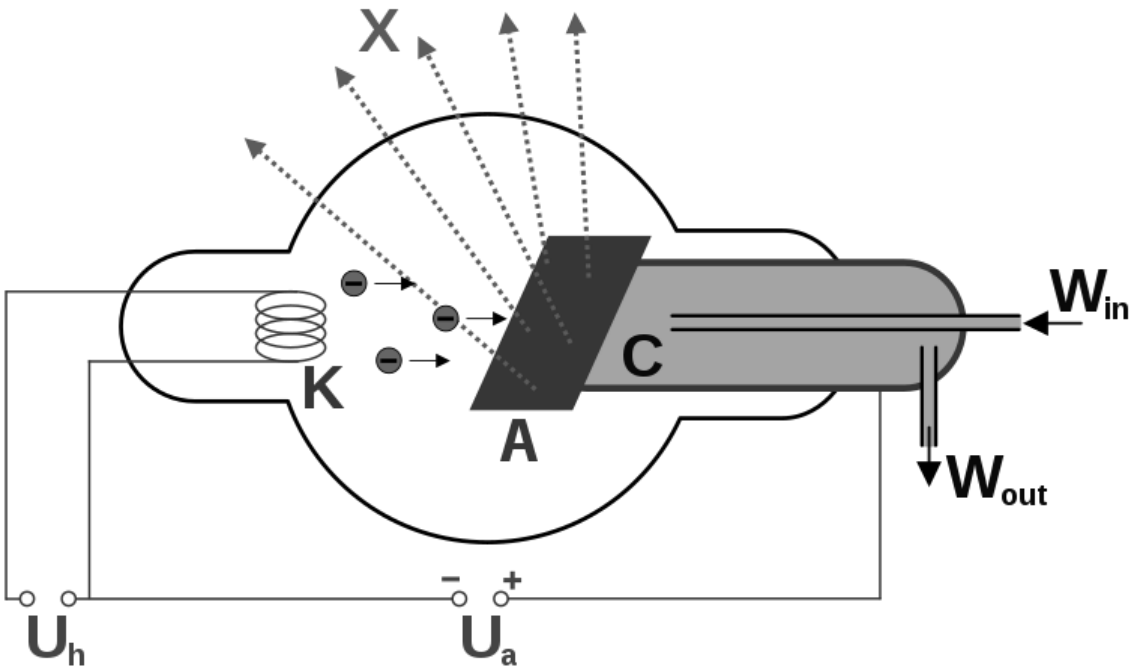

Figure 17. Scheme of X-ray tube with water cooling

at a certain distance (Figure 17). The electrically heated (U_h) cathode, K (normally a tungsten filament), is charged negatively and anode A is charged positively. The accelerating potential, U_a, between the electrodes is usually set at ~ 40kV. When the temperature of the cathode reaches a certain level, electron thermionic emission begins. These electrons bombard the anode and a spectrum of X-rays is produced. Anodes are designed such that the generated X-rays are focused on a single spot X in the tube. In this spot, manufacturers install windows, usually made of beryllium, which are strong enough to support the vacuum in the system and are very transparent for X-rays. Due to the constant electron bombardment and IR irradiation from the heated cathode, anodes increase their temperature rather quickly. This may cause deformations or even destruction of the X-ray emitting surface. To avoid this a water cooling system, C, is commonly used.

The spectrum of generated X-rays is dependent on the material the target is made of (Figure 18). It always consists of two main parts: Bremsstrahlung (radiation of deceleration of charged particles, white radiation or continuous spectrum background) and characteristic radiation of the anode target. The latter consists of peaks related to the transition of the electrons between levels in the atoms of the target. During the bombardment, the high-energy electron strikes electron from the 1s orbital (K shell) in the atom of the target, providing a hole. This is an unstable state for an atom. An electron from a higher energy level transits to fill this hole. The energy difference is emitted as an X-ray quantum. 2p(L shell) and 3p(M shell) electrons have the largest impact on this process. A transition from the

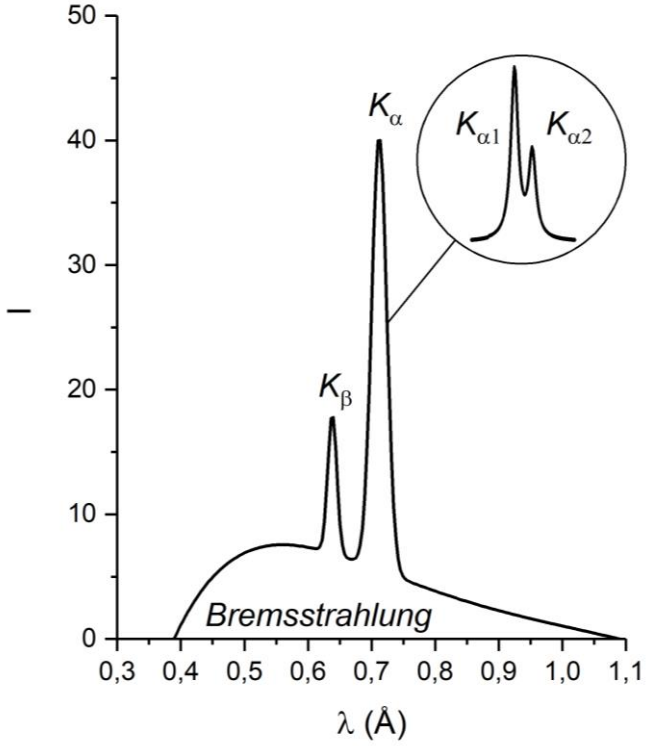

Figure 18. X-ray spectrum obtained from X-ray tube with Mo anode

L level is known as K_α; a transition from the M level is known as K_β. There are two possibilities for K_α transition: $K_{\alpha1}$ and $K_{\alpha2}$ corresponding to $2p_{\frac{3}{2}} \rightarrow 1s_{\frac{1}{2}}$ and $2p_{\frac{1}{2}} \rightarrow 1s_{\frac{1}{2}}$ respectively. There are 4 electrons in the $2p_{\frac{3}{2}}$ orbital and only 2 in the $2p_{\frac{1}{2}}$. This is why $K_{\alpha1}$ transition happens twice more often and therefore has higher intensity. The K_α transition itself happens more often than K_β due to closeness of L level. Because the energy of the K_α and K_β transitions is different for different atoms, the characteristic X-radiation can be altered by changing the material of the target.

Table 3. Wavelength (Å) of some common anode materials

Anode material	$K_{\alpha 1}$	$K_{\alpha 2}$	K_{β}
Ag	0.5594	0.5638	0.4971
Mo	0.7093	0.7136	0.6323
Cu	1.5406	1.5444	1.3922
Co	1.7890	1.7929	1.6208
Fe	1.9360	1.9400	1.7566

The other way of generation X-rays is to use a synchrotron. In such a facility, the electron beam is accelerated in a strong magnetic field and then forced to oscillate in the changing field of the insertion device (wiggler or undulator). These oscillations can generate a wide range of electromagnetic radiation and can be accurately modulated via tuning the magnetic properties of the insertion device. However, to obtain monochromatic radiation a high-energy electron acceleration facility is required. It is therefore impossible to carry out this method in the lab.

In order to obtain a clear diffraction pattern in the lab, the X-rays should be treated to give a monochromatic beam. This is important as every extra wavelength in the spectrum gives extra diffraction pattern. It can be difficult to analyse these patterns especially for complex, low symmetry systems. Normally, the K_{α} wavelength is used as the most intensive. The less intense K_{β} wavelength is filtered off using a thin foil. These filters are made of elements with have an atomic number that is one lower than the material of the X-ray tube anode. These elements have absorption maxima close to K_{β} of the X-ray source. For example, a Ni filter is used to remove Cu K_{β} wave whilst a Fe filter is used to remove Co K_{β}. In this approach, we lose about 50% of the beam intensity and still have both $K_{\alpha 1}$ and $K_{\alpha 2}$ radiation.

The other way to obtain only the $K_{\alpha 1}$ X-rays is to use monochromator. Typically this is a single crystal of germanium or silicon aligned to reflect only $K_{\alpha 1}$ X-ray waves. There are, however, other types of monochromators available. Using a monochromator decreases the initial intensity of the X-radiation but allows higher resolution diffraction patterns to be obtained.

It is not enough to have a perfect monochromatic X-ray beam for a successful diffraction experiment. It is also very important to have sensitive detector to accurately distinguish and evaluate the diffraction signal. Considering that the experiment requires the diffraction pattern to be measured at different incident beam angles, there are two approaches. The first is to use a scintillation detector, which measures the intensity of the signal at a certain point and then moves to another point. In this case, the information collection time per point is relatively small and the resolution is defined by the size of the detector. The second approach is to use a position sensitive detector (PSD), where information is collected from many points simultaneously and independently over a wide range of θ. The total time per point in these systems is much higher, and hence the signal to noise ratio is much better. The best PSD covers the whole range of scanned angles and therefore collects all the information simultaneously whilst only requiring a small amount of time for scanning. Such detectors are common for synchrotron and neutron diffraction instruments.

The alignment of beam optics is important for any diffraction experiment. One of the most common geometries used for the experiment is reflection (Figure 19). The X-ray tube (XRT) generates X-rays and they come out from the F point

(source). The beam passes through parallel slits (PS), which are also called Soller slit, to limit axial divergence. Then it goes through an entrance (divergence) slit (ES) with the required aperture (α_{ES}) and hits the sample surface (S) at θ Bragg angle. The beam diffracts at 2θ reflection angle and passes through receiving slit (RS) with required aperture (α_{RS}) into the monochromator (M) via an antiscatter slit (AS). Specific wavelength reflects on the monochromator and goes to detector (D) via another antiscatter slit (AS) to minimise parasitic reflections from the air. In Figure 19, SFC is a specimen focusing circle related to the alignment of diffracted beam. MFC is a monochromator focusing circle related to the monochromator alignment. DC is a diffractometer circle (goniometer) which is used for obtaining the geometry parameters.

This set up can be varied for different diffraction experiments. If the monochromator is installed in the incident beam, both fluorescence and radiation damage of the specimen are reduced by removing Bremsstrahlung. If the monochromator is placed in the diffracted beam, it eliminates fluorescence. If the monochromator is not used, and there is no elimination of $K_{\alpha 2}$ wavelength, the collected diffraction pattern becomes more complex. The whole set up can also be executed, with or without monochromator in transmission geometry. In this, the X-ray beam passes through the sample and diffracts on the other side. Transmission geometry can provide some advantages in a number of applications as it is more convenient to measure large interplanar distances, a smaller volume of sample is required, and the negative effect of the surface roughness (for powders) is largely reduced.

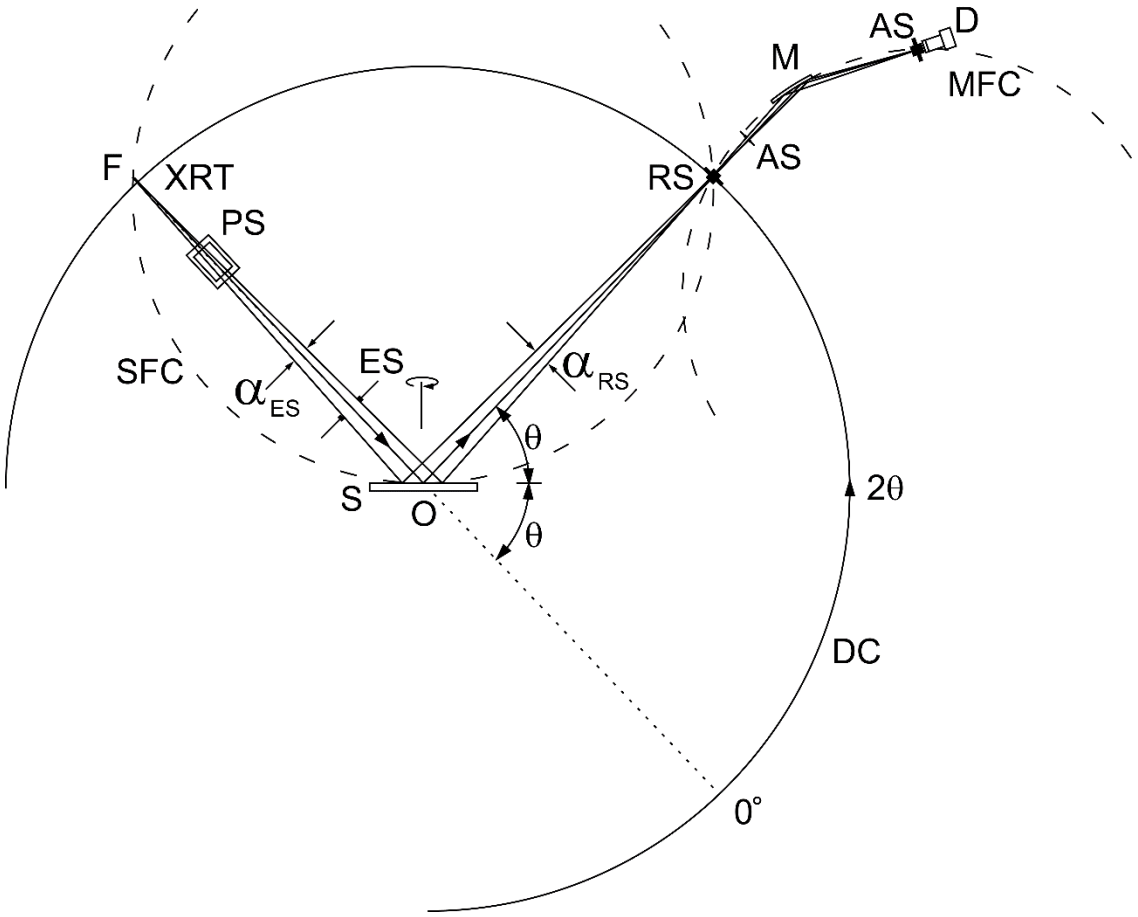

Figure 19. X-ray optics in the focusing plane of a conventional diffractometer in reflection geometry with monochromator

The diffraction experiment set up is almost equivalent for powders and single crystal data collection. The most significant difference is that if for powder diffraction a 2D diffraction data is collected, whereas a whole 3D diffraction sphere can be collected for a single crystal experiment. Every crystal is a 3D object and has anisotropy in diffraction properties. Depending on the side on which the incident beam enters, different patterns containing diffraction spots are obtained. Due to fundamental properties, despite the crystal orientation, d-spacing related angles (θ) remain the same. The angles (φ) related to the crystal orientation will vary with each

sample, while keeping the angular distance between the same pairs of spots constant. Such 3D pattern is very informative and allows even very difficult crystal structures to be solved.

A powder is a system containing numerous single crystals, each giving an individual 3D diffraction pattern. The entire picture is thus a superposition of these individual patterns. In these conditions, the diffraction spots are evenly distributed over all φ angles and form a diffraction line at certain θ angles. The simple summarizing of the single crystal 3D pattern along the same θ angles gives the same

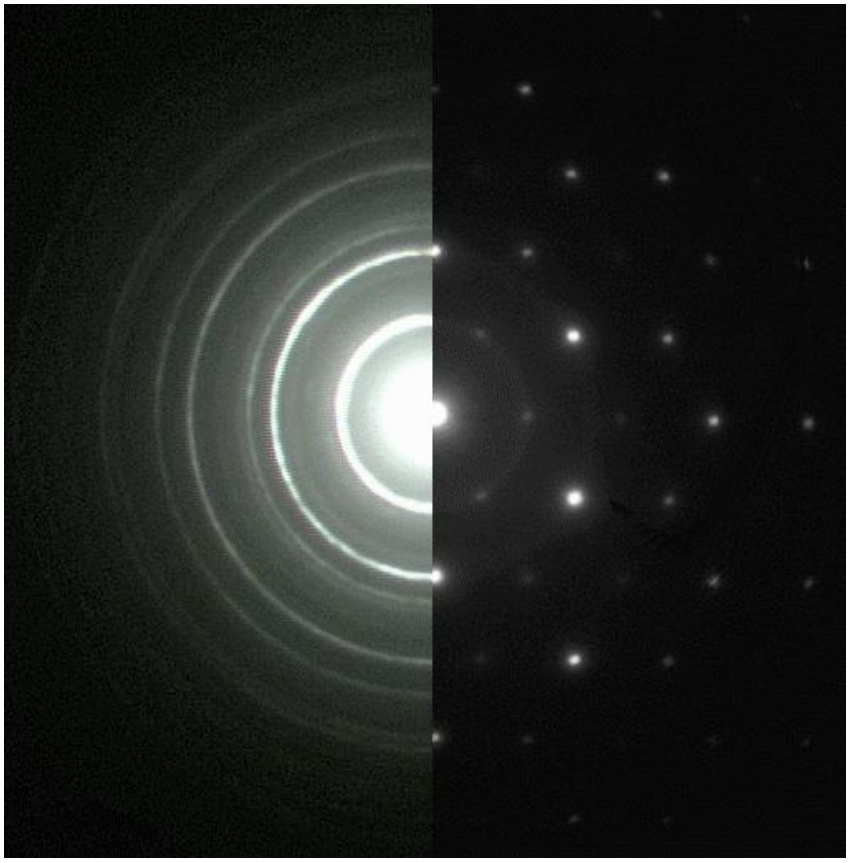

Figure 20. Comparison of single crystal and polycrystalline sample obtained via Debye-Scherer method. (Used with permission from the educational web-site Farlabs[199])

2D picture. This pattern is called powder diffraction pattern. In order to maximise the amount of crystal orientations in the powder sample it is rotated during the data collection. Figure 20 represents a comparison of a Debye-Sherrer polycrystalline powder pattern and single crystal pattern. Radial lines on powder pattern appear at the same d-spacing instead of peak spots.

Neutron diffraction

In general, a neutron diffraction study is very similar to a X-ray diffraction experiment. A beam of neutrons is scattered from a sample at a certain angles from the incident beam and a detector collects the data. Due to the wave-particle duality of neutrons, we can calculate their wavelength (λ) via the de Broglie equation:

$$\lambda = \frac{h}{mv}$$

In this equation, h is Planck's constant, m is the mass of a neutron (1.67×10^{-27} kg) and v is a velocity of the neutron. According to this equation, neutrons in equilibrium at room temperature have a wavelength of the correct order of magnitude (~1.4 Å) to conduct a diffraction study.

Unlike X-rays, the neutrons interact with the nuclei of atoms instead of the electron cloud. This is an advantage as all nuclei have similar sizes and the scattering power only depends on the nature of the atom. Nuclei of the different elements have different scattering power and there is no direct relation to the atomic number. Furthermore, different isotopes scatter neutrons differently. The cause of this is

apparently related to the structure of atomic core, which is still arguable in the scientific society[99]. By using neutron diffraction light elements in the first two periods of periodic table can be accurately determined and other elements with similar X-ray scattering factors can be distinguished via this technique. Another significant benefit of using neutrons is that, unlike X-rays, the signal remains intense even for high scattering angles, what allows the accurate measurement of very small features in crystal lattice. Neutrons also have a magnetic moment and so can be applied to study magnetic materials. There are, however, some disadvantages of neutron diffraction: not all the isotopes can be used in this experiment as some, like ^{10}B or ^{6}Li, are significant neutron absorbers and others would be induced to be radioactive. Further, a large complex facility is required to generate neutrons and, although it is possible to study both powders and single crystal, larger size of the sample is needed, as neutron-nucleus interactions are less intensive than X-ray-electron cloud collisions, while the intensities of neutron beams are lower.

Two main methods are used to produce neutrons for the study of materials. The first is the use of a nuclear reactor, where neutrons are generated as a constant polychromatic flow during the fission chain reaction. The other way is spallation of heavy atoms by accelerated high-energy protons. When the accelerated particle hits the nucleus, it falls apart, releasing neutrons. Due to the cyclic nature of proton acceleration, the polychromatic neutrons are generated in pulses; therefore, this kind of source is called pulsed spallation. Neutron diffraction experiments in this work were carried out in ISIS Neutron and Muon Spallation Source, Oxfordshire UK, where neutrons are generated at the Ta target stations.

Because the neutrons produced have velocities that are much higher than necessary they are decelerated using a moderator. At the ISIS facility, Gd-poisoned liquid methane at 110K is commonly used.

A diffraction experiment with neutrons can be conducted in the same geometry as X-ray experiment. The incident beam of neutrons must pass via a monochromator to separate one wavelength that is suitable for the experiment. In this case, the d-spacing will be a function of the measured angle of reflection. The collected diffraction pattern is no different to those obtained in a standard X-ray experiment except the peak intensities. However, during monochromatisation, a significant part of the neutron beam is lost. Therefore, to obtain enough information a longer collection time is required. To overcome this problem another experimental set up was introduced: time-of-flight neutron diffraction (TOF ND).

In TOF ND, the 2θ angle of diffracted beam remains fixed but the wavelengths of neutrons vary. According to Bragg's Law, different d-spacings are still accessible at different λ. Nevertheless, it is still necessary to separate the required neutrons from the main pulse. Returning to the de Broglie equation it is given that neutrons with different velocities have different wavelengths. Considering that source is pulsed, it is obvious that in each cycle neutrons with higher velocities and therefore smaller λ will come first. These are followed by slower neutrons and the slowest neutrons, with the longest λ will be last. This gives a range of wavelengths distributed over a known time. It is then easy to calculate the current wavelength and therefore the measured d-spacing.

$$\lambda = \frac{ht}{mL} = 2d \sin\theta$$

$$d_{hkl} = t\frac{h}{mL \sin\theta}$$

Where t is the time-of-flight, L is the distance defined by instrument (constant), m is the mass of a neutron (1.67×10^{-27} kg) and θ is the diffraction angle defined by the instrument (constant). In these conditions, the d-spacing is a linear function of time elapsed since the spallation event. This allows the whole neutron beam to be utilised and more data in a smaller amount of time can be collected.

As the general approach to the experiment has been altered, the methods used to improve the resolution are different. The main way to improve resolution in TOF diffractometers is to increase the flight path in order to allow more time for neutrons to separate over the velocities. For example, HRPD (High Resolution Powder Diffraction) TOF in ISIS with flight path ~96m is the highest resolution diffraction instrument at the facility. To eliminate the "frame overlap problem" appearing in an experiment when slow neutrons are overtaken by fast neutrons in the next cycle, especially in long flight path diffractometers, rotating beam choppers are applied.

Powder diffraction pattern

A powder diffraction pattern is a 2D function of d-spacing, which describes the intensity of diffracted beams. A diffraction pattern contains four main types of information:

1. Diffraction peak positions are determined by the size and shape of crystal lattice and are influenced by the instrument geometry (zero correction, sample displacement);

2. Peak intensities are determined by the type of atoms in the cell, their positions and amount in the diffraction planes, and their thermal motions. Further, some microstructural features like the preferred orientation of crystals can affect intensities. The nature of the beam may also affect the intensity.

3. Peak width is determined by instrument optics and microstructural features such as crystallite size or microstrain.

4. Background is determined by the instrument geometry and optics, the fluorescence of the sample and the presence of any amorphous phases. It may contain short-range order information as well.

In this way, a powder diffraction pattern is a function of background, peak positions, peak broadening, and structural factors. Normally, to obtain crystal structure during the standard experimental data processing, most attention is paid to the peak positions and peak intensities. Peak broadening and background are treated only as mathematical functions that are not related to the sample. However, in some cases, particularly where the microstructure is being studied, the experiment may be set up in a way that the peak shape and background provide extra significant information.

Peak positions can be defined via the equations discussed in the "Diffraction" section. In general, any peak position can be expressed as:

$$2\theta_{hkl} = F(d_{hkl}) + ZC + \frac{2\Delta H \cos\theta}{R},$$

where F(d_{hkl}) is a peak position in 2θ, defined via the cell parameters, with the current wavelength , ZC is the goniometer zero correction, ΔH is the sample height displacement and R is the goniometer radius.

Peak intensities are dependent on many factors:

$$I_{hkl} = K * |F_{hkl}|^2 * P_{hkl} * E_{hkl} * T_{hkl} * (LP)_\theta * A_\theta * DW_\theta$$

where K is a scale factor, F_{hkl} is a structure factor that is related to the planar alignment of atoms within the unit cell, P_{hkl} is the multiplicity of symmetrically equivalent reflections (e.g. for a cubic cell there are 8 planes (1 1 1), (-1 1 1), (1 -1 1), (1 1 -1), (-1 -1 1), (-1 1 -1), (1 -1 -1) and (-1 -1 -1) which have the same d-spacing such that the reflection multiplicity is 8), E_{hkl} is the extinction coefficient, T_{hkl} is the preferred orientation, i.e. texturing of the sample crystals, $(LP)_\theta$ is the Lorentz-polarisation factor ($\frac{1+\cos^2 2\theta}{\sin\theta \sin 2\theta}$), A_θ is the wavelength absorption coefficient, DW_θ is the Debye-Waller factor (atomic displacement parameters, ADPs).

The structure factor is a complex mathematical function that describes the amplitude and phase of a diffracted wave. In other words, the structure factor gives the scattering power from the crystal lattice planes that are characterised by Miller indices h, k, l, and is dependent on the atom types and their coordinates:

$$F_{hkl} = \sum_{n=1}^{N} (f_a)_n (\cos[2\pi(hx_n + ky_n + lz_n)] + i \sin[2\pi(hx_n + ky_n + lz_n)])$$

f_a is an atomic scattering factor that is unique for every type of atom. This factor changes over the 2θ range and can be calculated by the equation:

$$f_a\left(\frac{\sin\theta}{\lambda}\right) = \sum_{i=1}^{4} a_i e^{-b_i \frac{\sin^2\theta}{\lambda^2}} + c$$

This expression is valid over the range $0 < \frac{\sin\theta}{\lambda} < 2\ \text{Å}^{-1}$ and requires nine coefficients (also called Cromer-Mann constants).

The Debye-Waller factor describes how the electron density of the scatterer is spread in space. Crystals are complex systems where the ions vibrate on their sites: with an increase in temperature, these vibrations get larger. The vibrations may be isotropic (spherical), but often have a more complex shape due to the structure formed by the surrounding ions. The vibrations are more noticeable at lower d-spacing. The coefficient for isotropic thermal displacement is given by:

$$DW_\theta = e^{-\frac{2\pi^2 U_{iso}}{d^2}}$$

For a more accurate description of ions is the lattice, the anisotropic thermal displacement parameters for ellipsoidal vibrations can be used:

$$DW_\theta = e^{-(\beta_{11}h^2+\beta_{22}k^2+\beta_{33}l^2+2\beta_{23}kl+2\beta_{13}hl+2\beta_{12}hk)}$$

This equation uses the reciprocal thermal parameters tensor, which is more convenient to use in a computational process. The following equations are used to convert these into real space displacements that are independent from unit cell dimensions:

$$U_{11} = \frac{4\beta_{11}}{8\pi^2 a^{*2}}$$

$$U_{22} = \frac{4\beta_{22}}{8\pi^2 b^{*2}}$$

$$U_{33} = \frac{4\beta_{33}}{8\pi^2 c^{*2}}$$

$$U_{23} = \frac{4\beta_{23}}{8\pi^2 b^* c^*}$$

$$U_{31} = \frac{4\beta_{31}}{8\pi^2 c^* a^*}$$

$$U_{12} = \frac{4\beta_{12}}{8\pi^2 a^* b^*}$$

Roughly, U_{11}, U_{22}, U_{33} are related to the shape of the ellipsoid, whilst U_{12}, U_{13}, U_{23} are related to its orientation. U_{iso} can be obtained straight from the real-space metric (g_{ij}) and atomic displacement (b^{ij}) tensors via the contraction:

$$U_{iso} = \frac{1}{6\pi^2} g_{ij} b^{ij}$$

This kind of fine information can only be extracted from the very good data collected at very small d-spacings (down to 0.5Å).

The background can normally be modelled using various functions (e.g. Chebyshev, cosine, logarithmic, linear approximation). The most suitable approach should be selected for each pattern collected.

Several functions can be used to describe the peak shape. The most common function for XRD is the modified Thompson-Cox-Hastings pseudo-Voigt function. This is a combination of Gaussian and Lorentzian peak functions.

$$P(x)_{PV} = \eta\Gamma_L + (1-\eta)\Gamma_G$$

where η is a ratio of the Lorentzian to Gaussian with the same width, and Γ_G is given by:

$$\Gamma_G = \sqrt{U\tan^2\theta + V\tan\theta + W + Z\cos^2\theta}$$

$$\Gamma_L = X\tan\theta + Y/\cos\theta$$

A polynomial equation may be used to relate η and the full width at half maximum ($fwhm$) of the peak:

$$\eta = 1.36603\left(\frac{\Gamma_L}{\Gamma}\right) - 0.47719\left(\frac{\Gamma_L}{\Gamma}\right)^2 + 0.11116\left(\frac{\Gamma_L}{\Gamma}\right)^3$$

$$\Gamma = \sqrt[5]{{\Gamma_G}^5 + a{\Gamma_G}^4\Gamma_L + b{\Gamma_G}^3{\Gamma_L}^2 + c{\Gamma_G}^2\,{\Gamma_L}^3 + d\Gamma_G\,{\Gamma_L}^4 + \,{\Gamma_L}^5}$$

$$a = 2.69269, b = 2.42843, c = 4.47163, d = 0.07842$$

This function has no physical interpretation. However, if also obtained on a corresponding standard, the function can be used as a basis for other microstructure related studies.

For PXRD, several kinds of standards of well-characterised materials are available. These are used for angular calibration of diffractometers to reveal systematic errors, to obtain instrument impact to peak shapes and background, and for quantitative analysis for intensity calibration. One of the most common standards suitable for angular calibration are silicon powder (NIST SRM640c, a=5.4311946Å at 298K), silicon single crystal with Si/Ge epitaxial layer (NIST SRM2000 d(220)=1.920161Å at 296K), and Mica powder for low angles (NIST SRM675 d(001)=9.98101 Å at 298K). The main standard for peak shape calibration is lanthanum hexaboride LaB_6 (NIST SRM660c a=4.15695Å at 299K). Sintered alumina plates (NIST SRM1976b) are widely used for instrument response calibration.

Rietveld refinement

Hugo Rietveld reported this method in 1967 for neutron powder diffraction data[100]. Subsequently this method has been successfully used on data collected in all the other types of powder diffraction experiments. At this time, the processing of single crystal data was a relatively routine operation, even though it was not always possible to collect sufficient quality data for structure determination. However, the sustainable processing of powder patterns was nearly impossible due to the overlapping of peaks. The introduction of this method became a significant boost for crystallography and material science.

To perform a Rietveld refinement on a powder pattern there should be initial model close to the studied crystal structure. This model is refined by least-squares procedure of the residual.

$$M = \sum_{i=1}^{N} w_i [y_i(obs.) - y_i(calc.)]^2$$

Where $y_i(obs.)$ is the intensity of an observed point i on the diffraction pattern, $y_i(calc.)$ is the calculated intensity, taking into account the impact of the background and peak broadening, w_i is the weight of the data point given by $1/y_i(obs.)$.

The calculated intensity of each data point can be obtained by considering the overlapping of peaks via the equation:

$$y_i(calc.) = B + \sum_{k=k_1}^{k_2} I_{hkl} P(x)$$

where B is the background intensity of the point, I_{hkl} is the intensity of the peak (discussed above) and P(x) is a profile function. This allows the impact of all overlapping reflections to be included.

The whole process is iterative and is best applied in a computational manner. An improvement shift is calculated for every iteration and once this reaches a certain level the process stops. The following statistical indicators are used to estimate the agreement with the refinement model[101].

Profile R factor:

$$R_p = \frac{\sum_i | y_i(obs.) - y_i(calc.)|}{\sum_i y_i(obs)}$$

Weighed profile R factor:

$$R_{wp} = \sqrt{\frac{\sum_i w_i |y_i(obs.) - y_i(calc.)|^2}{\sum_i w_i y_i^2(obs.)}}$$

Bragg R factor:

$$R_I = \frac{\sum_k | I_k(obs.) - I_k(calc.)|}{\sum_k I_k(obs.)}$$

Expected R factor:

$$R_{exp} = \sqrt{\frac{N - P}{\sum_i w_i y_i^2(obs.)}}$$

Goodness-of-fit:

$$GOF = \chi^2 = \frac{R_{wp}}{R_{exp}}$$

In the above equations I is the integrated intensity of a single reflection, N is the number of observed points, P is the number of refined parameters. R_{exp}

represents the quality of the data and R_{wp} indicates the quality of the fitted pattern. The Bragg R factor can be used to evaluate the structural parameters without profile influence. The best parameter to evaluate the quality of the refinement is a topic that remains under discussion[102]. Currently, the best approach is considered to be a combined revision of Goodness-of-fit, weighed profile R factor (R_{wp}) and visual evaluation of fitted and difference curves on the refinement graph.

Several computer programs for performing Rietveld analysis of diffraction data are available. In this work GSAS-II[103] and TOPAS-Academic[104] were used.

Structure solution techniques

In this work, three methods were used for structure solutions: charge flipping, intrinsic phasing and simulated annealing. Charge flipping is a method based on algorithms that work with dual-space (direct and reciprocal). It allows a Fourier map of scattering densities in the lattice to be obtained. This method only requires the lattice parameters and intensities of indexed peaks to be known: no symmetry information or chemical composition is required. This method can be used for all kind of diffraction experiment. Initially, every observed amplitude (F_{hkl}) is assigned to a randomly generated phase and all missing amplitudes are assigned to be zeros (reciprocal space). The iterative algorithm then begins by obtaining a map of electron densities in the lattice via inverse Fourier transform of observed amplitudes (direct space). The sign of the electron densities that are below a certain threshold level is flipped i.e. multiplied by -1, all others remains unchanged. The

obtained perturbed electron density map undergoes Fourier transform to gain provisional structure factors with new phase values (φG). Final structure factors are calculated by combining the experimental structure factors with phases φG and all unobserved F_{hkl} are reset to zeros. These calculated factors are compared with the experimental factors to find the convergence of solution. If the result is not satisfactory, the cycle is repeated. The disadvantage of this method is that the relatively high-resolution data (d<1.3 Å for light atoms) with reasonable completeness is required.

The Intrinsic Phasing algorithm uses information obtained via the Patterson method (direct generation of the Fourier map with zero phase angles from square structural factors). Using indexed group, the equivalent reflections are averaged and the cell is transformed into the *P1* space group. Unlike charge flipping, the intrinsic phasing starts with the defined Patterson superposition minimum function. Further dual-space recycling, which is similar to charge flipping, is accompanied by intermediate space group redetermination and followed by the averaging of equivalent reflections to enhance the quality of the electron density model. To improve the refinement, statistical noise is introduced in every cycle via the random omission of a certain fraction of reflections. This algorithm allows good results to be obtained (even with incomplete datasets) and requires slightly less computational resources.

Simulated annealing is a method of structure solution based on randomising the parameters of the known model. Normally this method can be successfully used when some information about the system is known, for example

the expected range of cell parameters or the atomic composition of the lattice. The initial parameters of the model can be widely divergent from the actual structure. The model parameters are randomly modified within an amplitude that is related to the virtual temperature. The diffraction pattern of the new model is calculated and compared to the observed data. If the new parameters give an improved fit, they are accepted as the best and next point. If the new parameters make the fit worse, they are accepted as the next point with a probability depending on the current temperature. The temperature slowly decreases during the cycles and makes the probability of accepting the worse fit smaller. Eventually, when the temperature reaches zero, the system stabilises with the best-fit parameters. This method allows relaxation of a known system to fit the experimental data when regular Rietveld refinement cannot converge with such changes.

All of these methods give an approximate model that should be further refined by the Rietveld method to obtain an accurate structure.

Mössbauer spectroscopy

Mössbauer spectroscopy is a method of studying a crystalline material and is based on the Mössbauer effect. The principles of this effect are rather simple. A radioactive nucleus emits a gamma quantum without energy loss due to recoil and transits into a non-radioactive state. Subsequently another nucleus of the same kind in the sample to be studied, absorbs the emitted gamma quantum and turns into a radioactive isomer.

Not all isotopes are Mössbauer-active. To date, more than 40 elements were reported to have Mössbauer-active isotopes, but not all of them are convenient to use. The most commonly used are ^{57}Fe, ^{119}Sn, ^{121}Sb, ^{129}I.

The experimental conditions, like the source of the initial radioactive nucleus, the temperature and the structure of the spectra may vary significantly depending on the element used. In all cases, there is a source of γ-rays containing the radioactive isomers of the studied isotope and an absorbing sample containing the same non-radioactive isotopes.

For example, ^{57}Co is used as the γ-ray source to study the state of iron in a crystal lattice. First, ^{57}Co decays via electron capture into ^{57m}Fe:

$$^{57}_{27}Co + \bar{e} \rightarrow {}^{57m}_{26}Fe + \nu_e$$

The metastable isomer ^{57m}Fe turns into the stable condition ^{57}Fe emitting a γ–quantum:

$$^{57m}_{26}Fe \rightarrow {}^{57}_{26}Fe + h\nu_\gamma(\sim 14.4\ keV)$$

The emitted γ–quantum irradiates the absorbing sample that contains ^{57}Fe:

$$^{57}_{26}Fe + h\nu_\gamma \rightarrow {}^{57m}_{26}Fe$$

This last process is called nuclear gamma-resonance. This process is only possible when the γ-quantum has a very specific energy. For a gas or liquid, even the very weak energy of recoil during the emission process may be dissipated, affecting the gamma-quantum to the extent that it never has the required energy to be in a window for the corresponding nuclear gamma-resonance. In the case of a solid material, however, the crystal lattice may absorb only a discrete amount of energy

that is larger than a single γ-quantum of such transition and recoil energy loss does not happen.

The energy of the emitted gamma-quantum varies depending on the surroundings due to thermal motion and the electron state of isotope. Thus, if the isotopes in the source and in the sample are in the same electron and crystallographic environment, there is no difference in energy and therefore no issues with gamma-resonance. However, if the oxidation state or surrounding atoms are not the same we need to modulate the energy of γ-rays very slightly in order to obtain gamma-resonance. The very elegant solution for this problem was done by use of the Doppler Effect (movement of γ-ray source from and towards the sample). Calculations have shown that already 1mm/s allows a successful change of γ–quantum energy to potentially achieve resonance again.

The two main options for the geometrical set up of Mössbauer experiment are transmission and reflection. When γ-rays are absorbed by the isotopes in the sample, they relax in the same way they do on the source. As this process happens isotropically (in all directions), there is the possibility to work out the change in the intensity of the beam caused by gamma-quantum absorption of the sample. In the case of a transmission experiment, the detector counts the amount of energy passed through the sample depending on the speed of moving source (absorption mode). In the case of reflection geometry being used, the detector distinguishes the amount of energy came from the sample only as well depending on the speed of moving source (fluorescence mode). Transmission geometry is more sensitive, but it is inapplicable for large samples, where reflection geometry has much more use.

The data obtained is interpreted by doing a comparison with the crystallographic state of the source. In the case where the source and sample are in the same state, a peak is observed at 0mm/s speed as there is no difference in energy. This difference is called chemical shift (isomeric shift, IS). For example, the chemical shift values for iron depends on the electron density in both the 4s and 3d-orbitals. Increasing the oxidation state for iron ions normally changes the chemical shift towards negative values. The electronegativity of the ligands in the crystal also plays a significant role on the chemical shift (Table 4).

Table 4. Examples of chemical shifts of the different compound of iron with different oxidation states

Compound	Oxidation state	Chemical shift
FeF_2	+2	1,34
$FeCO_3$	+2	1,23
FeF_3	+3	0,48
FeOF	+3	0,41
α-Fe_2O_3	+3	0,36
α-Fe	0	0
$SrFeO_3$	+4	-0,17
La_2LiFeO_6	+5	-0,41
K_2FeO_4	+6	-0,89

Another informative part of the data obtained is the quadrupole splitting (QS) of the resonant peaks. In practice, this depends on the symmetry of the surroundings of the studied atom. Highly symmetrical surroundings give very narrow quadrupole splitting while the opposite is true for unsymmetrical surroundings. In this work Mössbauer spectroscopy was used to gather more information on the Fe environment in doped $NaFe(SO_4)_2$. This allows local disorder that is invisible for other techniques to be evaluated.

Raman and IR spectroscopy

Raman and IR spectroscopies are used to obtain information about the vibrational and rotational modes of functional groups in the crystal lattice. For liquid or gas phases, these techniques are relatively straightforward: the vibrations and rotations of the functional group are almost unaffected by the media and thus are very similar for different systems, making them easy to analyse. In crystalline systems however, the vibrations and rotations of functional groups are strongly affected by the lattice environment. Therefore the task of correlating the Raman/IR spectra with the structure is more challenging.

When functional group adsorbs a photon ($h\nu$) with an energy that corresponds to the medium or far IR spectrum, it transits from one vibrational energy level (ground state) to another (virtual exited state). The system cannot stay in the exited state and relaxes back to the ground state with photon emission (Figure

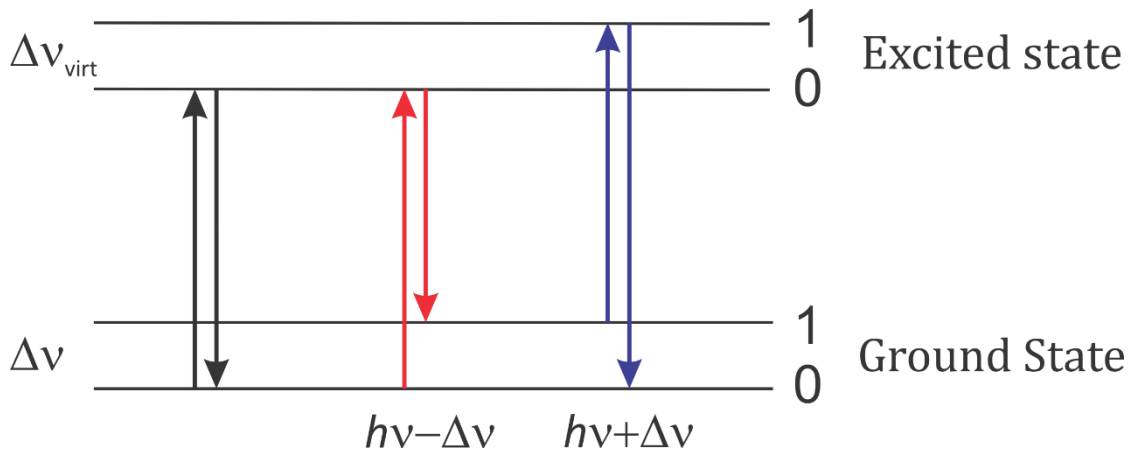

Figure 21. Rayleigh scattering (black), Stokes scattering (red) and anti-Stokes scattering (blue)

21). If the photons are scattered elastically, the system returns to the same energy state: this is Rayleigh scattering. If however, the photons are scattered inelastically, the system returns to a different state. If it is lower in energy, the transition is called Stokes scattering; if it is higher in energy such case is called anti-Stokes scattering. The elastic scattering mode is IR active; inelastic scattering modes are Raman active.

An IR spectrum is an absorption spectra as a function of wave number. There are two main ways to collect an IR absorption spectrum: with a monochromatic wavelength, where the intensity of each IR wavenumber is recorded separately; and with a polychromatic IR beam, when the whole spectrum is recorded using a Michelson interferometer and processed via Fourier transform.

Raman spectrum data collection is a more complex task. A monochromatic laser light induces the polarisation of the functional groups in the sample. As most of the photons scatter elastically and only a few scatter inelastically, the signal is very weak. Complex interferometers are used to separate the elastic Rayleigh scattering from the inelastic Stokes and anti-Stokes scattering. Stokes and anti-Stokes photons have a lower or higher frequency (Raman shift) than the source. A combination of the intensities of Raman shifts and their frequencies is the Raman spectrum. Normally, frequencies are converted to wavenumbers for convenience in the data processing.

The intensity of the IR active line is a function of the dipole moment of the functional group. The intensity of the Raman active line is a function of the polarizability of the functional group. Therefore, these two spectroscopic techniques are complimentary and allow the study of how the bonds in functional groups vary

depending on the crystalline surrounding. Different neighbouring features in the crystal lattice give different dipole moments and polarisation of the functional group, therefore changing the intensities and/or positions of the peaks in the spectra. Compression caused by the lattice also affects the line positions and this can also be an important source of information.

Electrochemical impedance spectroscopy

Electrochemical impedance spectroscopy (EIS) is a method of investigating the conductive behaviour of a system with an alternating current. The technique varies depending on the physical state of the studied system. In this work only ceramic systems are considered.

Every solid ceramic system contains certain elements responsible for charge transfer (red line on Figure 22). The first is the bulk grain conductivity of the material (G on the Figure 22). This is process happening in the mass of single crystal, i.e. conductivity of ideal crystal. Real ceramic systems are not ideal and consist of

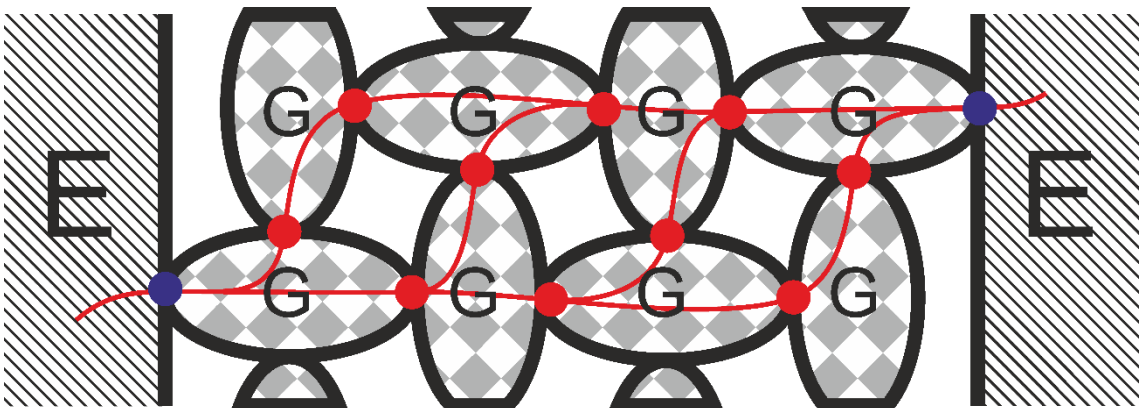

Figure 22. Model of charge transfer in ceramics during the EIS experiment

agglomerations of such crystals (grains). The charge passes through contact surface of grains – grain boundaries, second element (red dot on the Figure 22). To collect the charge from the ceramics it should be in contact with the current collector E, third element (blue dot on the Figure 22). This typical scheme represents all three main processes in conductive ceramics.

In ceramics, these processes are not simply the movements of the charge carrier (electron or ion). All these transitions can be considered as heterogeneous passage between two phases. Thus for a single act of charge transfer to occur, the charge carrier must have enough energy, which can be designated as polarisation. Act of charge transfer happens once it exceeds certain level of polarisation.

The nature of the polarisation depends on the surrounding and the type of the charge transfer. For bulk grain conductivity, the polarisation is between two small sites in the crystal lattice where the charge carrier may sit. For conductivity at the grain boundaries, the polarisation is between two relatively large grains that have charge carriers on their surfaces. In case of charge transfer between the grains and the electrode, there are polarisations responsible for possible transformations (electrochemical oxidation-reduction), adsorption on the surface or simple transition into a media with significantly different conductivity.

The concept of polarisations is very important for understanding the impedance experiment. It is very difficult to make an analytical equation that accurately describes the charge transfers in a system. In impedance spectroscopy, the equivalent electrical circuit that approximately corresponds to the processes of

charge transfer is built. Polarisation of the charge carrier can be considered as a capacitor with a certain capacity (C), given by:

$$C = \frac{Q}{U}$$

Here Q is a charge and U is a polarisation. Given that a capacitor does not conduct electricity once charged, an extra element is needed to allow current to leak – a resistor connected in parallel. Initially, when current is applied to the system, the resistance of the capacitor is ideally close to 0 Ohm and therefore all the current goes through the capacitor i.e. polarises the media. Once the capacitor is charged i.e. polarisation exceeds a certain level, the charge carrier is able to transfer to another site with some resistance (resistor impact) (Figure 23).

In the standard case of ion conducting ceramics, there are two different polarisations with electricity leakages (grain bulk and grain boundaries) and one without leakage (electrode blocking). In the case of a material showing electronic conduction or electrochemical transition, the electrode blocking also has a leakage. From Figure 22, it is obvious that in such a model the elements responsible for grain bulk, grain boundaries and electrode part should be connected in series. Considering the infinite amount of grains in the sample, the total impact of one type

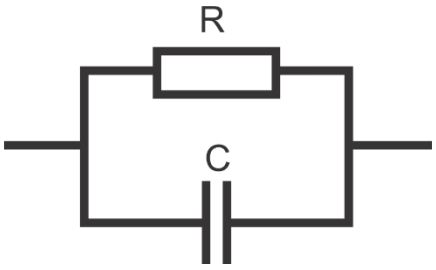

Figure 23. Equivalent circuit of transition of charge carrier

can be modelled as a single element in superposition. This way the complete electric circuit would contain only three elements (Figure 24).

Impedance is the total resistance of the system to alternating current. Alternating current is the current that changes direction according to sinusoidal function over the time:

$$i = I_{max} \sin \omega\tau$$

Where *i* is the current at time τ, ω is the frequency of sign change and I_{max} is the current at maximum amplitude.

Direct current (DC) is not used as it does not provide enough information to build an equivalent circuit. However, if alternating current (AC) is applied the response of the system is different depending on the frequency of current. At a given current, the charge of the capacitor is a function of time, therefore at high enough frequencies the polarisation may not be completed until the current reverses in direction. As a result, the total resistance of the single element varies depending on AC frequency. This resistance is called active (real) resistance. Furthermore, when the direction of the current changes there is some time required for capacitor

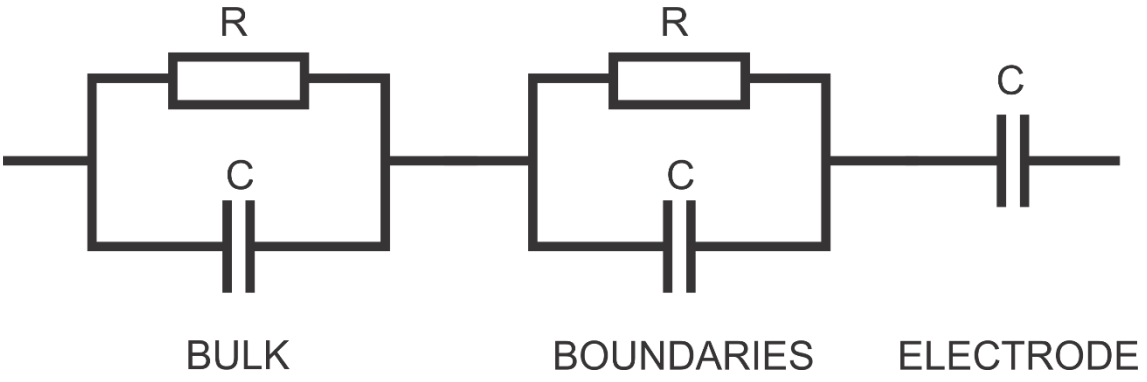

Figure 24. Equivalent circuit of ceramic ion conductor

discharging. This discharge is having a slightly different phase (φ) to the initial current. Accurate measurement of the difference between phases allows the reactive (imaginary) resistance to be calculated.

$$\tan\varphi = \frac{\vec{Z}_{Imaginary}}{\vec{Z}_{Real}}$$

Impedance is a complex number, which can be represented as a vector sum of these two resistances.

$$\vec{Z} = \vec{Z}_{Real} + \vec{Z}_{Imaginary} = R + i\frac{1}{\omega C}$$

R is the resistance of the system, $i = \sqrt{-1}$, ω is the AC frequency, C is the capacitance of the system.

Knowing the real and imaginary resistances at different frequencies, it is easy to build a Nyquist plot $\vec{Z}_{Imaginary} = -f(\vec{Z}_{Real})$. Each point on this plot is a complex number and has extra information about the applied frequency (Figure 25).

There are three main elements on the graph: two semicircles and a direct line. Semicircles represent the impact of the grain bulk and the grain boundaries; a direct line is the product of the electrode response. Often semicircles may slightly change their shape, for example, to be compressed, when extra processes happen in the material. To model this behaviour, an extra element can be introduced to the circuit – the Constant Phase Element (CPE). Whilst this element does not have any real world meaning, since it describes very complex processes, it introduces a coefficient showing how close it is to a regular capacitor.

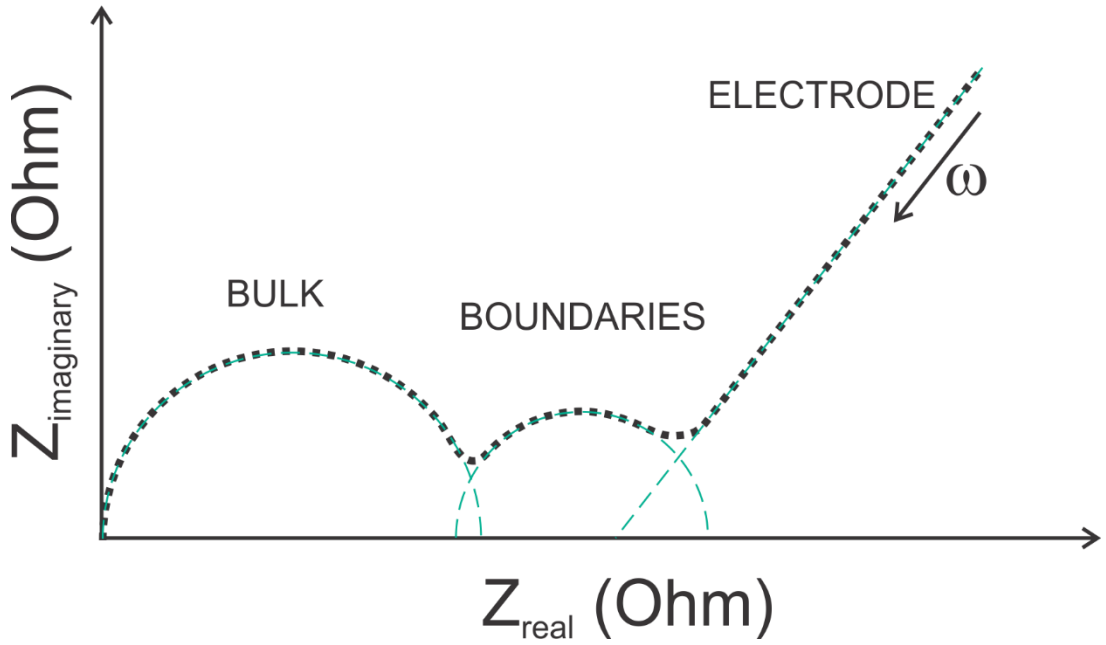

Figure 25. Nyquist plot of typical ceramic ion conductor

The method of electrochemical impedance spectroscopy does not directly give any values (resistance, capacitance of elements) for the charge transfer processes occurring in the sample. However, a known model can be fitted via a least squares refinement, to extract all the necessary data. In this work this refinement procedure was performed using the ZView software[105]. The reliability of the obtained values should be judged on statistical indexes, graphical fit and the values themselves. The latter is important as the complexity of the model can, in some instances, give false minima in the fitting process. Any fit therefore should be a subject of careful investigation.

The main information gathered from an EIS study are resistances of the components in the ceramic that are responsible for charge transfer. Nevertheless, it is also possible to extract some data about the capacitances of these elements. It should be noted that for each circuit elements, the values of the parameters remain

similar across different systems[106]. For example, capacitance for grain bulk conductivity is typically of the order of 10^{-10}-10^{-12}F and the compression coefficient is close to 1. The capacitance for grain boundaries is normally of the order 10^{-7}-10^{-8}F and the compression coefficient is near 0.8. The capacitance of the electrode response usually shows values of the order of 10^{-3}-10^{-6}F and the compression coefficient is in the range 0.2-0.5.

Samples for EIS are usually pellets that have two parallel sides and are of a known area and thickness. The electrodes applied to both sides, are usually noble metals that are inert to the sample (e.g. silver, gold, platinum), but can be made of a material that has the necessary redox properties. Often the electrodes are applied as a slurry in a polymer solution and are cured at a high temperature.

To calculate the conductivity of sample the following equation is applied:

$$\sigma = \frac{l}{SR}$$

Where *l* is the distance between the electrodes, S is the area of the electrode and R is a resistance of the circuit element.

Another interesting value to extract from conductivity data is the activation energy of ion migration (E_a). This energy can be calculated if measurements are repeated at different temperatures. In this case, an Arrhenius equation for conductivity can be applied:

$$\sigma = Ae^{-\frac{E_a}{RT}}$$

Where A is a pre-exponential coefficient, R is a gas constant and T is absolute temperature. In practise, this equation needs to be transformed:

$$\lg \sigma = \lg A - \frac{1000}{T} \cdot \frac{E_a}{2300R}$$

Using the data obtained by carrying out the impedance experiment at different temperatures, a graph of $\lg \sigma = f(\frac{1000}{T})$ can be plotted. If the studied sample does not undergo any changes, the plot is a straight line with a gradient equal to $-\frac{E_a}{2300R}$. If however, there is a break in the line direction, the activation energy must have changed suggesting a change in the charge transfer mechanism as the result of structural changes due to temperature. This method can allow phase transitions that are invisible to other methods (e.g. small rearrangement of atoms) to be detected. However, this method has a significant disadvantage in that it is also sensitive to impurities, as they overlap with the matrix making data interpretation very difficult. Furthermore, sometimes it is not possible to extract enough data as grain bulk and grain boundaries in the sample cannot always be separated.

In this work, a system for the automatized collection of impedance data at different temperatures has been set up in order to allow long consistent measurements with reliable repeatability without any operator supervision. For this, the furnace and the impedance analyser were connected to a computer. A control program was written in the LabView Software environment[107]. This control program consists of several elements: the furnace/temperature control module, the impedance analyser control unit, the output data recording/calculation procedure, the schedule builder and a cycling module. There are three stages in a typical cycle. The first is the Temperature Set stage, where program sends a required temperature to the furnace and monitors it until the required heat level is reached. Once

temperature has stabilised in a defined corridor (usually ±1-2^{o}C), the second, Equilibration stage begins: the program waits for a certain amount of time (15-30 min, defined by user) to ensure equilibration. The Scanning stage starts when temperature is stable and the program send a signal to an impedance analyser with settings to execute the scanning. The analyser sends back to the computer the impedance spectrum that is reprocessed within the software and recorded to a file. After that, the program sets a new temperature point and the cycle repeated.

Thermogravimetric analysis

The idea behind thermogravimetric analysis (TGA) is simple: samples may change their mass during a change of temperature. It happens because of either elimination or absorption of gaseous components due to a chemical reaction as well as simple physical process. For inorganic materials, the most common elimination phase is either surface or bound water, although the elimination of carbon dioxide or oxygen also happens often. Normally the only thing responsible for an increase in mass during the TGA is oxygen incorporation causing sample oxidation and therefore mass gain.

Whilst the change in mass of the sample is an important information, another technique is needed for the complete understanding of gases evolved. A mass-spectrometry is very helpful as it allows the mass of released gas to be identified. In a mass-spectrometer the gas molecules are charged (normally to 1+) in an ioniser. The system utilised in the present work uses an electron strike ioniser

to charge molecules. The beam of electrons strikes the flow of gas and picks off an electron of the molecule charging it. The ions produced travel through a quadruple mass-analyser that only allows ions with a specific mass-to-charge (m/z) ratio to pass to a detector. The presence of a signal indicates the presence of an ion. For an inorganic TGA experiment, the identification of the evolved gas is not difficult as there are not many options could be. For example, a single charged water molecule has the m/z ratio 18, carbon dioxide – 44. There are other fragments can also be generated during the ionisation process but their amount is normally rather small and constant.

Another important feature of the sample normally studied during a TGA experiment, is the differential thermal analysis (DTA). This is an analysis of temperature difference between the sample and reference during temperature change. Most of the processes happening during the TGA are either exothermic or endothermic. It could be an energy adsorbed/emitted during the phase decomposition or phase transition of first/second order. This analysis allows detecting processes noticeable on TGA curve, as well as those not noticeable like melting or structural phase transitions where there is no change in mass.

In this way, a TGA-MS experiment allows a simultaneous analysis of thermal changes in the sample, the change in mass and the gases emitted.

The instrumental set-up consists of a highly sensitive balance in a furnace that is isolated from the external atmosphere. There is a constant controlled gas supply into the chamber with an exhaust after passing over the sample. The small part of the exhaust gas transfers into a mass-spectrometer for analysing.

Scanning electron microscopy

Scanning electron microscopy (SEM) is a technique where a micro image is obtained pixel by pixel using a high-energy electron beam. As the wavelength of electrons is much smaller than that of visible light, a magnification of up to 10^6-x can be achieved. When the electron beam hits a point on the surface of the sample, most of the beam is absorbed. However, secondary electrons with low energy are emitted from the same point and are detected. The fine electron tip required for an SEM study is generated in an electron gun using a known accelerating voltage. The beam is focused using electromagnetic condenser lenses. Two perpendicular deflection coils are used to control the point on the surface where the beam hits.

The intensity of the signal depends on the nature of the sample (less significant) and topography of the surface (more significant). An image of the surface is built by accumulating these points.

Samples for SEM should conduct electricity as most of the electrons remain on the sample surface. If these electrons do not move away then surface charging occurs and this interferes with the scanning process, as the beam scatters differently. Poorly conducting samples are coated in a very thin layer of conductive material (e.g. carbon, gold) to overcome this issue. Samples are scanned in a vacuum to eliminate interferences due to air scattering.

Chapter Three

Synthesis and characterisation of $Li_{3x}La_{2/3-x}TiO_3$ perovskite doped with silicate and borate

Many studies recently have shown that the perovskite material, $Li_{3x}La_{2/3-x}TiO_3$ ($0.03 \leq \times \leq 0.167$) (LLTO), have high grain ion conductivity at room temperature. However the grain boundary conductivity tends to be significantly lower, and so the total conductivity is much smaller than 10^{-3}S/cm[108]. Numerous studies have been performed on A and B site cation substitution[65,71], for example Inaguma et al. showed that LLTO doped with 5 mol% Sr showed higher ionic conductivity of the grain ($1.5 \cdot 10^{-3}$ S/cm at 300K) than the pure lanthanum lithium

titanate[64]. However, in all cases the total conductivity was limited by the grain boundary contribution.

Recently boron addition led to good performance for lithium lanthanum zirconium garnet oxides (LLZ)[109,110]. It was proposed that boron decreased the sintering temperature to 900°C, so the lithium loss during heat-treatment is considered to be suppressed. In particular it was proposed that the lithium acted as an accelerator for inter-reaction of grains at grain boundaries and enhanced grain growth. The garnet phase thus formed as the dense composite with Li_3BO_3 at the grain boundary as an amorphous phase. The total electrical conductivity of the composite at room temperature was $1 \cdot 10^{-4}$ S/cm. Considering these promising results for garnet Li ion conductors, the introduction of boron has been investigated in this work for potentially improving sintering and conductivity of LLTO materials, which, however, was not shown to be beneficial.

Another potential related dopant is SiO_2. By adding SiO_2 particles into polymer electrolytes based on polyethylene oxide PEO, the ionic conductivity and lithium ion diffusion were shown to be enhanced[111]. Furthermore in prior work on LLTO it was shown that the total ionic conductivity of LLTO was enhanced to about 10^{-4} S/cm at room temperature due to the formation of some amorphous lithium silicate in the grain boundary[62]. In this case, silica was added to an already prepared LLTO phase. In the current work we have investigated adding silica in to mixture at very first stage in order to try to form a perovskite phase with Si on the B cation site. An attempt, however, was shown to be unsuccessful in these systems. This follows

recent reports from our group on the successful incorporate of Si into perovskite systems[97,112].

Experimental

Dried Li_2CO_3 (10% extra to avoid evaporation losses during sintering), La_2O_3, TiO_2 were accurately weighed in a stoichiometric ratio and milled using a ball mill to obtain 3g of a sample. In order to prepare the silicon and boron doped samples, SiO_2 and B_2O_3 were added to the mixture in the first stage of preparation in the required stoichiometric ratio. The mixture was placed in an alumina crucible with a lid and heated at a temperature of 700°C for 12 hours. The product was reground in an agate mortar and pestle and pressed in a pellet (0.4-0.7g) with a diameter of 13mm under a pressure of 3 tons. These pellets were again placed in an alumina crucible with a lid and sintered at temperature 1100-1350°C for 6 hours. To avoid reaction of the pellet with the crucible at the elevated reaction temperatures, the pellet was placed on platinum foil.

Phase purity was determined using powder XRD (Bruker D8 Diffractometer). Data were collected in the range from 10 to 90^o in Bragg-Brentano geometry with Cu (Kα) X-rays. The program GSASII was used for the cell parameters determination[103].

Pellets for the impedance spectroscopy were weighed and their dimensions were measured. They were coated with silver paste on both sides and two silver electrodes were attached. The conductivities of the obtained pellets were measured

in air by electrochemical impedance spectroscopy using a HP 4204 impedance analyser within a frequency range 5 – 1.3×10^7 Hz. Measurements were carried on in the temperature range 25-300˚C on cooling.

Results and discussion

Structural Study

XRD analysis confirmed the successful synthesis of single phase $Li_{0.3}La_{0.567}TiO_3$; patterns at different temperatures are shown in Figure 26. The

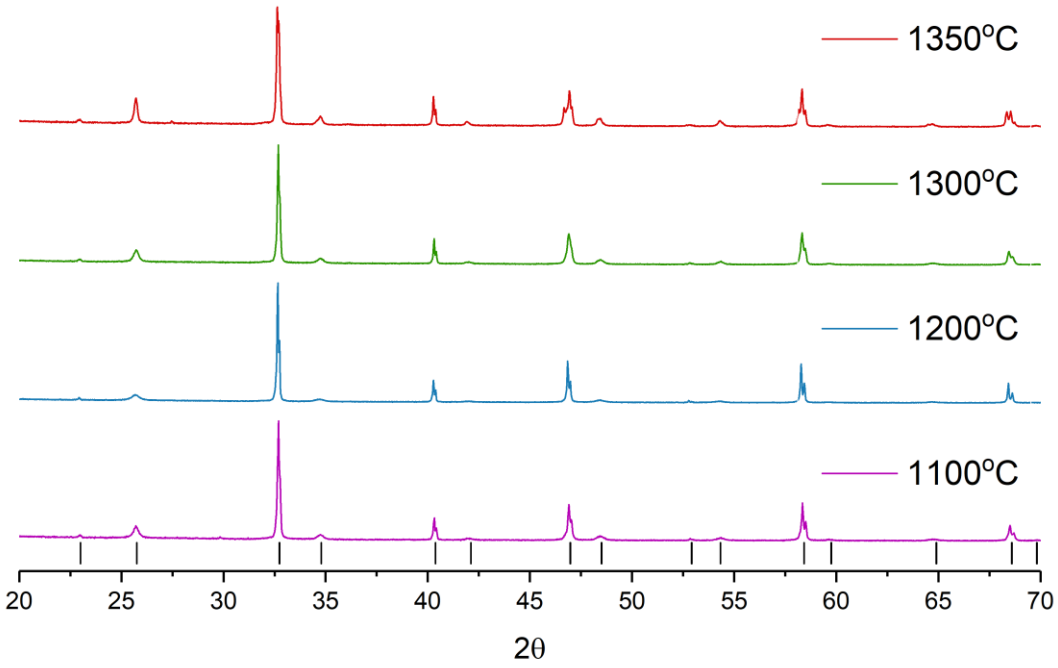

Figure 26. XRD data of undoped $Li_{0.3}La_{0.567}TiO_3$ prepared at various temperatures Tickmarks designate tetragonal perovskite phase

observed phase has a tetragonal structure with a doubling along the c direction. The calculated parameters are shown in Table 5.

Table 5. Calculated cell parameters of undoped $Li_{0.3}La_{0.567}TiO_3$ prepared at various temperatures

Temperature	a, Å	c, Å	c/a	Pellet Density (% theor.)	Cell Volume, Å^3
1100°C	3.8698(2)	7.7455(3)	2.0015(5)	72.9%	115.99(2)
1200°C	3.8731(3)	7.7516(5)	2.0014(8)	70.8%	116.28(3)
1300°C	3.8713(1)	7.7537(2)	2.0029(3)	77.1%	116.20(1)
1350°C	3.8691(2)	7.7760(5)	2.0098(7)	77.0%	116.41(2)

As this table shows the lattice parameters do not change substantially with the synthesis temperature, but there is a slight increase in the c/a ratio which indicates a reduction in tetragonal distortion. The density of the pellets increased with increasing temperature, as expected.

Boron doping

Initially B (0.5-2.5 wt.%) was added to the $Li_2CO_3/La_2O_3/TiO_2$ mixture. At a synthesis temperature of 1100°C the samples showed large impurities. With increasing temperature the phase purity was slightly improved (Figure 27). At a temperature 1300°C, some samples began to melt, which indicates that the addition of boron lowers the melting temperature, and thus the maximum temperature was shown to be limited to not more than 1300°C.

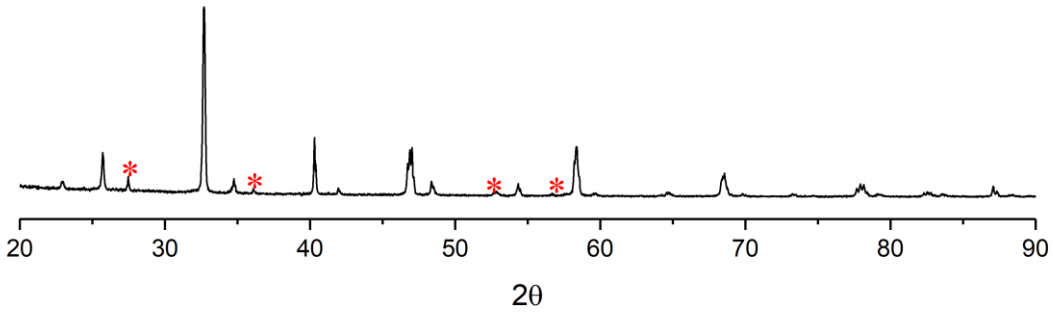

Figure 27. XRD data of $Li_{0.3}La_{0.567}TiO_3$ with addition of 1% weight B 1200°C. Asterisks show impurity peaks

However, after several attempts, phase pure samples could not be obtained by this B addition process. This may relate to reaction with the boron to give Li_3BO_3 which leads to the sample being off stoichiometric.

Since a recent report[97] has shown that boron can be introduced on the B cation site in perovskites, a B doping strategy was investigated. Assuming boron incorporates as BO_3^{3-} the formula $Li_{3x}La_{2y/3-x}Ti_yB_{1-y}O_{1.5(1+y)}$ (x=0.06; 0.1; 0.117; y=0.95) was applied, and a number of samples were prepared. The successful introduction of boron would lead to a loss of lattice positive charge, both through the fact that B^{3+} has a lower charge than Ti^{4+} and lower coordination number leading to oxide ion vacancies. A number of charge balancing strategies were then investigated. Here three cases of Li content were examined: lowered at x=0.06, normal at x=0.1 and enriched at x=0.117. If consistent with the results of Ibarra et al. tetragonal cells should be formed [66].

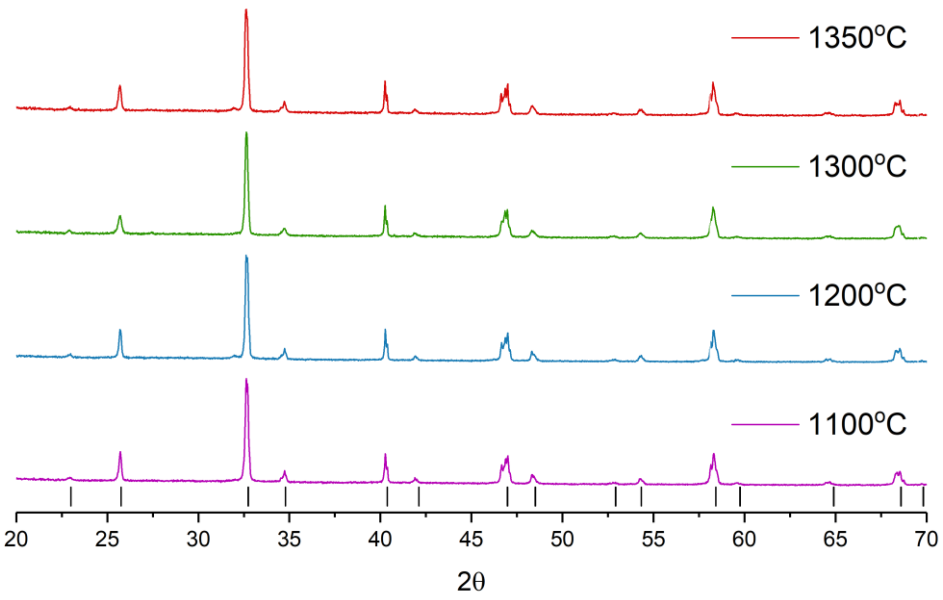

Figure 28. XRD data of $Li_{0.2}La_{0.567}Ti_{0.95}B_{0.05}O_{2.925}$ prepared at various temperatures. Tickmarks designate tetragonal perovskite phase

$Li_{0.2}La_{0.567}Ti_{0.95}B_{0.05}O_{2.925}$

In the first instance, the charge was balanced with lowered Li content. XRD results showed that a pure phase was formed at a temperature 1100°C, but at higher temperatures, there were a small amount of impurities (Figure 28). The impurity appear to consist of $La_{0.67}TiO_3$, which may indicate too much lithium evaporation from the crucible during calcination. Impurities containing boron compounds were not found.

In order to investigate the samples in more detail, Raman spectroscopy data were collected. For comparison, Raman spectra for pure B_2O_3 and $Li_{0.3}La_{0.567}TiO_3$

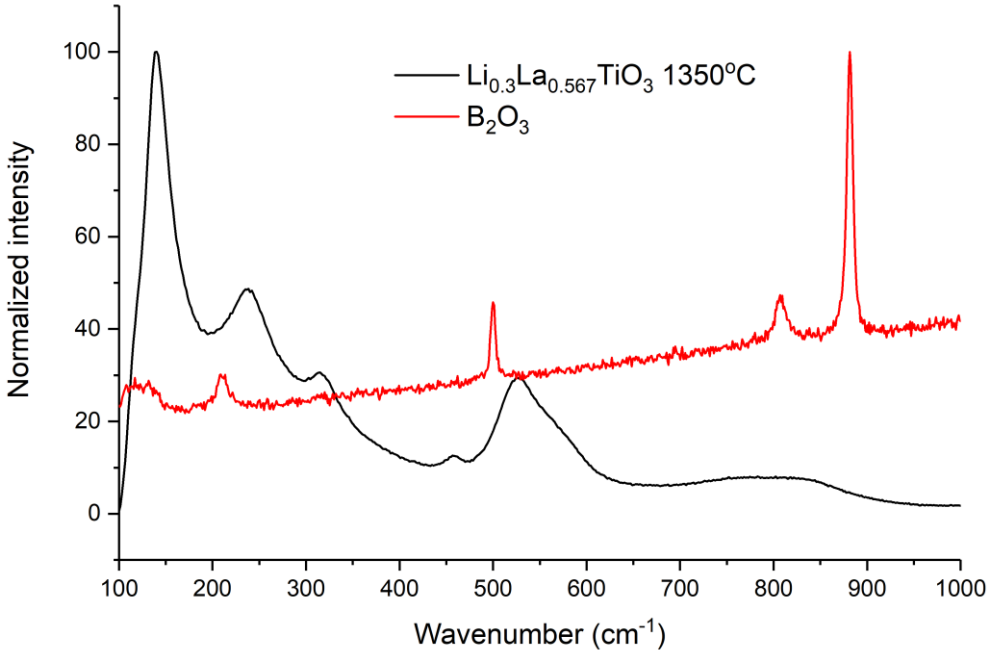

Figure 29. Raman spectra of pure B_2O_3 and $Li_{0.3}La_{0.567}TiO_3$ (according to XRD data)

were also collected. Figure 29 shows the collected data. Boron oxide spectra showed five peaks at 128cm^{-1},210cm^{-1}, 500cm^{-1},810cm^{-1} and 880cm^{-1}, with the latter the most intense. For LLTO six peaks were observed at 140cm^{-1}, 238cm^{-1}, 315cm^{-1}, 458cm^{-1}, 527cm^{-1} and broad peak at 752-824cm^{-1}. These peaks agree with previous reports[62,113].

The Raman spectra of the B doped samples showed peaks corresponding only to the LLTO phase (Figure 30). Since the detected impurity ($La_{0.67}TiO_3$) is also similar perovskite, their peaks overlap with those of the LLTO phase. Peaks belonging to borate components were not detected, which may be related to the low boron content and hence low intensity of peaks.

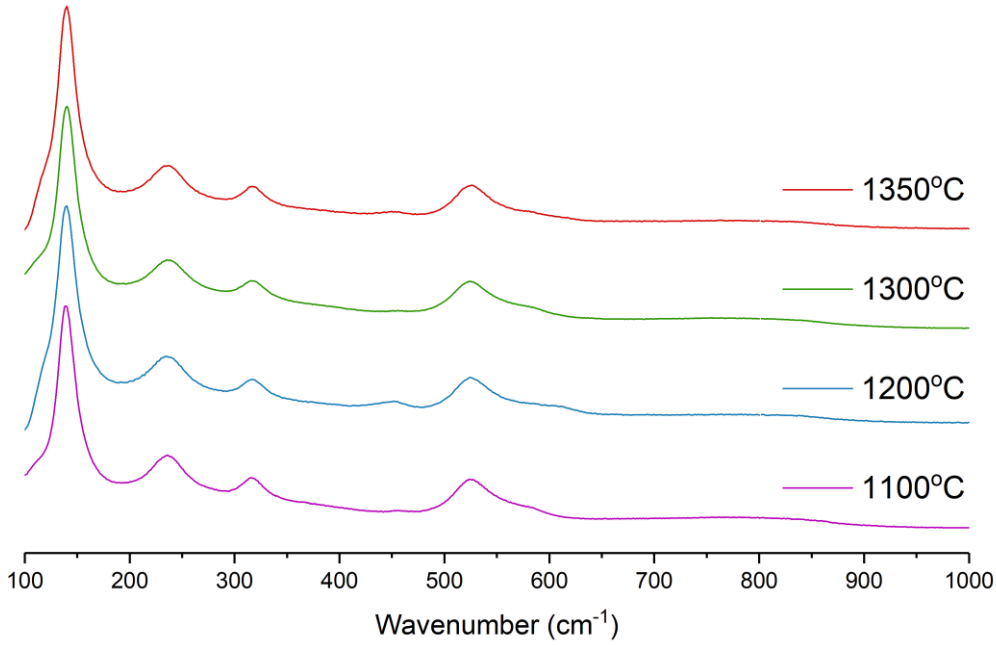

Figure 30. Raman spectra of $Li_{0.2}La_{0.567}Ti_{0.95}B_{0.05}O_{2.925}$ prepared at various temperatures

As shown in table 6 the pellet densities were similar for all cases with values of 83-88% illustrating better sintering compared to LLTO without B doping. The 1200°C and 1350°C samples were closer as representative samples for conductivity studies.

Table 6. Calculated cell parameters of $Li_{0.2}La_{0.567}Ti_{0.95}B_{0.05}O_{2.925}$ prepared at various temperatures

Temperature	a, Å	c, Å	c/a	Pellet Density (% theor.)	Cell Volume, Å^3
1100°C	3.8686(2)	7.7812(5)	2.0114(7)	83.3%	116.45(2)
1200°C	3.8704(3)	7.7828(5)	2.0109(8)	87.5%	116.59(3)
1300°C	3.8705(2)	7.7731(6)	2.0083(8)	85.4%	116.45(2)
1350°C	3.8697(2)	7.7834(5)	2.0114(7)	86.0%	116.55(2)

$Li_{0.3}La_{0.533}Ti_{0.95}B_{0.05}O_{2.925}$

The next charge balance was investigated with the Li content maintained, while the La content was reduced. In this case, at various calcination temperatures the impurities $La_{0.67}TiO_3$ and TiO_2 are observed. Only TiO_2 is present as an impurity at the higher temperatures (Figure 31). This may also indicate that too much lithium evaporation from the system occurs. Perhaps the presence of boron increases its volatility or there could be the formation of an amorphous Li/La borate phase.

The Raman spectra of these phases showed similar results to before with no additional peaks (Figure 32). This probably indicates that existing impurity

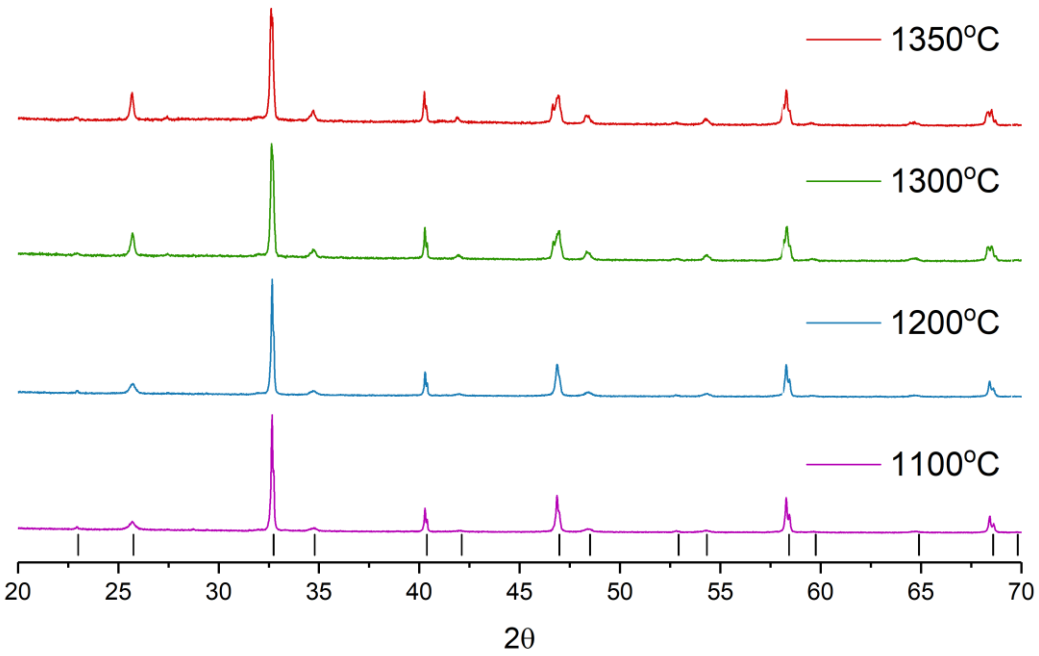

Figure 31. XRD data of $Li_{0.3}La_{0.533}Ti_{0.95}B_{0.05}O_{2.925}$ prepared at various temperatures. Tickmarks designate tetragonal perovskite phase

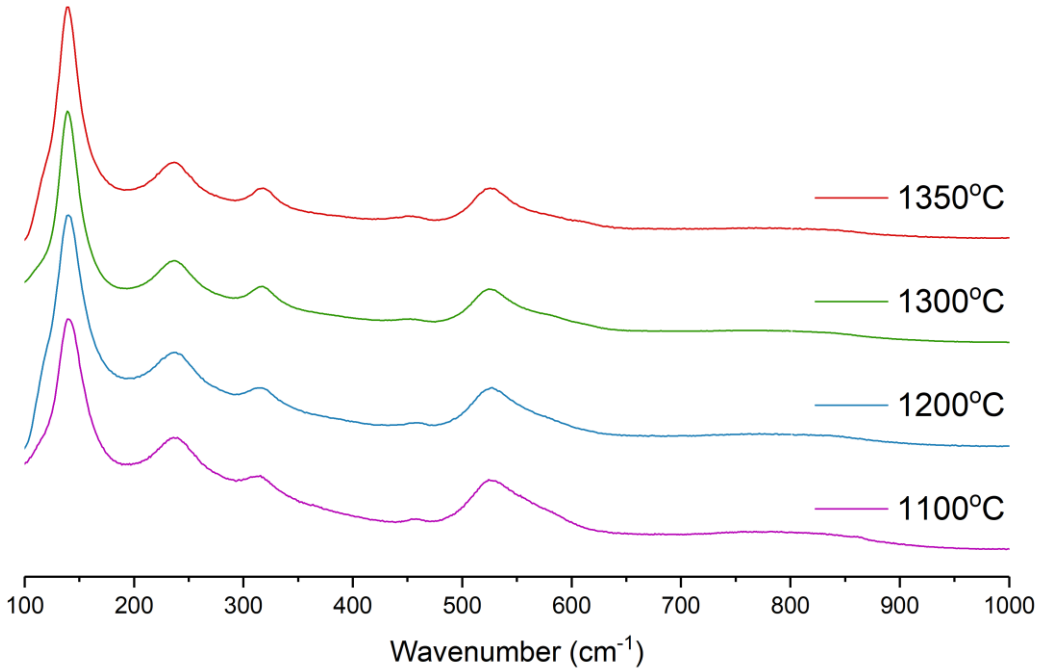

Figure 32. Raman spectra of $Li_{0.3}La_{0.533}Ti_{0.95}B_{0.05}O_{2.925}$ prepared at various temperatures

peaks (e.g. these due to TiO_2) coincide with the peaks from the perovskite phase. Borate containing components were not identified.

The cell parameters were determined from the XRD data. Similar cell parameters were observed, albeit with a small increase in the tetragonality with increasing temperature.

The density of the obtained samples was shown to increase with increasing temperature (Table 7). Samples with higher density should have a higher total conductivity. Therefore, for further conductivity investigations, the samples sintered at 1200°C and 1350°C were selected.

Table 7. Calculated cell parameters of $Li_{0.3}La_{0.533}Ti_{0.95}B_{0.05}O_{2.925}$ prepared at various temperatures

Temperature	a, Å	c, Å	c/a	Pellet Density (% theor.)	Cell Volume, Å^3
1100°C	3.8728(3)	7.7526(6)	2.0018(9)	74.5%	116.28(3)
1200°C	3.8735(2)	7.7582(5)	2.0029(7)	79.2%	116.40(2)
1300°C	3.8693(2)	7.7753(5)	2.0095(7)	83.3%	116.41(2)
1350°C	3.8675(2)	7.7727(5)	2.0098(7)	87.5%	116.26(2)

$Li_{0.35}La_{0.517}Ti_{0.95}B_{0.05}O_{2.925}$

The next charge balancing strategy investigated was to maintain the total A site occupancy which was achieved through increasing the Li content and lowering the La content. At lower temperatures, the XRD data showed a perovskite phase, which was very similar to a single cubic structure, and then, as the temperature increased, the peaks splitting indicative of the tetragonal cell become more apparent (Figure 33). Cell parameters are given in a table 8.

Table 8. Calculated cell parameters of $Li_{0.35}La_{0.517}Ti_{0.95}B_{0.05}O_{2.925}$ prepared at various temperatures

Temperature	a, Å	c, Å	c/a	Pellet Density (% theor.)	Cell Volume, Å^3
1100°C	3.8724(3)	7.7559(6)	2.0029(9)	82.2%	116.30(3)
1200°C	3.8725(4)	7.7522(9)	2.0019(13)	87.5%	116.25(4)
1300°C	3.8706(3)	7.7567(8)	2.0040(11)	87.5%	116.21(3)
1350°C	3.8660(2)	7.7680(4)	2.0093(6)	85.0%	116.10(2)

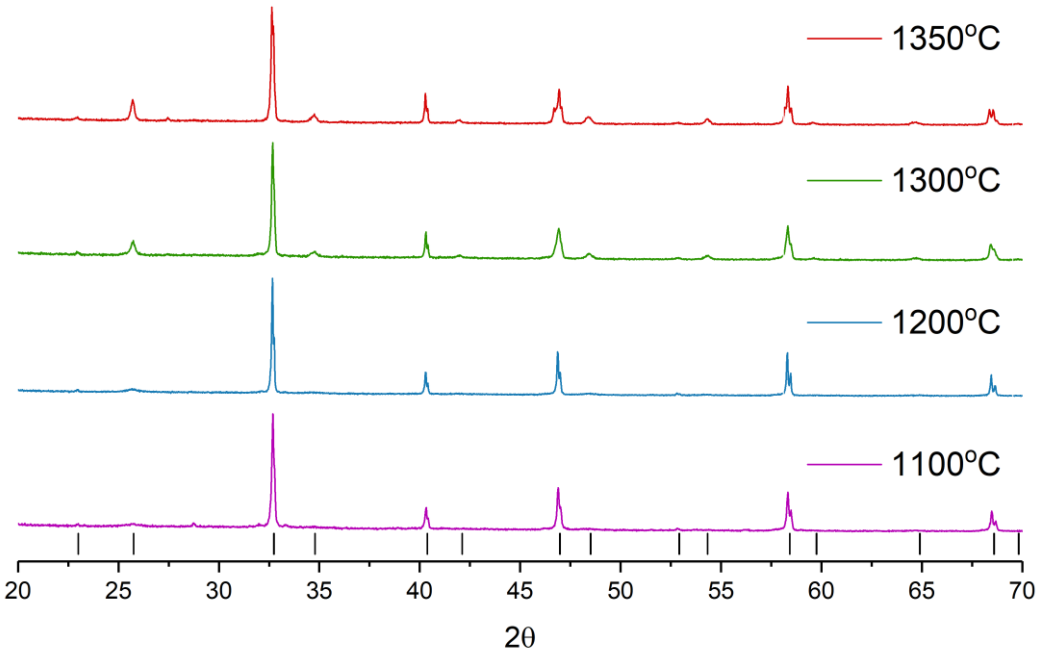

Figure 33. XRD data of $Li_{0.35}La_{0.517}Ti_{0.95}B_{0.05}O_{2.925}$ prepared at various temperatures. Tickmarks designate tetragonal perovskite phase

Raman data of these samples showed that at a temperature 1100°C there was an additional peak at 860 cm^{-1}, which subsequently disappeared at higher temperatures (Figure 34). This peak may correspond to a borate group or B_2O_3 as on the Figure 29. This may indicate that at low temperatures the boron component have difficulty in entering into the crystal structure of lanthanum lithium titanate. Moreover, as can be seen by the results of XRD (Figure 33), possibly replacing titanium with boron results in a transition to tetragonal from cubic symmetry and appear of superstructural peaks.

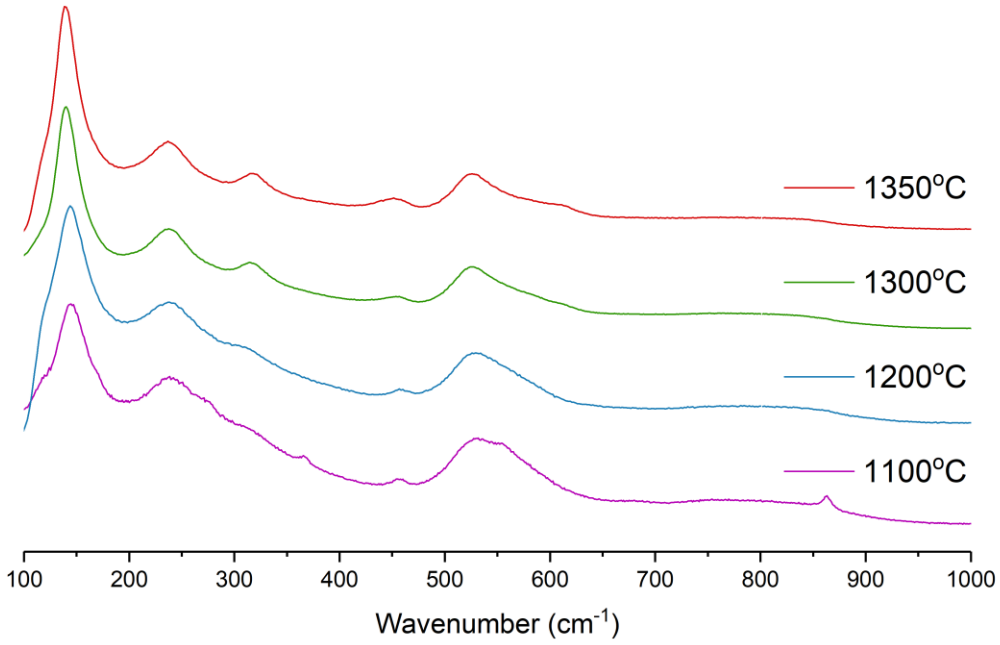

Figure 34. Raman spectra of $Li_{0.35}La_{0.517}Ti_{0.95}B_{0.05}O_{2.925}$ prepared at various temperatures

The density of the obtained samples was shown to increase with increasing temperature. Therefore, for further conductivity investigations, the samples sintered at 1200°C and 1350°C were selected.

Table 9 shows cell parameters for samples with different Li content prepared at 1350°C. In general, a decrease in the volume of the crystal lattice with increasing lithium content is observed, due to the decrease in the number of large lanthanum ions. The cell parameters for are consistent with prior studies[114].

Table 9. Cell parameters for $Li_{3x}La_{0.633-x}Ti_{0.95}B_{0.05}O_{2.925}$ samples with different Li content prepared at 1350°C

x	a, Å	c, Å	c/a	Cell Volume, Å^3
0.067	3.8697(2)	7.7834(5)	2.0114(7)	116.55(2)
0.1	3.8675(2)	7.7727(5)	2.0098(7)	116.26(2)
0.117	3.8660(2)	7.7680(4)	2.0094(6)	116.10(2)

Silicon doping

A recent report from our group[97] has shown that silicon can be introduced on the B cation site in perovskites. Considering this a range of doping strategies was investigated. Assuming silicon incorporates as SiO_4^{2-} the formula $Li_{3x}La_{\frac{2y}{3}-x}Ti_ySi_{1-y}O_{y+2}$ (x=0.06; 0.1; 0.117; y=0.9) was used. Introduction of silicon would lead to a loss of negative charge, since although Si^{4+} has the same charge as Ti^{4+}, it prefers a lower coordination number (CN_{Si}=4, CN_{Ti}=6) thus leading to oxide ion vacancies. A number of charge balancing strategies were therefore investigated. Here were examined three cases of Li content compared to undoped materials[114]: lowered at x=0.06, normal at x=0.1 and enriched at x=0.117.

$Li_{0.2}La_{0.533}Ti_{0.9}Si_{0.1}O_{2.9}$

In the first instance, the charge was balanced with lowered Li content. XRD results showed that a pure phase is obtained only at a temperature 1350°C, with

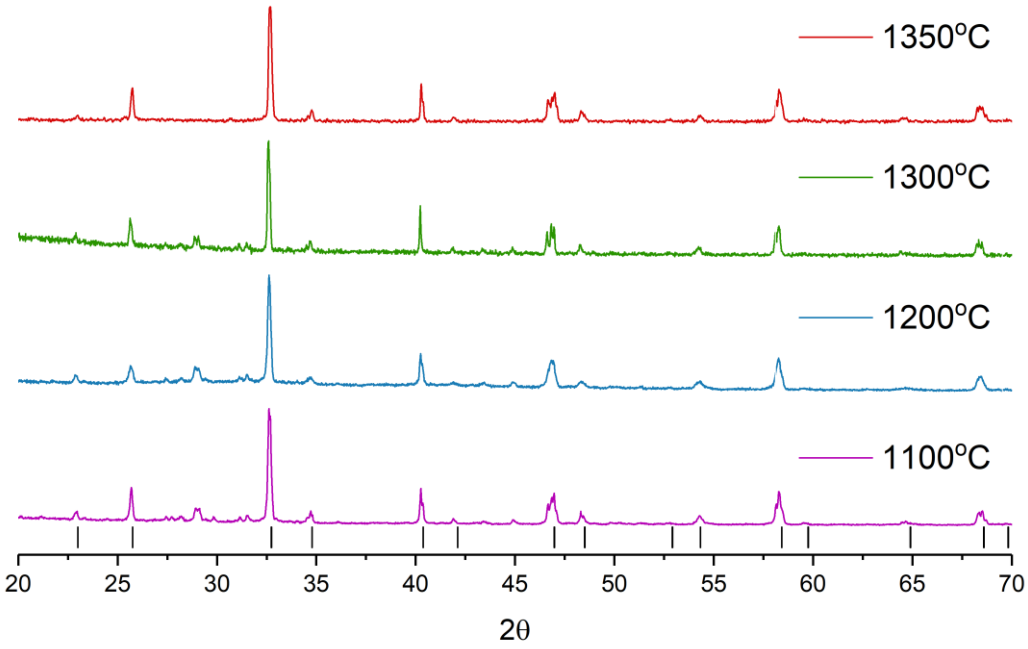

Figure 35. XRD data of $Li_{0.2}La_{0.533}Ti_{0.9}Si_{0.1}O_{2.9}$ prepared at various temperatures. Tickmarks designate tetragonal perovskite phase

extra impurity peaks observed at 1300°C and below (Figure 35). The main perovskite phase was shown to have a tetragonal cell, as for the undoped system.

The Raman spectra showed peaks corresponding to the LLTO phase, but at 1100°C a significant amount of additional peaks due to impurity are observed (Figure 36). There is a peak at 800-830 cm^{-1} that is consistent with the presence of SiO_4 group. Possibly, at lower temperature, lithium silicates are formed and then it reacts further at elevated temperature.

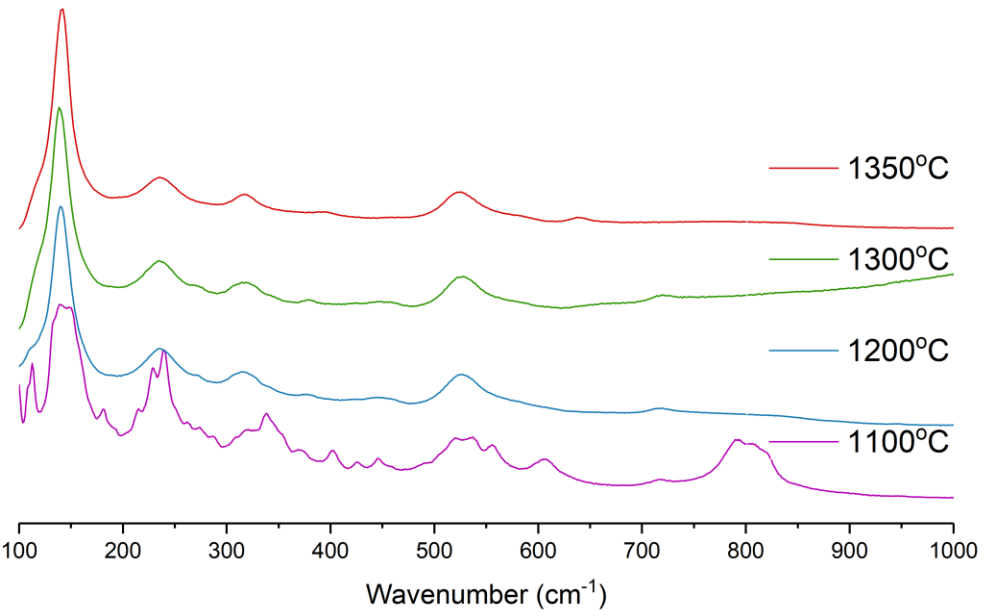

Figure 36. Raman spectra of $Li_{0.2}La_{0.533}Ti_{0.9}Si_{0.1}O_{2.9}$ prepared at various temperatures

The density of the obtained pellets was shown to be increased to almost 90% of the theoretical value at a temperature of 1200°C (Table 10). Melting of lithium silicates at lower temperatures likely produces a beneficial effect on the sintering process and leads to the production of high-density samples.

Table 10. Calculated cell parameters of $Li_{0.2}La_{0.533}Ti_{0.9}Si_{0.1}O_{2.9}$ prepared at various temperatures

Temperature	a, Å	c, Å	c/a	Pellet Density (% theor.)	Cell Volume, Å^3
1100°C	3.8696(3)	7.7781(6)	2.0101(9)	70.8%	116.47(3)
1200°C	3.8713(2)	7.7661(5)	2.0061(7)	89.6%	116.39(2)
1300°C	3.8725(2)	7.7737(4)	2.0074(6)	89.6%	116.58(2)
1350°C	3.8720(2)	7.7842(6)	2.0104(8)	89.6%	116.70(2)

$Li_{0.3}La_{0.5}Ti_{0.9}Si_{0.1}O_{2.9}$

Maintaining the Li content, while charge balancing with a reduction in the La content was analysed next. XRD showed that a pure phase formed at a temperature of 1200°C (Figure 37). The phase has a tetragonal lattice, and no further significant changes were observed with increasing temperature. Compared to the Si-doped LLTO with $Li_{0.2}$ sample it has a very small amount of impurities.

Raman spectra showed similar results to the previous B-doping series. For the sample prepared at a temperature 1100°C a peak indicative of a SiO_4 group was observed, which then disappeared for higher temperatures (Figure 38).

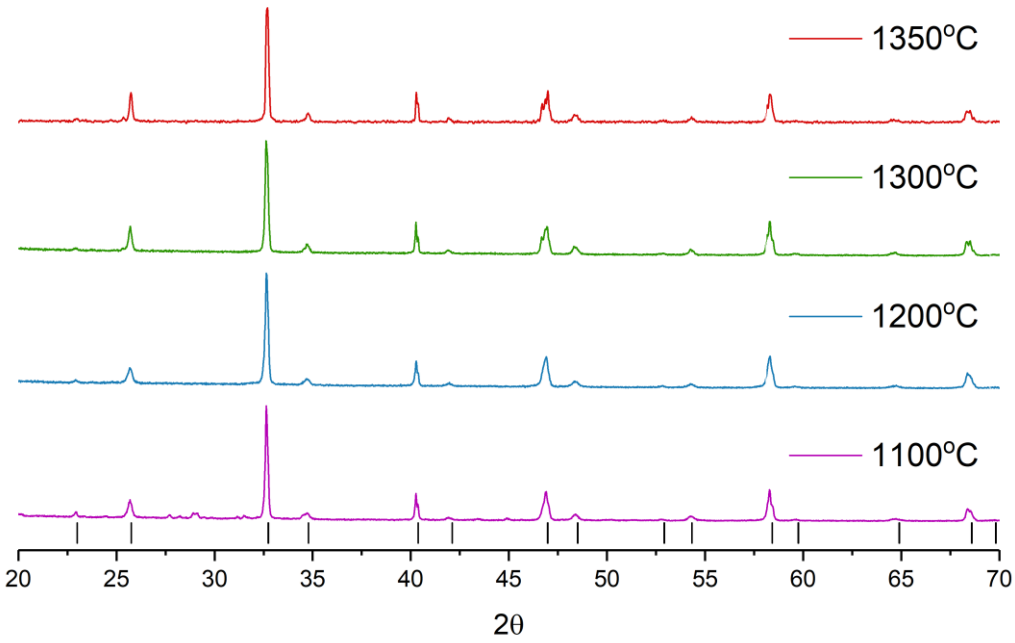

Figure 37. XRD data of $Li_{0.3}La_{0.5}Ti_{0.9}Si_{0.1}O_{2.9}$ prepared at various temperatures. Tickmarks designate tetragonal perovskite phase

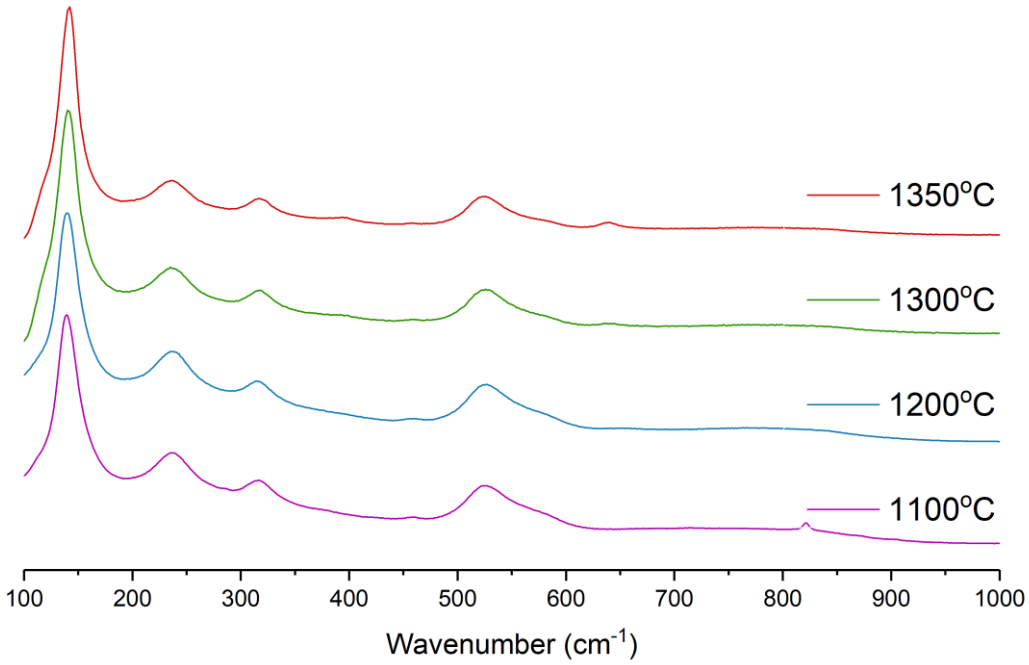

Figure 38. Raman spectra of $Li_{0.3}La_{0.5}Ti_{0.9}Si_{0.1}O_{2.9}$ prepared at various temperatures

Table 11 shows that the ratio of cell height to its width remains essentially constant with temperature. The highest density pellet was observed for sintering at a temperature 1300°C. In addition, there is a slight increase in the crystal lattice, probably for similar reasons of lithium evaporation.

Table 11. Calculated cell parameters of $Li_{0.3}La_{0.5}Ti_{0.9}Si_{0.1}O_{2.9}$ prepared at various temperatures

Temperature	a, Å	c, Å	c/a	Pellet Density (% theor.)	Cell Volume, Å^3
1100°C	3.8699(3)	7.7601(6)	2.0052(9)	72.9%	116.22(3)
1200°C	3.8714(4)	7.7706(7)	2.0072(11)	85.4%	116.46(3)
1300°C	3.8701(2)	7.7751(4)	2.0090(6)	87.5%	116.45(2)
1350°C	3.8725(2)	7.7803(7)	2.0091(9)	85.4%	116.68(2)

$Li_{0.35}La_{0.483}Ti_{0.9}Si_{0.1}O_{2.9}$

The last charge balancing strategy was investigated with enriched Li content that led to decreasing of lanthanum amount on A site. XRD showed a pure tetragonal perovskite phase at the temperatures 1300°C and above (Figure 39).

Raman spectra showed similar results to the previous samples. A peak indicative of a SiO_4 group appears only for the sample prepared at 1100°C (Figure 40). Perhaps at temperatures higher than 1100°C, loss of Si as Li silicate occurs.

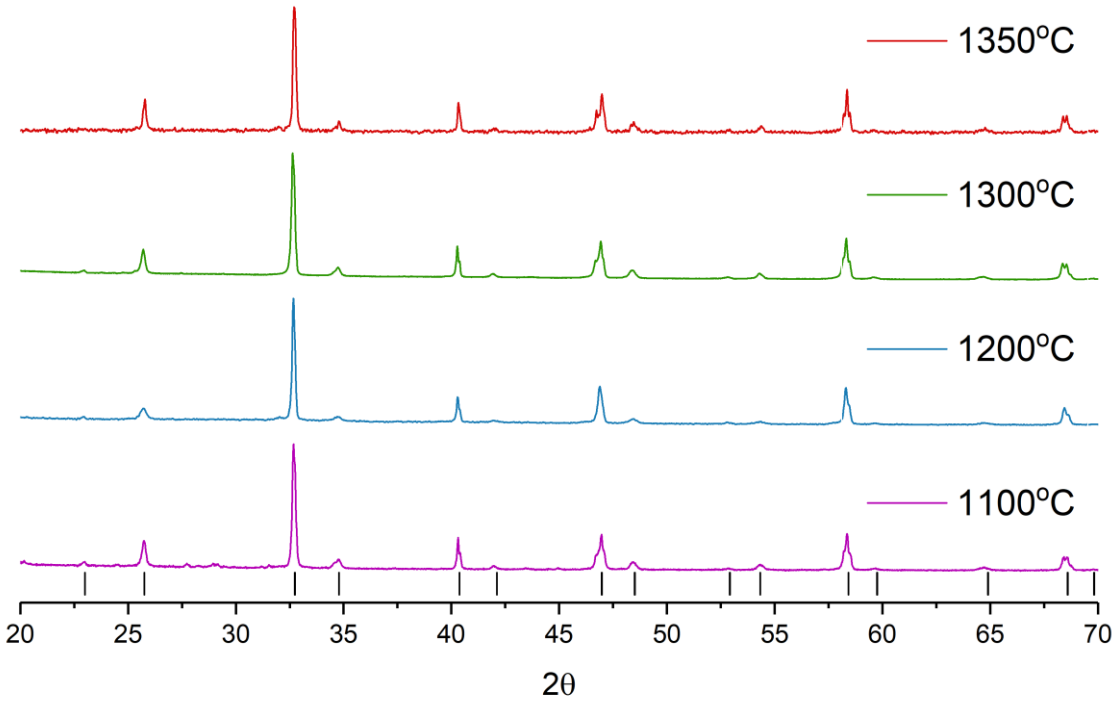

Figure 39. XRD data of $Li_{0.35}La_{0.483}Ti_{0.9}Si_{0.1}O_{2.9}$ prepared at various temperatures. Tickmarks designate tetragonal perovskite phase

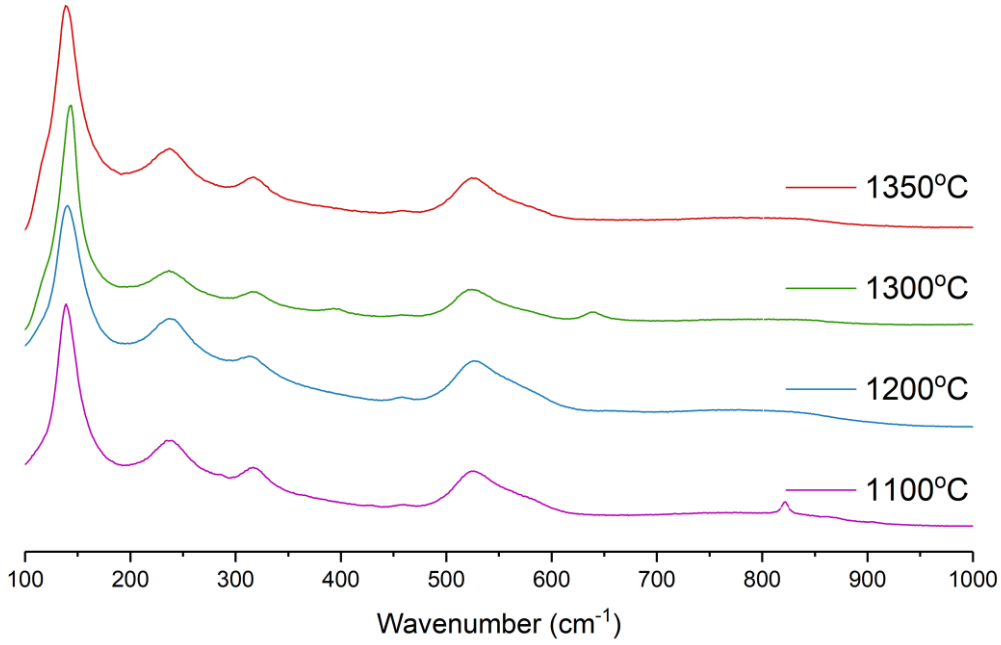

Figure 40. Raman spectra of $Li_{0.35}La_{0.483}Ti_{0.9}Si_{0.1}O_{2.9}$ prepared at various temperatures

Table 12 shows that the pellet density of the obtained samples increases and reaches a maximum at a temperature 1350°C. The c/a ratio varies slightly depending on the temperature.

Table 12. Calculated cell parameters of $Li_{0.35}La_{0.483}Ti_{0.9}Si_{0.1}O_{2.9}$ prepared at various temperatures

Temperature	a, Å	c, Å	c/a	Pellet Density (% theor.)	Cell Volume, Å^3
1100°C	3.8673(2)	7.7664(4)	2.0082(6)	72.9%	116.15(2)
1200°C	3.8742(2)	7.7370(5)	1.9971(7)	85.4%	116.13(2)
1300°C	3.8763(1)	7.7299(2)	1.9941(3)	85.4%	116.15(1)
1350°C	3.8707(3)	7.7787(7)	2.0096(10)	91.7%	116.54(3)

Table 13 shows cell parameters for $Li_{3x}La_{0.6-x}Ti_{0.9}Si_{0.1}O_{2.9}$ samples with different Li content prepared at 1350°C. The increase of the Li content with

simultaneous decrease of the La content causes small insignificant volume contraction. In comparison to undoped samples there is a very small expansion, which is, however, can be neglected as the doped sample has higher density and, therefore, could have different microstrain behaviour.

Table 13. Cell parameters for $Li_{3x}La_{0.6-x}Ti_{0.9}Si_{0.1}O_{2.9}$ samples with different Li content prepared at 1350°C

x	a, Å	c, Å	c/a	Cell Volume, Å^3
0.067	3.8720(3)	7.7842(8)	2.0104(11)	116.70(3)
0.1	3.8725(2)	7.7803(6)	2.0091(8)	116.68(2)
0.117	3.8707(3)	7.7787(7)	2.0096(10)	116.54(3)

To evaluate potential changes in the ionic diffusion in the conductivity study, samples prepared at 1200°C and 1350°C for boron doping and at 1300°C and 1350°C for silicon doping were examined.

Conductivity study

Boron doped samples

The conductivity data were collected on the boron doped LLTO samples sintered at 1200°C and 1350°C. In all cases the total conductivity is similar nearly 2 orders of magnitude lower than the grain bulk conductivity just like in undoped LLTO (Figure 41). The grain bulk conductivity has a slightly wider range of observed values. However, due to the nature of experiment and predominance of the grain boundary resistance in the system, these values have larger uncertainty. The similar gradient of lines on Arrhenius plot indicates that the activation energy of Li ion

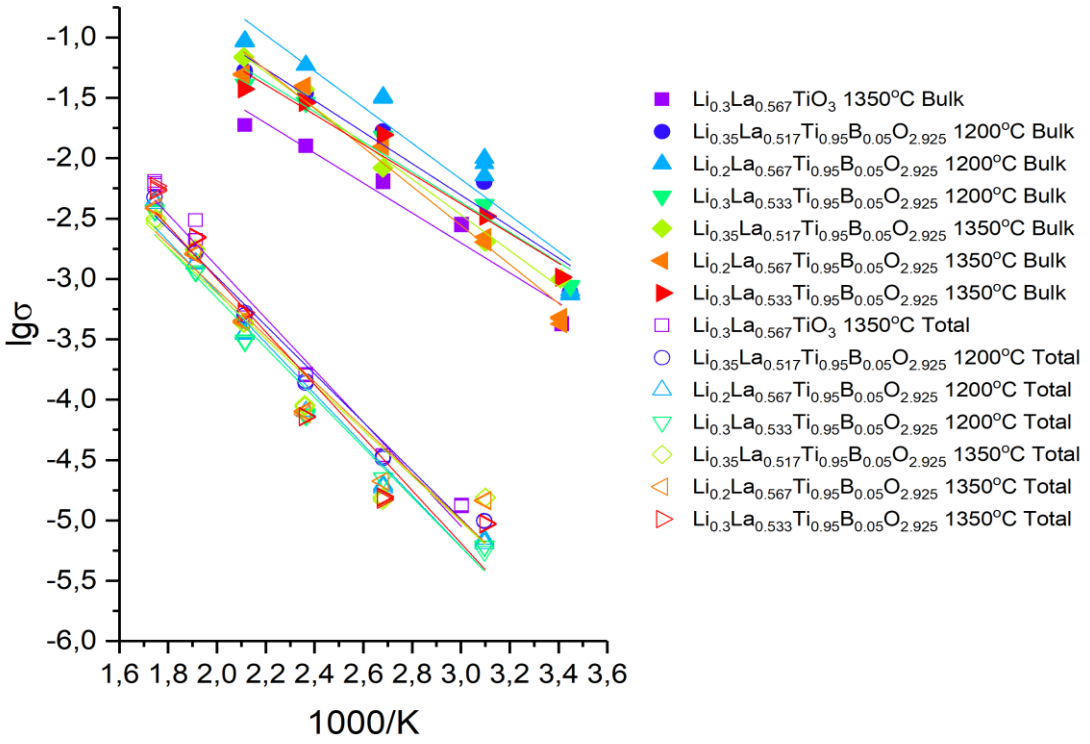

Figure 41. Bulk (filled markers) and total (empty markers) conductivity of B-doped samples

migration is very similar for all samples. Thus boron addition to LLTO does not appear to affect the Li ionic transport in these materials. This is unusual as the density of doped samples is significantly higher than the undoped, and so a higher total conductivity might be expected. It is possible that the positive sintering effect of doping is countered by formation of very small amount of less conductive B containing impurities.

Silicon doped samples

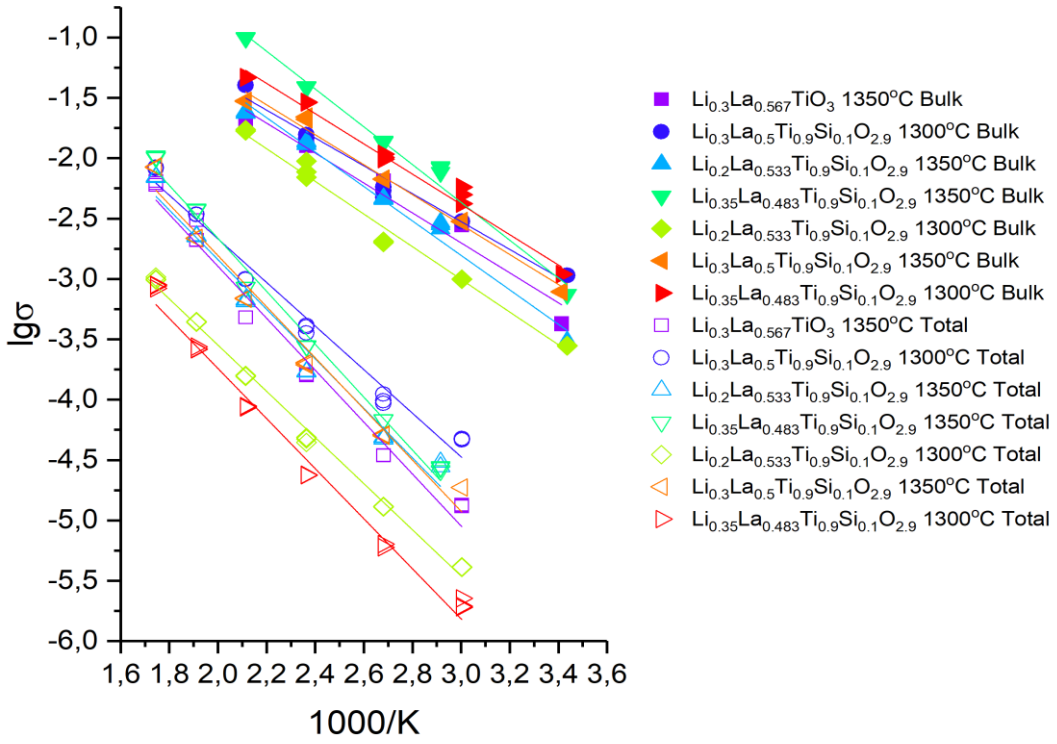

Figure 42. Bulk (filled markers) and total (empty markers) conductivity of Si-doped samples

The conductivity data were collected on the silicon doped LLTO samples sintered at 1300°C and 1350°C. For the end series, we observe similar conductivity behaviour as for B doped samples. The total conductivity of all samples is about 2 orders of magnitude lower than the grain bulk conductivity (Figure 42). The grain bulk conductivity values have the same measurement uncertainty as in the case of B-doped compounds and, therefore, can be assumed to have negligible difference. Somewhat surprisingly the total conductivity of most of the samples remains constant despite significant Li content changes. Similarly the slope of lines on Arrhenius plots is similar for all samples suggesting no significant variations in Li-

ion transport. The Si-doped samples sintered at 1350°C did show some noticeable reduction in total conductivity, however, which may be related to the formation of a thin lithium silicate layer with higher resistivity on the surface of the grain. Partial melting of this impurity might also account for the good sinterability at this temperature.

Conclusion

The cell parameter data does not support incorporation of the boron or silicon into LLTO lattice. The small changes observed for the cell volume probably instead related to a small change of Li/La ratio.

The addition of boron or silicon to LLTO perovskite showed negligible effect on ionic conductivity. While there is a significant improvement in the sintering giving denser pellets, it is possible that the formation of a higher resistivity Li borate/silicate layer on the grain negates any beneficial effect from the density increasing.

Chapter Four

Synthesis and characterisation of $Li_{5+y}La_3M_2O_{12}$ (0<y<2, M=Nb/Ta/Zr) garnet doping with Na^+

The high ionic conductivity, good chemical stability vs. lithium metal and wide electrochemical stability range makes the lithium-containing garnet oxides potential candidates for solid electrolytes in all-solid-state lithium ion batteries. The classic garnet structure is based on the orthosilicates $A^{II}_3M^{III}_2(SiO_4)_3$ which consists of a framework of corner linked MO_6 octahedra and SiO_4 tetrahedra with the A cations filling eight coordinate cavity sites within this framework[78]. More recently Li containing garnets have attracted attention following reports of high Li ion conductivity in these systems[82]. One of the most interesting aspects of these Li ion garnets is their ability to accommodate excess Li ions far and above that expected

for the simple garnet structure. Thus, the general formula is $Li_xA_3M_2O_{12}$, where $3 \leq x \leq 7$, with these Li ions accommodated in a combination of the traditional tetrahedral garnet site and other distorted interstitial six coordinate sites[115]. The first report of high Li ion conductivity in garnets was for the $Li_5La_3M_2O_{12}$ (M=Nb, Ta) systems[79]. Although the conductivity at room temperature was relatively low (10^{-6} S/cm), the system showed high stability towards molten Li. This early seminal work by Thangadurai et al. has since inspired a wide range of doping studies on this material to increase conductivity[87]. It has been shown that substitution of La(III) with divalent alkaline earth metals Ba(II)[88,89,116], Ca(II)[90,91], Sr(II)[89,91] in $Li_5La_3M_2O_{12}$ (M=Nb, Ta) leads to an improvement in the Li-ion conductivity due to an increase in the Li content. Monovalent alkali metal substitution was also reported, with potassium doping successfully applied to improve Li conductivity in Nb based garnet[92].

Another promising garnet first reported by Murugan et al in 2007[83] is $Li_7La_3Zr_2O_{12}$ with conductivity about 10^{-4} S/cm at room temperature initially reported. This system has, however, proved to be quite complex, and it has since been shown that this phase $Li_7La_3Zr_2O_{12}$ (as well as the related $Li_7La_3Sn_2O_{12}$ and $Li_7La_3Hf_2O_{12}$) is actually tetragonal with low Li ion conductivity, due to Li ordering which is necessary to accommodate 7 Li ions per formula unit within the structure, while avoiding too short Li-Li interactions[81,84,117–119]. The frequently observed cubic symmetry for this material was shown to actually arise from Al^{3+} incorporation from reaction with the alumina crucible to give $Li_{7-3x}Al_xLa_3Zr_2O_{12}$[86,120]. This was

confirmed by experiments investigating the deliberate incorporation of Al and other multivalent ions, e.g. Ga, on the Li site[84,85].

In addition to doping strategies into $Li_7La_3Zr_2O_{12}$ and $Li_5La_3M_2O_{12}$ (M=Nb, Ta), many researchers have investigated the solid solution between these two systems, with this work showing very high conductivities for Li contents of the order of 6.5-6.75[93,121]. One issue with these garnet systems, however, is the difficulty in obtaining dense pellets while limiting Li loss. As a result, we have been interested in the introduction of Na into $Li_5La_3M_2O_{12}$ and $Li_{7-x}La_3Zr_{2-x}M_xO_{12}$ (M=Nb, Ta) to substitute La and subsequently increase Li-content/conductivity, and hopefully improve the sintering ability. During the course of this work Peng et al.[122] reported results on Na incorporation into $Li_5La_3Nb_2O_{12}$ garnet prepared via a sol-gel route, with some significant differences in the results, which will be discussed in this chapter.

With a view to investigate the influence of having 7Li per formula unit, there was recently reported new high Li ion content garnets $Li_7LnSr_2Ta_2O_{12}$ (Ln = La, Pr, Nd, Sm, Gd)[81], which gave tetragonal cell for all systems. In addition to the main experiment reported in this chapter, such studies are extended and here the synthesis and conductivity of high Li ion content garnets $Li_7LaM_2Nb_2O_{12}$ (M = Ba, Sr, Ca) are reported, correlating the conductivities with the effect of ordering of the Li ions.

Experimental

Two series of Na doped and a range of divalent alkali-earth metal doped garnets were prepared in this work via solid-state reaction: $Li_{5+2x}La_{3-x}Na_xM_2O_{12}$, $Li_7La_{3-x}Na_xZr_{2-2x}M_{2x}O_{12}$ (x=0-1, M=Nb, Ta) and $LaX_2Nb_2Li_7O_{12}$ (X = Ba, Sr, Ca). Dried Li_2CO_3 (Alfa Aesar) and Na_2CO_3 (Alfa Aesar) (10% excess to compensate evaporated lithium and sodium losses at high temperatures), $BaCO_3$ (Aldrich), $SrCO_3$ (Aldrich), $CaCO_3$ (Alfa Aesar), La_2O_3 (Aldrich), Nb_2O_5 (Alfa Aesar), Ta_2O_5 (Alfa Aesar), ZrO_2 (Acros Organics) were wet milled (zirconia balls and bowls, hexane solvent) in a Fritsch Pulverisette 7 planetary ball mill to obtain 3g of a sample. After allowing for evaporation of the solvent, the powder was heated up to 700ºC for 12 hours. Then mixtures were reground in the planetary ball mill and pressed into pellets. These pellets were sintered at 900ºC for 12 hours under a layer of mother powder, and then analysed by X-ray diffraction and electrochemical impedance spectroscopy. X-ray diffraction data on a ground pellet were collected on a Panalytical Empyrean X-ray diffractometer in Bragg-Brentano geometry with Cu (Kα) X-rays. The observed data were collected in the range from 15 to 145°, analysed to determine phase purity and lattice parameters were refined by the Rietveld method in TOPAS software[104].

Single crystals were grown via LiOH flux method on silver foil at 500ºC for 48 hours. The prepared melt containing crystals was cooled down to 100ºC and washed in boiling deionised water. Crystals were filtered and dried at 300ºC for 6 hours. Single crystals were mounted on glass fibre and diffraction data were collected on an Agilent SuperNova diffractometer using an Atlas detector. The

crystals were kept at 100K during data collection using an Oxford Cryosystems Cryostream. Using Olex2[123], the structure was solved with the ShelXT[124] structure solution program using Intrinsic Phasing, and refined with the ShelXL[125] refinement package using a least squares approach.

The conductivities of the obtained pellets were measured in air by electrochemical impedance spectroscopy using a HP 4204 impedance analyser within a frequency range 5 – 1.3×10^7 Hz. Measurements were carried in the temperature range 25-300˚C on cooling. Pellets were coated an both sides with silver ink and dried at 150˚C for 2 hours. Zview software was used to analyse the obtained data[105]. The diffusion coefficients were calculated using Nernst-Einstein relation: $D = \frac{\sigma k_B T}{\bar{e}^2 n}$, where k_B is the Boltzmann constant, $\bar{e}$ is the electron charge and n is charge carrier concentration (number of Li cations per unit-cell volume)[126,127].

Results and discussion

Structural study

Na doping in $Li_5La_3(Ta/Nb)_2O_{12}$

Na doping in $Li_5La_3(Ta/Nb)_2O_{12}$ was investigated to increase the Li content through partial substitution of La^{3+} by Na^+. Figure 43 shows the XRD powder patterns for the $Li_{5+2x}La_{3-x}Na_xNb_2O_{12}$ (x = 0, 0.2, 0.4, 0.6, 0.8, 1) samples prepared. These patterns indicate the formation of a single-phase garnet up to x=0.4. At higher values of x an impurity phase of $5Li_2O{\cdot}Nb_2O_5$ (first reported by Nalbandyan in 1989[128]) was observed. In order to confirm that the obtained garnet phases are not

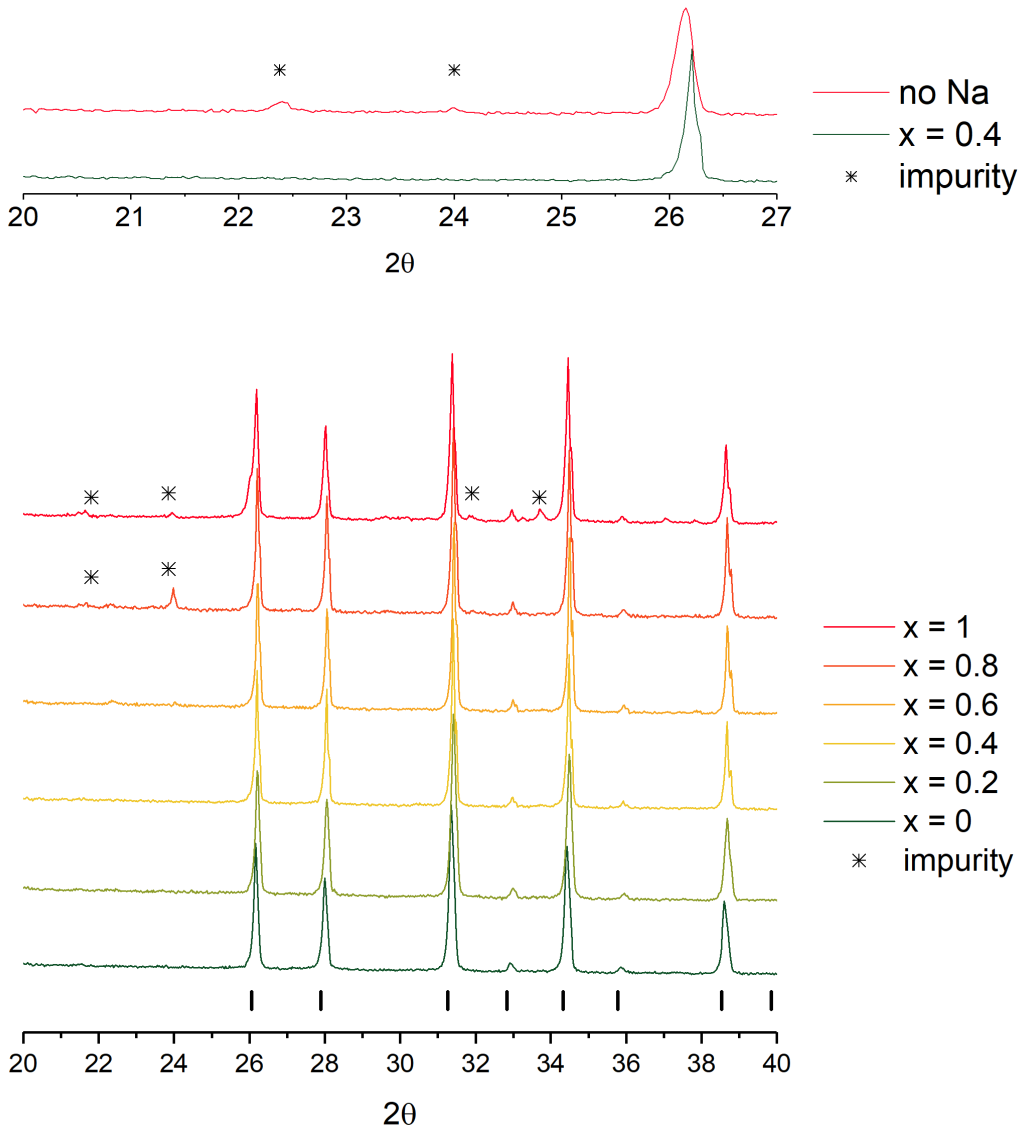

Figure 43. XRD patterns of $Li_{5+2x}La_{3-x}Na_xNb_2O_{12}$ (x = 0, 0.2, 0.4, 0.6, 0.8, 1). Top graph contains patterns of $Li_{5.8}La_{2.6}Na_{0.4}Nb_2O_{12}$ and $Li_{5.8}La_{2.6}Na_{0.0}Nb_2O_{12}$ (tickmarks designate cubic garnet phase peaks)

simply La deficient (with no Na incorporated) a corresponding La deficient phase $Li_{5+2x}La_{3-x}Nb_2O_{12}$ was prepared for x=0.4 without Na added. A comparison of the X-ray diffraction patterns with and without Na addition (Figure 43 top) support the presence of Na in the garnet phase; samples without Na show significant amounts of impurities, mostly consisting of lithium-niobium mixed oxide.

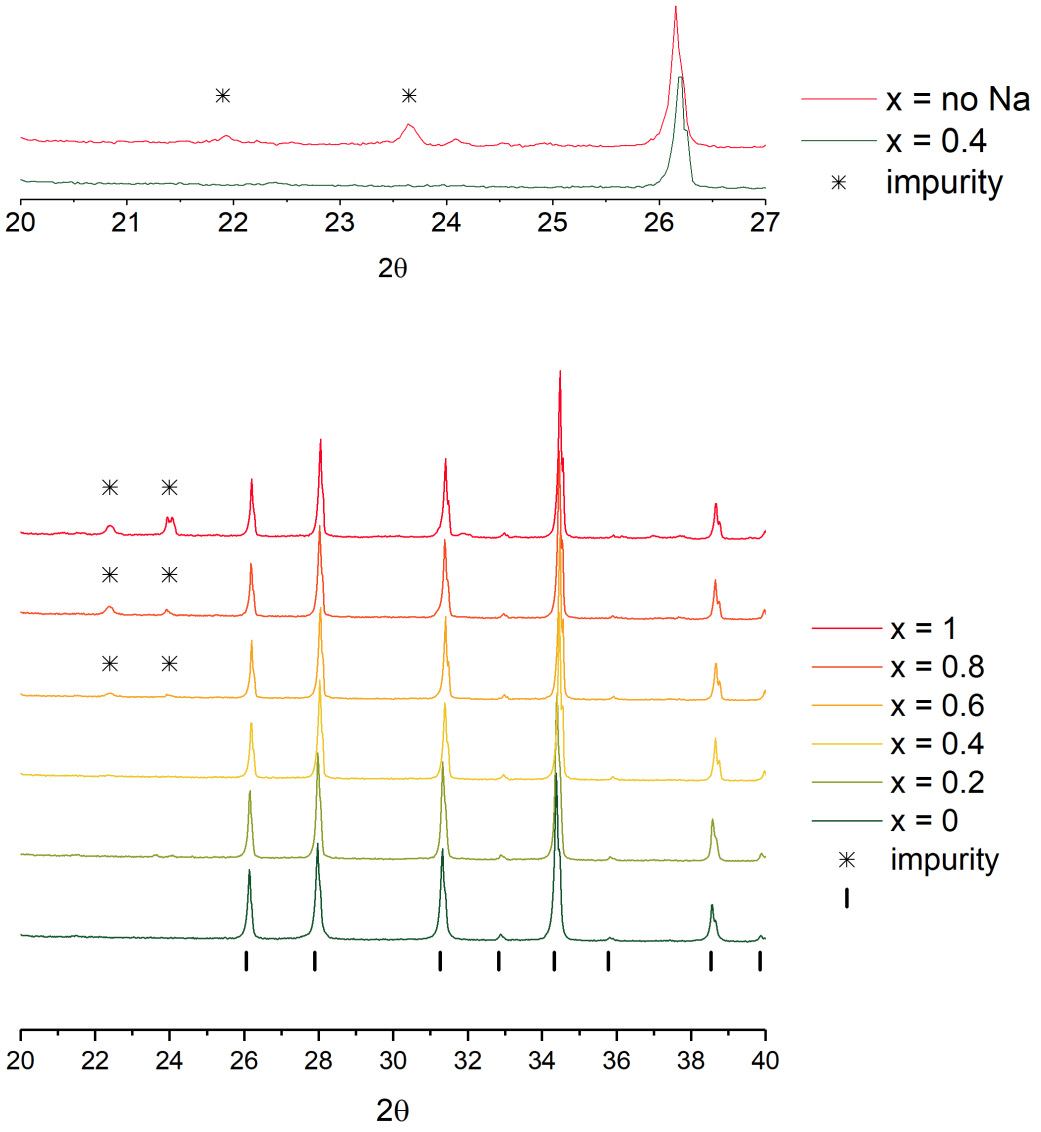

Figure 44. XRD patterns of $Li_{5+2x}La_{3-x}Na_xTa_2O_{12}$ (x = 0, 0.2, 0.4, 0.6, 0.8, 1). Top graph contains patterns of $Li_{5.8}La_{2.6}Na_{0.4}Ta_2O_{12}$ and $Li_{5.8}La_{2.6}Na_{0.0}Ta_2O_{12}$ (tickmarks designate cubic garnet phase peaks)

A generally similar picture can be observed for the XRD powder patterns of the $Li_{5+2x}La_{3-x}Na_xTa_2O_{12}$ (x = 0, 0.2, 0.4, 0.6, 0. 8, 1) samples (Figure 44). A pure garnet phase is formed up to x=0.4, while above this level a similar impurity ($5Li_2O{\cdot}Ta_2O_5$) appears. A similar experiment to confirm the presence of Na in the structure was

carried out for the x=0.4 sample, with the results showing the presence of a Li - Ta rich impurity phase when no Na was added (Figure 44 top). As above, this supports the conclusion that Na is also going into garnet structure for the Ta systems. The successful incorporation of Na is further supported by Rietveld structure refinement using the XRD data for powders with and without Na addition (Figures A7 and A8, Appendix). In order to stabilise the occupancy refinement isotropic thermal displacement parameters were constrained to a general variable. In particular, the Na doped sample was shown to have smaller cell parameters as well as a lower La occupancy value than undoped $Li_5La_3Nb_2O_{12}$, consistent with the smaller size and lower X-ray scattering factor of Na^+ versus La^{3+}. In contrast, the sample without Na revealed cell parameters very similar to the starting undoped phase $Li_5La_3Nb_2O_{12}$, and no reduction in La occupancy value.

If we examine the changes across the $Li_{5+2x}La_{3-x}Na_xTa_2O_{12}$ series, the lattice parameters for both Nb and Ta containing garnets showed a decrease in the cell parameter up to x=0.4 ($Li_{5.8}La_{2.6}Na_{0.4}(Nb/Ta)_2O_{12}$ (Table 14)) consistent with increasing Na incorporation.

Table 14. Lattice parameters for $Li_{5+2x}La_{3-x}Na_xM_2O_{12}$ (x=0-1, M=Nb, Ta)

Nominal Na content	V-valent metal	a, Å	Cell Volume, Å^3	La occupancy	Na occupancy (1-La)	Refined Na content	Pellet density, % of theoretical	GOF
0	Nb	12.8226(1)	2108.29(6)	1	0	0	58.6	1.486
0.2	Nb	12.8011(2)	2097.70(11)	0.939(5)	0.061(5)	0.183(15)	66.7	1.609
0.4	Nb	12.7931(1)	2093.75(5)	0.921(5)	0.079(5)	0.237(15)	64	1.701
0.6	Nb	12.7949(1)	2094.62(3)	0.875(3)	0.125(3)	0.375(9)	61.5	1.673
0.8	Nb	12.7950(1)	2094.71(4)	0.872(5)	0.128(5)	0.384(15)	62.6	1.839
1	Nb	12.7967(1)	2095.53(6)	0.865(4)	0.135(4)	0.405(12)	62.5	2.114
0	Ta	12.8375(1)	2115.67(3)	1	0	0	59	1.641
0.2	Ta	12.8278(1)	2110.85(3)	0.969(3)	0.031(3)	0.093(9)	62.3	1.546
0.4	Ta	12.8034(1)	2098.80(3)	0.884(3)	0.116(3)	0.348(9)	60.7	2.08
0.6	Ta	12.8023(1)	2098.27(3)	0.867(4)	0.133(4)	0.399(12)	59.7	2.54
0.8	Ta	12.8023(1)	2098.27(3)	0.877(4)	0.123(4)	0.369(12)	59.7	2.439
1	Ta	12.8036(1)	2098.93(5)	0.877(5)	0.123(5)	0.369(15)	58.9	3.731

The nominal La site occupancy factor was also refined, and it was shown that this value also decreases, and indeed further decreases are seen up to x=0.6, albeit this latter phase contains impurities (Figure 44). As noted above, the decrease in the nominal La site occupancy can be related to the lower X-ray scattering factor of Na^{+} versus La^{3+}. In order to obtain more information on the actual amount of Na incorporation on the La site, the occupancy of Na on the lanthanum site was refined, assuming the constraint that the sum of the Na and La site occupancies=1. A plot of these refined Na site occupancies versus the cell parameters are shown in Figure 45. Initially there is the expected trend of decreasing cell parameters with increasing of the Na content on the La site. However, for the Nb system in particular the cell parameters remain approximately constant for refined Na content above 0.23 of total Na on La site. In this respect, it is interesting to note that these refined Na occupancies were lower than the expected from the starting stoichiometry (as

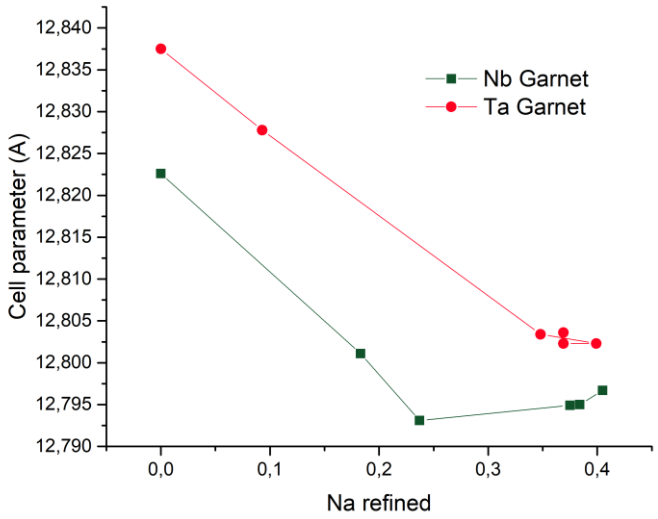

Figure 45. Cell parameter versus refined Na occupancy on La site in Nb and Ta based garnet

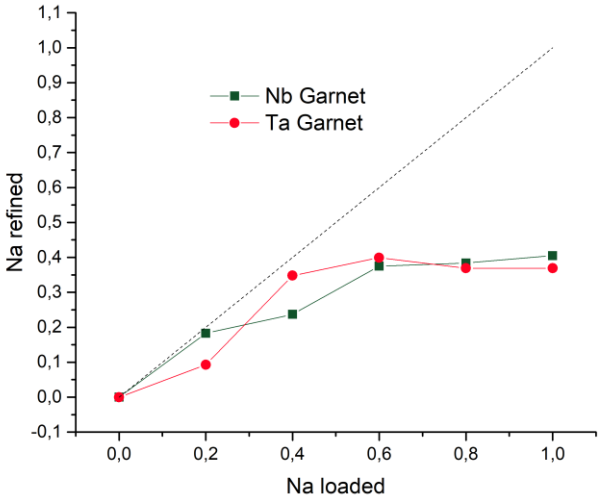

Figure 46. Refined Na occupancy versus expected composition based on the amount of Na added. Dash line represents 1:1 ratio

illustrated in Figure 46). Thus it suggests that not all the Na added is going onto the La site. There are two main possibilities to explain this discrepancy: (1) Na is being lost due to volatilisation at high temperatures, and (2) some of the Na is occupying another site within the cell, for example the lithium sites.

Considering these data and presence of impurities the total Na solubility limit is around 0.4 Na per formula unit for both series. The limits for the individual La-site and Li-site are so far unclear.

Na doping in $Li_7La_3Zr_2O_{12}$

We also investigated the possibility of Na incorporation onto the La site in $Li_7La_3Zr_2O_{12}$. Since it is not possible to increase the Li content above 7 per formula unit in garnet systems, this doping strategy required charge balance by co-doping with Nb/Ta on the Zr site. Figure 47 shows the resulting XRD powder patterns for

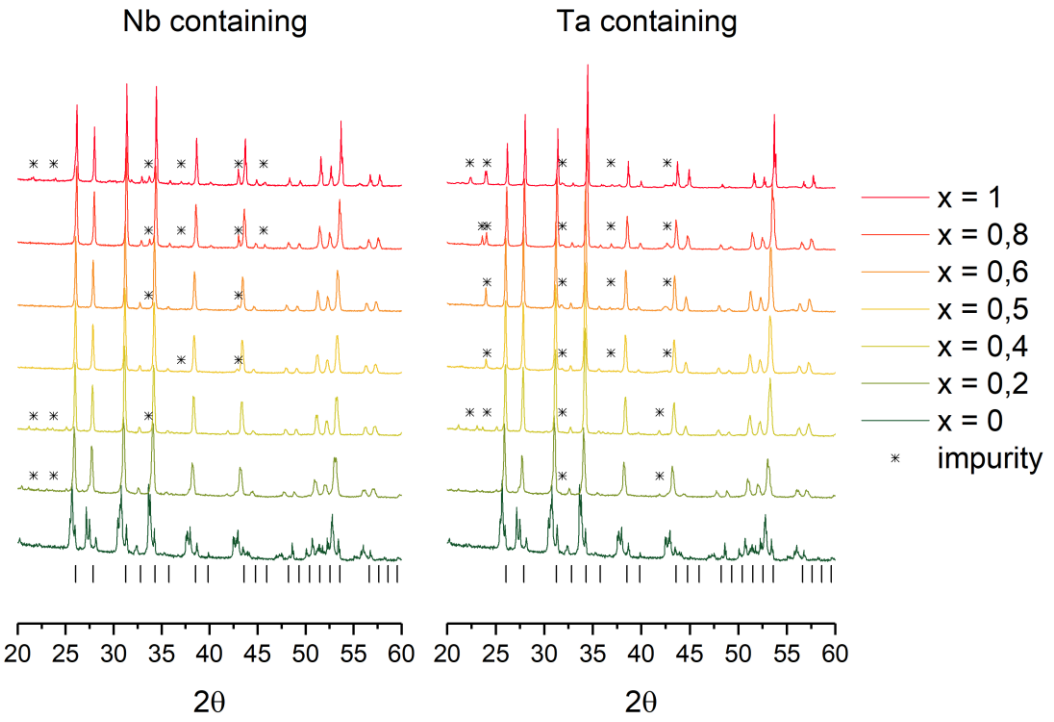

Figure 47. XRD patterns of $Li_7La_{3-x}Na_xZr_{2-2x}M_{2x}O_{12}$ (x=0-1, M=Nb, Ta),*-impurities, tickmarks designate cubic garnet phase peaks

$Li_7La_{3-x}Na_xZr_{2-2x}M_{2x}O_{12}$ (x = 0, 0.2, 0.4, 0.5, 0.6, 0.8, 1, M=Nb, Ta). All the doped samples were shown to have a cubic lattice, while a mixture of tetragonal and cubic garnet phases were observed for undoped $Li_7La_3Zr_2O_{12}$ due to partial contamination from the crucible. For the simultaneous Na and Nb/Ta doped samples, impurities were observed for all samples. Moreover, the amount of impurity phases, consisting of Li-Ta, Li-Nb, Li-Zr oxides, appeared to increase with Na content. In order to gather more information on these systems, Rietveld refinement was performed as for earlier synthesis (Table 15).

Table 15. Lattice parameters of $Li_7La_{3-x}Na_xZr_{2-2x}M_{2x}O_{12}$ (x=0-1, M=Nb, Ta)

Nominal Na content	Base metal	a, Å	Cell Volume, Å^3	La occupancy	Na occupancy (1-La)	Refined Na content	GOF
0.2	Nb	12.9505(3)	2171.99(15)	0.971(4)	0.029(4)	0.09(1)	2.011
0.4	Nb	12.9183(2)	2155.82(11)	0.970(4)	0.030(4)	0.09(1)	1.772
0.5	Nb	12.9092(2)	2151.29(10)	0.943(6)	0.057(6)	0.17(2)	1.615
0.6	Nb	12.8923(2)	2142.85(8)	0.926(3)	0.074(3)	0.22(1)	2.211
0.8	Nb	12.8471(2)	2120.39(11)	0.904(4)	0.096(4)	0.29(1)	2.368
1	Nb	12.7967(1)	2095.53(6)	0.865(4)	0.135(4)	0.41(1)	2.114
0.2	Ta	12.9514(3)	2172.46(18)	0.972(4)	0.028(4)	0.08(1)	1.88
0.4	Ta	12.9151(3)	2154.22(13)	0.942(4)	0.058(4)	0.17(1)	2.713
0.5	Ta	12.9090(2)	2151.18(9)	0.963(3)	0.037(3)	0.11(1)	1.898
0.6	Ta	12.8906(2)	2141.97(10)	0.945(5)	0.055(5)	0.17(2)	2.686
0.8	Ta	12.8543(2)	2123.93(10)	0.896(4)	0.104(4)	0.31(1)	3.017
1	Ta	12.8036(1)	2098.93(5)	0.877(5)	0.123(5)	0.37(2)	3.731

It was previously reported that the change of the cell parameters with transition from Zr to Nb/Ta containing garnet shows a decrease with increasing Na content [93,129]. Those obtained for the $Li_7La_{3-x}Na_xZr_{2-2x}M_{2x}O_{12}$ series should decrease even more significantly considering the smaller size of the Na potentially being incorporated. Indeed, samples show a decrease in cell parameters with an increase of Ta/Nb content for both series (Figure 48). However, there is no significant deviation from the values corresponding to systems without Na doped – just $Li_{7-x}La_3Zr_{2-x}M_xO_{12}$ (dash line). There is only one sample that is noteworthy as being significantly different, and that is the Nb/Ta endmember phase discussed earlier. It

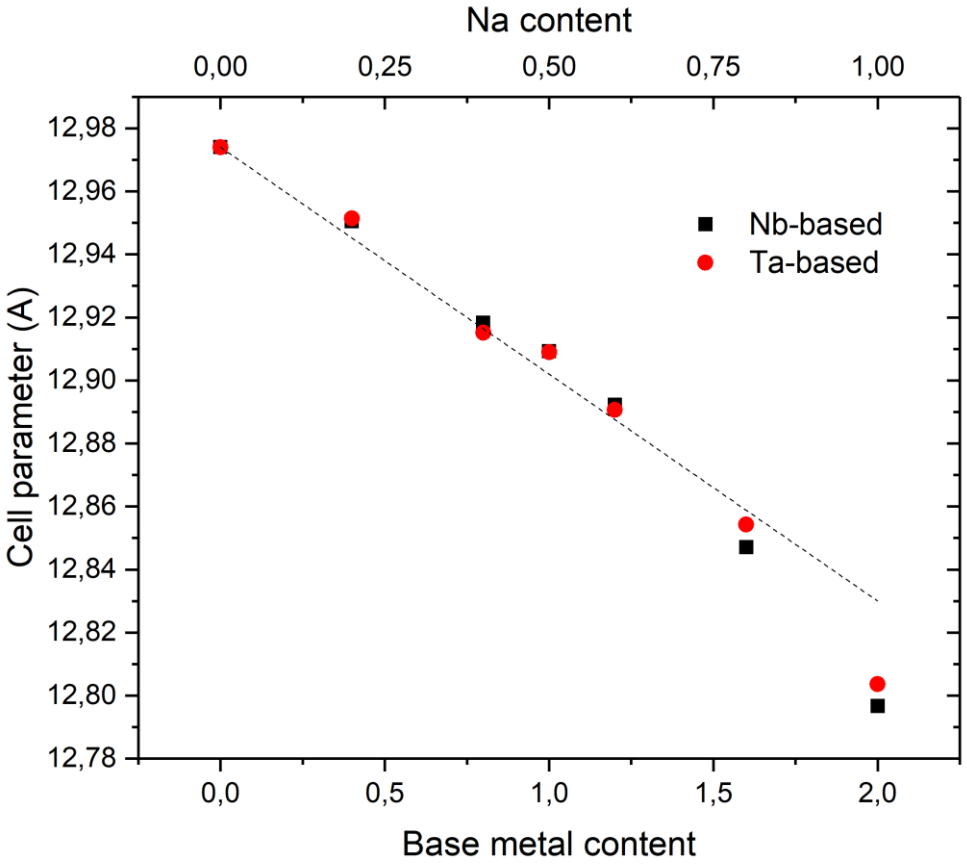

Figure 48. Cell parameters of $Li_7La_{3-x}Na_xZr_{2-2x}M_{2x}O_{12}$ (x=0-1, M=Nb, Ta) series. Dash line represents reported change of cell parameters in transition from Zr-garnet to Nb/Ta-garnet

therefore appears that zirconium forms a more thermodynamically stable phase with sodium that can be the source of impurities. Considering this fact, it is surprising to observe a small change of the La occupancy parameter in these series of samples. To investigate possibility of forming of La vacancies on their own in garnet the La-deficient samples were prepared. They showed the same cell parameters and La occupancy lower than 1 for both series. Previous similar experiment with only Nb/Ta containing garnet showed that these structures are intolerant to La deficiency. Obviously, in case of presence of Zr the system is more stable with higher strength margin. This can be due to larger ionic radii of Zr^{4+} causing formation of larger cell with smaller repulsion of oxygen atoms within the empty eight-coordinated La-site. Concluding this experiment, we can surely say that Na is not able to be on the La site in the Zr-containing garnets.

Conductivity study

Conductivity measurements were made on the pellets sintered at 900°C. Unfortunately, it did not appear that Na improved the sintering and all the pellet densities were relatively low (~60%). The measured impedance data could however be resolved into bulk, grain boundary and electrode responses (fitted with an equivalent circuit consisting of a series of two parallel resistance-CPE (constant element phase) contributions). The presence of a tail consistent with the electrode response confirms that the observed conductivity is ionic and that the electronic conductivity is negligibly small[130] (Figure A5, Appendix). Samples with higher Na

content (in which XRD data showed the presence of impurities) were also measured but the conductivities were found to be lower and accurate separation of bulk and grain boundary contributions could not be achieved.

The room temperature bulk conductivity for the undoped starting garnet-phases $Li_5La_3M_2O_{12}$ were found to be $2.5 \cdot 10^{-6}$ S/cm and $1 \cdot 10^{-6}$ S/cm for Nb and Ta, respectively. These values are comparable to values previously reported in literature for solid state synthesis route[79] but lower than reported in later studies by Peng at al[131]. The relatively poor sintering of the pellets is most likely the reason for this lower conductivity.

In addition, it was observed that the room temperature bulk and grain boundary conductivities decrease with increasing Na content. It therefore appears

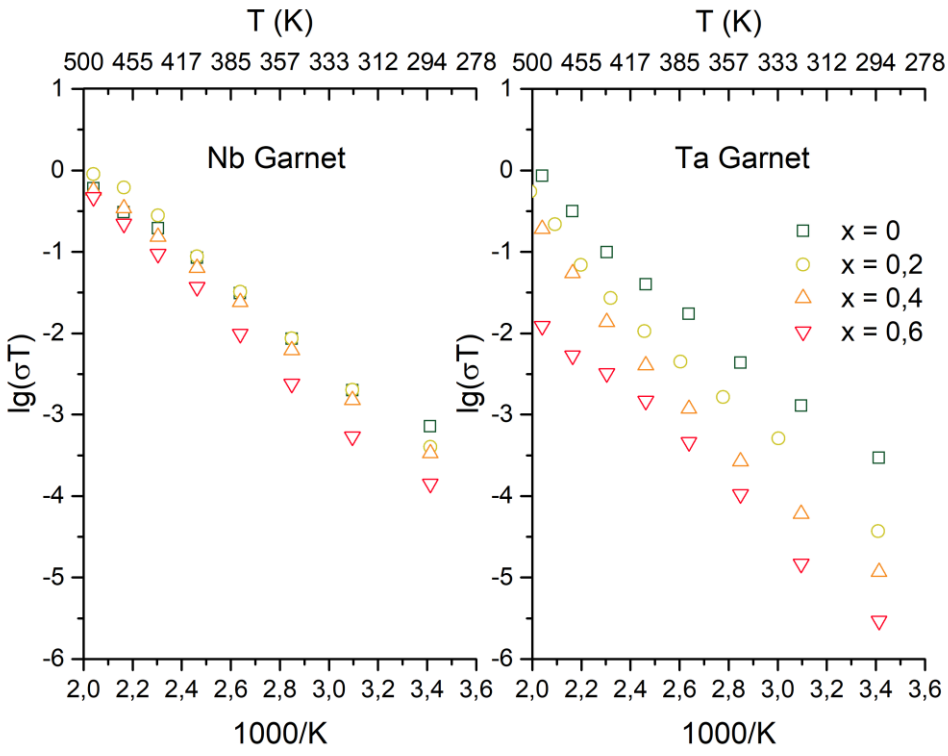

Figure 49. Arrhenius plots of $Li_{5+2x}La_{3-x}Na_xM_2O_{12}$ (x=0-0.6, M=Nb,Ta)

that in this case the general increase of Li content in the system does not increase the Li ion conductivity. Previous reports have shown that a reduction in the rare earth size lowers the conductivity of these garnet systems[132], and so the fact that Na^{+} is smaller than La^{3+} may at least partly explain the conductivity reduction. In addition, the possibility that a small amount of Na goes onto the Li site cannot be excluded. In this case, Na ions, due to their bigger size, could block the Li conduction pathways and therefore decrease conductivity. In this respect, Na substitution on the La site in perovskites ($(Li/La)_{1-x}TiO_3$) has been shown to decrease the lithium-ion conductivity[65]. In such cases the material turns from a typical fast ionic conductor, 10^{-3} S/cm, in to a good insulator, 10^{-10} S/cm, attributed to Na blocking Li transportation tunnels.

The variation of the conductivities with temperature are shown in Figure 49. For the Ta systems all the Na doped samples had lower conductivity over the whole temperature range studied. For the Nb systems the conductivity difference between the different samples was smaller and the x=0.2 sample showed higher conductivity than the undoped system at elevated temperatures. It is possible that for the Ta systems Li-Na disorder is increased and so has larger effect on ion transportation tunnels. Ion migration activation energy and diffusion coefficients at 293K are presented in Table 16.

Table 16. Ion migration activation energy and diffusion coefficients at 293K for $Li_{5+2x}La_{3-x}Na_xM_2O_{12}$ (x=0-0.6, M=Nb,Ta)

Nominal sample composition	σ_{293K} (S/cm)	D_{293K} (cm^2/s)	E_a (eV)
$La_3Li_5Nb_2O_{12}$	2.5×10^{-6}	1.4×10^{-11}	0.44(1)
$La_{2.82}Na_{0.18}Li_{5.37}Nb_2O_{12}$	1.4×10^{-6}	7.4×10^{-12}	0.50(1)
$La_{2.76}Na_{0.24}Li_{5.47}Nb_2O_{12}$	1.1×10^{-6}	6.1×10^{-12}	0.48(1)
$La_{2.63}Na_{0.38}Li_{5.75}Nb_2O_{12}$	4.8×10^{-7}	2.5×10^{-12}	0.53(1)
$La_3Li_5Ta_2O_{12}$	1.0×10^{-6}	5.6×10^{-12}	0.49(1)
$La_{2.91}Na_{0.09}Li_{5.19}Ta_2O_{12}$	1.3×10^{-7}	6.9×10^{-13}	0.54(1)
$La_{2.65}Na_{0.35}Li_{5.70}Ta_2O_{12}$	4.0×10^{-8}	2.1×10^{-13}	0.61(1)
$La_{2.60}Na_{0.40}Li_{5.80}Ta_2O_{12}$	1.0×10^{-8}	5.2×10^{-14}	0.54(1)

The activation energy increases with increase in Na content for both Nb/Ta series of $Li_{5+2x}La_{3-x}Na_xM_2O_{12}$, which may be due to Li-Na disorder and its' blocking effect on Li conduction pathways. The calculated diffusion coefficients decrease with increasing Na content and are in agreement with the data reported for this type of materials[133]. In order to fully clarify these differences further work is required to confirm the presence of Na on the Li site.

Structural study of $Li_7LaSr_2Nb_2O_{12}$

In order to gather further structural information on garnet Li ion conductors, new Li_7 tetragonal phases were prepared and their structures and conductivity examined.

The nominal samples of $LaX_2Nb_2Li_7O_{12}$ (X = Ba, Sr, Ca) were prepared at various conditions (800-1200C and 2-24 hours). It was found to not be possible to obtain barium and calcium containing tetragonal phases (Figure 50). This may relate to the large difference in size compared to La, which limits the level of

incorporation possible. However, in case of Sr doping we obtained a sample (prepared at 850°C for 12 hours) which contained 66% of tetragonal $Li_7LaSr_2Nb_2O_{12}$ and 34% of cubic garnet (Figure A6, Appendix). The inability to prepare sample containing 100% tetragonal garnet can be related to the fact that these systems are very difficult to make as they are extremely sensitive to the Li content and moisture.

The structural study was performed on the single crystals, which were extracted from the mixture containing both tetragonal and cubic garnet. Table 17 contains main crystal data, experimental parameters and refinement indices.

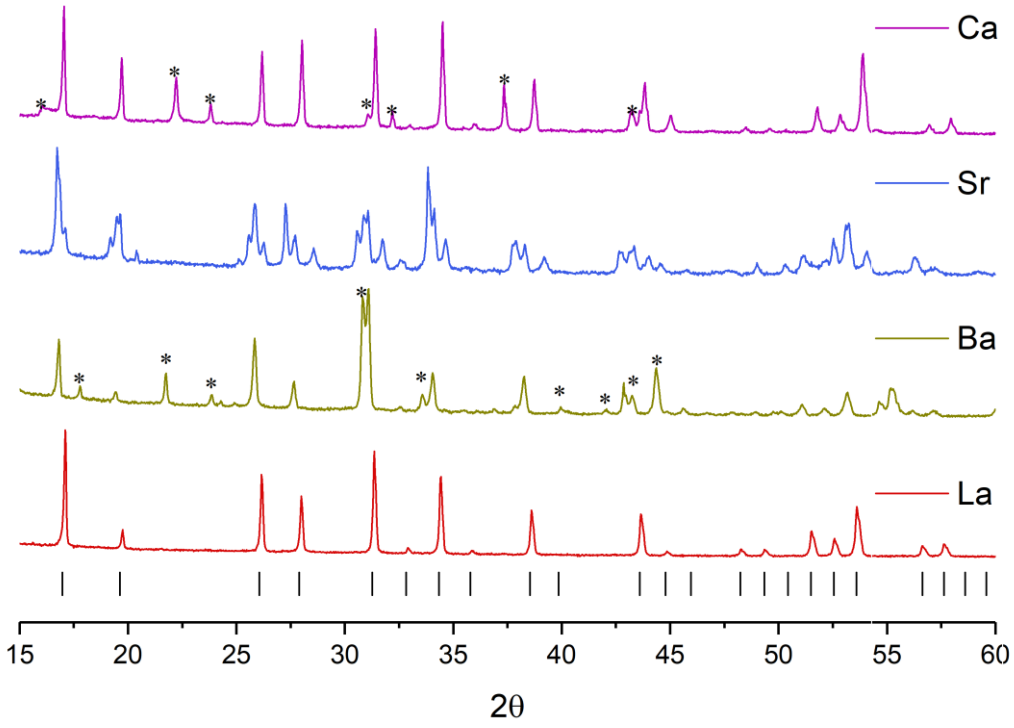

Figure 50. XRD patterns of $Li_7LaX_2Nb_2O_{12}$ (X = Ba, Sr, Ca) and $Li_5La_3Nb_2O_{12}$ for comparison. Asterisks designate non-garnet impurities, tickmarks designate cubic garnet phase peaks

Table 17 Crystal data and structure refinement parameters

Identification code	Tetragonal	Cubic
Empirical formula	$Li_7La_{0.99}Nb_2O_{12}Sr_{2.01}$	$Li_{6.63}La_{1.35}Nb_2O_{12}Sr_{1.65}$
Formula weight	739.97	756.07
Temperature/K	100.01(10)	100.00(10)
Crystal system	tetragonal	cubic
Space group	$I4_1/acd$	Ia-3d
a/Å	13.027(3)	12.8267(2)
b/Å	13.027(3)	12.8267(2)
c/Å	12.429(5)	12.8267(2)
α/°	90	90
β/°	90	90
γ/°	90	90
Volume/$Å^3$	2109.4(12)	2110.30(10)
Z	8	8
$\rho_{calc}g/cm^3$	4.66	4.759
μ/mm^{-1}	61.011	69.782
F(000)	2654	2701
Crystal size/mm^3	0.054 × 0.041 × 0.025	0.06 × 0.039 × 0.022
Radiation	CuKα (λ = 1.54184)	CuKα (λ = 1.54184)
2Θ range for data collection/°	13.594 to 149.902	16.932 to 149.766
Index ranges	-9 ≤ h ≤ 13, -10 ≤ k ≤ 16, -10 ≤ l ≤ 15	-15 ≤ h ≤ 15, -13 ≤ k ≤ 16, -15 ≤ l ≤ 16
Reflections collected	1709	8697
Independent reflections	530 [R_{int} = 0.0881, R_{sigma} = 0.0834]	184 [R_{int} = 0.0418, R_{sigma} = 0.0085]
Data/restraints/parameters	530/6/60	184/1/23
Goodness-of-fit on F^2	1.084	1.192
Final R indexes [I>=2σ (I)]	R_1 = 0.1094, wR_2 = 0.2656	R_1 = 0.0379, wR_2 = 0.1038
Final R indexes [all data]	R_1 = 0.1405, wR_2 = 0.2963	R_1 = 0.0379, wR_2 = 0.1038
Largest diff. peak/hole / e $Å^{-3}$	2.81/-2.88	1.35/-1.29

The least squares refinement of the structure of the tetragonal phase was difficult due to non-merohedral multi-twinning of the crystal. However, it was possible to extract the main component and refine it as the single crystal. This

approach affected the quality of the refinement and the final R_{int} is only 10.94% with the presence of electronic density artefacts related to the crystal twinning. Tables 18 and 19 contain the obtained atomic structural information for tetragonal $Li_7LaSr_2Nb_2O_{12}$.

Table 18. Fractional Atomic Coordinates and Equivalent Isotropic Displacement Parameters (Å²×100) for Tetragonal Garnet $Li_7LaSr_2Nb_2O_{12}$. U_{eq} is defined as 1/3 of the trace of the orthogonalised U_{IJ} tensor.

Atom	*x*	*y*	*z*	Occupancy	U_{eq}
La1	0.5	0.75	0.625	0.31(7)	2.78(17)
La2	0.6273(2)	0.5	0.75	0.34(6)	2.78(13)
Nb	0.5	0.5	0.5	1	2.84(14)
Sr2	0.6273(2)	0.5	0.75	0.66(6)	2.78(13)
Sr1	0.5	0.75	0.625	0.69(7)	2.78(17)
O2	0.5480(13)	0.6425(14)	0.4601(16)	1	3.0(4)
O1	0.5319(13)	0.4485(12)	0.3528(17)	1	2.8(4)
O3	0.6427(12)	0.4698(16)	0.5480(18)	1	3.4(5)
Li1	0.6620(40)	0.3340(40)	0.5610(40)	1	3.2(9)
Li2	0.5	0.75	0.375	1	1.8(15)
Li3	0.6780(40)	0.4280(40)	0.375	1	7.0(30)

Table 19. Anisotropic Displacement Parameters (Å²×100) for Tetragonal Garnet $Li_7LaSr_2Nb_2O_{12}$.

Atom	U_{11}	U_{22}	U_{33}	U_{23}	U_{13}	U_{12}
La1	2.41(17)	2.41(17)	3.5(3)	0	0	0.13(13)
La2	2.35(16)	2.52(16)	3.45(19)	0.03(10)	0	0
Nb	2.7(2)	2.22(18)	3.6(2)	-0.10(12)	-0.23(11)	-0.08(10)
Sr2	2.3.(16)	2.52(16)	3.45(19)	0.03(10)	0	0
Sr1	2.41(17)	2.41(17)	3.5(3)	0	0	0.13(13)
O2	2.8(8)	2.8(9)	3.3(10)	0.4(8)	1.0(8)	1.1(7)
O1	2.7(8)	1.1(7)	4.7(11)	-1.0(7)	0.1(8)	0.5(5)
O3	1.2(7)	4.4(11)	4.7(12)	-1.0(10)	1.2(8)	0.1(7)
Li1	3.6(12)	2.8(12)	3.2(12)	0.5(9)	0.6(9)	-0.4(9)
Li2	1.6(19)	1.6(19)	2.0(40)	0	0	0
Li3	6.0(30)	6.0(30)	10.0(80)	3.0(50)	-3.0(50)	-3.0(40)

The refined chemical composition confirms the presence of seven Li ions per formula unit corresponding to $Li_7LaSr_2Nb_2O_{12}$. As expected, the tetragonal phase

shows the presence of three fully occupied Li sites. There is an average 2.55Å distance between these Li sites without evidence of disorder. We also didn't observe any evidence of ordering of Sr and La between the two crystallographic sites, even with allowing relaxation of the symmetry down to orthorhombic.

The extracted single crystal with cubic structure had good quality and showed no twining, therefore least squares refinement of the cubic phase is more complete (R_{int} 3.79%) and has much less electronic density artefacts than tetragonal phase. Tables 20 and 21 contain atomic structural information for this cubic garnet.

Table 20. Fractional Atomic Coordinates and Equivalent Isotropic Displacement Parameters (Å²×100) for Cubic Garnet $Li_{6.63}La_{1.35}Sr_{1.65}Nb_2O_{12}$. U_{eq} is defined as 1/3 of the trace of the orthogonalised U_{IJ} tensor.

Atom	*x*	*y*	*z*	Occupancy	U_{eq}
La1	0.5	0.25	0.375	0.45(3)	1.53(6)
Sr1	0.5	0.25	0.375	0.55(3)	1.53(6)
Nb1	0.75	0.25	0.75	1	1.39(7)
O1	0.6059(4)	0.2998(4)	0.7172(4)	1	2.05(11)
Li1	0.6540(20)	0.3260(20)	0.5601(19)	0.42(3)	2.5(6)
Li2	0.5	0.25	0.625	0.52(10)	2.5(6)

Table 21. Anisotropic Displacement Parameters (Å²×100) for Cubic Garnet $Li_{6.63}La_{1.35}Sr_{1.65}Nb_2O_{12}$.

Atom	U_{11}	U_{22}	U_{33}	U_{23}	U_{13}	U_{12}
La1	1.42(6)	1.42(6)	1.75(7)	0	0	0.16(3)
Sr1	1.42(6)	1.42(6)	1.75(7)	0	0	0.13(3)
Nb1	1.39(7)	1.39(7)	1.39(7)	0.05(2)	-0.05(2)	-0.05(2)
O1	2.2(2)	2.0(3)	1.9(3)	-0.30(18)	0.0(2)	0.26(19)
Li1	3.4(10)	3.4(10)	0.6(9)	0	0	0
Li2	3.4(10)	3.4(10)	0.6(9)	0	0	0

The refined chemical composition gives a slightly smaller strontium content than expected, such that the overall stoichiometry is $Li_{6.63}La_{1.35}Sr_{1.65}Nb_2O_{12}$. Due to lower strontium content the cell has only 6.63 Li ions per formula unit to maintain

the charge balance and, therefore, the cell is cubic. The relaxation of the cell symmetry down to orthorhombic did not show any evidence for strontium – lanthanum ordering. The cubic phase has an evenly distributed partially occupied Li sites. The average distance between Li sites is small (1Å), indicating that the distribution of the Li on these partially filled sites must be such that adjacent sites cannot be filled at the same time.

Figure 51 represents the distribution of the Li ions in the tetragonal and cubic cells of garnet. As was already mentioned above, the average Li-Li interatomic distance is almost 2.5 times greater for tetragonal lattice than for cubic. Li ions in the cubic cell are very evenly distributed in the migration channels albeit adjacent sites cannot be occupied at the same time. In the tetragonal cell Li ions are instead ordered on specific sites and this ordering supresses Li ion mobility.

The conductivity study revealed very typical ionic conductivity values for tetragonal garnet. The Arrhenius plot showed that the tetragonal phase

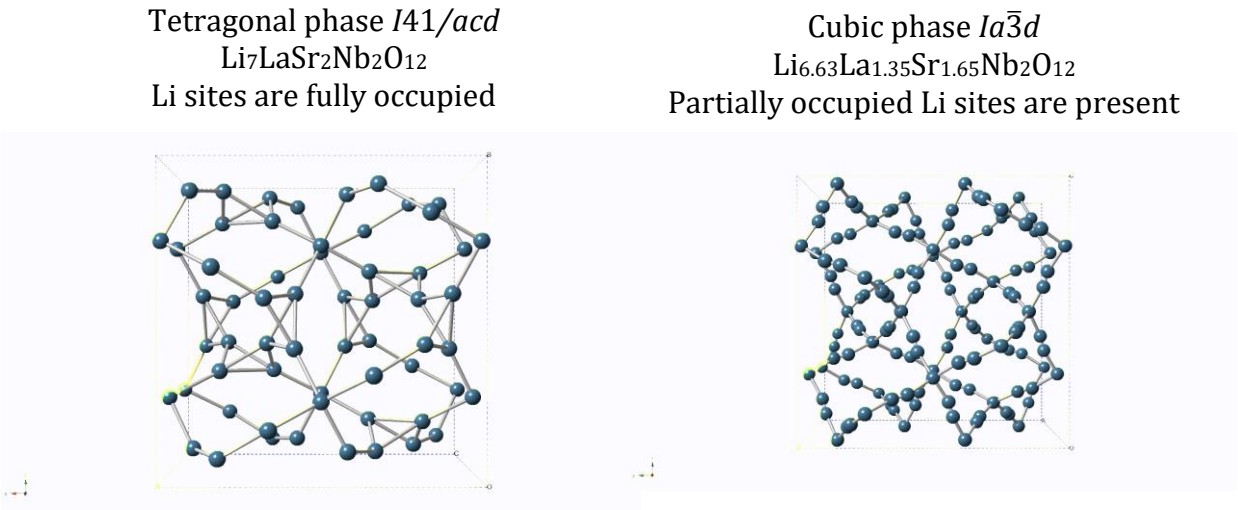

Figure 51. Distribution of Li sites for different structures of Li rich garnets

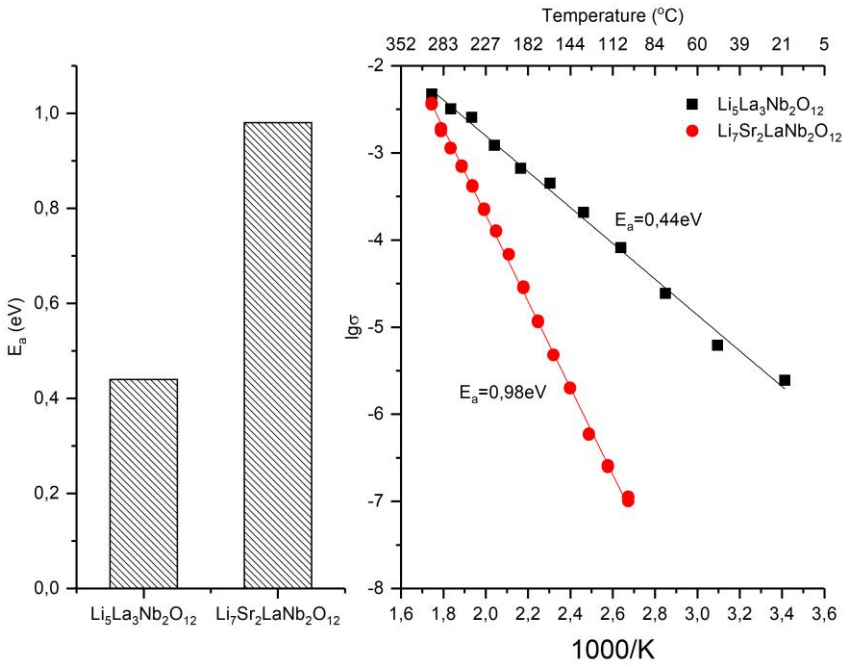

Figure 52. Activation energy and conductivity data for $Li_5La_3Nb_2O_{12}$ and $Li_7LaSr_2Nb_2O_{12}$ pellets

$Li_7LaSr_2Nb_2O_{12}$ has a much lower conductivity and a higher Li migration activation energy than the parent undoped cubic phase $Li_5La_3Nb_2O_{12}$, associated with the ordering of Li ions (Figure 52).

Conclusion

Sodium doped $Li_{5+2x}La_{3-x}Na_x(Nb/Ta)_2O_{12}$ (x = 0, 0.2, 0.4) garnet materials were successfully synthesized. Na incorporation onto the La site was supported by Rietveld refinement results. However, the conductivity data of the materials were found to be lower than for the undoped phase. Attempts to incorporate Na into mixed Ta/Zr and Nb/Zr systems suggested that the presence of Zr suppresses the accommodation of Na in the structure.

A new garnet $Li_7LaSr_2Nb_2O_{12}$ was synthesized showing tetragonal symmetry because of Li ordering. Due to this Li ordering the conductivity of obtained tetragonal phase is lower than that of the cubic phase.

Chapter Five

Structural features, phase changes and conductivity of $Na_2Mg_2(SO_4)_3$

Interest in sodium metal sulphate materials has grown in the last decade as a consequence of interest resulting from the development of new cathode materials for Na ion batteries[46,49,53,54,98,134–137]. In this area, nasicon and alluaudite-type materials have been attracting considerable interest. The former systems have also been widely investigated for their ionic conductivity following the reports of excellent Na ion conduction in the nasicon-type phosphate-silicates, $Na_{1+x}Zr_2(PO_4)_{3-x}(SiO_4)_x$ [38–44]. In the case of sulphate systems, previous studies have shown that nasicon materials could be formed in the $Na_xMg_xAl_{2-x}(SO_4)_3$ for $0 \leq x \leq 1.0$, with ionic conductivity increasing with Na content. The structure consists of a framework of corner linked Mg/AlO_6 and SO_4 tetrahedra, with the Na ions occupying

cavity sites within this framework. Attempts to increase the Na content above x=1 led to the appearance of impurities. Nevertheless, the nominal x=2 phase, $Na_2Mg_2(SO_4)_3$, has been highlighted in the literature, with it first being reported as an unknown mineral in 2008 by Jacobsson et al[138]. This mineral was found in a sample from the Eldfell volcano eruption, albeit the composition and structure were not confirmed and so the sample was simply labelled as "mineral EI". In later work, Balić-Žunić et al. reported the composition of this phase as $Na_2Mg_2(SO_4)_3$ from SEM studies, although they were unable to determine the room temperature structure[139]. However, the authors did report interesting changes with temperature; in particular, above 550^{o}C the phase was observed to transform into the langbeinite structure with cubic space group $P2_13$. The results further showed that this high temperature langbeinite-type phase was non-quenchable, i.e. the cubic langbeinite phase could not be obtained at room temperature by either slow or rapid cooling. The langbeinite structure shows some similarities with that of the nasicon-type structure in that it too consists of a framework of corner linked MgO_6 octahedra and SO_4 tetrahedra. However, in this structure, the cavity sites tend to be larger and so the structure is favoured by the presence of larger alkali ions such as potassium, caesium, and rubidium. Moreover, these two large cavity sites tend to be fully occupied, giving formulas such as $K_2Mg_2(SO_4)_3$ (the mineral langbeinite itself)[140,141]. The fact that an apparent langbeinite-type phase is observed for $Na_2Mg_2(SO_4)_3$ at elevated temperatures is therefore interesting, as sodium would normally be considered to be too small for the langbeinite structure, without the presence of a larger ion to help to stabilise the structure [142,143].

The aim of this study was therefore to determine the room temperature structure of $Na_2Mg_2(SO_4)_3$ and account for the transformation to the langbeinite structure at elevated temperatures. Through these studies it was shown that the structural changes in this $Na_2Mg_2(SO_4)_3$ system are more complex than initially reported, and these complexities are clarified through single crystal and variable temperature powder X-ray diffraction and Raman spectroscopy studies to provide a detailed understanding of this system.

Experimental

$Na_2Mg_2(SO_4)_3$ powder samples were prepared via a dissolution-evaporation route by dissolving stoichiometric amounts of Na_2SO_4 and $MgSO_4{\cdot}7H_2O$ (for 3g of sample) in water with subsequent evaporation to produce the precursor mixture. This precursor mixture was reground and heated in air at 750°C for 12 hours. Two cooling regimes were examined, quenching (removal of the sample from the furnace at 750°C) and slow cooling in the furnace (1°C/min). Powder XRD data were collected on a Panalytical Empyrean diffractometer with copper X-ray source in reflection geometry equipped with Pixcel 2D detector. Variable temperature powder XRD data up to 750°C were collected on a Bruker D8 advanced diffractometer with copper X-ray source and LynxEye detector in an Anton Paar HTK1200N furnace. Rietveld refinement of powder XRD data was performed using GSAS-II software[103].

Single crystals were prepared by two methods. In the first instance it was found that small crystals could be found in the powder (quenched or slow cooled) samples prepared above. For the second method, crystals were grown via crystallisation from the melt at 900^{o}C on gold foil with the cooling rate 0.2^{o}C/min in air. Single crystals were mounted on glass fibre and diffraction data for samples were collected on an Agilent SuperNova diffractometer using an Atlas detector. The crystals were kept at 100K during data collection using an Oxford Cryosystems Cryostream. Due to the large complex triclinic unit cell, data for one single crystal ($Na_2Mg(SO_4)_2$) sample were collected (at 100K) by the UK National Crystallography Service[144] on a Rigaku FRE+ diffractometer equipped with rotating anode with VHF Varimax confocal mirrors, an AFC12 goniometer and HyPix 6000 detector. Using Olex2 [123], the structure was solved with the ShelXT[124] structure solution program using Intrinsic Phasing, and refined with the ShelXL[125] refinement package using a least squares approach.

Powder samples were also studied by means of Raman spectroscopy using the 488 nm excitation line of an Ar^{+} ion laser in a DILOR XY spectrometer with a CCD detector and approximately 2 cm^{-1} of spectral resolution. The excitation and light collection were made through a 50X microscope objective lens, meaning that a small sample region is analysed at a time, and sampling was needed in order to confirm the homogeneity of the powder. High temperature Raman measurements were carried out in a LINKAM TS1500V stage up to 750°C, and laser output power was kept between 20 and 50 mW for measurements out/in the heating stage. Samples

were also analysed by thermal analysis (STA449 F1 Jupiter (Netzsch) TGA/DTA) to 750°C in N_2, heating at a rate of 5°C/min.

For the conductivity experiment, samples were pressed into 10mm pellets. These pellets were sintered the same way as the initial powders to keep the crystal structures the same. The conductivities of the obtained pellets were measured in air by electrochemical impedance spectroscopy using a HP 4204 gain-phase impedance analyser within a frequency range 5 – 1.3×10^7Hz. Pellets were coated on both sides with platinum ink and heated at 700°C for 2 hours. Zview software was used to analyse the obtained data[105].

Results and discussion

Initial results identifying the phase transitions

In the preparation of $Na_2Mg_2(SO_4)_3$ powders it was found that depending on the cooling process two different results were obtained. In particular, it was found that slow cooling in air led to a mixture of two phases (indicating phase separation), while quenching led to single phase $Na_2Mg_2(SO_4)_3$ (Figure 53). The quenched $Na_2Mg_2(SO_4)_3$ phase was shown to be a new phase, monoclinic ($P2_1$) $Na_2Mg_2(SO_4)_3$ from the structural analysis using single crystal data (discussed later). It is worth noticing that the potential influence of moisture on forming these structures was also studied. The samples sintered in dry nitrogen atmosphere have no difference to those sintered in air.

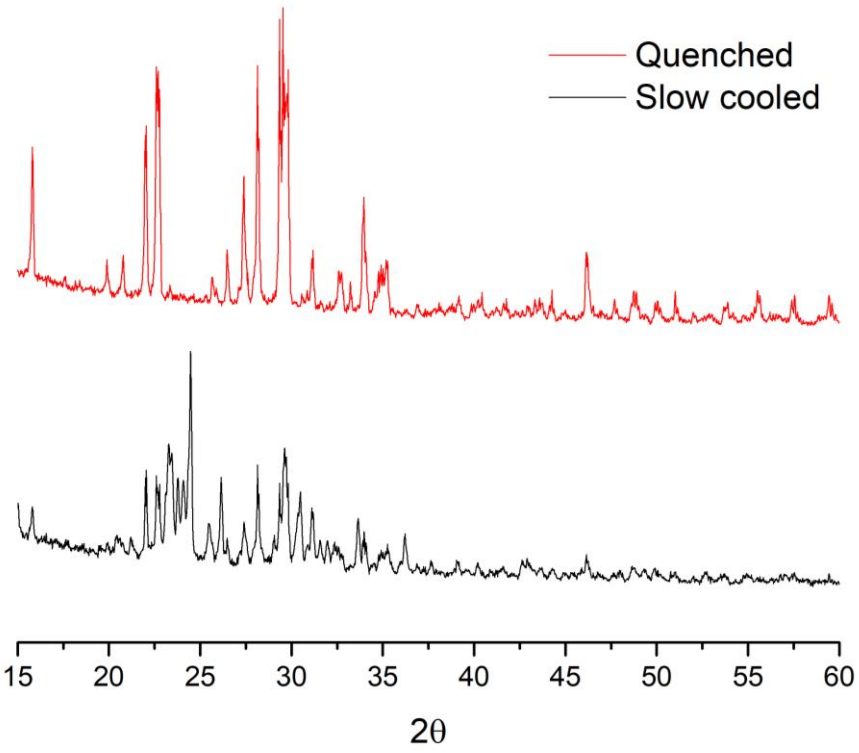

Figure 53. XRD patterns of $Na_2Mg_2(SO_4)_3$ at room temperature after quenching ($Na_2Mg_2(SO_4)_3$ phase maintained) and slow cooling (phase separation of $Na_2Mg_2(SO_4)_3$ to $Na_2Mg_3(SO_4)_4$ and $Na_2Mg(SO_4)_2$

In contrast to the single phase monoclinic $Na_2Mg_2(SO_4)_3$ obtained on quenching, the slow cooled sample shows a mixture of two phases. Via extraction of single crystals from a slow cooled melt we were able to identify these two phases and determine their crystal structures through single crystal XRD analysis. These two phases were identified as orthorhombic (*Pbca*) $Na_2Mg_3(SO_4)_4$ and triclinic ($P\bar{1}$) $Na_2Mg(SO_4)_2$, both of which have not been previously reported. The results therefore indicate that $Na_2Mg_2(SO_4)_3$ disproportionate during the slow cooling process, and so an overall phase scheme for the "$Na_2Mg_2(SO_4)_3$" system can be described as below:

$$\begin{matrix}\frac{1}{2}Na_2Mg_3(SO_4)_4\ (Pbca)\\ \frac{1}{2}Na_2Mg(SO_4)_2\ (P\bar{1})\end{matrix} \xleftarrow{\text{Slow cooling}} Na_2Mg_2(SO_4)_3\ (750^oC) \xrightarrow{\text{Quenching}} Na_2Mg_2(SO_4)_3\ (P2_1)$$

In order to gather further information on the phase changes in this "$Na_2Mg_2(SO_4)_3$" system, variable temperature powder XRD (Figure 54) studies were performed. These studies showed similar results to those previously reported by Balić-Žunić et al.[139], with the transformation of both the low temperature systems (quenched and slow cooled) into the cubic langbeinite ($P2_13$) $Na_2Mg_2(SO_4)_3$ structure at a temperature near 600°C during the heating stage (Figure 54).

In case of the slow cooled decomposed mixture of $Na_2Mg_3(SO_4)_4$ and $Na_2Mg(SO_4)_2$ we observe a simple reaction between these component phases resulting in formation of the langbeinite $Na_2Mg_2(SO_4)_3$ phase, starting at 610°C . This is a slow process, as highlighted by the fact that we can still observe peaks due to the starting phases in the pattern up to 675°C (Figure 54a). The cooling stage of the variable temperature data, highlights that, on slow cooling, decomposition of the langbeinite-type, $Na_2Mg_2(SO_4)_3$ phase to $Na_2Mg_3(SO_4)_4$ and $Na_2Mg(SO_4)_2$ occurs at ≈525°C (Figure 54c).

The variable temperature powder XRD studies on the quenched monoclinic $Na_2Mg_2(SO_4)_3$ phase, showed a different thermal behaviour on heating. This phase first transits into a cubic langbeinite phase at ≈250°C, and then decomposes at ≈350°C into the $Na_2Mg_3(SO_4)_4$ and $Na_2Mg(SO_4)_2$ mixture (Figure 54b). On heating to higher temperature, this $Na_2Mg_3(SO_4)_4$ and $Na_2Mg(SO_4)_2$ mixture recombines

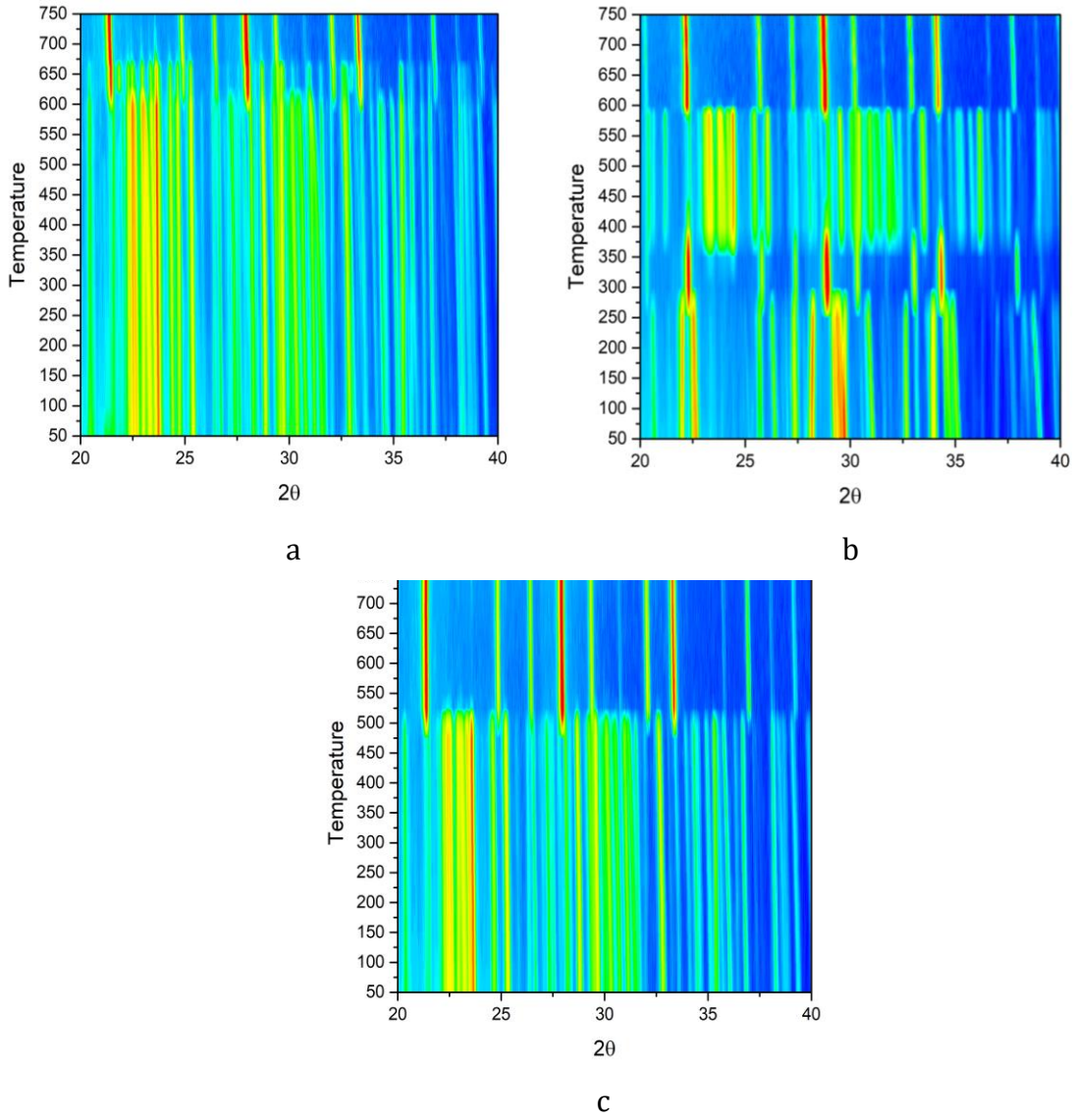

Figure 54. Contour plots of variable temperature XRD of $Na_2Mg_2(SO_4)_3$ compositions: a) heating the slow cooled sample (mixture of $Na_2Mg_3(SO_4)_4$ and $Na_2Mg(SO_4)_2$) shows one transition caused by reaction of components to give langbeinite-type $Na_2Mg_2(SO_4)_3$, b) heating the quenched ($Na_2Mg_2(SO_4)_3$) phase shows a range of different transitions caused by phase transformation and decomposition/recombination of components, c) slow cooling samples show a single decomposition point at ≈525°C into a mixture of $Na_2Mg_3(SO_4)_4$ and $Na_2Mg(SO_4)_2$.

(at ≈575°C) to give cubic langbeinite-type $Na_2Mg_2(SO_4)_3$ again. The whole phase transformation process for quenched $Na_2Mg_2(SO_4)_3$ can thus be expressed with the following scheme:

Monoclinic $P2_1 \xrightarrow{250°C}$ Langbeinite $P2_13 \xrightarrow{350°C}$ Mixture $Pbca + P\bar{1} \xrightarrow{575°C}$ Langbeinite $P2_13$

In this case reaction between $Na_2Mg_3(SO_4)_4$ and $Na_2Mg(SO_4)_2$ occurs completely after reaching 575°C, a slightly lower temperature than previously for the slow cooled system. The reason for this lower temperature is most likely related to the highly homogeneous distribution of the compounds after phase decomposition of the lower temperature langbeinite phase.

In addition to analysing $Na_2Mg_2(SO_4)_3$ we also managed to synthesise the pure triclinic $Na_2Mg(SO_4)_2$ phase by slow cooling (1°C/min) 1:1 mixtures of Na_2SO_4

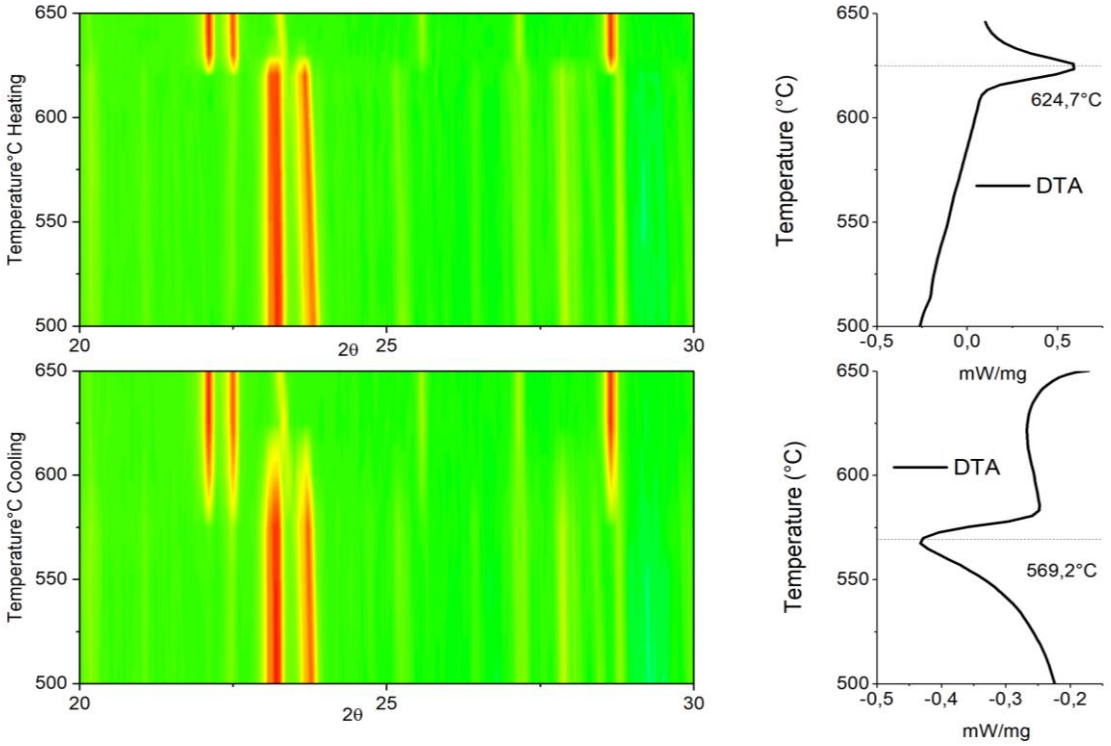

Figure 55. Contour plots of variable temperature XRD and DTA curves of $Na_2Mg(SO_4)_2$ showing a decomposition into langbeinite-type $Na_2Mg_2(SO_4)_3$ and high temperature vantgoffite $Na_6Mg(SO_4)_4$ at elevated temperature on heating, with a recombination on cooling to give $Na_2Mg(SO_4)_2$. For the latter, slow kinetics for this process means that there is a small range of temperatures where all three phases are present. Note the difference in temperature between the phase transition in XRD and DTA relates to these slow kinetics and the fact that the latter cooling stage corresponds to a faster rate

and $MgSO_4$ from 650°C. Interestingly, relatively rapid cooling gives a mixture of vantgoffite $Na_6Mg(SO_4)_4$ and $MgSO_4$. The thermal evolution of this $Na_2Mg(SO_4)_2$ phase is also interesting (Figure 55). In particular, high temperature powder XRD suggests that this phase decomposes at ~625°C into a langbeinite phase ($a_{923K} =$ 9.855(1)Å), and an extra phase which is related to the high temperature form of vantgoffite $Na_6Mg(SO_4)_4$ (triclinically distorted hexagonal lattice a=5.292(7)Å, b=7.775(3)Å, c=5.413(7)Å, α=89.62(3)°, β=91.25(5)°, γ=119.34(3)°). On cooling these two phases recombine to form the original $Na_2Mg(SO_4)_2$ although slow kinetics can lead to incomplete reaction/recombination for samples which are cooled rapidly, and so consequently slow cooling is required to produce pure $Na_2Mg(SO_4)_2$. These slow kinetics are highlighted in the variable temperature XRD data on cooling, which show that there is a small range of temperatures where all three phases are present.

Single crystal study

A small single crystal of monoclinic $Na_2Mg_2(SO_4)_3$ was picked from the freshly quenched powder. Single crystals of orthorhombic $Na_2Mg_3(SO_4)_4$ and triclinic $Na_2Mg(SO_4)_2$ were grown from the melt at 900°C on gold foil. In the case of the former, a small single crystal of the orthorhombic $Na_2Mg_3(SO_4)_4$ phase was picked from the decomposed slow cooled melt of $Na_2Mg_2(SO_4)_3$. Triclinic $Na_2Mg(SO_4)_2$ crystal was grown from the premade pure powder phase.

Due to the rather large and relatively simple orthorhombic cell, a copper X-ray tube was selected for the data collection on the $Na_2Mg_3(SO_4)_4$ crystal. Data collection for the complex monoclinic $Na_2Mg_2(SO_4)_3$ single crystal was more complicated because of the chirality of the cell and non-merohedral twinning of the single crystal. To handle this the whole diffraction sphere of the data was collected with a molybdenum X-ray source. No specific restraints were used for structural refinement.

Data collection for the triclinic $Na_2Mg(SO_4)_2$ phase proved to be a challenging task, given the complexity of the structure and the small size of the single crystal. In this case, collection of the whole diffraction sphere was performed with a molybdenum X-ray source. However, it was found that the crystal structure didn't produce many strong reflections and so we couldn't collect sufficient amount of data in adequate time on our in-house diffractometer. In order to solve this issue, crystals of the $Na_2Mg(SO_4)_2$ phase were sent to the UK National Crystallography Service (Southampton, UK) for data collection. It was found that the standard single crystal growth process is not efficient and during the high temperature synthesis process (complexities of phase formation noted in the variable temperature powder diffraction study) the crystals are formed with some defects. Therefore the data were collected on a non-merohedrally twinned crystal with one significant domain and several much smaller domains. It was found best to treat the main domain as if it was a dataset from a single crystal. This treatment of the data allowed us to successfully solve the structure. The main information about the single crystal experiments and results are shown in table 1 (the full refined structural parameters are given in the appendix).

Table 22. Single crystal study information

Empirical formula	$Mg_2Na_2O_{12}S_3$	$Mg_3Na_2O_{16}S_4$	$MgNa_2O_8S_2$
Formula weight	382.78	503.15	262.41
Temperature/K	100.00(10)	100.00(10)	100(2)
Crystal system	monoclinic	orthorhombic	triclinic
Space group	$P2_1$	*Pbca*	$P\bar{1}$
a/Å	13.6986(3)	9.51764(19)	11.14950(10)
b/Å	9.5323(2)	8.70474(15)	13.42540(10)
c/Å	21.3167(4)	29.1089(6)	16.9497(2)
α/°	90	90	99.7390(10)
β/°	105.114(2)	90	106.9960(10)
γ/°	90	90	105.2980(10)
Volume/Å³	2687.23(10)	2411.63(8)	2255.40(4)
Z	12	8	14
ρ_{calc}g/cm³	2.838	2.772	2.705
μ/mm⁻¹	1.138	10.567	1.068
F(000)	2280	2000	1820
Crystal size/mm³	0.092 × 0.082 × 0.057	0.238 × 0.171 × 0.113	0.11 × 0.09 × 0.05
Radiation	MoKα (λ = 0.71073)	CuKα (λ = 1.54184)	MoKα (λ = 0.71075)
2Θ range for data collection/°	4.336 to 64.062	11.108 to 139.948	3.264 to 61.012
Index ranges	-20 ≤ h ≤ 20, -14 ≤ k ≤ 14, -31 ≤ l ≤ 31	-11 ≤ h ≤ 7, -10 ≤ k ≤ 10, -35 ≤ l ≤ 20	-15 ≤ h ≤ 15, -19 ≤ k ≤ 19, -24 ≤ l ≤ 24
Reflections collected	36911	6016	155205
Independent reflections	36911 [R_{sigma} = 0.0613]	2274 [R_{int} = 0.0194, R_{sigma} = 0.0200]	13757 [R_{int} = 0.0456, R_{sigma} = 0.0177]
Data/restraints/ parameters	36911/1/1028	2274/0/226	13757/25/870
Goodness-of-fit on F²	0.977	1.055	1.032
Final R indexes [I>=2σ (I)]	R_1 = 0.0310, wR_2 = 0.0643	R_1 = 0.0246, wR_2 = 0.0666	R_1 = 0.0367, wR_2 = 0.0835
Final R indexes [all data]	R_1 = 0.0398, wR_2 = 0.0655	R_1 = 0.0263, wR_2 = 0.0678	R_1 = 0.0399, wR_2 = 0.0851
Largest diff. peak/hole e/Å³	0.54/-0.53	0.40/-0.55	3.69/-2.38
Flack parameter	-0.02(3)	n/a	n/a
CCDC deposition number	CCDC 1881701	CCDC 1881700	CCDC 1881702

Monoclinic $Na_2Mg_2(SO_4)_3$

The quenched sample of $Na_2Mg_2(SO_4)_3$ was shown to be monoclinic with space group $P2_1$. The unit cell is relatively complex and the whole structural pattern becomes clear only on examination of an enlarged supercell. The chiral structure consists of SO_4 tetrahedra corner sharing with MgO_6 or MgO_5 units. The latter MgO_5 units are mostly distorted square pyramids, although one in every three units adopts a more trigonal bipyramid arrangement due to local distortions. The

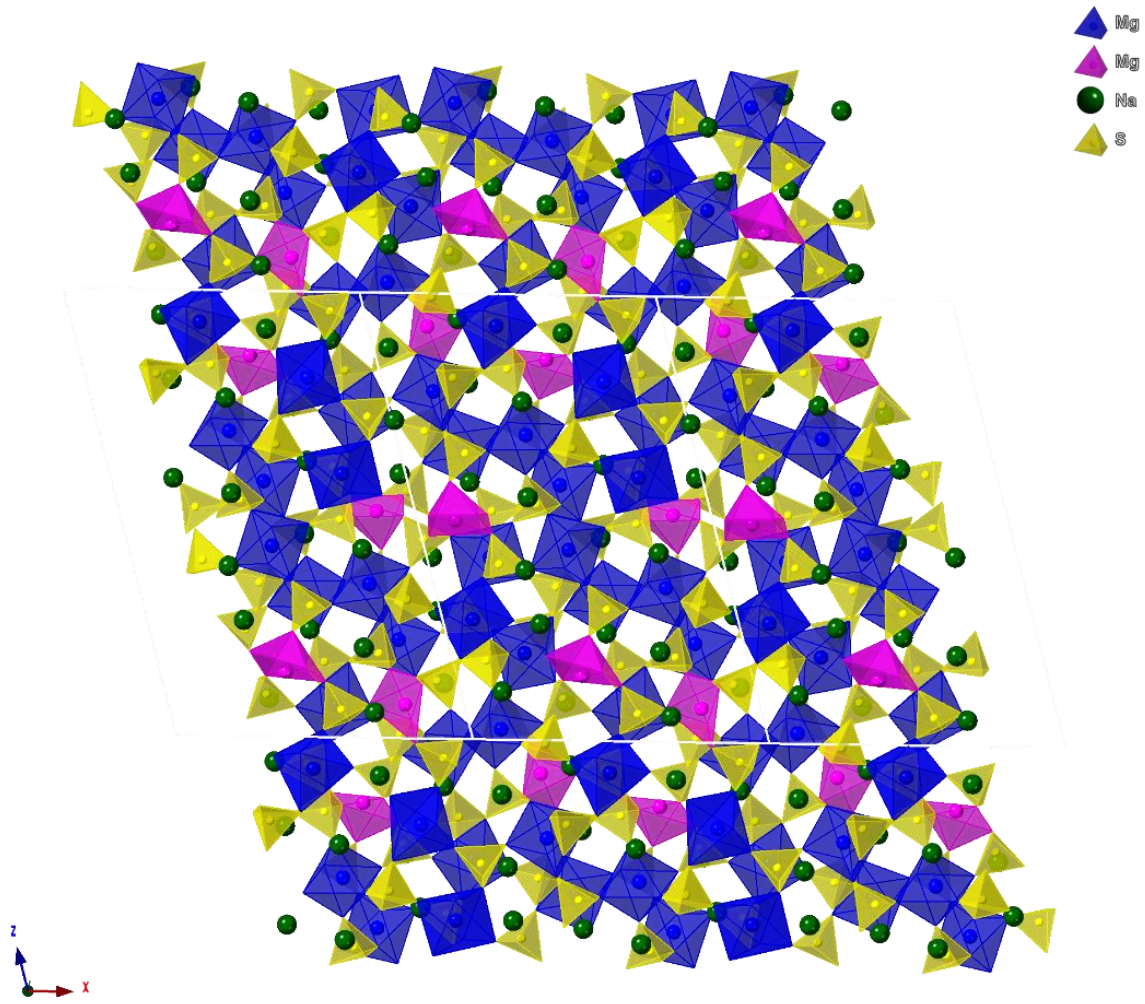

Figure 56. Single crystal structure of $Na_2Mg_2(SO_4)_3$ at 100K

distorted square pyramids have a dipole moment with positive base and negative top corner. These MgO_5 units are gathered in two types of clusters in the crystal lattice (Figure 56).

The first type is a cluster of two square pyramids with non-parallel base-facing. These double pyramid clusters via symmetry form a surface in the (0 0 2) plane with polarisation vector along *b* axis. The second cluster consists of an aggregation of four MgO_5 units forming helixes with positive polarisation in the centre directed along the axis of the helix (Figure 57). The resultant stack of helixes forms a layer in the (0 0 1) plane. In total, the structure consists of alternating parallel layers of helixes and double pyramid clusters. The overall polarisation vectors of both cluster systems are collinear. A close inspection of the MgO_5 square pyramids shows that they can also be described as distorted MgO_6 octahedra with one of oxygen atoms at a significantly longer distance. This can be illustrated by

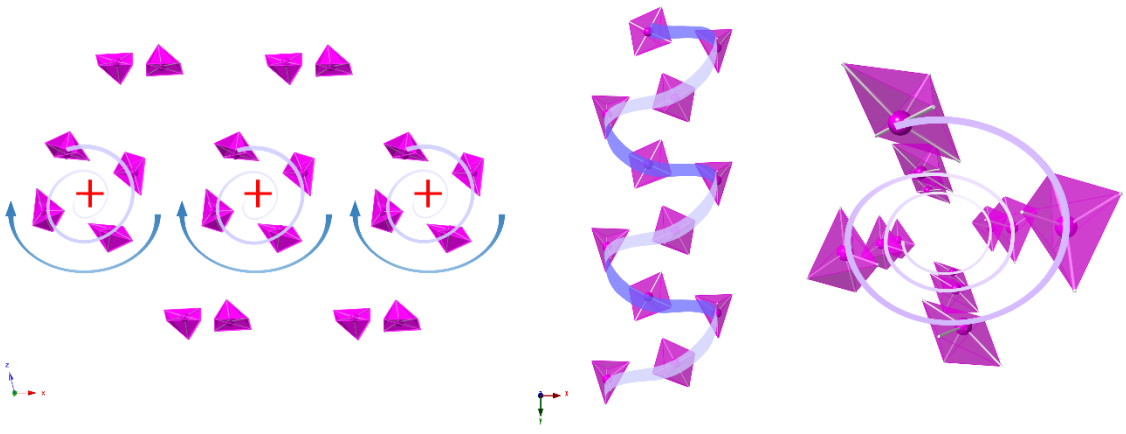

Figure 57. left) The orientations of MgO_5 pyramids forming helixes in monoclinic $Na_2Mg_2(SO_4)_3$ (100K). Arrows show downwards rotation of the helixes forming the layer. Double pyramid clusters layers are above and below the helix layer; middle) Single helix in profile; right) The enlarged helix view from top showing spiralling of pyramids.

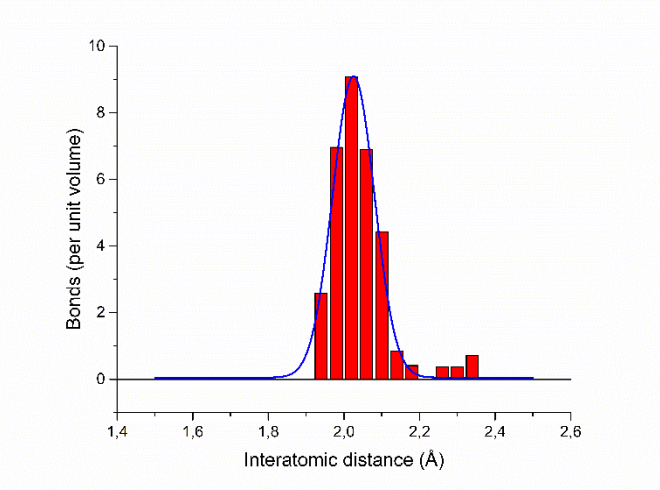

Figure 58. Distribution of interatomic distances in quenched $Na_2Mg_2(SO_4)_3$ for magnesium surroundings with Gaussian fitting.

Figure 58, which shows the distribution of interatomic distances at room temperature surrounding the magnesium, with Gaussian fitting. The main peak in the interatomic distances around Mg can be described with a maxima at 2.02Å corresponding to the expected Mg-O distance. However an extra peak is observed at around 2.3 Å corresponding to the longer bond to the oxygen atom making up the sixth bond to the MgO_5 units.

The low temperature (~250°C) phase transition to cubic langbeinite can be explained by the fact that, despite the apparent complex structure of $Na_2Mg_2(SO_4)_3$, in reality this phase is similar to langbeinite in that it requires only a small amount of rotation of the SO_4 units in langbeinite to conduct the change of the unit cell symmetry (cubic-monoclinic). The variable temperature data shows, however, that the structure is unstable at intermediate (≈350-≈600°C) temperatures, and so it decomposes into the two compounds $Na_2Mg_3(SO_4)_4$ and $Na_2Mg(SO_4)_2$. This phase decomposition is a complex process and so has relatively slow kinetics, and so the $Na_2Mg_2(SO_4)_3$ phase can be preserved at low temperatures by quenching. It is

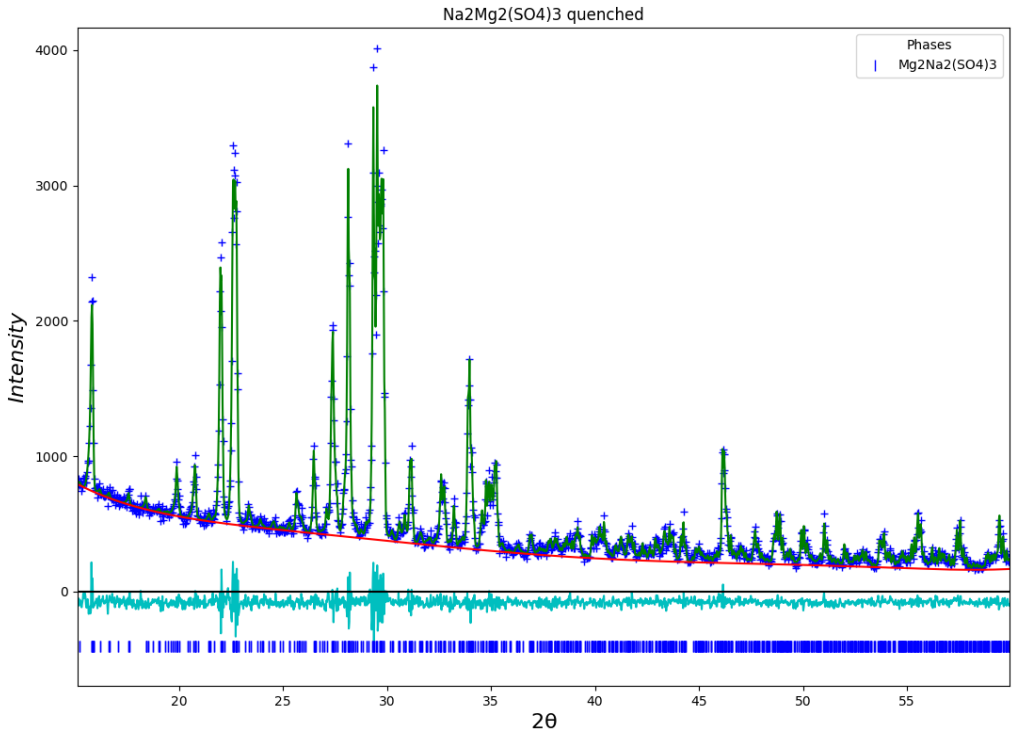

Figure 59. Observed, calculated and difference plots for structural refinement of $Na_2Mg_2(SO_4)_3$ using X-ray powder diffraction data. R_{wp}= 5.6%, GOF = 1.41

possible that the decomposition might also be avoided on heating by using rapid heating rates.

In order to confirm that the quenched $Na_2Mg_2(SO_4)_3$ powder was indeed monoclinic $Na_2Mg_2(SO_4)_3$, a basic Rietveld refinement was performed using the powder XRD data (using the single crystal structural parameters for monoclinic $Na_2Mg_2(SO_4)_3$). This refinement led to a good fit to the data, thus confirming that the quenched powder was indeed monoclinic $Na_2Mg_2(SO_4)_3$ (Figure 59).

$Na_2Mg_3(SO_4)_4$

The single crystal data showed that $Na_2Mg_3(SO_4)_4$ has an orthorhombic cell with space group *Pbca*. The crystal structure consists of the SO_4 tetrahedra corner sharing with MgO_6 or MgO_5 units. All the SO_4 tetrahedra are relatively undistorted and the average S-O bond length is 1.472 Å. The magnesium atoms in this system

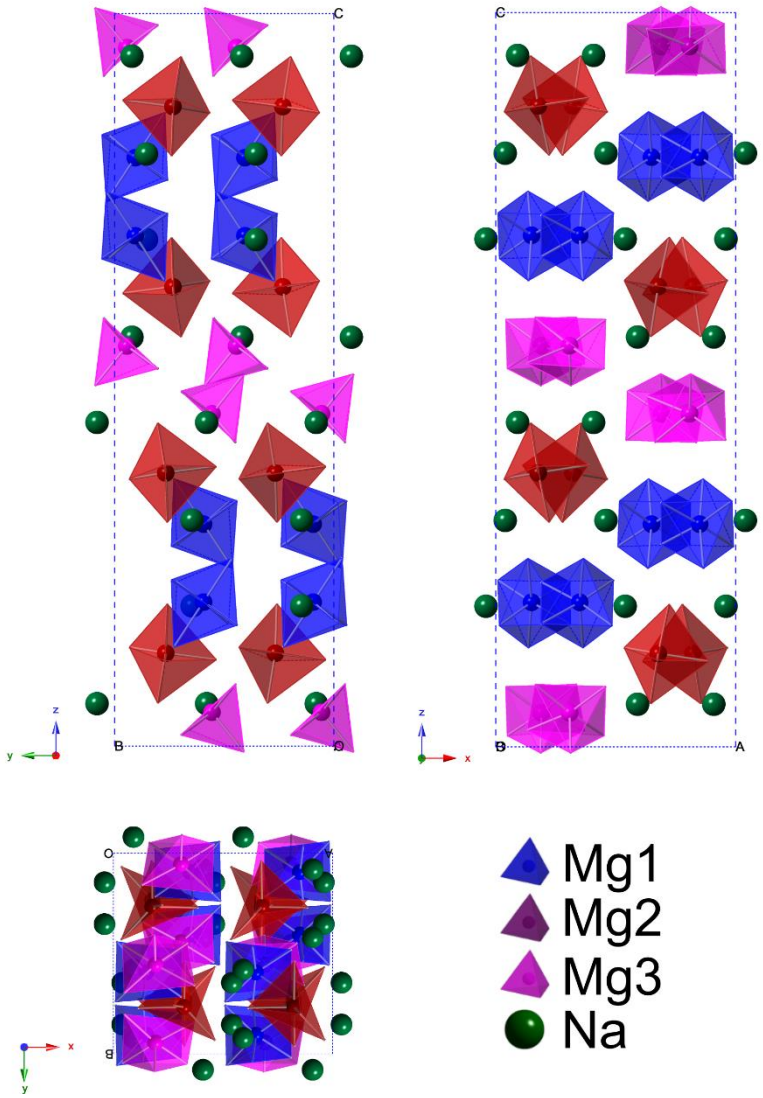

Figure 60. Structure of $Na_2Mg_3(SO_4)_4$ with different plane projections. SO_4 units are omitted for clarity. Top left – view along a axis, top right – view along b axis, bottom – view along c axis.

occupy three different sites. On the first site, Mg1, magnesium is six-coordinate and forms MgO_6 octahedra, where all the Mg-O bonds have similar lengths in the equatorial plane around 2.038 Å, while the axial oxygen atoms are at a slightly further average distance of 2.128 Å. On the Mg2 site, magnesium is five-coordinate trigonal bipyramidal. The central oxygen triangle is close to be isosceles with dimensions 2.38-2.95-3.07Å. The distances from Mg2 to O are also relatively similar - 2.02 Å. The third magnesium site, Mg3, is also five-coordinate, but in this case the MgO_5 unit forms a square pyramid. All the Mg-O distances in the pyramid are roughly the same. The four oxygen torsion angles within the pyramid base do not exceed 2˚ i.e. the base surface is fairly flat. The absence of the sixth oxygen leads to a Mg-O dipole, which causes polarisation of the adjacent MgO_6 octahedra as illustrated by the longer Mg-O_{axial} bond, and results in a long range (3.036Å) interaction of this axial O with the MgO_5 pyramid (Figure 61).

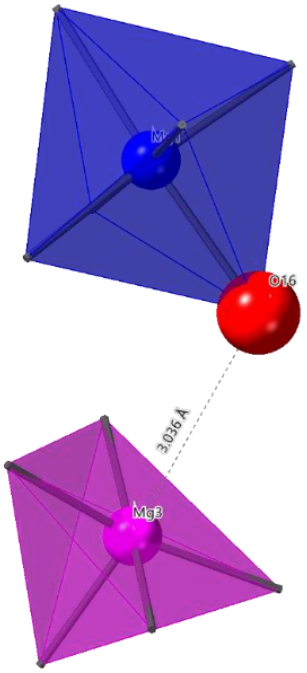

Figure 61. Arrangement of MgO_6 octahedra and MgO_5 pyramid

The overall crystal structure can be considered as layered. It consists of four symmetrical triple-layers of Mg1-Mg2-Mg3 units. Within each triple-layer MgO_5 square pyramids are collinear and point in the same positive direction at 42.4° towards the centre of the layer. The dipole vectors of the MgO_5 bipyramids alternate with 69.1° difference and therefore the

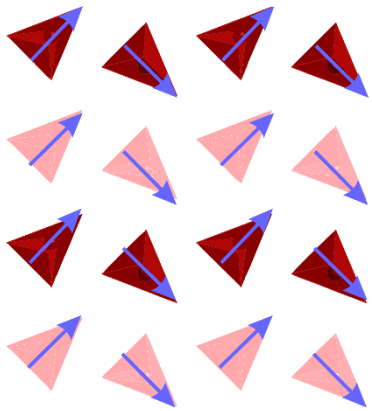

Figure 62. Alternations of bipyramids in half of the lattice. Dark and pale colours represent different levels of the lattice. Arrows show vector of positive polarisation

resulting dipole vector is non-zero (Figure 62). The next triple layer is the exact mirror reflection of the first layer along the plane perpendicular to *c* axis, beginning with the MgO_6 octahedra followed by the MgO_5 bipyramids and finishing with the MgO_5 square pyramids. The total dipole vector of the first two triple-layers associated with MgO_5 units is non-zero and lies parallel to the *b* axis. The next two layers are a centrosymmetric reflection of first two. Thus they have the same total dipole vector but with an opposite direction, resulting in the dipole sum over all four layers being equal to zero. This complex structural arrangement thus explains the rather large unit cell parameters for this compound. The differently oriented dipoles in this structure suggest an interesting 3D-landscape of local polarisations, which may be of interest for future dielectric studies.

The calculated bond valence sum (BVS) for the Mg2 and Mg3 sites are close to ideal at +2.005 and +1.995 respectively, which explains the stability of these five coordinate units. The BVS for the octahedral Mg1 site is, however, lower than

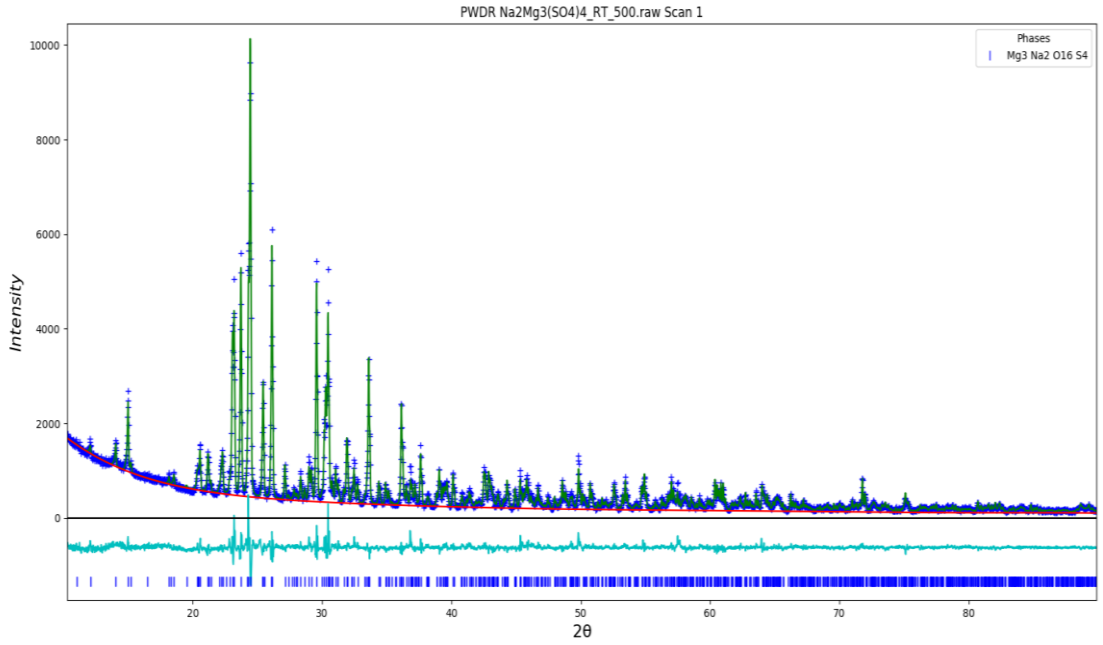

Figure 63. Observed, calculated and difference plots for structural refinement of $Na_2Mg_3(SO_4)_3$ using X-ray powder diffraction data. R_{wp} = 7.637% GOF = 1.80.

expected: +1.869, which may be the result of the polarisation caused by the adjacent MgO_5 pyramid as highlighted above (Figure 61).

Examination of $Na_2Mg_3(SO_4)_4$ through VT-XRD experiments shows that unlike $Na_2Mg_2(SO_4)_3$ or $Na_2Mg(SO_4)_2$, there are no phase transitions with temperature up to 750°C.

In order to confirm that single crystal of $Na_2Mg_3(SO_4)_4$ corresponds to the whole powder, a Rietveld refinement of the model obtained in SX experiment was performed using powder XRD data. The refinement demonstrated a relatively good fit of data for such complex unit cell confirming matching of structures (Figure 63).

$Na_2Mg(SO_4)_2$

Structure refinement using the single crystal data indicated that the $Na_2Mg(SO_4)_2$ phase is triclinic with space group $P\bar{1}$. The unit cell mostly consists of

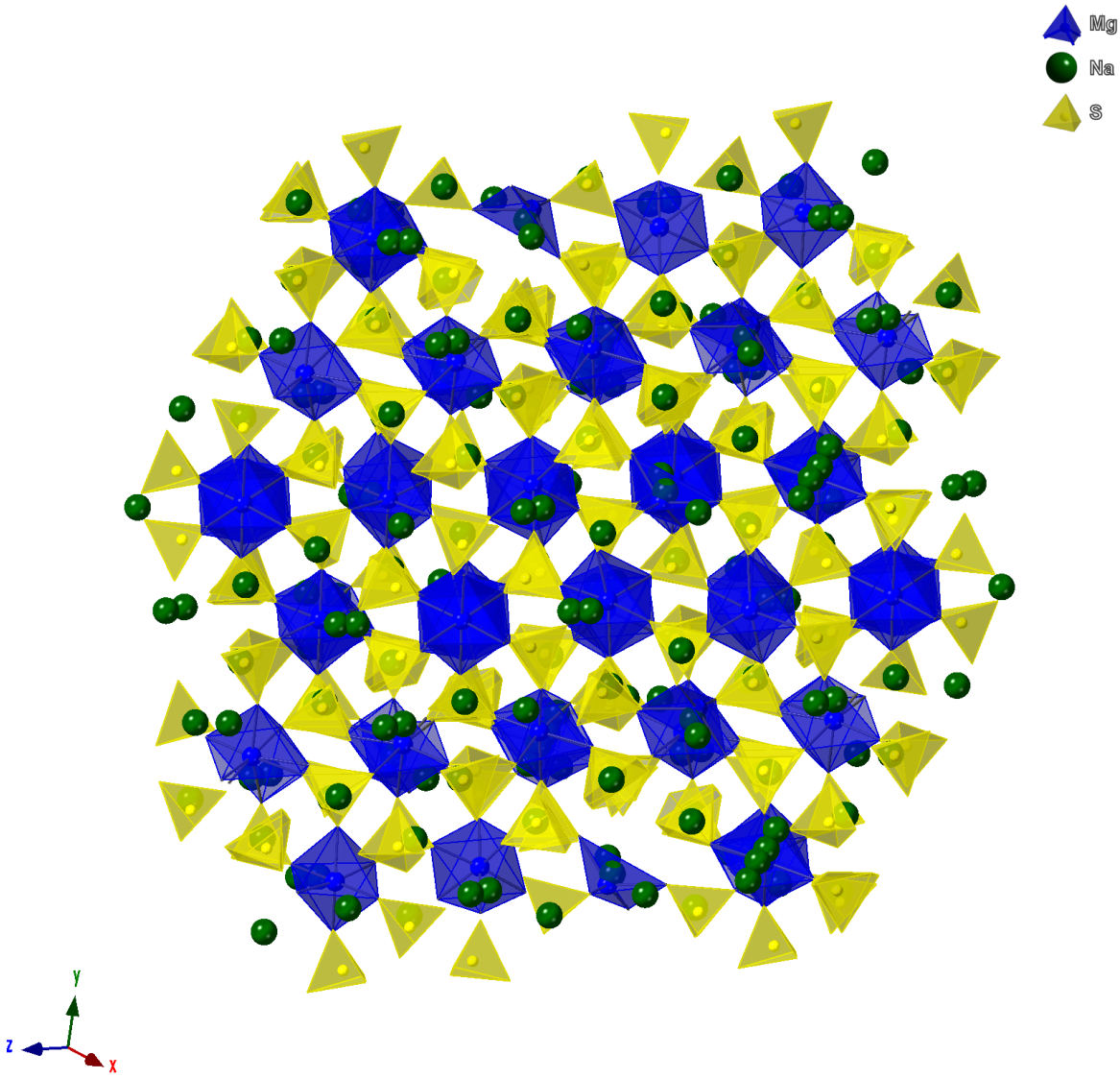

Figure 64. $Na_2Mg(SO_4)_2$ view perpendicular to plane (-4 0 -5)

SO_4 tetrahedra corner linked with MgO_6 octahedra, with the sodium ions distributed in the resultant network. The view along the vector perpendicular to plane (-4 0 -5) implies a hexagonal pattern structure similar to that of the Nasicon structure (Figure 64). However the crystal slice along the (1 -3 0) plane perpendicular to (-4 0 -5) shows a different pattern. While this has some elements similar to the Nasicon structure, such as two octahedral MgO_6 units linked via three tetrahedral SO_4 units (Nasicon lantern unit[145])(Figure 65, red selection), the presence of some Na occupying Mg sites causes deformation and disorder in the cell. In these regions, the structure is more similar to Na rich Vantgoffite ($Na_6Mg(SO_4)_4$) phase, where MgO_6 units are surrounded by Na ions with interstitial SO_4 tetrahedra (Figure 65, black selection). These areas can be classed as large cavities containing sodium ions, and the sulphate groups are rotationally distorted when surrounded by a large amount of Na ions in these regions. The presence of large disorder of the Na in the structure may suggest that this material might show significant ionic mobility. Furthermore, possible spontaneous polarisation within this structure can be generated via disordering and lowering the symmetry to P1 i.e. if Na ions would tend to occupy the same pole of the large cavities.

Indeed, while we have produced a good solution to the structure with space group $P\bar{1}$, the symmetry may possibly be lower ($P1$). Twinning artefacts from the data set may have affected the structure solution, causing the extra visual disorder. Indeed, the presence of large amounts of disorder, as well as mixed Na/Mg occupied sites across the centre of symmetry (pink labelled Mg8), may suggest that the space group is $P1$ rather than of $P\bar{1}$. The main difficulty in providing a conclusive

description either way is the mixed Na/Mg occupied sites. The scattering factors of these elements are essentially identical and so normally the only way to distinguish them is to compare the bond lengths. However, the large degree of complexity within this structure makes such an analysis impractical, and so we have kept the higher symmetry $P\bar{1}$ description. In order, to fully distinguish between these two possibilities, a neutron single crystal diffraction study would be required. However this method requires a much larger crystal which has not been achievable via the current synthesis route.

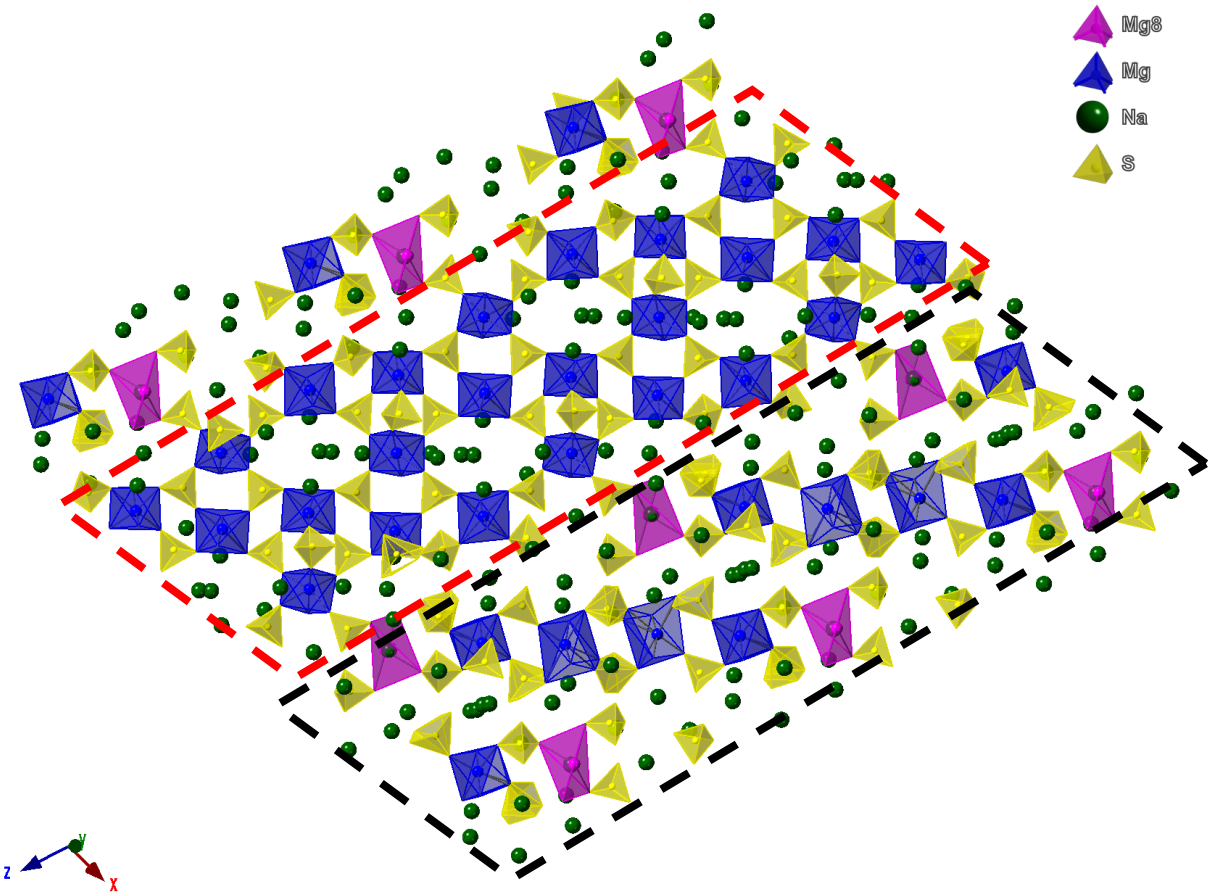

Figure 65. $Na_2Mg(SO_4)_2$ slice along (1 -3 0). Mg8 site labelled pink. The region that is similar to Nasicon is highlighted by the red dash line. The vantgoffite-like region is highlighted by the black dash line.

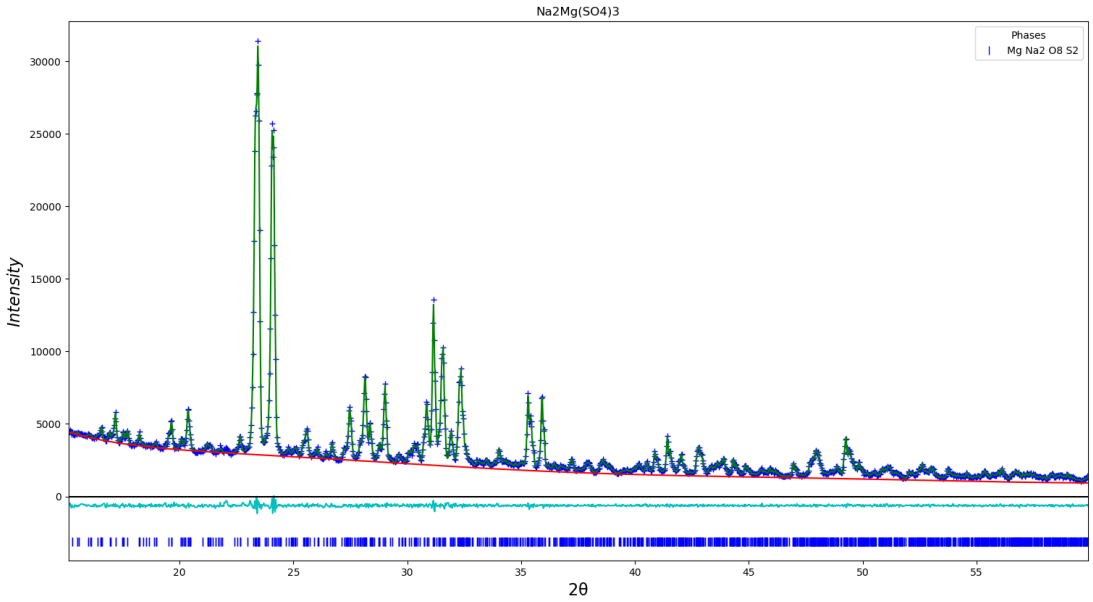

Figure 66. Observed, calculated and difference plots for structural refinement of $Na_2Mg(SO_4)_2$ using X-ray powder diffraction data. R_{wp}= 2.27%, GOF = 1.36

In order to confirm a correspondence of the single crystal structure to a powder, a basic Rietveld refinement was conducted on powder XRD pattern. Due to very high complexity of the cell, only cell parameters, background and profile function were refined (Figure 66). This pattern matches with pattern reported for mineral "EI" by Jacobsson et al.[138].

$Na_2Mg_2(SO_4)_3$ at higher temperatures

At elevated temperatures quenched monoclinic structure $Na_2Mg_2(SO_4)_3$ turns into cubic langbeinite at 250°C, which decomposes at 350°C and then is formed again at 575°C. The crystal cell has the standard regular langbeinite space group $P2_13$. Based on the data collected in the VTXRD experiment, the langbeinite

structural model was refined to obtain cell parameters of the sample at different temperatures. Na-rich langbeinites $K_{2-x}Na_xMg_2(SO_4)_3$ (discussed in the next chapter) were shown to have significant rotational disorder of the SO_4 group, and therefore, to model this system SO_4 tetrahedron was split into three units with the constant centre (atom S) and partial occupancy ⅓. Considering the lack of small d-spacing information in powder XRD due to high thermal motion at high temperatures, SO_4 tetrahedrons were treated as rigid bodies and the S-O distance was constrained to be equal for all tetrahedrons.

The cell has a linear expansion with increasing temperature (Figure 67). Indeed, despite the intermediate decomposition of the structure into mixture of orthorhombic $Na_2Mg_3(SO_4)_4$ and triclinic $Na_2Mg(SO_4)_2$, the cubic langbeinite

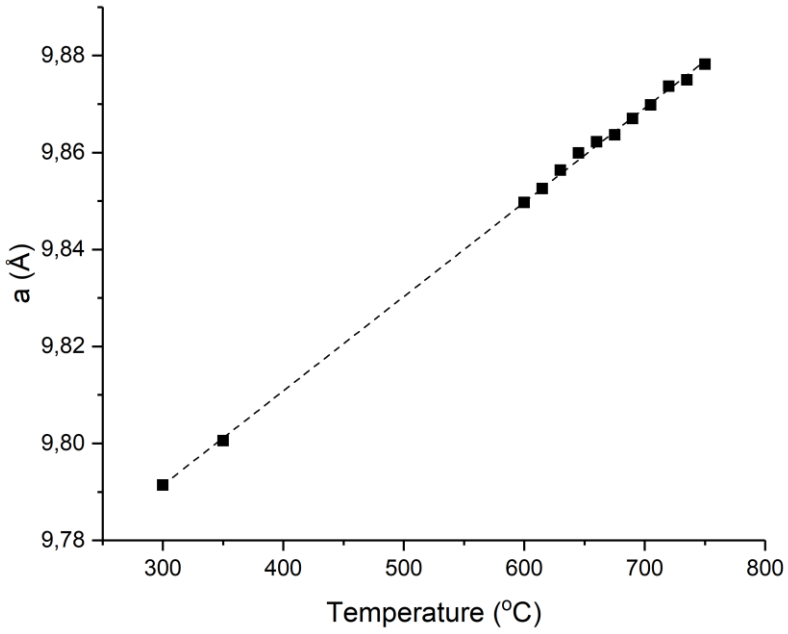

Figure 67. Cell parameter a of cubic langbeinite phase $Na_2Mg_2(SO_4)_3$ at different temperatures

formed at higher temperature has the same expansion properties as at lower temperatures.

The structural refinement was also performed on monoclinic $Na_2Mg_2(SO_4)_3$ phase before the transition into cubic langbeinite. If we assume that monoclinic cell is a rearrangement of the langbeinite supercell, then it can be treated as 1x1x3 supercell. Therefore, if we take ⅓ of the cell volume of the monoclinic cell, compared with the volume of cubic langbeinite cell (Figure 68). The graph shows that cell volume increases significantly with the transition into the langbeinite structure. This latter structure contains large cavities, which may be responsible for such a large expansion.

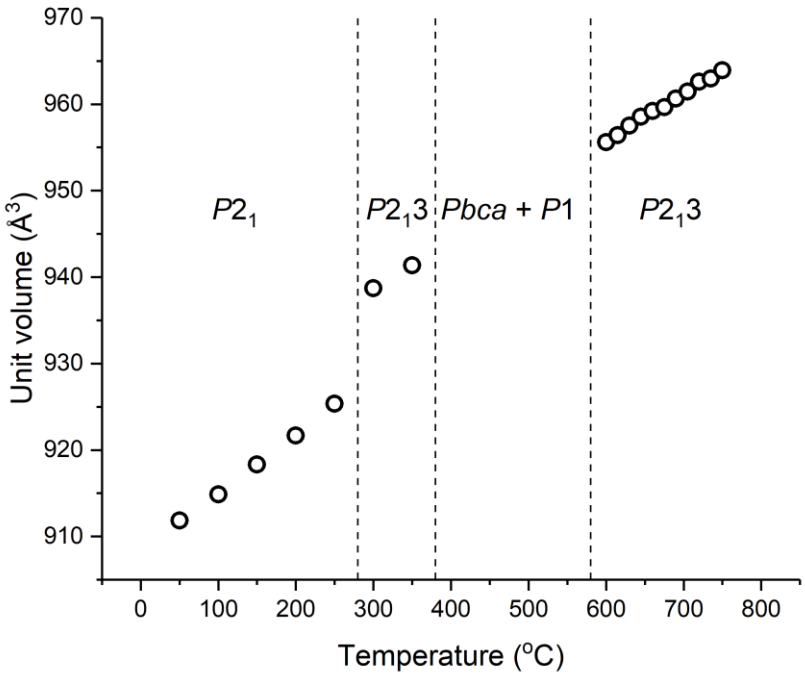

Figure 68. Unit cell volume of $Na_2Mg_2(SO_4)_3$ versus temperature obtained from refinement of powder VT-XRD data. Unit cell volume for the cubic phase is taken as it is, unit cell volume for the monoclinic phase is taken as ⅓of cell volume(due to the expanded unit cell)

Raman Spectroscopy

Further information about the thermal evolution of $Na_2Mg_2(SO_4)_3$ was obtained from Raman scattering measurements. Some surface hydration was observed in the stored samples, as denoted by the presence of a broad band in the 3500 cm^{-1} region as well as some narrow bands around 1000 cm^{-1} with variable intensity which did not belong to the proper $Na_2Mg_2(SO_4)_3$ phase. In order to avoid any humidity effect, the samples were thermally treated at 700°C in the measuring stage under an air flow just before the Raman measurements. Figure 69 shows the Raman spectrum of dried $Na_2Mg_2(SO_4)_3$, and although an exhaustive mode assignment is out of the scope of the present work, the bands in the 1040, 460 and 630 cm^{-1} regions would correspond to the ν_1, ν_2 and ν_4 internal modes of the

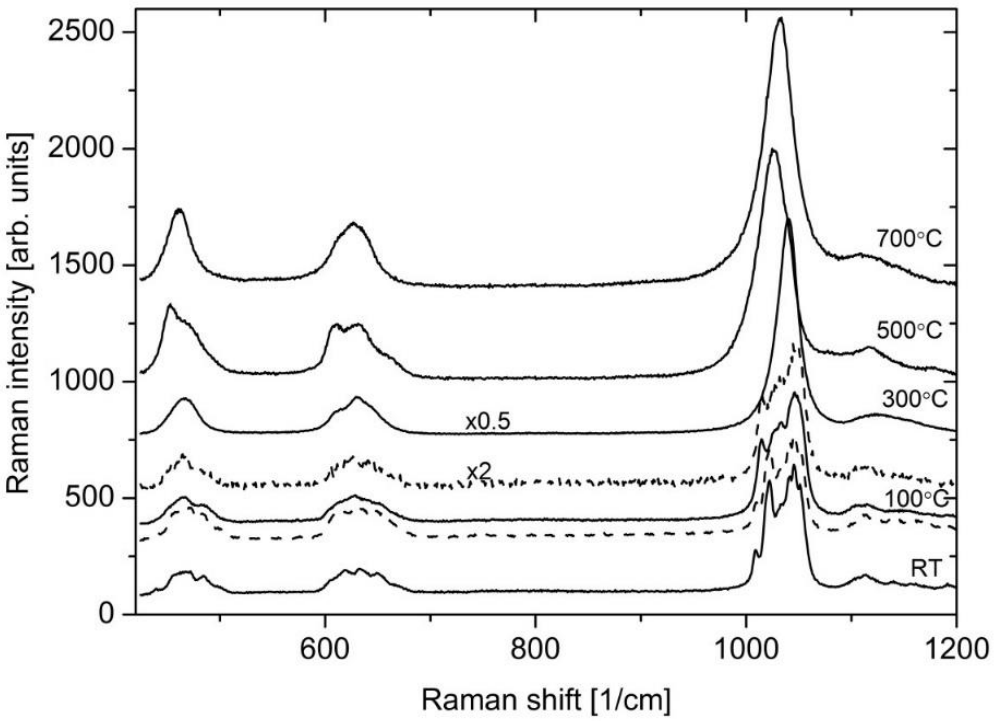

Figure 69. Thermal evolution of the Raman spectra of $Na_2Mg_2(SO_4)_3$. Dotted line, spectra at 100 ˚C and room temperature during the cooling step.

sulphate groups [146]. Bands above 1100 cm^{-1} are attributed to the ν_3 internal modes. More interesting is the evolution of the Raman spectrum with increasing temperature (Figure 69). From this evolution, a first phase transition seems to occur at 100°C, as suggested by the disappearance or coalescence of some bands in all groups of internal modes. This spectrum at 100˚C is remarkably similar to that of lightly (5%) K doped $Na_2Mg_2(SO_4)_3$, which we have shown to adopt a orthorhombic cell related to a heavily distorted langbeinite structure (see next chapter on mixed K/Na systems, shown in Figure 70 for reference purposes), which leads us to propose that $Na_2Mg_2(SO_4)_3$ is transforming from monoclinic to orthorhombic symmetry.

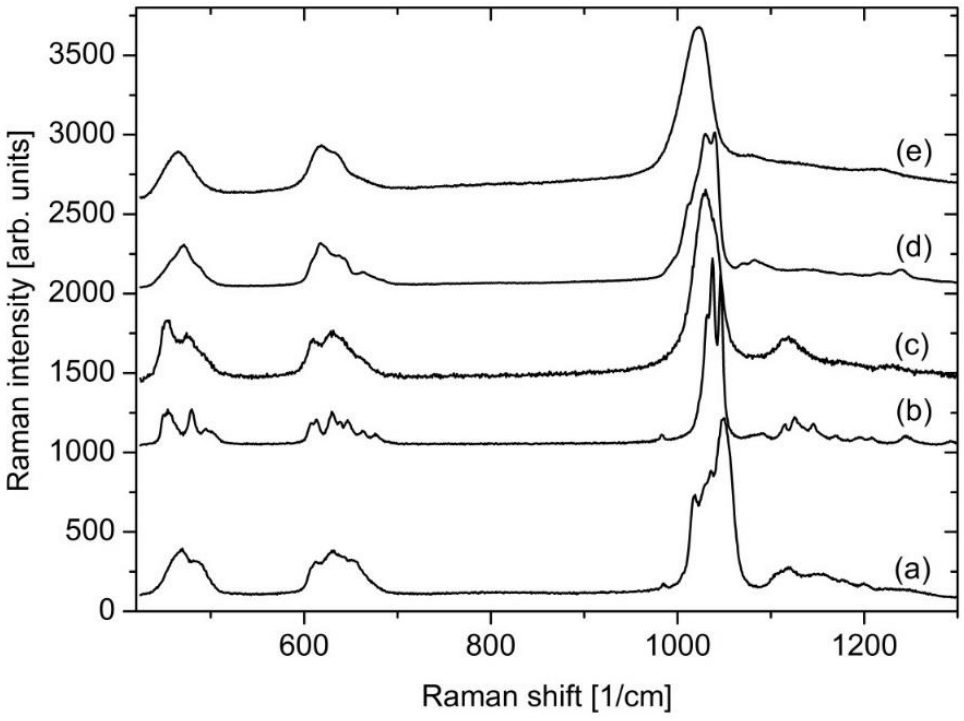

Figure 70. Reference Raman spectra of a) $K_{0.1}Na_{1.9}Mg_2(SO_4)_3$, b) $Na_2Mg_3(SO_4)_4$ at room temperature, c) $Na_2Mg_3(SO_4)_4$ at 500oC, d) $Na_2Mg(SO_4)_2$ at room temperature, c) $Na_2Mg(SO_4)_2$ at 500°C

The phase change is subtle, which may explain why the transition is not clearly observed in the variable temperature XRD study (Figure 54). At 290°C the spectrum transforms to that of the langbeinite phase, being identical to that of the high temperature phase, allowing for thermal broadening effects. In agreement with the variable temperature XRD data, as temperature increases, the sample decomposes into a mixture of $Na_2Mg_3(SO_4)_4$ and $Na_2Mg(SO_4)_2$ and the spectrum overlaps those of both phases. Figure 70 also includes the room temperature and 500°C spectra of both phases for reference purposes. It is interesting that the decomposition temperature (480°C) of $Na_2Mg_2(SO_4)_3$ to give $Na_2Mg_3(SO_4)_4$ and $Na_2Mg(SO_4)_2$ is significantly higher in the Raman measurements than in VTXRD (350°C). The difference is ascribed to the higher heating rates used in the Raman experiments, which help to retain the langbeinite phase to higher temperatures than in the XRD experiment. Finally, at 600°C the $Na_2Mg_3(SO_4)_4$ and $Na_2Mg(SO_4)_2$ phases recombine and the spectrum becomes that of the langbeinite $Na_2Mg_2(SO_4)_3$ phase, which is maintained on fast cooling (20°C/min) down to 250°C where it transforms to the orthorhombic phase, recovering the original monoclinic spectrum at room temperature. Once again, the relatively high cooling rates used in the Raman stage help to maintain the langbeinite phase, in this case completely avoiding the decomposition observed on cooling in the variable temperature XRD studies.

Conductivity study

Following the structure determination, the conductivities of these phases were assessed. The conductivity of $Na_2Mg_3(SO_4)_4$ was shown to be very low (Figure 71). Even at 300°C the conductivity is below 10^{-8}S/cm with a high activation energy of 1.3eV. This correlates with the structure determination which showed a lack of Na ion conduction channels. Conductivities on heating and cooling vary somewhat what may be related to the presence of a small amount of residual moisture in the sample.

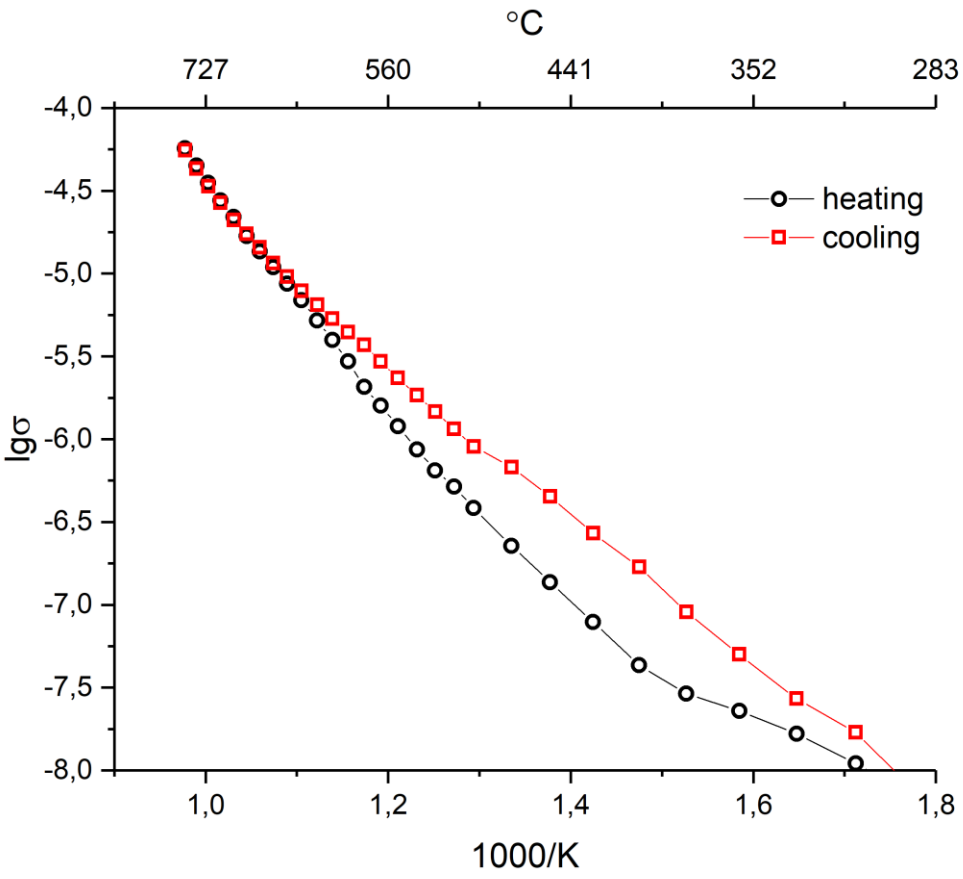

Figure 71. Arrhenius plot and dielectric permittivity of $Na_2Mg_3(SO_4)_4$ system via EIS

In contrast to $Na_2Mg_3(SO_4)_4$, the $Na_2Mg_2(SO_4)_3$ system shows some interesting features as revealed via conductivity measurements of the quenched phase. (Figure 72) The conductivity of this phase changes several times as phase transitions happen. Interestingly some temperatures of these phase transitions differ from those observed on VTXRD. Transformation of the monoclinic phase $P2_1$ (or orthorhombic, suggesting from Raman study) in to cubic langbeinite $P2_13$ around 250°C corresponds to the bend of the Arrhenius curve and an increase of the activation energy in the same region. Decomposition of the langbeinite phase into a $Na_2Mg_3(SO_4)_4$ and $Na_2Mg(SO_4)_2$ composite in VTEIS experiment happens only at 520°C and is accompanied with rise of conductivity. This stabilisation is apparently

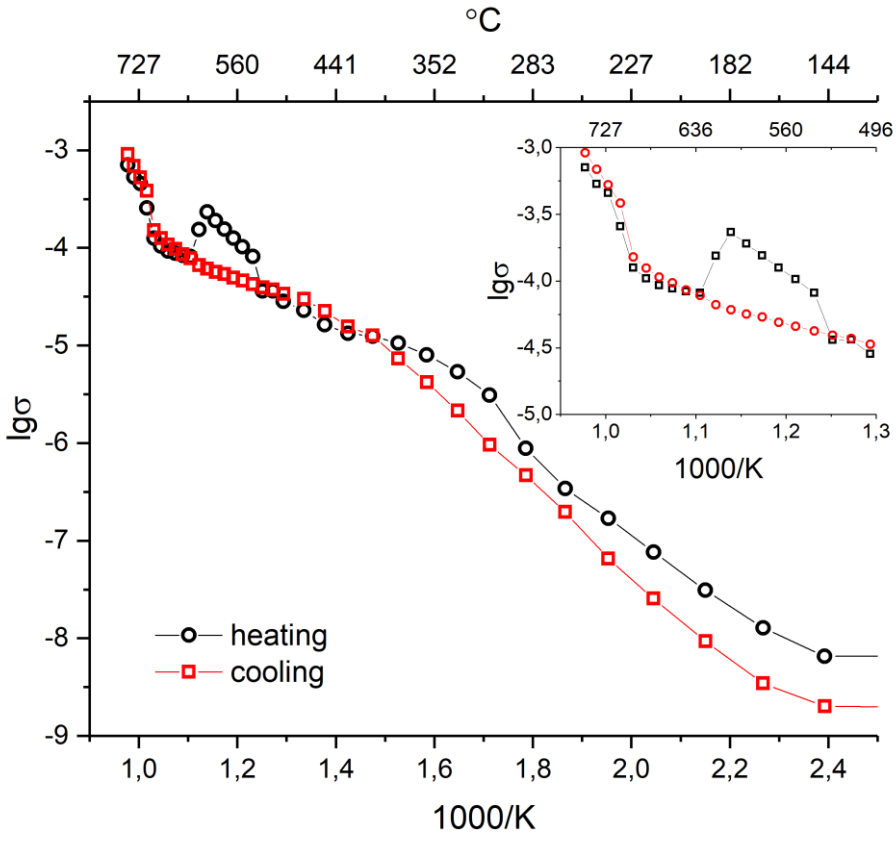

Figure 72. Arrhenius plot and dielectric permittivity of $Na_2Mg_2(SO_4)_3$ system via EIS

related to the rate of temperature change. After the phase transition at 620°C into the langbeinite structure, the conductivity drops, which is most likely due to the fact that in langbeinite, the two cavity sites are full. The final phase transition causing increase in conductivity may be related to similar feature seen in the related phase $Na_{1.9}K_{0.1}Mg_2(SO_4)_3$ (discussed in the next chapter), where the significant change in ordering of the SO_4 tetrahedra happens. In $Na_{1.9}K_{0.1}Mg_2(SO_4)_3$, the tetrahedra are disordered only rotationally before the phase transition while after the phase transition the disorder affects the tetrahedron position as well. It is postulated that this opens a small windows between langbeinite cavities allowing enhanced ionic transport in the crystal. However, it should be noted that for $Na_2Mg_2(SO_4)_3$ the structural refinement of the VTXRD data did not show strong evidence of such transition happening for $Na_2Mg_2(SO_4)_3$. Therefore the further investigation of this high temperature phase is required.

On the cooling the conductivity predictably changes with the apparent change of SO_4 tetrahedrons ordering. The other phase transition, as expected happens near 450°C, as the langbeinite structure decomposes into $Na_2Mg(SO)_2$ and $Na_2Mg_3(SO_4)_4$ composite. For comparison the linear extrapolation of the conductivity section responsible for the composite conduction on cooling (500°C-RT, red line Figure 72) fits with analogous section on heating (520-620°C black line Figure 72).

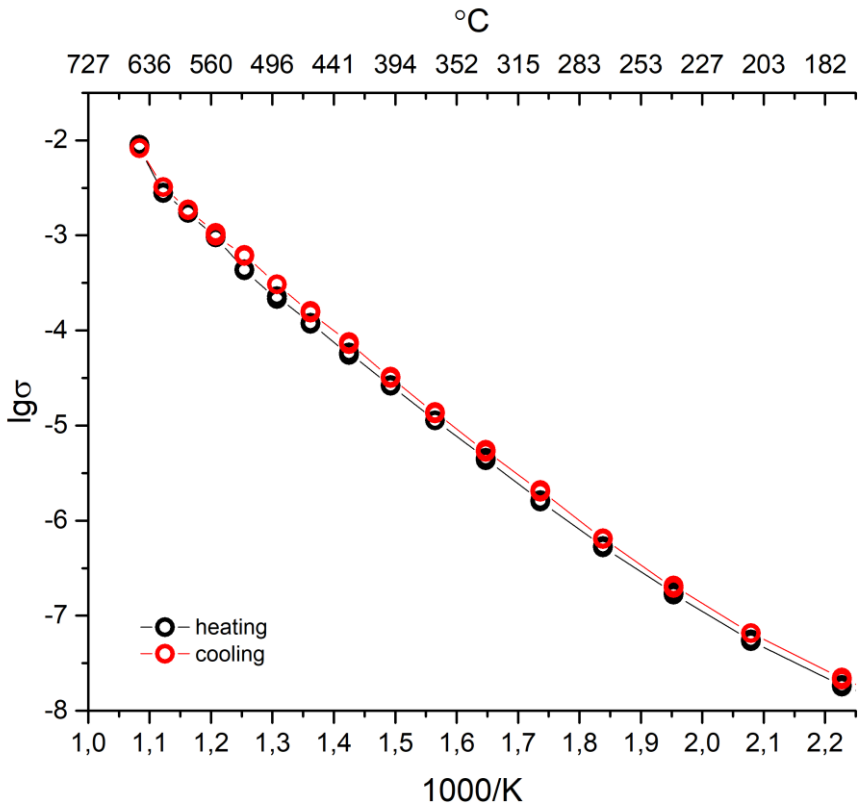

Figure 73. Arrhenius plot and dielectric permittivity of $Na_2Mg(SO_4)_2$ system via EIS

The $Na_2Mg(SO_4)_2$ showed higher Na-ion conductivity (Figure 73) than the rest of studied compounds, which can be related to the disorder within the cell. At high temperature there is the beginning of upward curvature related to the observed decomposition of the compound. The activation energy of ionic conductivity in this compound is 0.98eV.

The conductivity values at 400°C and activation energy of all samples in different phases are summarised in table 23.

Table 23. Summary of conductivities of compounds at 400°C and activation energy of different phases.

Compound	Composition	Stage	$\sigma_{400°C}$, S/cm	E_a, eV
$Na_2Mg_2(SO_4)_3$	$P2_1$	Heating	-	0,71(1)
	$P2_13$	Heating	1.24×10^{-5}	0,40(1)
	$Pbca$+ $P\bar{1}$	Heating	-	0,98(1)
	$P2_13$	Heating	-	0,34(1)
	$P2_13_{distorted}$	Heating	-	1,49(2)
	$P2_13_{distorted}$	Cooling	-	0,94(2)
	$P2_13$	Cooling	-	0,41(1)
	$Pbca$+ $P\bar{1}$	Cooling	1.26×10^{-5}	1,91(2)
$Na_2Mg_3(SO_4)_4$	$Pbca$	Heating	4.32×10^{-8}	1,32(1)
	$Pbca$	Cooling	1.69×10^{-7}	0,91(1)
$Na_2Mg(SO_4)_2$	$P\bar{1}$	Heating	3.15×10^{-5}	0,98(1)
	$P\bar{1}$	Cooling	2.62×10^{-5}	0,98(1)

Conclusion

This detailed X-ray diffraction and Raman spectroscopy study of the $Na_2Mg_2(SO_4)_3$ system highlights enormous complexities within this system. We show that single phase $Na_2Mg_2(SO_4)_3$ can only be prepared by quenching/rapid cooling from high temperature, as otherwise phase decomposition to give $Na_2Mg(SO_4)_2$ and $Na_2Mg_3(SO_4)_4$ results. These complexities are highlighted by the changes observed on heating quenched $Na_2Mg_2(SO_4)_3$ to elevated temperatures, with the XRD data showing the following phase transformations

Monoclinic $P2_1$, $Na_2Mg_2(SO_4)_3 \xrightarrow{250°C}$ Langbeinite $P2_13$, $Na_2Mg_2(SO_4)_3 \xrightarrow{350°C}$ Mixture $Na_2Mg(SO_4)_2$ and $Na_2Mg_3(SO_4)_4 \xrightarrow{575°C}$ Langbeinite $P2_13$, $Na_2Mg_2(SO_4)_3$

Moreover, Raman data suggest an additional transformation at ≈100°C to a distorted langbeinite-type phase. Another additional phase transition near 700°C,

probably related to the SO_4 units disorder increasing, is suggested by the conductivity study. Overall the chapter highlights the interesting observation of the langbeinite structure for $Na_2Mg_2(SO_4)_3$ at elevated temperature, which is unusual given that this structure is only usually formed for larger alkali metal ions, and it is likely that the local strain due to the smaller Na in the langbeinite framework is responsible for the complex changes in structure/composition that are observed on heating/cooling. Overall the interesting and complex structural features for these sodium magnesium sulphate systems highlight the need for detailed structural study of other Na mixed metal sulphate systems.

Chapter Six

Synthesis and structures of sodium doped $K_2Mg_2(SO_4)_3$ langbeinite phases

Materials with the langbeinite ($K_2Mg_2(SO_4)_3$) structure have attracted attention in a wide variety of areas. In geology, interest in them has principally derived from their study to help to understand sulphate planetochemistry and the formation of marine salt deposits on Earth[147]. In addition, there have been attempts to use $K_2Mg_2(SO_4)_3$ mineral for absolute dating via the $^{40}Ar/^{40}K$ method[148]. Other studies have involved investigations into thermoluminescence properties occurring in doped langbeinites[149,150]. While at room temperature, langbeinite systems show cubic symmetry, there have been reports of lowering of the symmetry to tetragonal and orthorhombic for some langbeinite-type phases at low temperature, leading to a polar crystal which shows ferroelectric properties[151–154]. More recently, there has

been interest in the potential use of these systems as Na ion conducting electrolytes, albeit with low conductivity observed[155]. Further interest has been generated in their potential use as electrodes for Na ion batteries. In this respect, Tarascon *et al*. have shown that $K_2Fe_2(SO_4)_3$ can be used in a Na-ion battery via electrochemical exchange of K by Na in a Na ion conducting electrolyte, albeit the capacity was low due to the low level of exchange[156].

The original structure of langbeinite ($K_2Mg_2(SO_4)_3$) itself was studied by Zemann and Zemann in 1957[140]. It consists of a framework of corner-sharing MgO_6 octahedra and SO_4 tetrahedra, which creates large cavities in which the potassium atoms sit. The coordination of the two potassium sites differs; the K1 site is 9-coordinate while the K2 site is 12 coordinate. A close inspection of the structure shows that the larger K1 site cavity could potentially be considered as 15-coordinated if evaluated from the centre of the cavity. However, due to the fact that the K in this site is slightly shifted off-centre, the effective coordination is 9-coordinate. These K ion cavities form a 1-3-3-1 pattern with respect to the metal octahedra that form the general cage containing them (Figure 74); two types of metal octahedra alternate (Mg1-Mg2-Mg1-Mg2) to form the cage through corner sharing with the SO_4 tetrahedra.

Structurally the general framework of corner linked octahedra and tetrahedra shows some similarity with that of the Nasicon structure, widely studied as excellent Li/Na ion conductors[42–44]. However, while the Nasicon structure has four cavity sites within the framework, a key aspect of the langbeinite structure is the presence of only two cavity sites within the structure. The large size of these

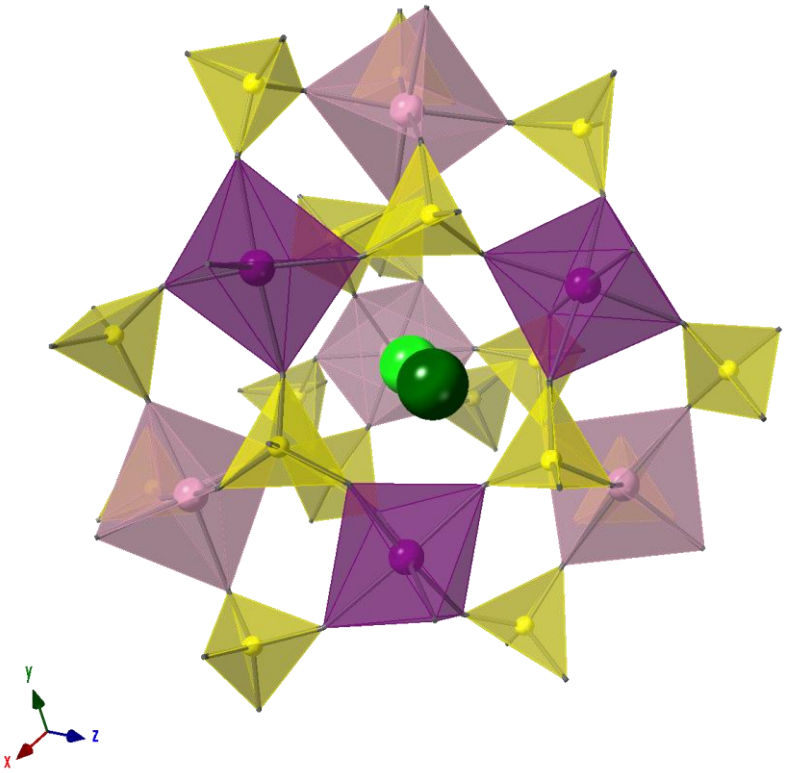

Figure 74. Langbeinite cage containing two alkali metals (green), view along the [1 1 1] axis

cavity sites means that the langbeinite structure favours larger alkali ions like potassium, caesium, and rubidium, while the nasicon structure prefers smaller alkali ions such as Na, Li. Despite this, there have been some reports of Na incorporation in langbeinite-type phase, provided that some larger cations are present to stabilise the framework, e.g. $NaBaM_2(PO_4)_3$ (M=transition metal) systems [142,143]. This would therefore suggest that it should be possible to prepare mixed K/Na langbeinite-type phase. Therefore in this work we have examined the solid solution range for $K_{2-x}Na_xMg_2(SO_4)_3$ to examine the range of Na content for which the langbeinite structure is retained. The results demonstrate a wide solid solution range and a

complex structural chemistry particularly for high Na contents. In this respect, our prior work on the $Na_2Mg_2(SO_4)_3$ endmember showed that while at room temperature, the material was shown to possess a complex monoclinic structure, there was a transition to cubic langbeinite at elevated temperatures for this phase [157]. This transition was attributed to the fact that, despite the apparent complex structure of room temperature $Na_2Mg_2(SO_4)_3$, only a small amount of rotation of the SO_4 units was required to convert it to the cubic langbeinite structure.

Experimental

A range of $K_{2-x}Na_xMg_2(SO_4)_3$ ($0 \leq x \leq 1.9$) powder samples were synthesised. These were prepared via a dissolution-evaporation route used previously for the synthesis of mixed metal sulphate systems [98,137,158]. In this method, stoichiometric amounts of Na_2SO_4, K_2SO_4 and $MgSO_4{\cdot}7H_2O$ (for 3g of sample) were dissolved in water. The solutions were then heated to evaporate the water; the resulting solid was then ground and heated at 750°C for 12 hours in air. Two cooling regimes were examined: slow cooling (1°C/min) and quenching by removal of the sample from the furnace at 750°C to room temperature.

Single crystal samples for selected compositions across the series were grown via spontaneous crystallisation from the melt at 900°C on the gold foil with a cooling rate of 0.2°C/min in air.

Powder XRD data were collected on a Panalytical Empyrean diffractometer with copper X-ray source, in reflection geometry, equipped with a Pixcel 2D

detector. Variable temperature powder XRD data, up to 750^{o}C, were collected on a Bruker D8 advanced diffractometer with copper X-ray source and LynxEye detector in an Anton Paar HTK1200N furnace. Rietveld refinement using powder XRD data was performed using GSASII software[103].

For the single crystal studies, a suitable crystal was selected, mounted on glass fibre, and diffraction data were collected on an Agilent SuperNova diffractometer using an Atlas detector. The crystals were kept at 100K during data collection using an Oxford Cryosystems Cryostream. Using Olex2 [123], the structure was solved with the ShelXT[124] structure solution program using Intrinsic Phasing, and refined with the ShelXL [125] refinement package using a Least Squares approach.

Samples were also analysed by TGA-MS (Netzsch), heating at a rate of 5°C/min to 750°C in the N_2 atmosphere.

Powder samples were studied by Raman spectroscopy using the 488 nm excitation line of an Ar^+ ion laser in a DILOR XY spectrometer with a CCD detector and approximately 2 cm^{-1} of spectral resolution. The laser output power was kept between 20 and 50 mW. The excitation and light collection were made through a 50X microscope objective lens. High temperature Raman measurements were carried out in a LINKAM TS1500V stage up to 775 °C. For measurements below RT, a SMC-TBT cryostat and liquid nitrogen were used.

For the conductivity experiment 0.1g of prepared samples were pressed into 10mm pellets. These pellets were sintered the same way as the initial powders to keep the crystal structures the same. The conductivities of the obtained pellets were measured in air by electrochemical impedance spectroscopy using a HP 4204

gain-phase impedance analyser within a frequency range 5 – 1.3×10^7Hz. Pellets were coated on both sides with platinum ink and heated at 700°C for 2 hours. Zview software was used to analyse the obtained data[105]. The activation energy was calculated using the Arrhenius equation: $\sigma = Ae^{-\frac{E_a}{RT}}$, where σ is the conductivity, A is the pre-exponential coefficient, E_a is the activation energy, R is the gas constant and T is the temperature.

Results and discussion

Solid solution range for $K_{2-x}Na_xMg_2(SO_4)_3$

The investigation of the effect of substitution of sodium for potassium in $K_2Mg_2(SO_4)_3$ langbeinite revealed the presence of two systems in the studied range. It was shown that the cubic langbeinite structure could accommodate a large amount of Na in place of K. Thus $K_{2-x}Na_xMg_2(SO_4)_3$ exhibits the cubic langbeinite structure for $0 \leq x \leq 1.75$ at room temperature (Figure 75). For higher Na levels, $1.8 \leq x \leq 1.9$, a new non-cubic phase, with very complex pattern, was observed. Through single crystal studies (see later), this phase was identified to be orthorhombic with a very large unit cell. The main information about collected data in single crystal experiments including cell parameters and refinement indexes is presented in table 24 (see two-page opening).

Table 24. Single crystal study data

Empirical formula	**$K_2Mg_2O_{12}S_3$**	**$K_{1.64}Na_{0.36}Mg_2O_{12}S_3$**	**$K_{1.33}Na_{0.67}Mg_2O_{12}S_3$**	**$K_{0.7}Na_{1.3}Mg_2O_{12}S_3$**
Formula weight	415	409.34	404.13	394.1
Crystal system	cubic	cubic	cubic	cubic
Space group	$P2_13$	$P2_13$	$P2_13$	$P2_13$
a/Å	9.89490(10)	9.86050(10)	9.82940(10)	9.75410(10)
b/Å				
c/Å				
Volume/Å³	968.80(3)	958.73(3)	949.69(3)	928.03(3)
Z	4	4	4	4
ρ_{calc}g/cm³	2.845	2.836	2.826	2.821
μ/mm⁻¹	16.754	15.84	14.743	12.871
F(000)	824	813	802	782
Crystal size/mm³	0.074 × 0.044 × 0.038	0.131 × 0.105 × 0.088	0.124 × 0.096 × 0.078	0.112 × 0.079 × 0.053
2Θ range for data collection/°	12.652 to 136.378	12.696 to 149.116	12.736 to 147.712	12.836 to 148.102
Reflections collected	5285	9769	18015	8983
Independent reflections	601 [R_{int} = 0.0585, R_{sigma}=0.0239]	661 [R_{int} = 0.0310, R_{sigma} = 0.0099]	660 [R_{int} = 0.0597, R_{sigma} = 0.0126]	636 [R_{int} = 0.0436, R_{sigma} = 0.0147]
Data/ restraints/ parameters	601/0/59	661/157/100	660/178/101	636/115/103
Goodness-of-fit on F^2	1.116	1.132	1.14	1.114
Final R indexes [I>=2σ (I)]	R_1 = 0.0183, wR_2 = 0.0484	R_1 = 0.0129, wR_2 = 0.0359	R_1 = 0.0146, wR_2 = 0.0395	R_1 = 0.0199, wR_2 = 0.0487
Final R indexes [all data]	R_1 =0.0185, wR_2=0.048	R_1 = 0.0129, wR_2 = 0.0359	R_1 = 0.0146, wR_2 = 0.0395	R_1 = 0.0203, wR_2 = 0.0490

$K_{0.53}Na_{1.47}Mg_2O_{12}S_3$	$K_{0.44}Na_{1.56}Mg_2O_{12}S_3$	$K_{0.23}Na_{1.77}Mg_2O_{12}S_3$	$K_{0.1}Na_{1.9}Mg_2O_{12}S_3$
391.38	389.87	386.41	384.47
cubic	cubic	cubic	orthorhombic
$P2_13$	$P2_13$	$P2_13$	$P2_12_12_1$
9.74080(10)	9.72610(10)	9.71040(10)	9.56550(10) 28.3065(3) 30.0116(3)
924.24(3)	920.06(3)	915.61(3)	8126.12(15)
4	4	4	36
2.813	2.815	2.803	2.828
12.308	12.039	11.322	11.041
777	774	767	6870
0.153 × 0.111 × 0.066	0.185 × 0.144 × 0.117	0.149 × 0.068 × 0.058	0.108 × 0.08 × 0.061
12.852 to 147.302	12.872 to 147.896	12.894 to 135.594	6.906 to 147.866
5222	9459	5044	77038
629 [R_{int} = 0.0751, R_{sigma} = 0.0285]	633 [R_{int} = 0.0305, R_{sigma} = 0.0096]	563 [R_{int} = 0.0479, R_{sigma} = 0.0196]	16241 [R_{int} = 0.0293, Rsigma = 0.0193]
629/187/98	633/5/103	563/76/98	16241/0/1589
1.097	1.139	1.093	1.064
R_1 = 0.0282, wR_2 = 0.0743	R_1 = 0.0192, wR_2 = 0.0495	R_1 = 0.0259, wR_2 = 0.0684	R_1 = 0.0266, wR_2 = 0.0694
R_1 = 0.0285, wR_2 = 0.0747	R_1 = 0.0193, wR_2 = 0.0496	R_1 = 0.0265, wR_2 = 0.0696	R_1 = 0.0288, wR_2 = 0.0710

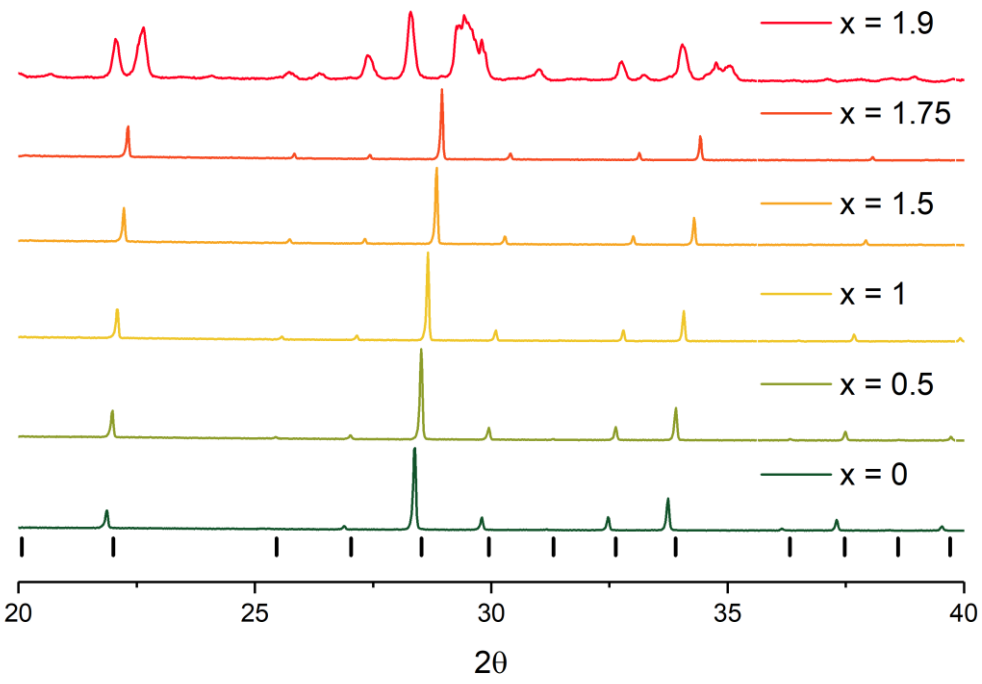

Figure 75. Powder XRD patterns for $K_{2-x}Na_xMg_2(SO_4)_3$ for $0 \leq x \leq 1.9$ at room temperature showing formation of a cubic langbeinite phase for $0 \leq x \leq 1.75$, with a more complex pattern for x=1.9. Tickmarks indicate peaks related to cubic phase

Structural features for $K_{2-x}Na_xMg_2(SO_4)_3$ ($0 \leq x \leq 1.75$)

As noted earlier, $K_{2-x}Na_xMg_2(SO_4)_3$ exhibits a cubic langbeinite structure at room temperature for $0 \leq x \leq 1.75$. The cell parameters obey Vegard's Law, showing a linear decrease with increasing Na content (Figure 76), confirming solid solution formation across the series.

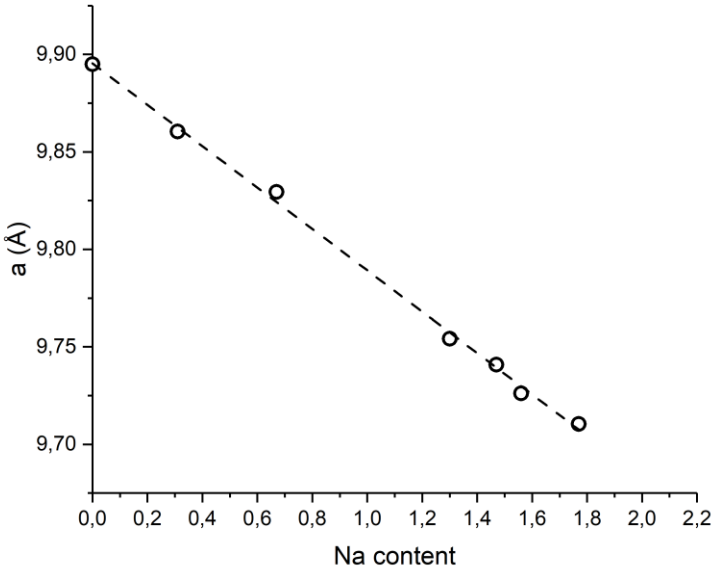

Figure 76. Cell parameters of $K_{2-x}Na_xMg_2(SO_4)_3$ where x is 0-1.75 at 100K

Detailed structural characterisations for selected samples across the series were performed on single crystals. These data showed that the S-O bond lengths remain essentially unchanged across the series with increasing of Na content. This confirms that the SO_4 unit is rigid and does not tolerate any distortions leading to loss of tetrahedral symmetry. However, there was evidence for significant rotational disorder of the SO_4 tetrahedra, which was fitted by three split sites with the same atomic displacement parameters (Figure 77). Speer et al. reported a similar

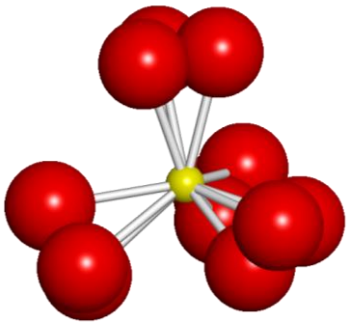

Figure 77. Rotational disorder of the SO_4 tetrahedra modelled through the use of split sites with partial occupancy

behaviour in a range of potassium containing langbeinites, where such disorder increased with increasing ionic radii of divalent cation (Zn-Co-Mn-Cd) [159]. In that previous study, the disorder was successfully modelled with prolate disk shaped thermal ellipsoids. In our case modelling with the same strategy did not demonstrate a good fitting result and therefore the split sites approach was used. Interestingly for the $K_{2-x}Na_xMg_2(SO_4)_3$ samples studied here, this disorder does not appear in the x=0 parent phase but rather becomes more significant with increasing sodium content. To provide a numerical measure of the rotational disorder in this system we have calculated a "disorder factor", which we define as the average separation between the oxygen split sites. Larger values suggest the presence of more significant rotational disorder. From this calculated "disorder factor", it is clear that increasing the Na content leads to increasing disorder (Figure 78), with a strong linear dependence for this parameter versus Na content.

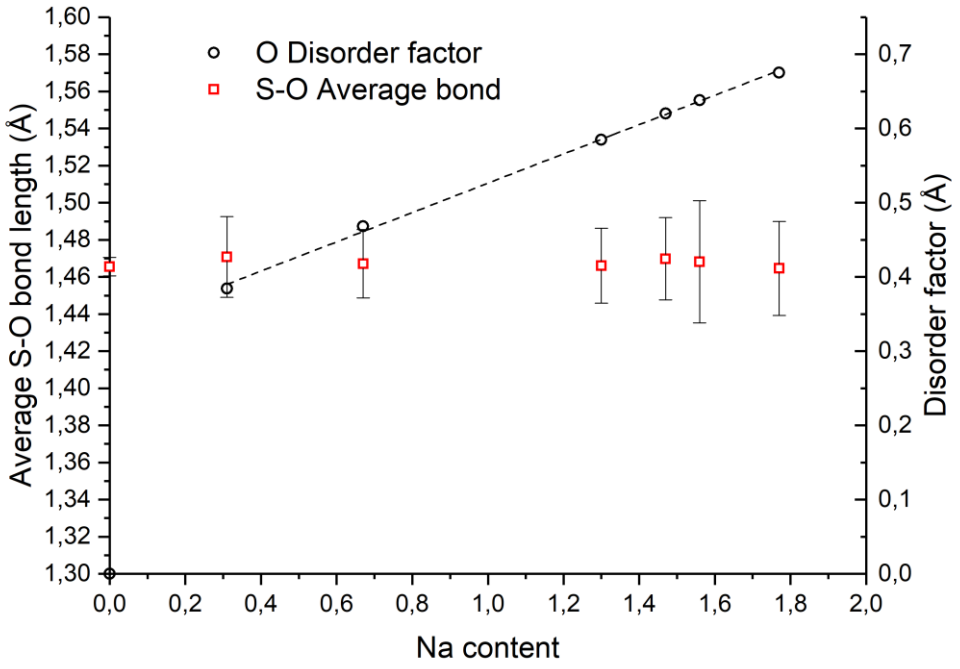

Figure 78. Variation of the disorder factor and average bond length of SO_4 tetrahedron with $K_{2-x}Na_xMg_2(SO_4)_3$ composition

From the single crystal experiments, we were also able to obtain information about the separate sodium and potassium positions, with a significant difference in the positions of sodium and potassium atoms on the same site. Potassium/sodium-oxygen environments were fitted to the ellipsoids to define the actual centre and shape of the cavities using ellipsoidal analysis of coordination polyhedral (PIEFACE software)[160]. This analysis showed that potassium (K1) is shifted off-centre of the larger cavity (axially stretched) towards the centre of the general cage and remains relatively close to the centre in the smaller one (K2) (axially compressed) (Figure 79). The size of this displacement increases as the potassium content decreases, which may explain the interesting rotational disorder

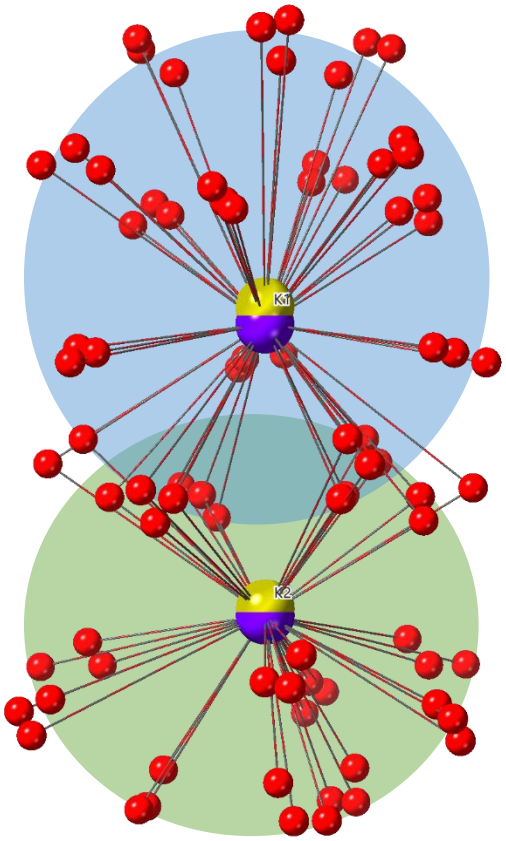

Figure 79. Langbeinite cage of $K_{0.4}Na_{1.6}Mg_2(SO_4)_3$ consisting of two cavities with off-centre displaced potassium. Blue (axially stretched) and green (axially compressed) areas are schematic representation of the ellipsoids fitted to cavities.

of the SO_4 tetrahedrons. It suggests that the cavities containing potassium have to distort to form a more spherical environment for K with similar K-O distances. For the sodium ions, the off-centre displacement is shown to be larger (Figure 80), and increases with increasing potassium content as the unit cell expands. This increasing displacement is not surprising, as conventionally the langbeinite cavities are favoured by larger alkali metal ions. From analysis of the displacement, it can be seen that sodium tends to shift towards the wall of each cage, to allow it to be closer

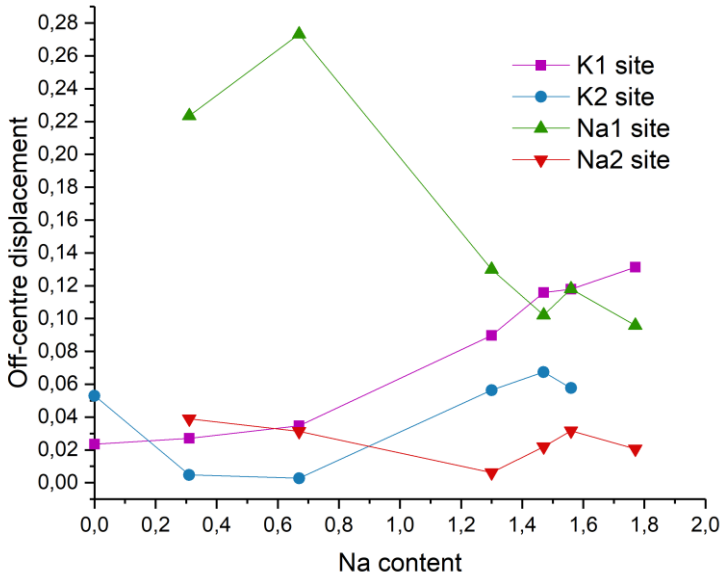

Figure 80. Potassium and sodium off-centre displacement within cavities of the cage for $K_{2-x}Na_xMg_2(SO_4)_3$

to those oxygen atoms and therefore achieve a more satisfactory bonding environment. These increasing off-centre displacements most likely account for the instability of sodium rich phases with respect to adopting the cubic langbeinite structure at room temperature. In particular, it is likely that local stresses result from the different cavity sizes/displacements for K/Na, and so the system reaches a point when it cannot tolerate any more stresses and so the cubic structure collapses to form the orthorhombic structure (described in the next section).

As highlighted in the introduction, there are two K sites in the langbeinite structure, and the data indicate that sodium shows some evidence of ordering between two sites within the cell favouring the smaller Na2 site (Figure 81), while correspondingly K shows a general preference for the larger K1 site.

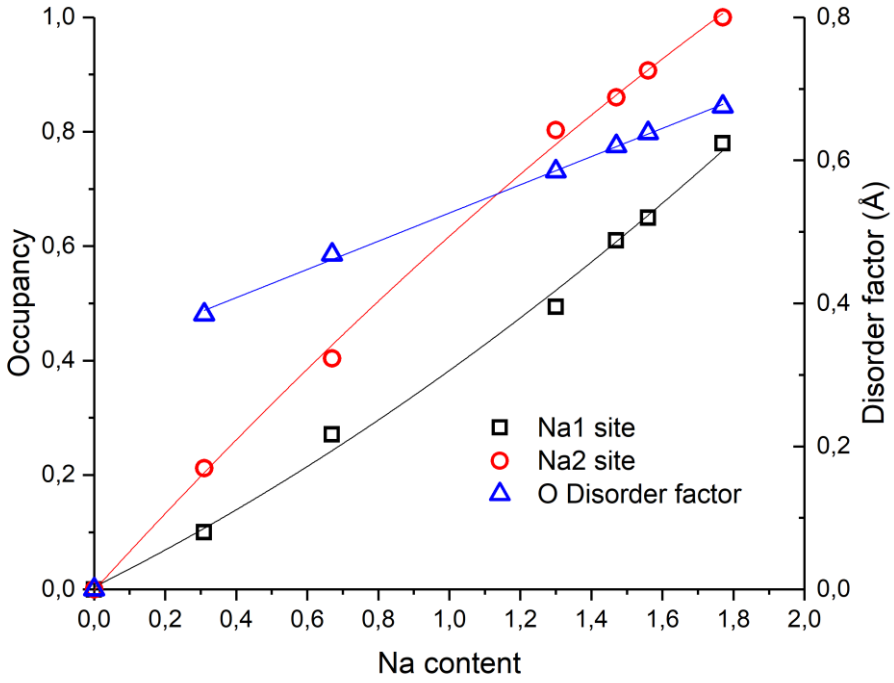

Figure 81. Disorder factor and sodium occupancies for $K_{2-x}Na_xMg_2(SO_4)_3$

In view of the structural complexity of these langbeinites and the limitations of diffraction techniques, where a high number of constraints are needed in order to obtain stable refinements, we have performed Raman measurements with the aim of providing further information about the local coordination around the SO_4 groups.

Figure 82 shows the evolution of the RT Raman spectrum of the $K_{2-x}Na_xMg_2(SO_4)_3$ series with composition in the region of the internal modes of the sulphate groups[146]. Only compounds crystallizing in the $P2_13$ cubic langbeinite phase at RT are included in the figure. Bands appearing around 460, 630, 1040 and above 1100 cm^{-1} are identified as arising from the ν_2 (symmetric bending), ν_4 (antisymmetric bending), ν_1 (symmetric stretching) and ν_3 (antisymmetric

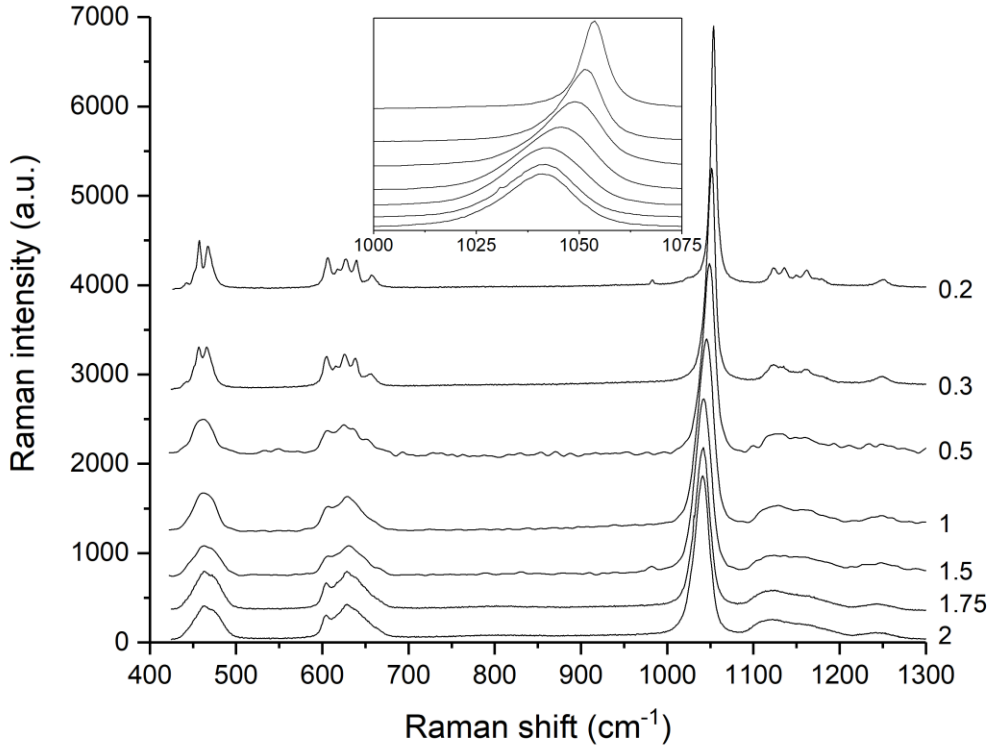

Figure 82. Raman spectra for $K_{2-x}Na_xMg_2(SO_4)_3$ at RT. The inset shows the evolution of the ν_1 band

stretching) tetrahedral modes. We shall focus on the ν_1 band, whose displacements involve the symmetric breathing mode of the four oxygen atoms forming the SO_4 tetrahedron. The inset shows in detail the evolution of the ν_1 band with composition. The band displays an unstructured aspect, as corresponds to a non-degenerate mode in a compound where all tetrahedra are crystallographically equivalent. However, a closer look highlights that this band is anomalous in several ways. First, and contrary to what would be expected according to lattice parameters, the ν_1 frequency increases with K content, suggesting shorter S-O bonds despite the lattice

expansion (Figure 76). This behaviour is not uncommon: lattice expansion may result in weaker SO_4 bonding with second neighbours, and thus in a reduction of the S-O bond lengths. While the crystallographic data suggest that the average S-O bond length appears to essentially remain constant throughout the series, the obtained structure showed quite large anisotropic atomic displacement parameters for oxygen, so that the actual oxygen sites might be even more disordered than initially accounted for using the split sites. In that case, the possibility of lengthening of the S-O bonds with increasing Na content cannot be discarded.

Another peculiarity of the ν_1 band is its composition-dependent broadening and asymmetric shape. Figure 83 shows the total linewidth and the difference between the left and right widths as a function of K content. Among the possible sources of asymmetry in the Raman spectra we propose that in the present case it is

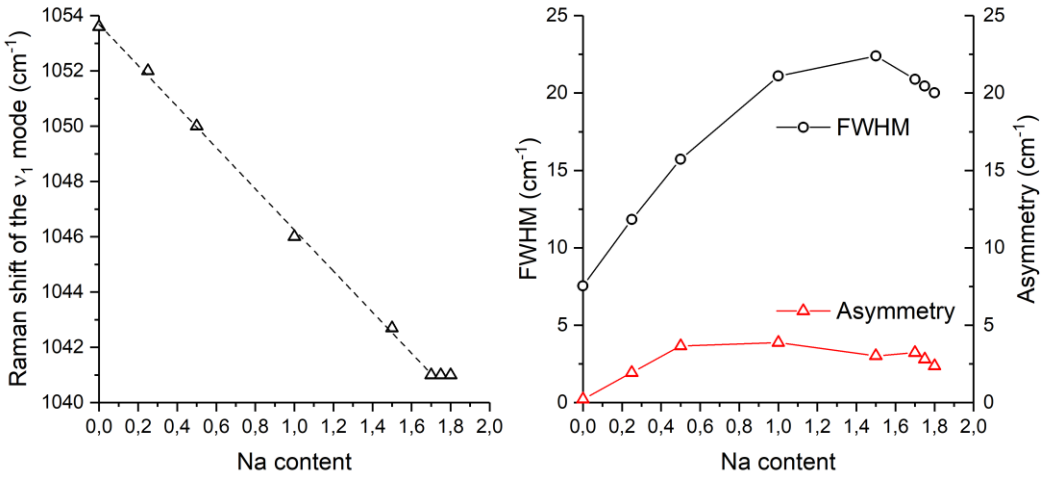

Figure 83. a) Raman shift of the ν_1 breathing mode at RT as a function of K content in the $K_{2-x}Na_xMg_2(SO_4)_3$ series; b) Full width at half maximum (black circles) and asymmetry (red triangles) of the ν_1 breathing mode at RT as a function of K content in the $K_{2-x}Na_xMg_2(SO_4)_3$ series. The asymmetry is defined as the difference between the left and right half widths.

caused by the positional disorder of oxygen and Na/K cations. Oxygen split sites are indeed expected to result in a distribution of SO_4 breathing mode frequencies, but the question arises as to what is the actual origin of this splitting. In the structural analysis, the oxygen disorder has been parameterized by the disorder factor (O-O distance between split sites) and this is seen to increase with Na content. Similarly, the linewidth of the ν_1 band increases toward the Na rich side with a maximum around [Na] = 1.5. We note that remarkable broadening is also observed for $Na_2Mg_2(SO_4)_3$ in its high temperature cubic langbeinite-type phase[157]. Thus, it seems likely that the positional disorder of Na ions is the main cause of broadening and asymmetry, with a smaller contribution of chemical disorder required to explain the presence of a maximum as a function of K/Na content. At this point we note that different coordinates were refined for Na and K atoms sharing sites, which suggests that local displacements may occur because of the large size of the (Na, K) cavities in the langbeinite structure, and that these displacements will be different for Na and K cations. Then, Na ions might be closer to the SO_4 tetrahedra than assumed, implying local O shifts toward the nearby Na atoms thus resulting in longer S-O distance and in site-splitting. Broadening and asymmetry, therefore, reflect the instability of the cubic langbeinite structure at room temperature, as the amount of the smaller Na cations is increased.

Variable temperature spectra of Na-rich members of the series with cubic symmetry at RT were recorded down to 77K with a twofold purpose: first, despite the fact that single crystal XRD at 100K does not show evidence of symmetry lowering for K content above x = 0.1, we thought that Raman scattering might unveil

local structures preluding to a change to orthorhombic symmetry for $K_{0.2}Na_{1.8}Mg_2(SO_4)_3$. The second goal was to see, in the event that no phase transition occurs, whether minimising thermal contributions to the linewidth helps to resolve underlying components of the ν_1 band belonging to different local configurations of the SO_4 tetrahedra. The $K_2Mg_2(SO_4)_3$ endmember compound was also measured for comparison purposes. Figure 84 shows the ν_1 band of $K_{0.2}Na_{1.8}Mg_2(SO_4)_3$ and of $K_2Mg_2(SO_4)_3$ at RT and 77K. The full spectra of $K_{0.2}Na_{1.8}Mg_2(SO_4)_3$, shown in figure A1 of the appendix, suggest that no phase transition occurs for this composition down to 77K. With regards to the totally symmetric mode, we can see that for $K_2Mg_2(SO_4)_3$ the band narrows and hardens on cooling in a conventional way. On the contrary, for $K_{0.2}Na_{1.8}Mg_2(SO_4)_3$, the band looks essentially the same at room and low temperature: the linewidth, intensity and even the frequency remain fairly constant, and the same can be said for the rest of the spectrum (Figure A1 appendix).

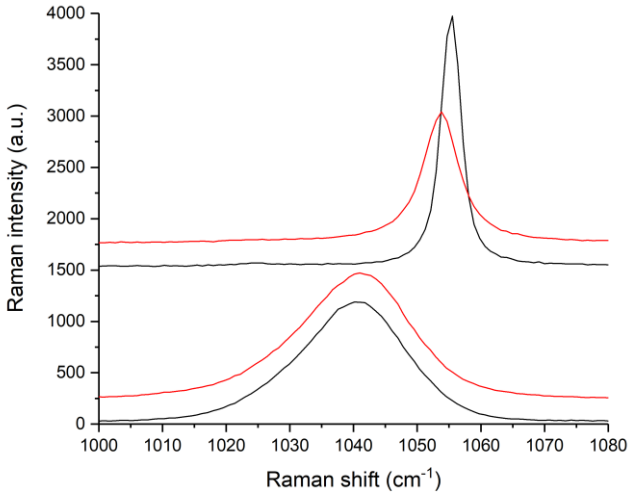

Figure 84. ν_1 band of $K_{0.2}Na_{1.8}Mg_2(SO_4)_3$ (lower graphs) and of $K_2Mg_2(SO_4)_3$ (upper graphs) at RT (in red) and 77K (in black)

This difference implies that for $K_{0.2}Na_{1.8}Mg_2(SO_4)_3$, the linewidth does not arise from the usual thermal broadening processes, neither from dynamic ones, but rather from static positional disorder, as proposed above. The non-observation of well resolved components is then attributed to the quasi-continuous distribution of O positions, which can be described by means of split sites and large thermal ellipsoids.

Structural features of $Na_{1.9}K_{0.1}Mg_2(SO_4)_3$

The structure of $Na_{1.9}K_{0.1}Mg_2(SO_4)_3$ was solved from single crystal data (see table A7 in the appendix information for the complete structural information). It is a non-centrosymmetric orthorhombic cell with space group $P2_12_12_1$. The structure is very complex, with a very large unit cell. The unit cell consists of the SO_4 tetrahedra corner sharing with MgO_6 octahedra or MgO_5 square pyramid units, with the latter essentially highly distorted six-coordinated octahedral with one longer bond distance (Figure 85). The average interatomic distances in the MgO_6 and the MgO_5 units are 2.031(3)Å and 1.978(2)Å respectively. The presence of MgO_5 square pyramids in sulphate crystals is not common, which is most likely due to the lower stability expected for polar units. Here a very narrow range of bond distances and close to ideal bond valence sum +2.030(27) might explain the formation of these polar pyramids.

Despite the orthorhombic symmetry and very large unit cell, structurally the system is closely related to that of langbeinite. Indeed, it can be considered as a highly relaxed 1x3x3 superstructure of langbeinite with some distorted MgO_6 units. The origin of this complex superstructure lies in the ordering of the MgO_5 pyramids (Figure 86). The MgO_5 pyramids are combined in two types of clusters in the crystal lattice. The first type is a cluster of two square pyramids with non-parallel base-facing (double pyramid cluster). There are two orientations of this type of cluster in the unit cell forming two almost perpendicular surfaces (0 1 1) and (0 -1 1) via symmetry. Both have polarisation along *a* axis with opposite direction to each other. Interestingly, 6 coordinated Mg11 site atoms, which have the largest BVS +2.24, are located at the crossing of these surfaces. This could mean that there is significant distorting polarisation present in this region, which places a large strain on these MgO_6 units. The surfaces divide the lattice into squares with a side length of around 20Å. Each square contains a second type of MgO_5 cluster - a combination of four MgO_5 units in the centre of square forming a helix with total polarisation in the centre directed along the axis of the helix. There are two types of helixes in the lattice

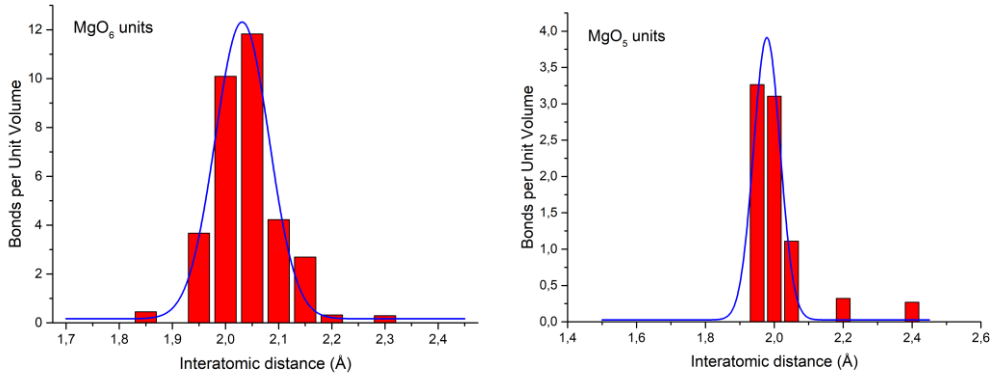

Figure 85. Distribution of bond lengths (with Gaussian fitting) for Mg sites.

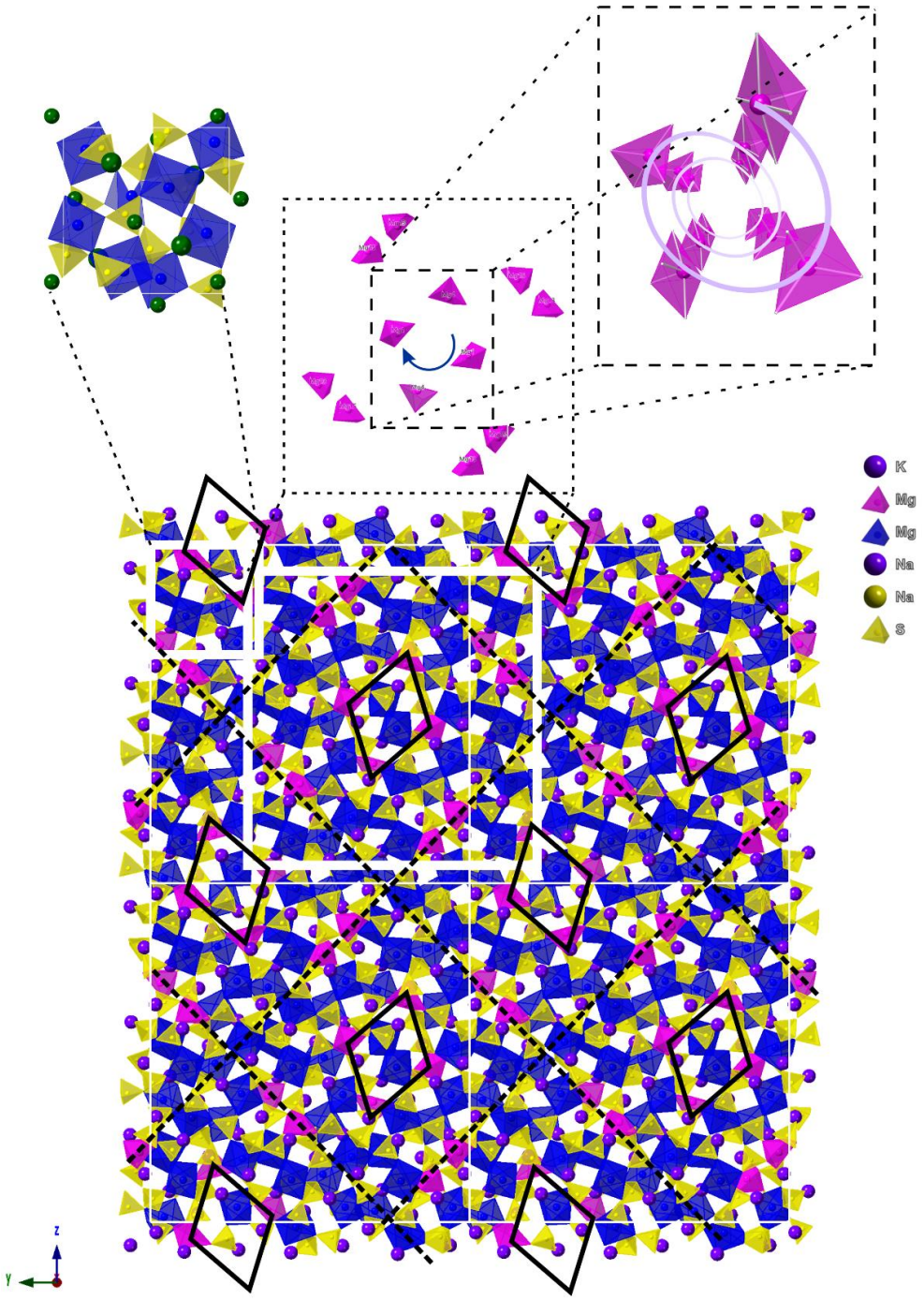

Figure 86. 2x2x2 super cell structure showing orientations of two types of helix pyramid clusters(black diamonds) separated by surfaces formed by double pyramid clusters (black dash lines) and comparison with high temperature langbeinite unit cell (top left corner) (MgO_5 pyramids are labelled pink). In the right top corner an enlarged view of the helix showing the spiralling of the pyramids

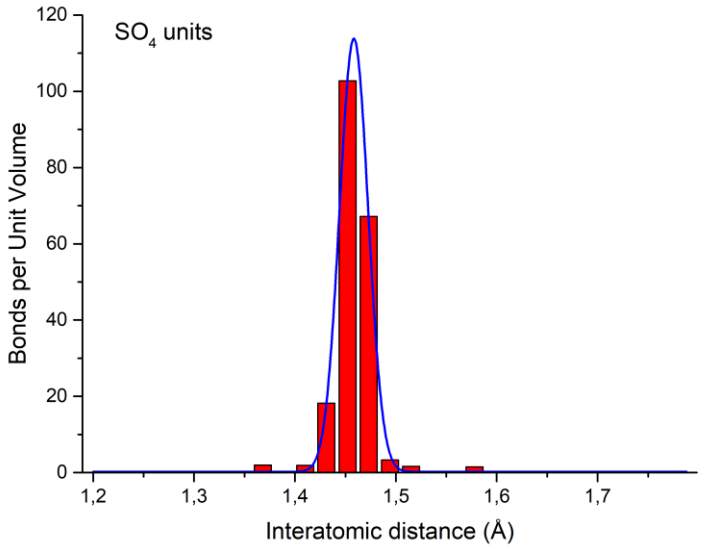

Figure 87. Distribution of bond lengths in SO_4 units with Gaussian fitting

organised in a chequered fashion in relation to the squares formed by the surfaces. Both types have the same clockwise downwards rotation, with, however, the opposite polarisation. As for the cubic langbeinite structure series, the SO_4 tetrahedra are symmetrical, with a narrow distribution of bond lengths (Figure 87), and an average S-O bond length of 1.458(1) Å. Similarly, some of the tetrahedra show evidence of rotational disorder, modelled as split sites, which could be related either to alignment of helixes and formation of an even larger supercell or to local variations in Na/K content as suggested for the cubic langbeinite series.

The cell contains 18 alkali metal sites, with only half of these containing potassium ions, with an average occupancy of ≈0.1. The other sites are only occupied by sodium (Table 25), which can be explained by the different sizes of these cavity sites.

Table 25. Selected Atomic Occupancies for $K_{0.1}Na_{1.9}Mg_2(SO_4)_3$. Not mentioned sites here are all equal 1.

Atom	Occupancy	Atom	Occupancy	Atom	Occupancy
K1	0.116(13)	K2	0.108(12)	K4	0.110(12)
K6	0.090(12)	K9	0.104(13)	K12	0.096(12)
K13	0.110(12)	K15	0.095(11)	K18	0.115(12)
Na1	0.884(13)	Na2	0.892(12)	Na4	0.890(12)
Na6	0.910(12)	Na9	0.896(13)	Na12	0.904(12)
Na13	0.890(12)	Na15	0.905(11)	Na18	0.885(12)
O1	0.57(2)	O2	0.562(16)	O7	0.584(5)
O10	0.584(5)	O11	0.584(5)	O13	0.531(8)
O103	0.535(3)	O104	0.636(15)	O105	0.535(3)
O106	0.535(3)	O108	0.465(3)	O109	0.465(3)
O110	0.465(3)	O111	0.416(5)	O112	0.416(5)
O113	0.416(5)	O114	0.364(15)	O115	0.469(8)
O116	0.522(8)	O117	0.478(8)	O118	0.43(2)
O119	0.438(16)				

The sodium sites form a 3D chiral network with relatively high translational symmetry related to a 1x⅓x⅓ subcell unit. Sites partially occupied with potassium form the same chiral network with opposite rotation. Figure 88 shows that the distribution of the Na-O bonds for the Na only sites has sharp peak at 2.471Å. At the same time distribution of Na/K-O bonds for mixed sites is more complex. The figure shows the presence of more than three broad distribution peaks. These can be

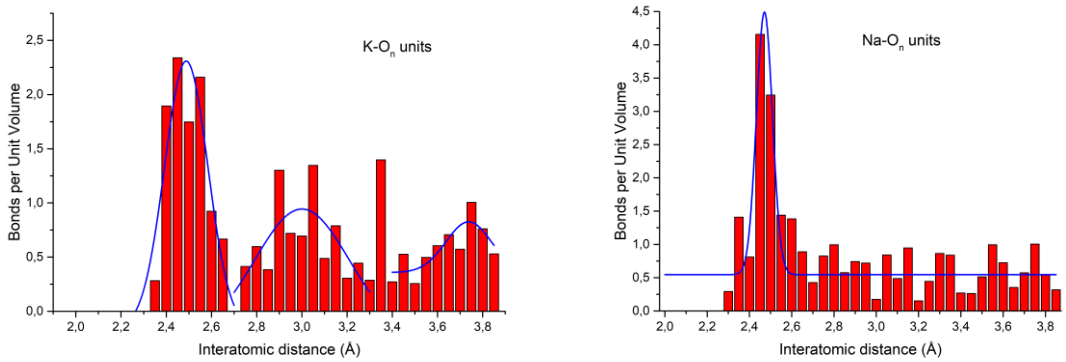

Figure 88. Distribution of interatomic distances (with Gaussian fitting) for selected potassium and sodium surroundings.

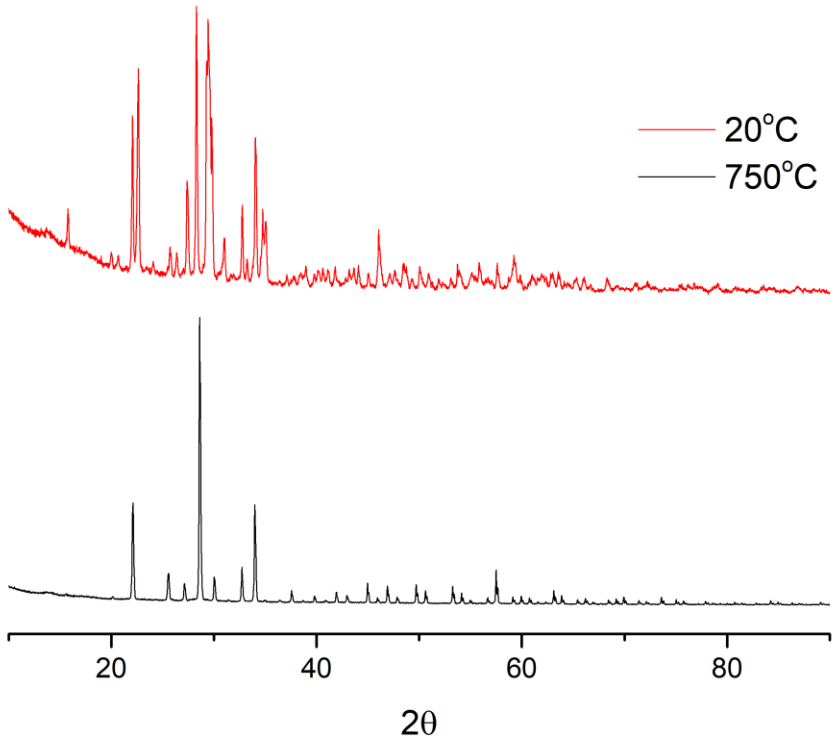

Figure 89. XRD patterns of $K_{0.1}Na_{1.9}Mg_2(SO_4)_3$ at 20°C and 750°C

described as spheres of oxygen surrounding the potassium containing sites, with the first peak at 2.488 Å, second at 3.000 Å and third at 3.738Å. This may indicate that K containing cavities are larger and have lower symmetry.

At higher temperature the structure of $Na_{1.9}K_{0.1}Mg_2(SO_4)_3$ converts into the simple cubic $P2_13$ langbeinite structure (Figure 89). A similar transition was previously reported for $Na_2Mg_2(SO_4)_3$[157]. VTXRD showed that the phase transition into the cubic langbeinite structure occurs at a temperature slightly below 200°C (Figure 90), which is a slightly lower temperature than observed for $Na_2Mg_2(SO_4)_3$. In agreement with this phase transition, the DTA curve of the TGA experiment also

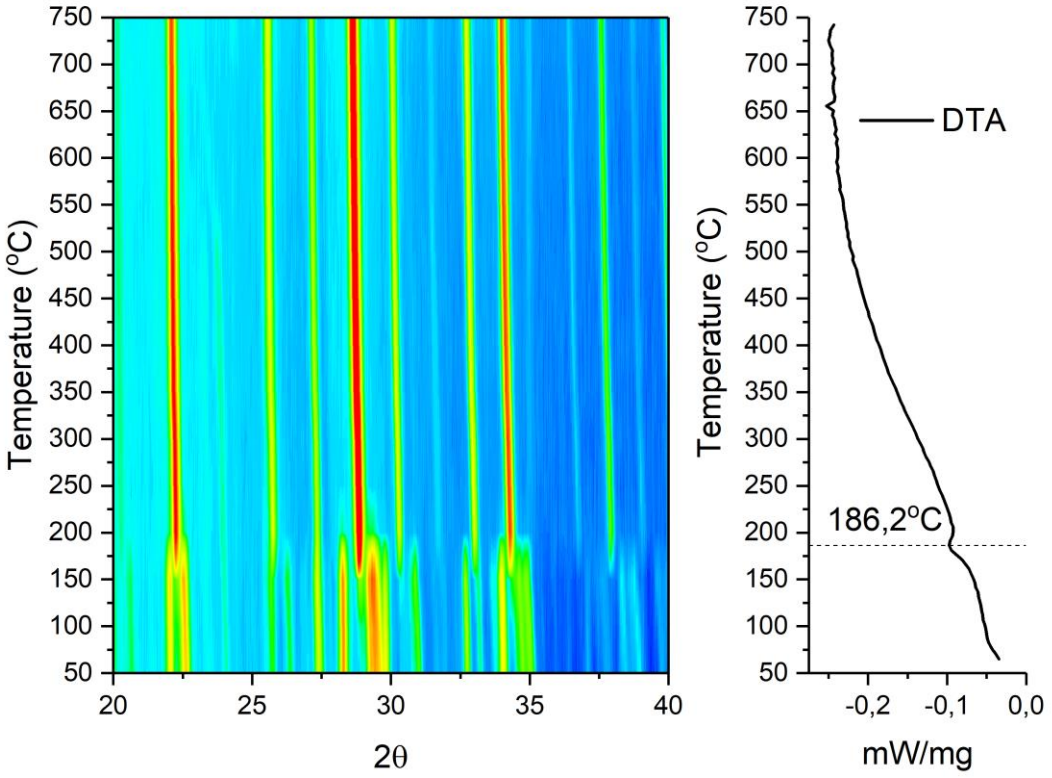

Figure 90. Contour plot of variable temperature XRD and DTA curve of $K_{0.1}Na_{1.9}Mg_2(SO_4)_3$ during the cooling stage. The results show a transition to a cubic langbeinite structure at elevated temperatures

showed a peak at 186.2°C (Figure 90), corresponding to the phase transition. Cell volume data show a clear change at this phase transition (Figure 18), with an effective discontinuous expansion at this temperature.

Considering strong motions of ions at high temperatures and the previously described significant rotational disorder of SO_4 units in related cubic langbeinite phases at room temperatures, we assumed that in this case similar rotational disorder might be observed. Rietveld refinement using the high temperature powder diffraction data was, therefore, performed using a rigid body approach for

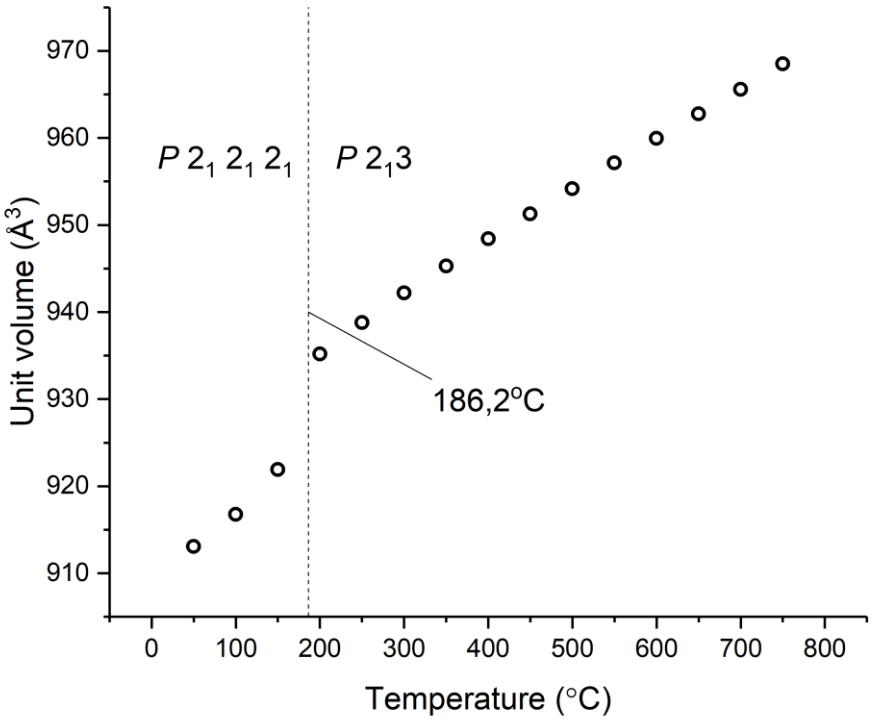

Figure 91. Unit cell volume of $K_{0.1}Na_{1.9}Mg_2(SO_4)_3$ versus temperature obtained from refinement of powder VT-XRD data. Unit for cubic phase is taken as it is, unit for orthorhombic phase is taken as $^1/_9$.

the SO_4 unit with splitting into three tetrahedrons with partial occupancy ⅓ in order to model rotational disorder around a single sulphur atom. The size of the rigid body, i.e. S-O bond length, was allowed to refine as well. Isotropic thermal displacement parameters were constrained to be the same for all oxygen atoms, while the alkali metals were constrained to be on the same site and the site occupancy constrained to the values expected from the chemical composition.

This approach allowed us to improve the R_{wp} from ~15% down to ~10% while maintaining a sensible structural solution (Figure A4 appendix). Further improvements to the model would require the introduction of anisotropic atomic

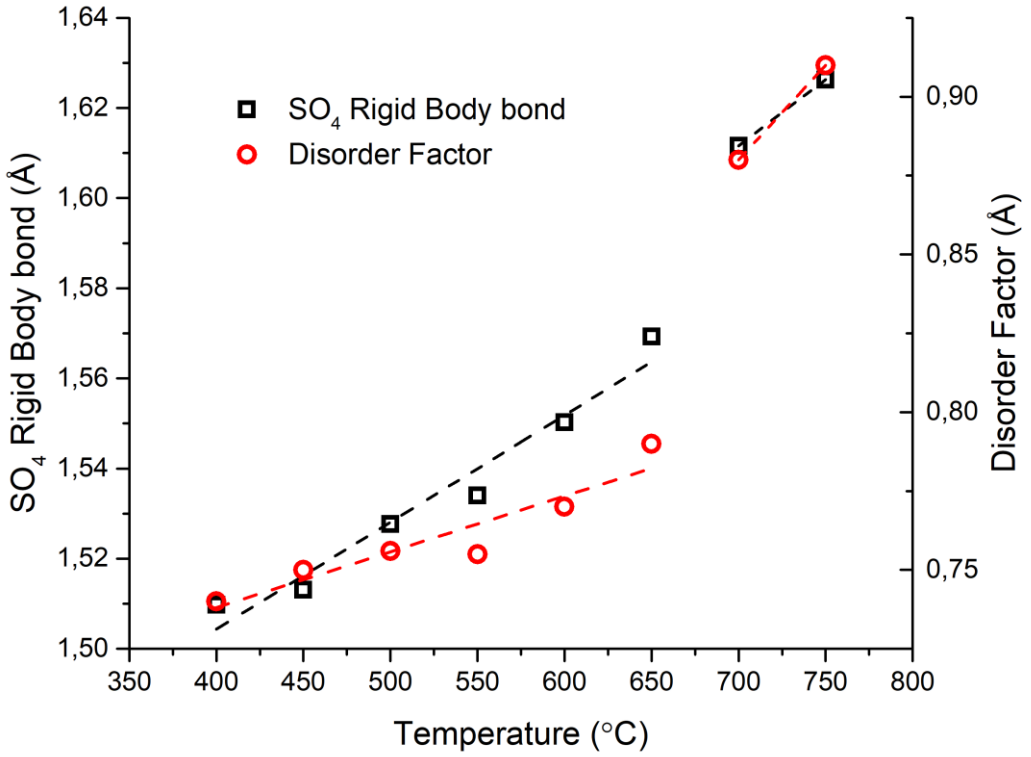

Figure 92. Rigid body bond length and disorder factor for $K_{0.1}Na_{1.9}Mg_2(SO_4)_3$ with varying temperature.

displacement parameters, however this makes the refinement unstable due to the high number of variables and the insufficient amount of data available in powder XRD. Table A8 in appendix contains structural information about $K_{0.1}Na_{1.9}Mg_2(SO_4)_3$ at 750°C.

The refined structure at 750°C suggested very large rotational distortions of the SO_4 unit, with a disorder factor in this system of up to 0.94 (Figure 92). In addition the apparent S-O bond length in the rigid body converged to a value of 1.638(4)Å. This value is much larger than expected for a sulphate group, and would suggest that there are some local displacements of the sulphur. It is particularly

noteworthy that the disorder factor and apparent rigid body bond length significantly rise in value between 650 and 700°C. This could be an indication of another phase transition, although at the same time, the cell does not appear to change symmetry. There is, however, a weak feature in the DTA curve in this region (Figure 17). Fractional occupancies of sodium and potassium show the same ordering between two sites as at room temperature (potassium favours the larger cavity, while sodium the smaller).

The transition from the low temperature orthorhombic cell to high temperature cubic langbeinite can be explained by the fact that the structure of the former is similar to a 1x3x3 langbeinite supercell. Thus, the low temperature orthorhombic phase can be classed as a highly disordered variant of the langbeinite structure. While orthorhombic langbeinite phases have been previously reported below room temperature, e.g. $K_2(Ca/Cd)_2(SO_4)_3$[150,151], the orthorhombic distortion is much lower than observed for the $K_{0.1}Na_{1.9}Mg_2(SO_4)_3$ system reported here, and there was no evidence for an enlarged supercell in the former studies.

The structural evolution of $K_{0.1}Na_{1.9}Mg_2(SO_4)_3$ was also followed by Raman scattering from 77 K to 775°C (1048 K) (see the whole series of spectra in figures A2 and A3 of the appendix). Measurements below RT were undertaken in the search for a possible phase transition from orthorhombic to monoclinic symmetry, similar to the one detected in our previous study on $Na_2Mg_2(SO_4)_3$ at around 100 °C [157]. As figure A2 shows, no clear evidence of new modes or of mode splitting can be ascertained, although some modes display an anomalous intensity increase that might be a hint of a nearby transition occurring perhaps below 77K. On the contrary,

the phase transition to cubic symmetry is clearly observed between 150 and 200 °C, in perfect agreement with the XRD results (Figure A3 appendix). Above 200 °C the cubic phase spectrum varies very little with increasing temperature; the observed broadening is ascribed to conventional thermal effects.

The conductivity of $K_{0.1}Na_{1.9}Mg_2(SO_4)_3$ phase was investigated and it was shown to possess low conductivity 1.2×10^{-5} S/cm at 400°C with a high temperature activation energy of 0.38 eV. This can be explained by low mobility of alkali metal ions in the cell as transport channels are not wide and vacancies are not present in the system. The Arrhenius plot shows a step-like rise in the conductivity at around 180°C that corresponds to the phase transition from orthorhombic structure into cubic langbeinite (Figure 93). This change is reversible as shown by measurements

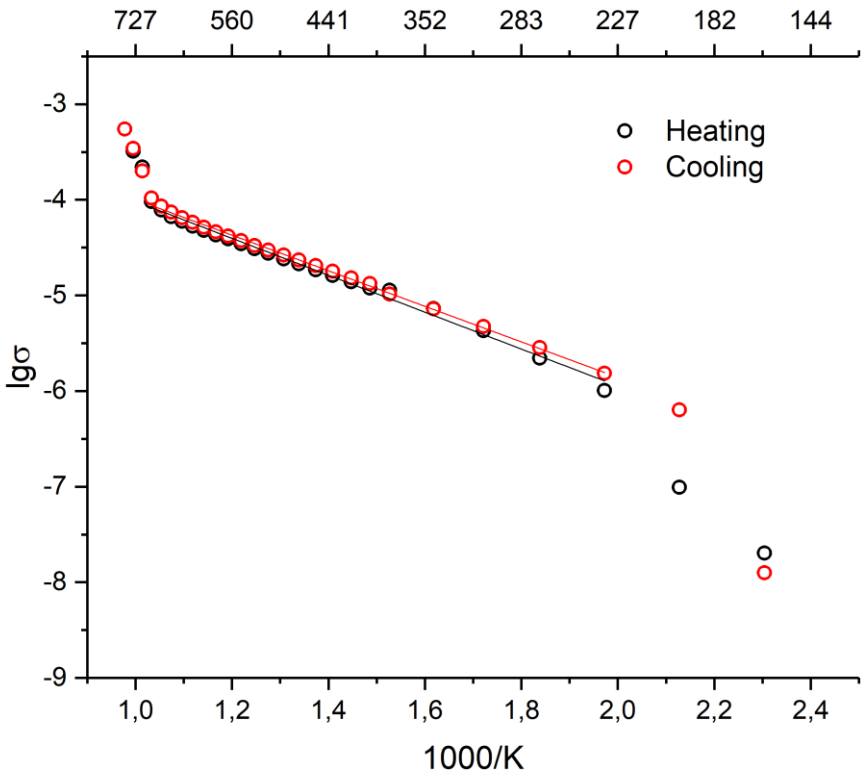

Figure 93. Arrhenius plot of $K_{0.1}Na_{1.9}Mg_2(SO_4)_3$ via EIS

on both heating and cooling. In addition, the conductivity data show a bend near 688^{o}C what can be related to enlarged disorder of SO_4 tetrahedrons and partial opening of the general cages to each other. DTA curve has a small peak in this temperature area as well.

Conclusion

In this work we show that Na can be incorporated into the langbeinite phase, $K_2Mg_2(SO_4)_3$. The cubic langbeinite structure is maintained at room temperature for high Na levels; $K_{2-x}Na_xMg_2(SO_4)_3$ ($0 \leq x \leq 1.75$). For higher Na levels, $1.8 \leq x \leq 1.9$, an enlarged orthorhombic cell is obtained, with the structure resembling a highly distorted variant of the langbeinite structure. This relationship is also illustrated by the fact that the latter phases transform to the cubic langbeinite structure at relatively low temperature (≈200°C). The work therefore highlights the flexibility of the langbeinite structure to accommodate high levels of Na ions, thus offering another avenue to manipulate the properties of materials with this structure-type.

Chapter Seven

Synthesis and study of Eldfellite based materials doped with SeO_4, HPO_4 and PO_3F

The growing demand for low cost large-scale energy storage to balance the intermittency of renewable energy technologies is driving renewed interest in Na ion batteries, which are viewed as lower cost alternatives to lithium-ion batteries. As a result there is renewed interest in the development of new cathode materials for Na ion batteries. While layered Na transition metal oxide materials are currently the favoured cathode materials[161–164], there is growing interest in alternative materials containing oxoanion groups, as for Li ion batteries. In this respect, a wide range of such materials have been investigated: including $Na_3V_2(PO_4)_3$[165–168],

$NaFePO_4$[169,170], $Na_2MnP_2O_7$[171], $Na_4Co_3(PO_4)_2P_2O_7$[172], $Na_3V_2O_2(PO_4)_2F$[173–176], $Na_{2.5}Fe_{1.75}(SO_4)_3$[46], Na_2FeSiO_4[177], $NaFe(SO_4)_2$[54].

As shown by the examples above, the focus of this research has been on systems containing a single oxoanion, despite the potential for tuning both structure and properties by substitution on the oxoanion site. Recently we have illustrated how isovalent substitution of SO_4^{2-} by SeO_4^{2-} and PO_3F^{2-} in the bimetallic metal sulphates $Na_2M(SO_4)_2{\cdot}2H_2O$ (M=transition metal)[98], and the resultant phases obtained on dehydration[158]. In this work, we extend such studies to investigate the effect of SeO_4^{2-}, PO_3^{2-}, HPO_4^{2-} into the layered eldfellite structured $NaFe(SO_4)_2$. This phase was first reported by Balić-Žunic et al.[178] and more recently evaluated as a potential cathode for a Na-ion battery by Singh et al.[54]. In this latter work, $NaFe(SO_4)_2$ was shown to have a capacity near 80 mAh/g (at 0.1 C) for more than 80 cycles, with an average voltage of 3.2V versus sodium. Banerjee et al. predicted by DFT calculations that this material can be improved by transition metal substitution[56]. However, while partial substitution of iron with chromium demonstrated better thermal properties, the inactivity of the Cr^{2+}/Cr^{3+} redox couple meant that the electrochemical performance was poorer[179]. Given that the nature of oxoanion group plays a great role in polarisation effects in the crystal lattice of these compounds[180], the partial substitution at this site is of interest. With this in mind, here we report a study of oxoanion doping in $NaFe(SO_4)_2$ to give $NaFe(SO_4)_{1.5}(X)_{0.5}$ (X=SeO_4, HPO_4, PO_3F), examining the effect on structure and properties. It was observed later that fluorophosphate undergoes hydrolysis into hydrophosphate.

Experimental

$NaFe(SO_4)_{1.5}(X)_{0.5}$ samples were prepared via a dissolution-evaporation route. In this facile route, stoichiometric amounts of $Fe_2(SO_4)_3$ and Na_2X (X=SeO_4, HPO_4, PO_3F, SO_4) (for 3g of sample) are dissolved on heating in water. Evaporation of the water is then performed to obtain a thick slurry. This slurry was then dried for 12 hours at 150°C in a drying oven, the powder was then ground and heated in alumina crucible for 12 hours at 300°C in a furnace. The obtained products were then analysed by powder XRD experiment with data collected on Panalytical Empyrean diffractometer with copper X-ray source ($\lambda_{CuK\alpha1}$ = 1.54056 Å, $\lambda_{CuK\alpha2}$ = 1.54439 Å) in Bragg-Brentano reflection geometry equipped with Pixcel 2D detector in the range from 15 to 145°. Time of flight powder neutron diffraction (TOF) data were collected on the POLARIS diffractometer (Backscattering bank) at the ISIS pulsed spallation source (Rutherford Appleton Laboratory, Harwell, UK). 3g of powder were loaded into 8 mm diameter thin-walled cylindrical vanadium sample cans. Data were collected at room temperature for 150 μAh proton beam energy to the ISIS target for each sample. Structural refinements (doped systems: neutron diffraction data, undoped system: X-ray diffraction data) were performed by the Rietveld method with the program GSASII[103].

In order to investigate the thermal stability and possible presence of water or carbonate in the samples, thermogravimetric analysis (TGA-MS, Netzsch) was performed at a rate of 10°C/min to 400°C in a nitrogen atmosphere with the MS detection of volatile substances for m/z = 18, 44 and 64 corresponding to water,

carbon dioxide and sulphur dioxide. In order to determine more information on the oxoanion groups, Fourier transform infrared spectroscopy (Perkin Elmer FTIR Spectrum Two) as well as Raman spectroscopy (Renishaw inVia) data were collected. SEM images were collected on Philips XL-30 FEG Environmental SEM with Oxford Inca EDS.

In order to determine more information on the Fe oxidation state, ^{57}Fe Mössbauer spectra were recorded in constant acceleration mode using a 25mCi ^{57}Co/Rh source. All spectra were computer fitted and all chemical isomer shift data are quoted relative to metallic iron at room temperature.

The conductivities of the obtained pellets were measured in air by electrochemical impedance spectroscopy using a PSM impedance analyser within a frequency range 1 – 10^6 Hz. Measurements were carried on in the temperature range 50-300˚C on cooling in dry N_2 atmosphere. Pellets were coated from both sides with silver paste and dried at 150˚C for 2 hours. Zview software was used to analyse the obtained data[105]. The diffusion coefficients were calculated using Nernst-Einstein relation: $D = \frac{\sigma k_B T}{\bar{e}^2 n}$, where k_B is the Boltzmann constant, $\bar{e}$ is the electron charge and n is charge carrier concentration (number of Na cations per unit-cell volume)[126,127].

Results and discussion

Diffraction study

The XRD data (Figure 94) indicated the successful synthesis of $NaFe(SO_4)_{1.5}(X)_{0.5}$ (X is SeO_4, HPO_4, PO_3F, SO_4). The data indicated that all materials were isostructural without any traces of impurity phases.

Neutron diffraction (ND) data were collected for the doped materials and the structures were refined using the Rietveld method, with the previously reported structural model for $NaFe(SO_4)_2$ (space group $C\ 1\ 2/m\ 1$) used[178] (Figure 95). For comparison, we also prepared undoped $NaFe(SO_4)_2$ and performed a structure refinement using the XRD data. The obtained cell parameters for both doped and undoped samples are shown in table 26.

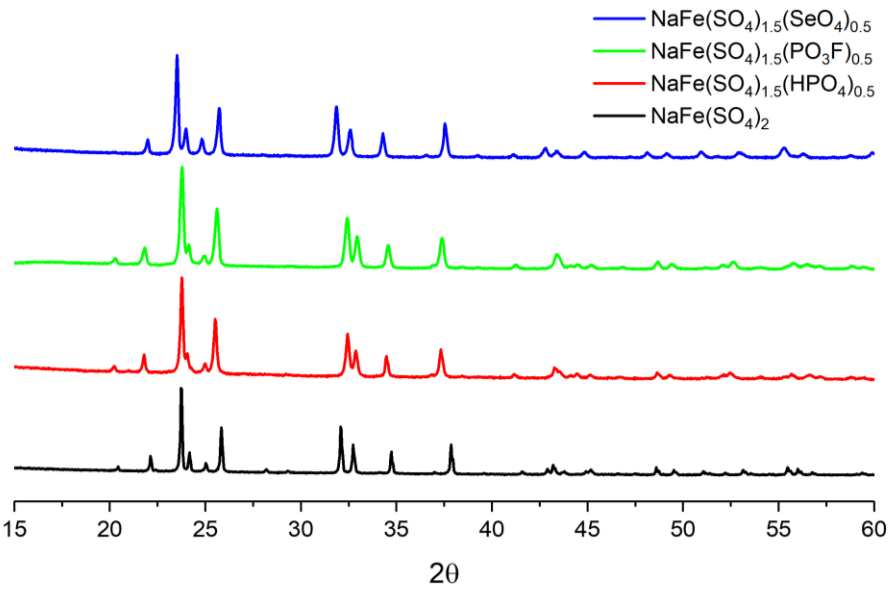

Figure 94. XRD patterns for $NaFe(SO_4)_{1.5}(X)_{0.5}$ (X=SeO_4, HPO_4, PO_3F, SO_4), showing single phase isostructural samples

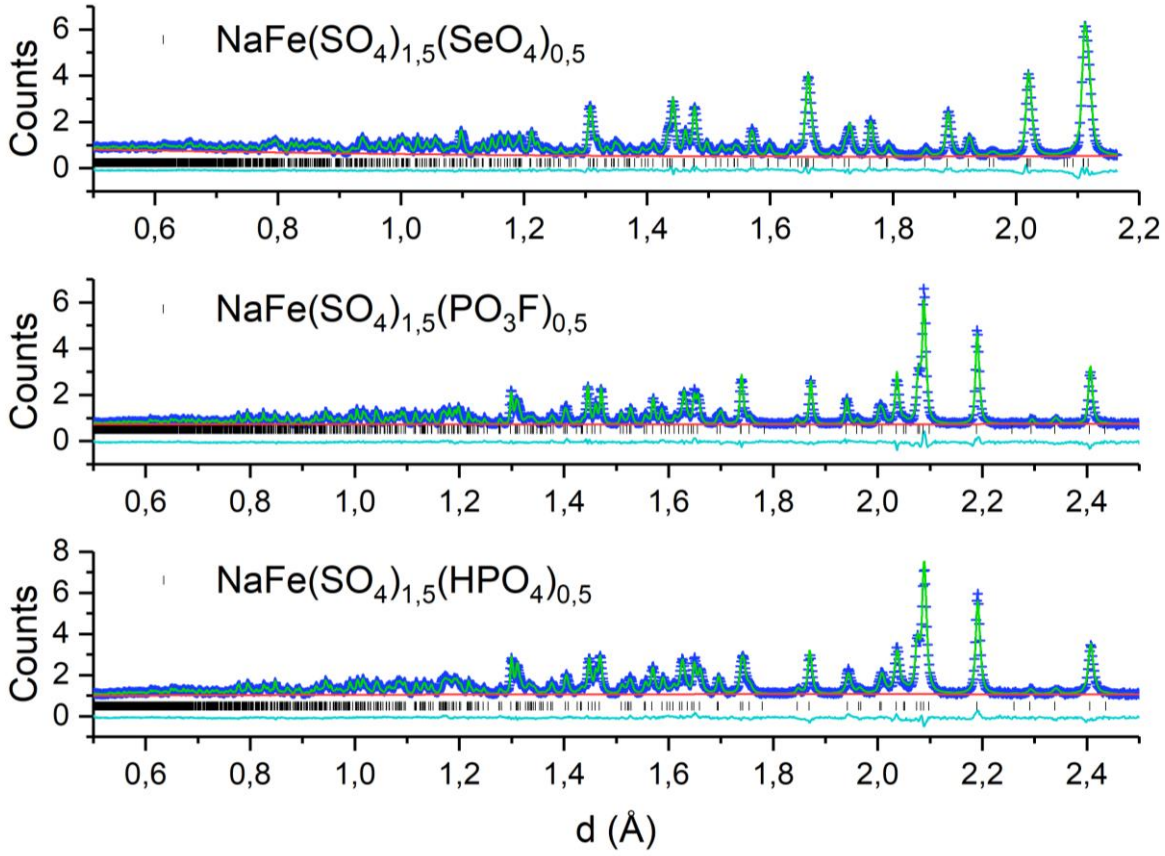

Figure 95. Plot for structural Rietveld refinement of ND data for $NaFe(SO_4)_{1.5}(X)_{0.5}$ (X = SeO_4, HPO_4, PO_3F)

Table 26. Cell parameters and refinement quality indexes for $NaFe(SO_4)_{1.5}(X)_{0.5}$ (X=SeO_4, HPO_4, PO_3F, SO_4)

C12/m1	SeO_4^{2-}	PO_3F^{2-}	HPO_4^{2-}	SO_4^{2-}
a(Å)	8.0786(3)	8.1441(3)	8.1445(4)	8.0227(1)
b(Å)	5.2203(2)	5.1920(2)	5.1942(2)	5.1596(1)
c(Å)	7.1709(3)	7.0199(3)	7.0184(3)	7.1506(1)
β(°)	92.311(2)	91.684(2)	91.401(3)	92.097(1)
Volume(Å³)	302.169(29)	296.705(27)	296.822(31)	295.791(9)
R_{wp}	1.90%	2.16%	1.84%	2.09%
GOF	1.81	1.92	1.94	1.83

As shown previously, the structure of $NaFe(SO_4)_2$ consists of corner sharing FeO_6 octahedra and SO_4 tetrahedra forming a triple layer SO_4-FeO_6-SO_4 perpendicular to the *c* axis with Na ions lying between these layers (Figure 96). It

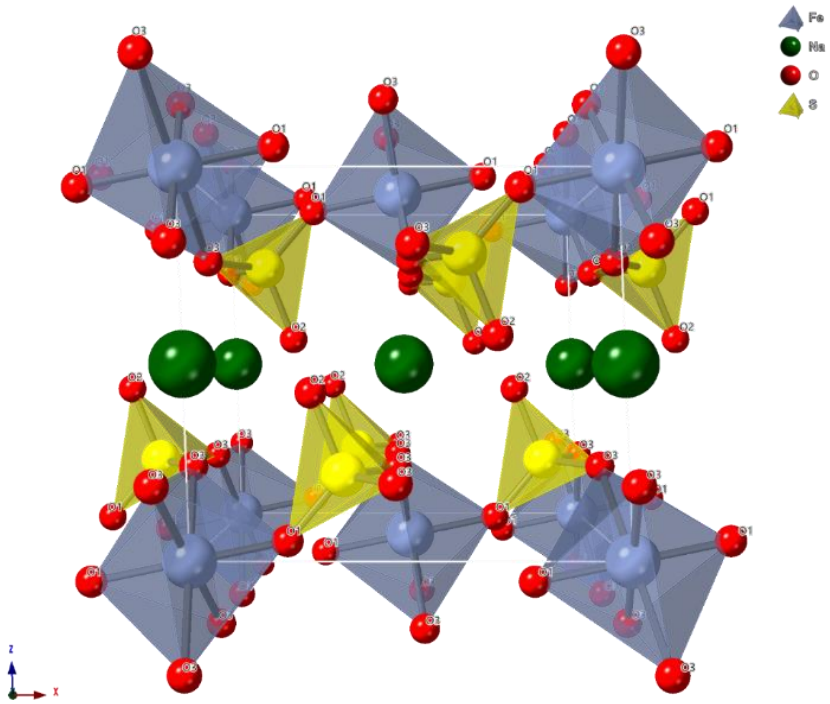

Figure 96. Structure of Eldfellite $NaFe(SO_4)_2$

has been proposed that the relatively rigid framework of layers allows a facile change in size of the cell along *c* axis without decomposition during Na intercalation-deintercalation into these layers.

From the cell parameter data, it is clear that the unit cell expands on doping, with the largest expansion on selenate doping. In all cases an expansion along the *a* and *b* axes are observed. However, for the samples doped with HPO_4^{2-}, or PO_3F^{2-}, a contraction along the *c* axis is observed.

The refined occupancies confirm successful incorporation of the dopants (Table 27-28). An attempt to refine the sodium occupancies showed no significant deviations from full occupancy, as expected. Consequently, in the final refinement, the sodium site occupancy was fixed to 1.

Table 27. Structural parameters obtained for $NaFe(SO_4)_{1.5}(X)_{0.5}$ (X=SeO_4, HPO_4, PO_3F)

Atom	Multiplicity	x	y	z	Fractional occupancy	U_{eq}×100(Å^2)
			$NaFe(SO_4)_{1.5}(SeO_4)_{0.5}$			
Na	8	0.0226(14)	0.0402(10)	0.5094(25)	0.25	1.00(37)
Fe	2	0	0	0	1	0.70 (5)
S	4	0.3624(3)	0	0.2260(3)	0.727(8)	0.63(5)
Se	4	0.3624(3)	0	0.2260(3)	0.273(8)	0.63(5)
O1	4	0.2375(2)	0	0.0598(2)	1	1.20(6)
O2	4	0.2906(2)	0	0.4070(2)	1	2.40(5)
O3	8	0.4716(1)	0.2370(2)	0.2016(2)	1	1.80(4)
			$NaFe(SO_4)_{1.5}(PO_3F)_{0.5}$			
Na	8	0.0306(8)	0.0422(12)	0.5018(12)	0.25	0.90(25)
Fe	2	0	0	0	1	0.90(7)
S	4	0.3619(3)	0	0.2242(4)	0.727(22)	0.60(7)
P	4	0.3619(3)	0	0.2242(4)	0.273(22)	0.60(7)
O1	4	0.2343(2)	0	0.0688(3)	1	1.40(8)
O2	4	0.2896(2)	0	0.4143(3)	1	2.50(7)
O3	8	0.4648(2)	0.2354(2)	0.2044(2)	1	1.50(6)
			$NaFe(SO_4)_{1.5}(HPO_4)_{0.5}$			
Na	8	0.0268(12)	0.0420(16)	0.5118(24)	0.25	1.00(49)
Fe	2	0	0	0	1	0.90(7)
S	4	0.3602(4)	0	0.2244(4)	0.732(21)	0.56(7)
P	4	0.3602(4)	0	0.2244(4)	0.268(21)	0.56(7)
O1	4	0.2348(2)	0	0.0686(3)	1	1.20(8)
O2	4	0.2894(2)	0	0.4154(3)	1	2.50(7)
O3	8	0.4640(2)	0.2356(3)	0.2051(2)	1	1.50(5)

Table 28. Anisotropic Displacement Parameters Å²×100 for $NaFe(SO_4)_{1.5}(X)_{0.5}$ (X=SeO_4, HPO_4, PO_3F)

Atom	U_{11}	U_{22}	U_{33}	U_{12}	U_{13}	U_{23}
			$NaFe(SO_4)_{1.5}(SeO_4)_{0.5}$			
Na	0.53(53)	0.76(32)	1.72(33)	-0.18(17)	0.29(39)	-0.25(27)
Fe	0.62(6)	0.43(6)	1.11(6)	0	0.08(4)	0
O1	0.65(5)	0.97(5)	1.88(6)	0	0.06(5)	0
O2	2.14(6)	2.87(5)	2.15(5)	0	0.05(4)	0
O3	1.86(6)	1.48(4)	2.05(4)	-0.69(3)	-0.72(3)	0.99(3)
			$NaFe(SO_4)_{1.5}(PO_3F)_{0.5}$			
Na	2.67(28)	1.51(40)	1.00(12)	-0.21(17)	0.79(27)	0.52(21)
Fe	0.71(7)	0.27(7)	1.83(7)	0	-0.35(6)	0
O1	1.22(8)	1.49(7)	1.51(8)	0	-0.70(6)	0
O2	3.62(7)	2.09(7)	1.76(8)	0	0.79(5)	0
O3	1.74(5)	1.29(6)	1.37(6)	-0.56(4)	-0.50(4)	0.55(4)
			$NaFe(SO_4)_{1.5}(HPO_4)_{0.5}$			
Na	1.06(55)	1.19(54)	0.84(42)	-0.05(24)	0.02(46)	0.05(30)
Fe	0.42(7)	0.56(7)	1.62(7)	0	-0.07(6)	0
O1	0.42(8)	1.47(7)	1.60(8)	0	-0.48(5)	0
O2	3.90(7)	1.94(7)	1.70(8)	0	1.17(6)	0
O3	1.41(5)	1.12(5)	1.92(5)	-0.79(4)	-0.56(4)	0.47(4)

Selected bond distances are given in Table 4, and these show a particular increase in average distance for the selenate doped sample, as expected (Table 29), while there is little change in the Fe-O distances.

Table 29. Selected interatomic distances (Å) and it's multiplicity from TOF neutron Rietveld refinement of $NaFe(SO_4)_{1.5}(X)_{0.5}$ (X=SeO_4, HPO_4, PO_3F)

$NaFe(SO_4)_{1.5}(SeO_4)_{0.5}$					
S/Se-O1	1	1.530(2)	Fe-O1	2	1.949(1)
S/Se-O2	1	1.443(2)	Fe-O3	4	2.013(1)
S/Se-O3	2	1.533(2)			
$NaFe(SO_4)_{1.5}(PO_3F)_{0.5}$					
S/P-O1	1	1.484(2)	Fe-O1	2	1.955(2)
S/P-O2	1	1.474(2)	Fe-O3	4	2.013(1)
S/P-O3	2	1.490(1)			
$NaFe(SO_4)_{1.5}(HPO_4)_{0.5}$					
S/P-O1	1	1.478(2)	Fe-O1	2	1.960(2)
S/P-O2	1	1.472(2)	Fe-O3	4	2.016(1)
S/P-O3	2	1.495(1)			

For the PO_3F^{2-} doped sample, it was expected that there may be a significant change in one of the average S/P-O bond lengths, as a result of the P-F bond, assuming there is an ordered arrangement for the PO_3F^{2-} group. However, the data showed this not to be the case. Further discussion on this sample is outlined in the Raman data section. For the HPO_4^{2-} doped sample, the H position could not be defined, most likely due to random distribution and high thermal motion. However, considering the observed contraction along the *c* direction, we suspect that the proton is located pointing at adjacent layers to allow the formation of hydrogen bonds between layers and hence a contraction in this direction.

The sodium ions in these structures occupies an essentially 6 coordinated site, with a further 4 oxygen ions in an outer sphere at longer distance. The calculated volumes of distorted NaO_6 octahedra and extended NaO_{10} coordination spheres reveal an increase in the order HPO_4-PO_3F-SeO_4-SO_4 (Table 30). Thus, the largest Na-O coordination volume was found in the undoped material. Given that a larger coordination volume may improve Na-ion diffusion, this may indicate that the

doping strategies may be detrimental to diffusion rates, particularly for the HPO_4/PO_3F doped samples.

Table 30. Volumes of NaO_6 and NaO_{10} units for $NaFe(SO_4)_{1.5}(X)_{0.5}$ (X=SeO_4, HPO_4, PO_3F)

Dopant	Volume NaO_6(Å^3)	Volume NaO_{10}(Å^3)
HPO_4^{2-}	18.41	40.45
PO_3F^{2-}	18.53	40.36
SeO_4^{2-}	19.02	42.23
SO_4^{2-}	19.29	42.53

Vibrational spectra

In order to gather more information on these materials, IR and Raman spectra were recorded (Figure 97). In all cases corresponding spectra are relatively similar showing the same bands. The bands from the SO_4^{2-}, HPO_4^{2-}, SeO_4^{2-} and PO_3F^{2-} in most cases can be distinguished separately as tetrahedral (T_d) anions, however overlapping of the peaks does complicate the assignments. The proposed assignments[181] are shown in table 31. In all cases ν_1 symmetrical vibrations (XY_4) of SO_4 are located in a similar region of frequencies in the Raman as well as in the IR spectra. For the phosphate containing compound there can be observed small shift towards lower frequencies. This shift is most likely attributed to the overlapping of the peaks of PO_4 and SO_4 groups which therefore couldn't be individually distinguished accurately. The shift in the SeO_4 group compared to the SO_4 group is clearer, with the former found in the expected region 830-850 cm^{-1} in both IR and Raman spectra. The ν_3 asymmetric vibrations (XY_4) for SO_4 were located in the same

region for all compounds with slight shift towards higher frequencies for the doped phases. The same vibration mode peaks of the SeO_4 group are observed in the expected range as well. The ν_3 vibrations are found at lower frequencies than expected for the PO_4 group. The $\nu_4(f_2)$ $\delta(XY_3)$ vibrations of SO_4 group are very consistent for all compounds and located at the same energy ($600cm^{-1}$ and $673cm^{-1}$). However, there is splitting of these peaks for $NaFe(SO_4)_{1.5}(PO_3F)_{0.5}$ indicating local disorder on this site.

For the fluorophosphates doped sample, there was no trace of the expected ν(P-F) band in the region 700-$800cm^{-1}$ [182]. This may be an indication that the PO_3F^{2-} group has been hydrolysed during the synthesis leading to the formation of HPO_4^{2-} anion instead. In this regard, the overall similarity of the spectra for both HPO_4^{2-} and PO_3F^{2-} would support this suggestion. It also explains unexpected location of the ν_3 asymmetric vibrations for $NaFe(SO_4)_{1.5}(PO_3F)_{0.5}$ as such a region was reported for hydrophosphate compounds by Frost et. al.[183]. The similar cell parameters for the HPO_4^{2-} and PO_3F^{2-} doped samples would also support this, although there may still be the presence of small amount of residual fluorine.

An interesting additional band at around $515cm^{-1}$ is also observed for the doped samples. This peak is not present in the undoped system, and we suggest that it may be related to the asymmetry of FeO_6 caused by different anions generating extra vibrations in anion with undefined vibrational mode. The larger signal of this band on the IR spectra suggests that there is significant polarisation associated with this mode.

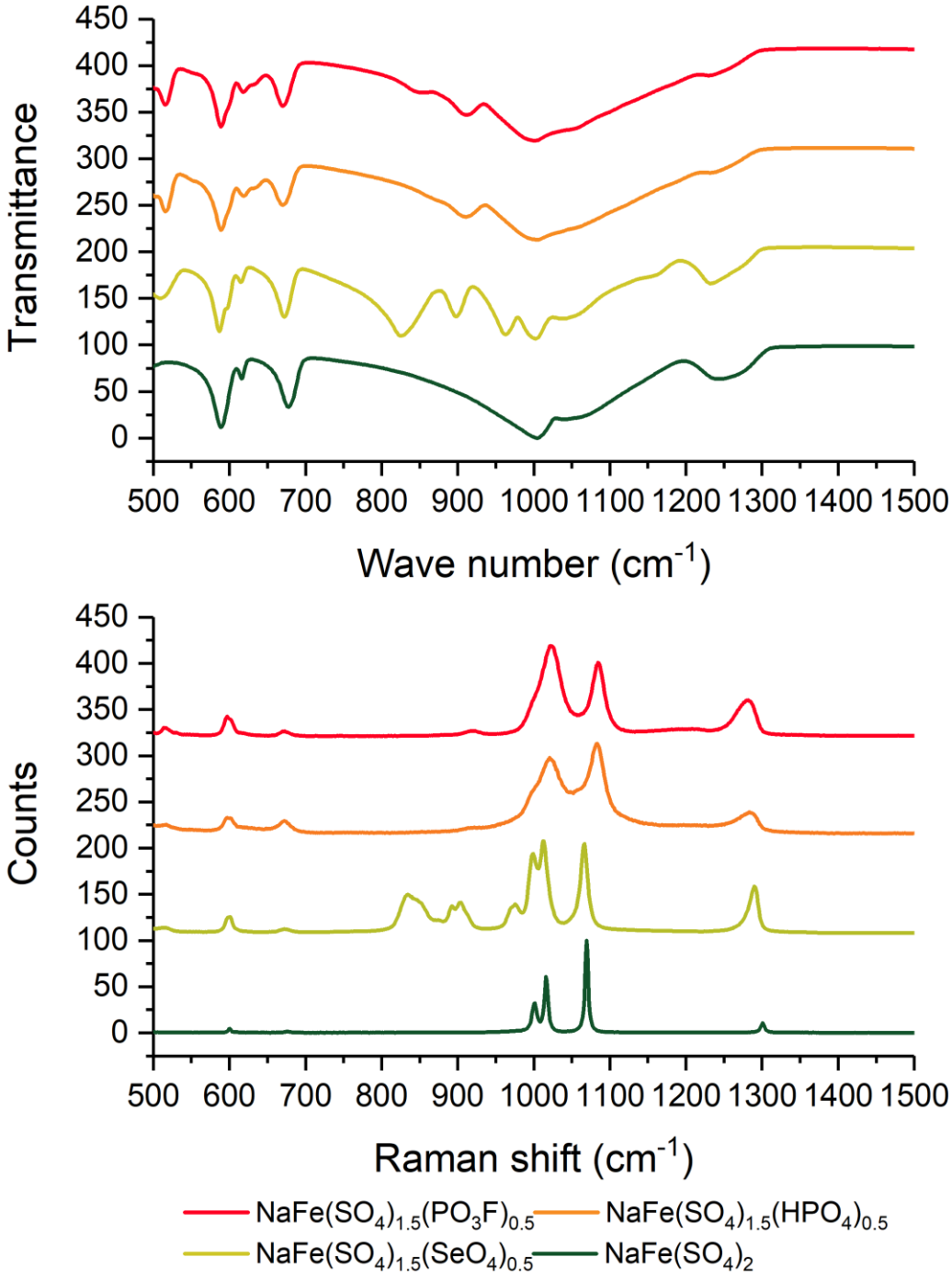

Figure 97. IR and Raman spectra of $NaFe(SO_4)_{1.5}(X)_{0.5}$ (X = SeO_4, HPO_4, PO_3F, SO_4)

Table 31. Assignments of the IR and Raman Spectra of $NaFe(SO_4)_{1.5}(X)_{0.5}$

Assignment	Band position, cm^{-1} (intensity)			
	$NaFe(SO_4)_3$	**$NaFe(SO_4)_{1.5}(SeO_4)_{0.5}$**	**$NaFe(SO_4)_{1.5}(HPO_4)_{0.5}$**	**$NaFe(SO_4)_{1.5}(PO_3F)_{0.5}$**
$\nu_1(a_1)$ $\nu_{sym}(XY_4)$	1000.8(30) (SO_4) 1016.4(60) (SO_4) 1069.6(100) (SO_4)	832.7(32) (SeO_4) 849.2(27) (SeO_4) 973.2(24) (SO_4) 998.4(71) (SO_4) 1013.1(86) (SO_4) 1066.2(94) (SO_4)	916.1(5) (PO_4) 999.7(18) (SO_4/PO_4) 1022.1(66) (SO_4/PO_4) 1059.5(18) (SO_4/PO_4) 1083.5(82) (SO_4/PO_4)	922.6(3) (PO_4) 914.8(3) (PO_4) 1010.3(46) (SO_4/PO_4) 1026.0(89) (SO_4/PO_4) 1084.5(75) (SO_4/PO_4)
$\nu_3(f_2)$ $\nu_{asym}(XY_4)$	1300.9(10) (SO_4)	874.3(4) (SeO_4) 891.8(16) (SeO_4) 904.5(28) (SeO_4) 1288.6(50) (SO_4)	1132.1(5) (PO_4) 1211.7(6) (PO_4) 1270.5(11) (SO_4) 1286.1(16) (SO_4)	1180.7(6) (PO_4) 1211.2(6) (PO_4) 1284.3(28) (SO_4) 1271.1(24) (SO_4)
$\nu_4(f_2)$ $\delta(XY_3)$	600.2(5) (SO_4) 676.5(1) (SO_4)	599.7(18) (SO_4) 672.9(3) (SO_4)	599.4(15) (SO_4) 672.1(12) (SO_4) 627.6(3) (PO_4)	596.2(16) (SO_4) 602.5(13) (SO_4) 672.5(5) (SO_4) 619.1(1) (PO_4)
Unknown		514.3(4)	516.3(5)	514.3(5) 519.4(5) 530.4(1)

Mössbauer spectroscopy

The ^{57}Fe Mössbauer spectra recorded at 298K are shown in Figure 98 and the ^{57}Fe Mössbauer parameters are collected in Table 32.

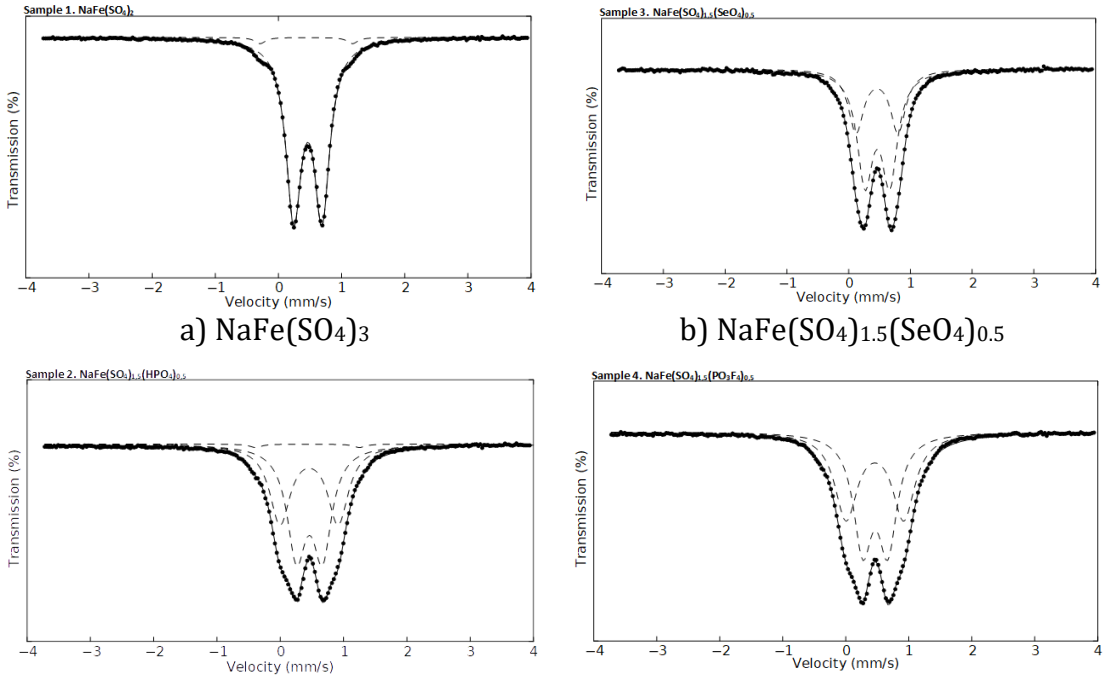

a) $NaFe(SO_4)_3$ b) $NaFe(SO_4)_{1.5}(SeO_4)_{0.5}$

c) $NaFe(SO_4)_{1.5}(HPO_4)_{0.5}$ d) $NaFe(SO_4)_{1.5}(PO_3F)_{0.5}$

Figure 98. Mössbauer spectra recorded at 298K of $NaFe(SO_4)_{1.5}(X)_{0.5}$ (X = SeO_4, HPO_4, PO_3F, SO_4)

We associate the small (<2%) components in the spectra recorded from $NaFe(SO_4)_2$ and $NaFe(SO_4)_{1.5}(HPO_4)_{0.5}$ with the presence of a small impurity phase which is below the limits of detection by X-ray powder diffraction. The chemical isomer shifts of all spectral components in all spectra were characteristic of Fe^{3+}. The values are at the higher end of the positive range expected for Fe^{3+} indicative of higher ionicity which is normal for iron sulphate compounds[184].

Table 32. ^{57}Fe Mössbauer parameters recorded from materials of composition $NaFe(SO_4)_{1.5}[X]_{0.5}$ X=SeO_4, HPO_4, PO_3F at 298K.

Compound	δ ±0.02(mms^{-1})	Δ ±0.04 (mms^{-1})	Area ±5%	Comment
$NaFe(SO_4)_2$	0,46	0,45	98	
	0,44	1,46	2	Impurity
$NaFe(SO_4)_{1.5}(SeO_4)_{0.5}$	0,46	0,40	64	
	0,46	0,68	36	
$NaFe(SO_4)_{1.5}(PO_3F)_{0.5}$	0,47	0,40	52	
	0,46	0,91	48	
$NaFe(SO_4)_{1.5}(HPO_4)_{0.5}$	0,46	0,41	55	
	0,45	0,92	44	
	0,43	1,64	1	Impurity

The spectrum recorded from $NaFe(SO_4)_2$ showed a single quadrupole split absorption with Δ= 0.45 mm/s which we attribute to Fe^{3+} coordinated to only SO_4 units. Similar sites were observed in the spectra recorded from the SeO_4^{2-}, HPO_4^{2-} and PO_3F^{2-} doped materials. However, the spectra recorded from these doped materials showed an additional doublet with larger quadrupole splitting indicative of the distorting effect of these substituents on the environment of the Fe^{3+} ions to which they are coordinated, by reason of their increased size and polarisabilty. The similar parameters recorded from the materials in which X= HPO_4 and PO_3F supports the evidence from Raman spectroscopy (see above) for hydrolysis of the fluorophosphate group to a hydrophosphate unit in $NaFe(SO_4)_{1.5}(PO_3F)_{0.5}$.

Scanning electron microscopy

The SEM images of obtained materials exhibit similar planar layered structures. All structures consist of crumbled platelets of agglomerated layers.

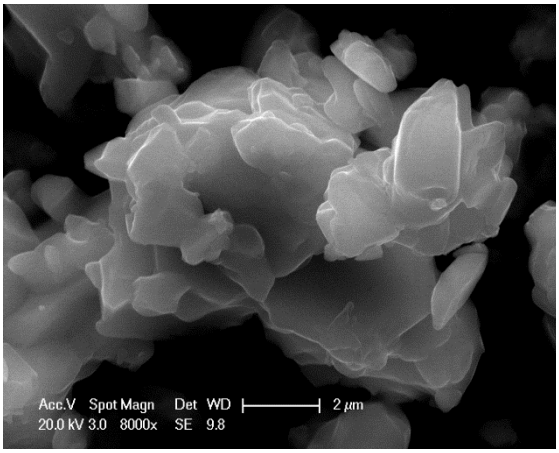

a) $NaFe(SO_4)_3$

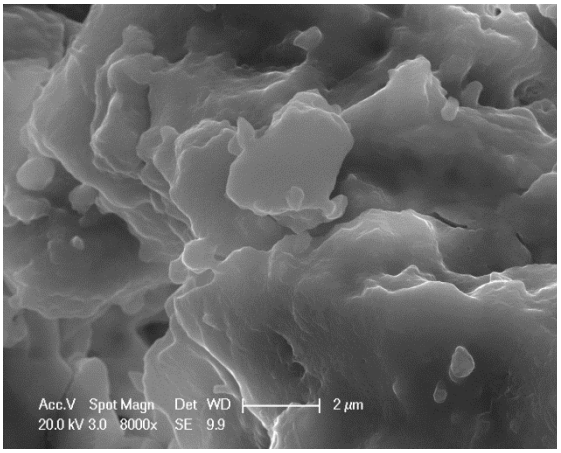

b) $NaFe(SO_4)_{1.5}(SeO_4)_{0.5}$

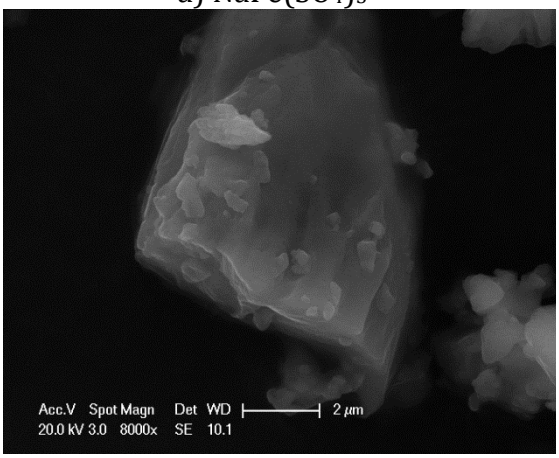

c) $NaFe(SO_4)_{1.5}(HPO_4)_{0.5}$

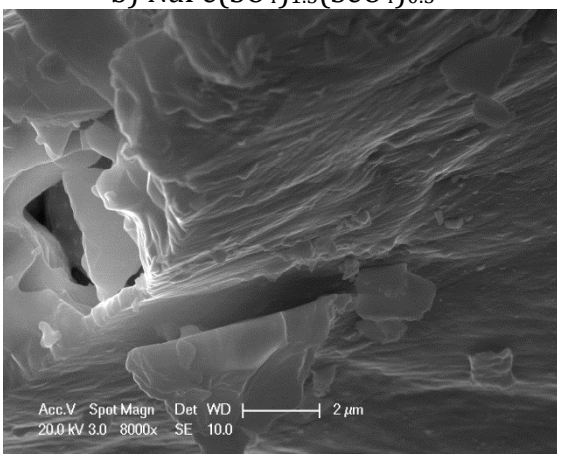

d) $NaFe(SO_4)_{1.5}(PO_3F)_{0.5}$

Figure 99. SEM images of $NaFe(SO_4)_{1.5}(X)_{0.5}$ (X = SeO_4, HPO_4, PO_3F, SO_4)

Thermogravimetric analysis

As was expected, all the synthesised compounds have relatively low decomposition temperatures (Figure 100). While undoped $NaFe(SO_4)_2$ is stable up to ~570°C, the doped materials are less thermally stable, as illustrated by weight losses above 350°C.

The peak m/z 64 corresponding to SO_2^+ appears only above 600°C in every case. Both hydrophosphate and fluorophosphate doped compounds decompose

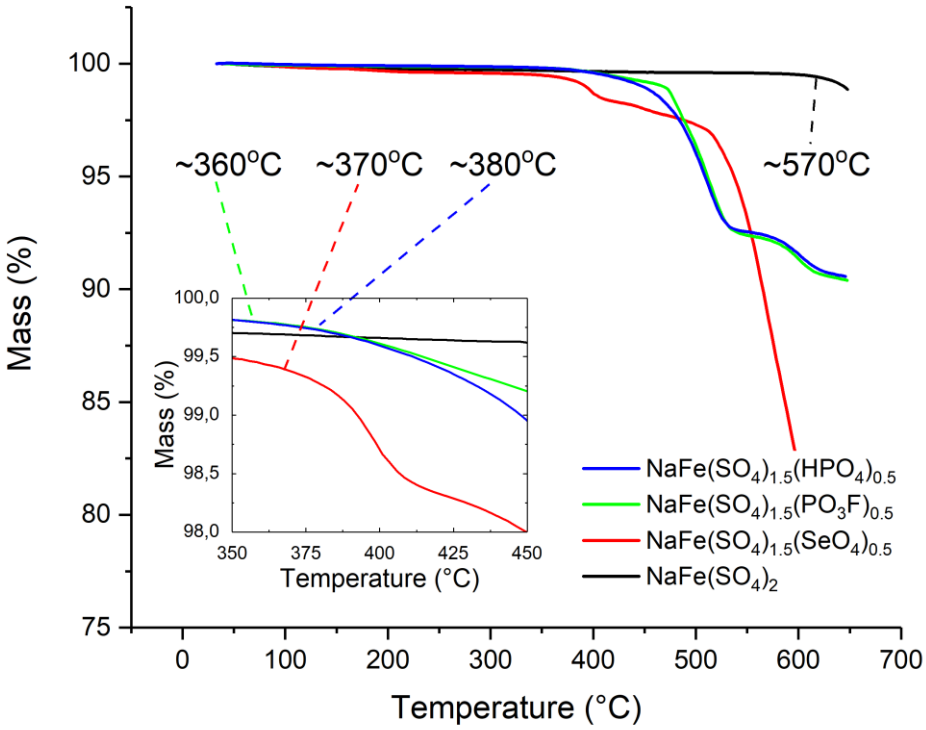

Figure 100. Thermogravimetric analysis data for $NaFe(SO_4)_{1.5}(X)_{0.5}$ (X = SeO_4, HPO_4, PO_3F, SO_4)

with significant water elimination, which can be correlated with a condensation of two hydrogenphosphate anion into a pyrophosphate anion. The fact that the data for the fluorophosphate doped compound are similar for the hydrogenphosphate doped compound, supports the hypothesis about the hydrolysis of the fluorophosphates group during the synthesis.

Ionic conductivity study

Conductivity measurements were performed on pellets sintered at 350°C. Overall density showed relatively high values (~75%) for such low temperature

sintering. Due to very low conductivity, the impedance data could not be resolved into bulk and grain boundaries and so total conductivity are reported (fitted with a single semi-circuit element (constant phase element with resistor in parallel)). To perform accurate evaluation of activation energy and minimise instrumental error due to very low conductivity of samples only data in the temperature region 150-300°C was used and room temperature conductivity values reported are extrapolated estimates (Figure 101).

Estimated room temperature conductivities for undoped and selenate doped samples were found to be very similar near 10^{-14} S/cm (Table 33). Therefore

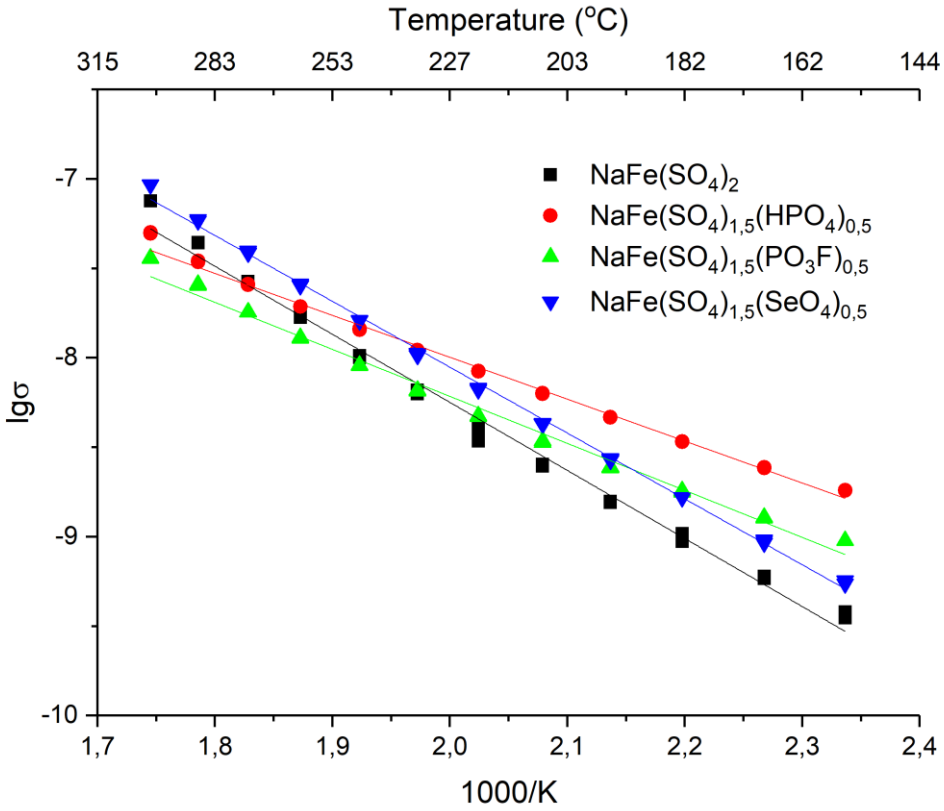

Figure 101. Conductivity Arrhenius plot for $NaFe(SO_4)_{1.5}(X)_{0.5}$ (X = SeO_4, HPO_4, PO_3F, SO_4)

diffusion coefficients showed similar values. Activation energies for both samples are around 0.74eV slightly higher than values calculated by Yu et al. (0.6eV)[55].

On the other hand, the estimated conductivities for the phosphate doped compounds were two orders of magnitude higher, along with a lower activation energy. Such a significant difference may be related to the presence of a proton in the crystal lattice and, therefore, the observed conductivity is mixed Na^+/H^+. Nearly equal parameters for the hydrophosphate and fluorophosphate doped samples once again suggest that fluorophosphate has apparently hydrolysed during the synthesis.

Table 33. Ion migration activation energy and diffusion coefficients at 293K for $NaFe(SO_4)_{1.5}(X)_{0.5}$ (X = SO_4, SeO_4, HPO_4, PO_3F)

Compound	Pellet density, (% of theor.)	σ_{293K} (S/cm)	D_{293K} (cm^2/s)	E_a (eV)
$NaFe(SO_4)_2$	71%	2.37×10^{-14}	5.53×10^{-19}	0.75(1)
$NaFe(SO_4)_{1.5}(SeO_4)_{0.5}$	76%	5.56×10^{-14}	1.32×10^{-18}	0.73(1)
$NaFe(SO_4)_{1.5}(PO_3F)_{0.5}$	75%	1.18×10^{-12}	2.76×10^{-17}	0.52(1)
$NaFe(SO_4)_{1.5}(HPO_4)_{0.5}$	77%	4.92×10^{-12}	1.15×10^{-16}	0.46(1)

Overall the ion diffusion is low in these systems. Such poor ion-diffusion behaviour for oxyanion compounds is not unusual. For example, commercially successful cathode material $LiFePO_4$ has very similar conductivity[20]. The key for such successful utilisation of these systems in batteries is an electron conductive additive (carbon) and minimisation of the powder particle size to reduce ion diffusion path lengths.

Conclusion

The work presented in this chapter shows that anion doping can be successfully applied for modification of the eldfellite materials. Hydrophosphate and selenate was incorporated in to the structure. Structure suggests that ionic mobility could be inhibited for doped phases due to contraction of the ion transport pathways. Conductivity measurements however do not reveal any significant difference between samples. It was noted that fluorophosphate anion hydrolyses in this synthesis route. The further work is needed to evaluate electrochemical performance of obtained materials in batteries.

Chapter Eight

Synthesis and structure of mixed K/Na containing langbeinite phosphates

$K_{2-x}Na_x(Ti/V)_2(PO_4)_3$

Alkali metal containing transition metal phosphates with general formula $M_x(Ti/V)_2(PO_4)_3$ have been shown to have promising properties for alkali ion batteries. The structure they adopt depends on the nature of the alkali metal M. $K_xTi_2(PO_4)_3$ ($1<x<2$) forms a cubic crystal lattice with a langbeinite framework[185]. In contrast, the Na and Rb containing compounds crystallize with a NASICON framework[186,187]. The Cs containing compounds form a complex garnet framework[188]. For compositions where two alkali metals are present per formula unit, the transition metal in these phosphates has mixed valency. Thus $K_2Ti_2(PO_4)_3$

was shown to contain both Ti^{3+} and Ti^{4+} for charge balance[189]. A similar situation is observed for V containing phosphates.

Apart from potential applications in batteries, the high chemical and thermal stability of phosphate systems provides the possibility to utilise langbeinite compounds in nuclear waste disposal[186]. There have been also reports of using these phosphates for their luminescence[190], while $NaTi_2(PO_4)_3$ systems have been widely investigated as a potential cathode material for sodium ion batteries[191–193]. Considering the low cost of K and its ability to intercalate into graphite, there is growing interest in similar K containing compounds for K ion batteries[194,195]. Studies by Tarascon et al.[156] have showed that a sulphate langbeinite structured material can potentially be used in rechargeable batteries albeit the performance was rather limited. It was proposed that the lack of connecting tunnels between isolated cavities in the langbeinite structure inhibits ionic transport for alkali ions. However, modification of the composition could potentially stabilise other structures to alter the ionic transport for these K rich compounds. For example, some studies of this system showed the possibility for the accommodation of Na ions in the langbeinite systems for $K_2Ti_2(PO_4)_3$ with the formation of vacancies on alkali ion site[142,196]. However the absence of detailed investigation of these systems related to framework formation dependencies inhibits further development of such materials. In this chapter we report initial structural findings on new potential electrode materials for K/Na-ion batteries based on mixed $Ti^{4+}/(V^{3+}/Ti^{3+})$ phosphates.

Experimental

$K_{2-x}Na_xTi_2(PO_4)_3$ and $K_{2-x}Na_xTiV(PO_4)_3$ samples were prepared via the solid-state route. Stoichiometric amounts of K_2HPO_4, Na_2HPO_4, TiO_2, Ti_2O_3/V_2O_3 and $NH_4H_2PO_4$ (for 3g of sample) were mixed and heated at 350°C for 8 hours in N_2 atmosphere. The powders were then reground in a planetary ball mill, pressed into pellets and sintered at 850°C in a N_2 atmosphere for 8 hours. The ball milling and sintering procedures were then repeated until phase pure samples were achieved. The resulting samples were then examined using X-ray diffraction with a Panalytical Empyrean diffractometer in Bragg-Brentano reflection geometry with Cu X-rays, ($\lambda_{CuK\alpha1}$ = 1.54056 Å, $\lambda_{CuK\alpha2}$ = 1.54439 Å) equipped with a Pixcel 2D detector in the range from 15 to 145°. Using these data, the lattice parameters were refined by the Rietveld method in GSASII software[103]. In order to obtain more information on potential Ti/V ordering, time of flight powder neutron diffraction (TOF) data were collected for one sample ($K_{1.5}Na_{0.5}TiV(PO_4)_3$) on the POLARIS diffractometer at the ISIS pulsed spallation source (Rutherford Appleton Laboratory, Harwell, UK). 3 g of powder was loaded into 8 mm diameter thin-walled cylindrical vanadium sample cans, and data were collected at room temperature for 150μAh proton beam energy to the ISIS target. Structure refinements of the neutron TOF data were performed using the Rietveld method with the program TOPAS.

Further structure determination was performed using single crystal X-ray diffraction. For these experiments small single crystals were picked from the prepared powder sample, mounted on glass fibre and diffraction data were

collected on an Agilent SuperNova diffractometer using an Atlas detector. The crystals were kept at 100K during data collection using an Oxford Cryosystems Cryostream. Using Olex2 software[123], the structure was solved with the ShelXT[124] structure solution program using Intrinsic Phasing, and further refined with the ShelXL[125] refinement package using a least squares approach.

Results and discussion

$K_{2-x}Na_xTi_2(PO_4)_3$ system

A range of samples with composition $K_{2-x}Na_xTi_2(PO_4)_3$, where $0<x<2$, was synthesised. A three-stage ball-milling-heating process was required to eliminate impurity phases consisting of K or Na pyrophosphates. XRD analysis show that the langbeinite structure is observed up to the K:Na ratio of 1.1:0.9 (Figure 102). Above this level the amount of NASICON type ($(Na/K)_2Ti_2(PO_4)_3$) impurity becomes significant.

Rietveld refinement was performed for these phases in order to clarify the structure and occupancy of the alkali metal sites (Figure A9, Appendix). The determination of the phase fraction of langbeinite from structural refinement allows us to determine that a pure langbeinite phase can be synthesized only up to $x \approx 0.87$, although cell parameter data suggest this range may be lower, and so there may be another impurity present. Cell parameters and goodness-of-fit indexes are given in table 34. The refinement of Na/K site occupancies was performed with the total sum per site constrained to 1.

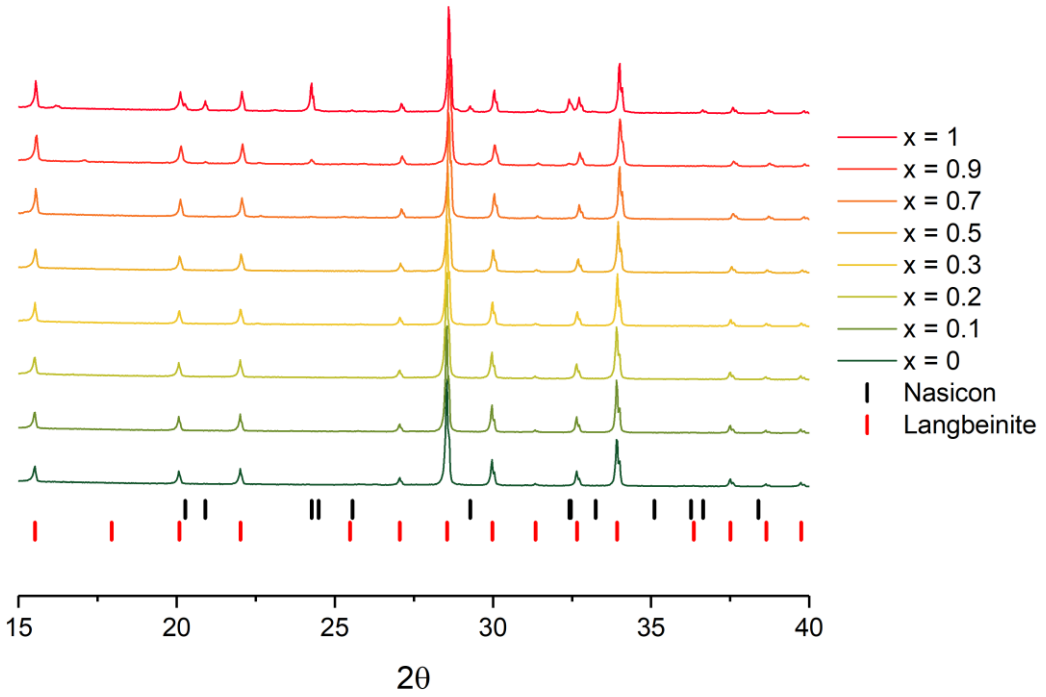

Figure 102. XRD patterns for $K_{2-x}Na_xTi_2(PO_4)_3$ for $0 \leq x \leq 1$.

Table 34. Lattice parameters for $K_{2-x}Na_xTi_2(PO_4)_3$ for $0 \leq x \leq 1$. K content given (Na content = 1 – K content).

x	*a*,Å	Volume,Å^3	K1 occ	K2 occ	K_{total}	GOF	R_{wp}
0	9.8771(1)	963.569(17)	1	1	2	1.84	4.43
0.1	9.8777(1)	963.763(7)	1.023(21)	0.865(21)	1.888	1.589	3.814
0.2	9.8777(1)	963.763(9)	1.003(23)	0.874(23)	1.877	1.683	4.011
0.3	9.8724(1)	962.208(7)	0.979(21)	0.770(22)	1.749	1.558	3.759
0.5	9.8675(1)	960.769(9)	0.894(22)	0.691(21)	1.585	1.497	3.509
0.7	9.8533(1)	956.624(9)	0.800(23)	0.617(22)	1.417	1.531	3.663
0.9	9.8498(1)	955.608(15)	0.690(26)	0.522(26)	1.212	1.634	3.768
1	9.8536(1)	956.712(13)	0.514(25)	0.737(31)	1.252	1.971	4.621

These cell parameter data show an interesting behaviour with varying sodium content (Figure 103). In particular, negligible change is observed until x=0.2

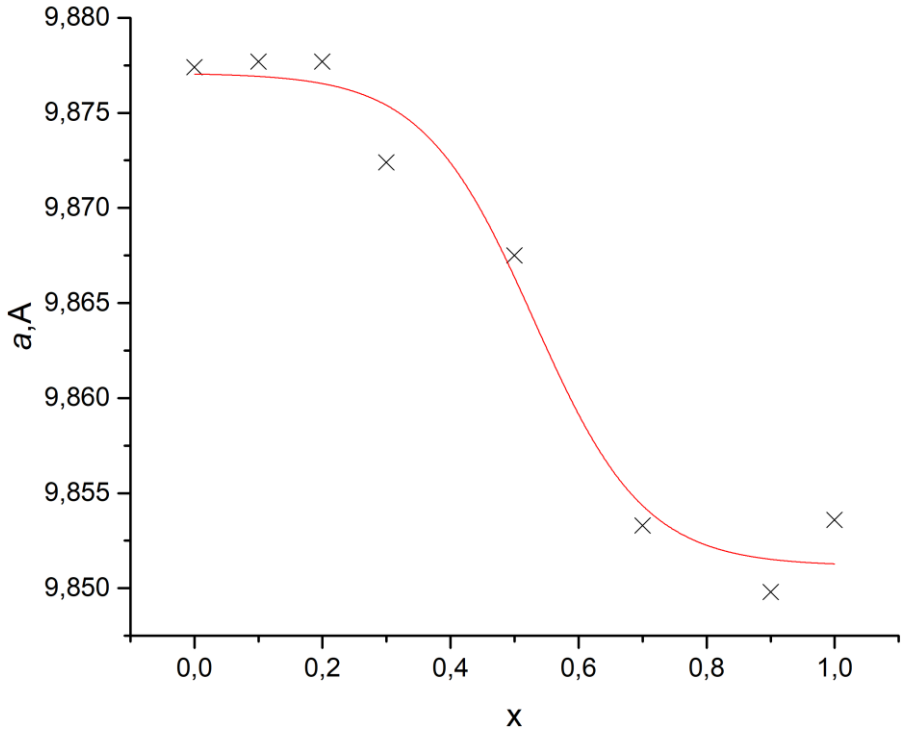

Figure 103. Cell parameter *a* vs Na content for $K_{2-x}Na_xTi_2(PO_4)_3$ for $0 \leq x \leq 1$

(9.878Å) with then the expected decrease up to x=0.7, where the cell parameters level out again (average 9.853Å).

As noted above, the alkali metal site occupancies were refined assuming the total K and Na content equal to 1 per site. These data show an approximate linear dependence up to $x \approx 0.8$. The occupancy for total K has linear dependence up to x=0.9($K \approx 1.1$) (Figure 104).

From the site occupancy variation it appears that there is a preference for sodium to go to the site 2 which is the smaller cavity of langbeinite structure (Figure 104), as might be expected. At lower levels, up to x = 0.2, the K1 site appears to be

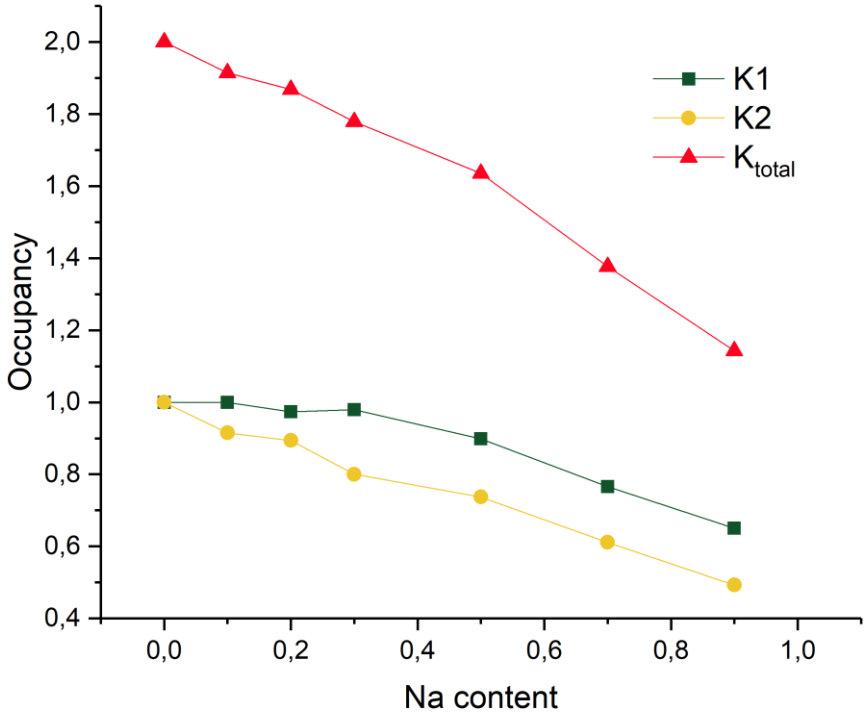

Figure 104. Potassium site occupancies for $K_{2-x}Na_xTi_2(PO_4)_3$ for $0 \leq x \leq 1$ (Na site occupancy = 1 – K site occupancy)

fully occupied by K, with some evidence for Na incorporation on this site above this level, which might account for the unusual initial lack of change in cell parameters up to x = 0.2.

To maintain the charge balance in this compound the Ti is mixed valence, +3 and +4. The langbeinite structure has two crystallographic sites for transition metal and, therefore, Ti with two oxidation stages can potentially be ordered across them. In particular, there is a significant difference between the ionic radii of Ti^{4+}(0.61Å) and Ti^{3+}(0.67Å).

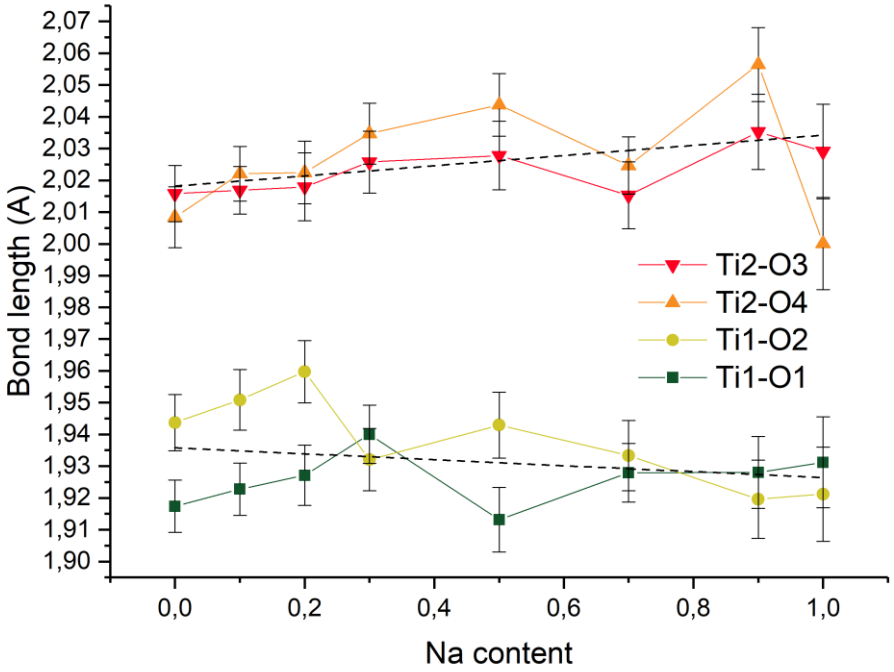

Figure 105. Bond lengths of TiO_6 units for $K_{2-x}Na_xTi_2(PO_4)_3$ for $0 \leq x \leq 1$

From the structural data the size of the $Ti(2)O_6$ (average bond length is 2.025Å) octahedra is larger than for $Ti(1)O_6$ (average bond length is 1.932Å). Considering this fact, we can suggest that the larger octahedra is occupied mostly by Ti^{3+} and smaller octahedra by Ti^{4+}. The larger octahedra (Ti^{3+}) is mostly surrounding the K favoured site, while the smaller octahedra (Ti^{4+}) in general is closer to the Na favoured site. The difference between the sizes of the octahedra becomes more significant with the rise of Na content (Figure 105), which could be related to changes in the ordering of the Ti^{3+}/Ti^{4+} in the lattice. However, further work is required to conclusively confirm this proposed Ti^{3+}/Ti^{4+} ordering in this structure.

$K_{2-x}Na_xTiV(PO_4)_3$ system

The study of samples with general formula $K_{2-x}Na_xTiV(PO_4)_3$ where $0<x<2$ showed that up to x = 0.6, a pure langbeinite phase could be synthesized, while above this Na level, NASICON type impurity starts to appear (Figure 106). As for the Ti only system, a third ball-milling stage was required to eliminate Na and K pyrophosphate impurities. Moreover in this system the temperature regime is important for phase formation. The experiments show that the NASICON phase requires lower heating temperature to be formed (700°C). Going above this temperature leads to a partial decomposition of the phase giving a complex mixture.

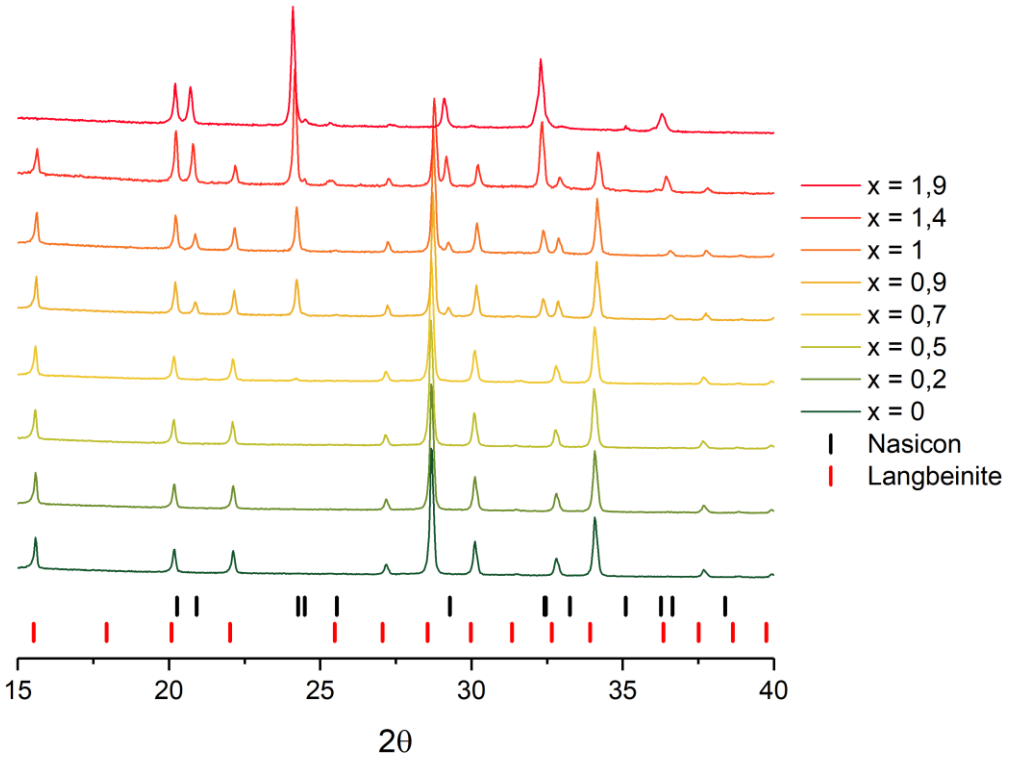

Figure 106. XRD patterns for $K_{2-x}Na_xTiV(PO_4)_3$ for $0 \leq x \leq 2$.

The transition from langbeinite to NASICON with change from K to Na happens without the formation of intermediate phases.

Table 35. Lattice parameters for $K_{2-x}Na_xTiV(PO_4)_3$ for 0 ≤ x ≤ 1. K content given (Na content = 1 – K content).

x	*a*,Å	Volume,Å^3	K1 occ	K2 occ	K_{total}	GOF	R_{wp}
0	9,8334(1)	950.847(34)	1	1	2	1,56	3,73
0,2	9,8350(1)	951.316(35)	0,993(31)	0,790(32)	1,783	1,53	3,7
0,5	9,8383(1)	952.277(38)	0,824(33)	0,678(35)	1,502	1,58	3,83
0,7	9,8344(1)	951.144(41)	0,856(34)	0,444(40)	1,300	1,63	3,87
0,9	9,8154(1)	945.635(38)	0,967(41)	0,635(41)	1,602	1,99	4,67
1	9,8116(1)	944.547(39)	0,909(40)	0,546(37)	1,455	1,4	3,31

Surprisingly the cell parameters of the langbeinite phase in the range 0 ≤ x ≤ 1 (Table 35) remain relatively constant, and decreases significantly above x

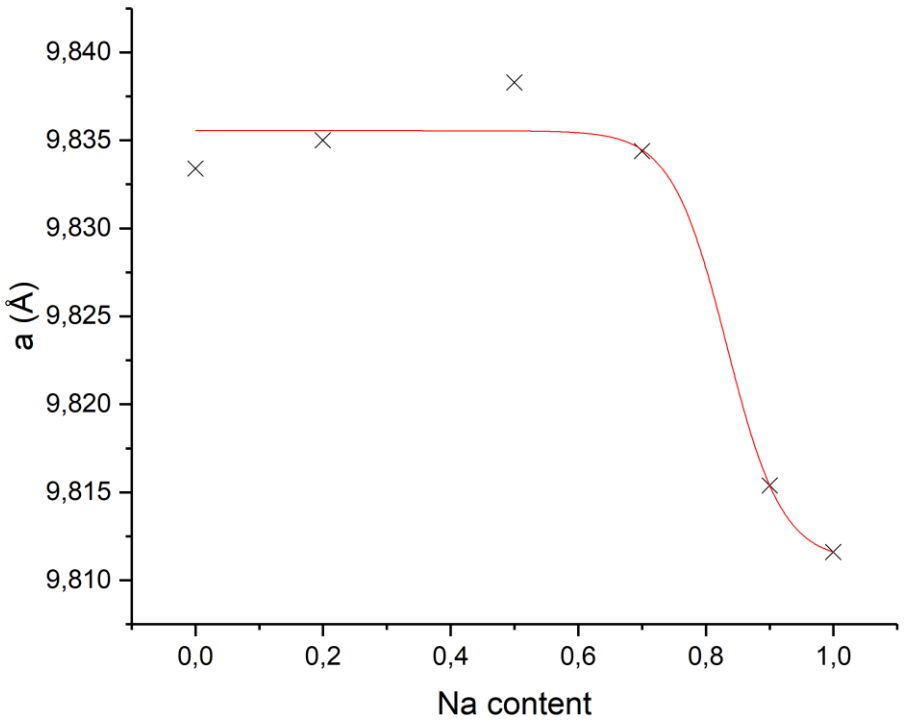

Figure 107. Cell parameter *a* vs Na content for $K_{2-x}Na_xTiV(PO_4)_3$ for 0 ≤ x ≤ 1

= 0.7 before reaching a plateau at x = 1 (Figure 107). Interestingly, the refined potassium site occupancies decrease linearly until x = 0.7, which appears to confirm incorporation of Na, although the cell parameter data do not show the expected linear decrease. Such behaviour of the langbeinite lattice may be explained by rotation of PO_4 tetrahedra causing cell expansion, which balances the contraction caused by presence of the smaller Na ions in the cavity. A similar process is observed for materials which exhibit negative thermal expansion[197]. Above x = 0.6, the formation of a NASICON type phase starts to occur. The decrease in cell parameters for the langbeinite phase corresponds to this beginning of the formation of the NASICON phase. However, it does not explain why after formation of the NASICON phase, the cell parameters for the langbeinite structure change, if the extra Na is going to form the NASICON second phase. The explanation may be rather simple. In particular, the formation of the V rich langbeinite could explain such a step-like change as the vanadium ion is smaller than titanium and, therefore, should form smaller structures. In this case it could mean that the NASICON formed is titanium rich.

There are two sites in the langbeinite structure for alkali ions. The Rietveld refinement (Figure A10, Appendix) shows that potassium has a preference to occupy the larger cavity (K1) (Figure 109) with Na occupying the smaller site as expected. The similar behaviour was observed for $K_{2-x}Na_xMg_2(SO_4)_3$ (see Chapter Six) and $K_{2-x}Na_xTi_2(PO_4)_3$ (see above).

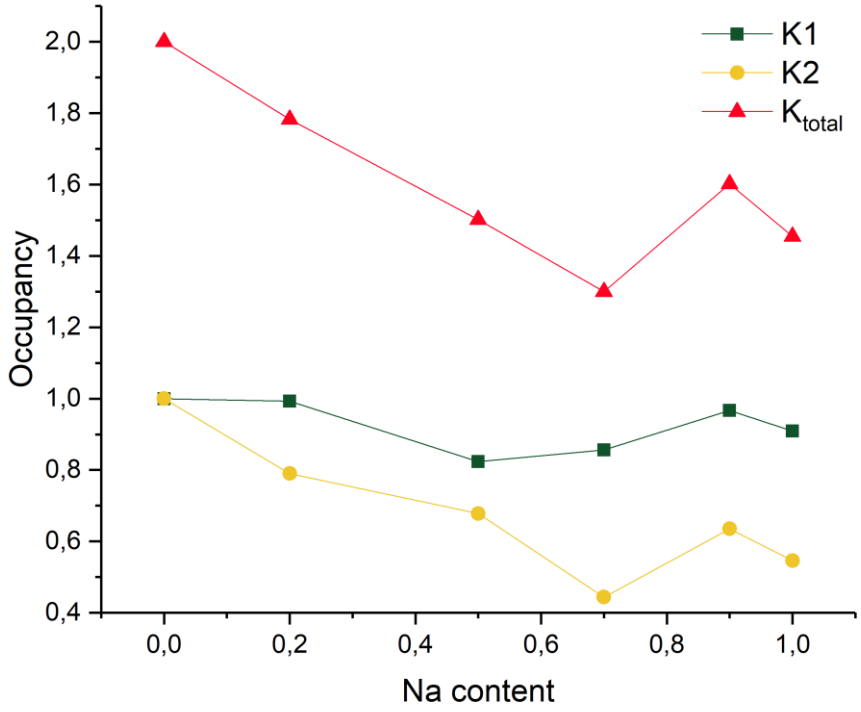

Figure 109. Potassium occupancies for $K_{2-x}Na_xTiV(PO_4)_3$ for $0 \leq x \leq 1$

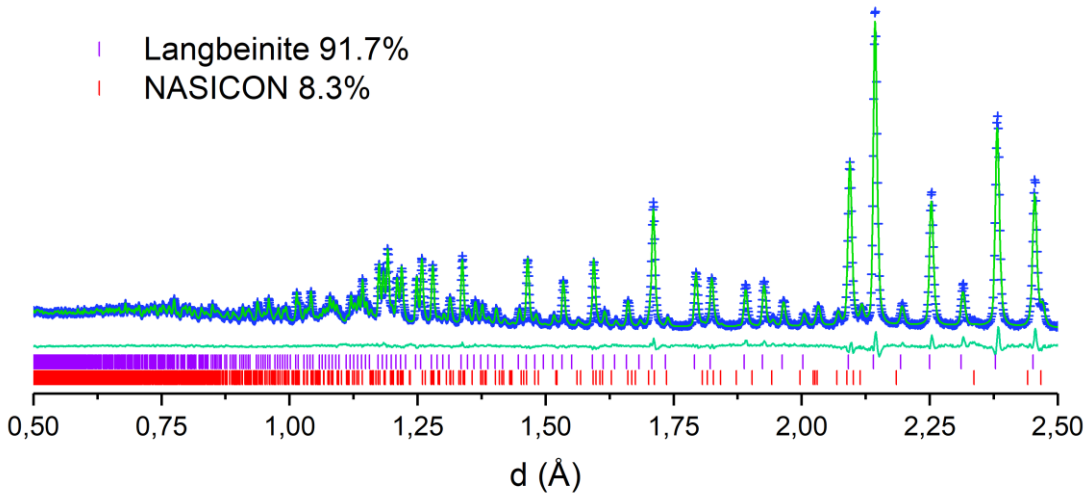

Figure 108. Plot for structural Rietveld refinement of ND data for $K_{1.5}Na_{0.5}TiV(PO_4)_3$, R_{wp}=1.57, GOF = 1.64

The potential ordering of V and Ti between two sites was investigated in a neutron diffraction experiment at the ISIS facility using POLARIS diffractometer. Following structure refinement it was found that the sample had an impurity of NASICON phase (8.3 wt.%) (Figure 108). From the structure refinement there was no strong evidence for V/Ti ordering in this phase (Table 36). At the same time the impurity NASICON phase appeared to be titanium rich. Indirectly this observation supports the idea that there is some partitioning of Ti and V between NASICON and langbeinite phases. Thus it appears that titanium prefers formation of a NASICON type phase. Further investigations on this system are required to fully rationalise this.

In order to gain further structural information a single crystal experiment was performed on crystals extracted from a higher Na content sample mixture. Interesting results were obtained for a sample with general composition $K_{0.5}Na_{1.5}TiV(PO_4)_3$. Powder XRD showed the presence of two phases: langbeinite and NASICON. The crystal extracted from the sample mixture demonstrated trigonal symmetry, indicating it was NASICON-type. The results and the main refinement indices for this crystal are presented in table 37.

Table 36. Structural parameters obtained for $K_{1.5}Na_{0.5}TiV(PO_4)_3$ ND data

Atom	Site multiplicity	x	y	z	Fractional occupancy	U_{eq}×100(Å²)
Ti1	4	0.8574(5)	0.8574(5)	0.8574(5)	0.411(16)	0.58(7)
V1	4	0.8574(5)	0.8574(5)	0.8574(5)	0.589(16)	0.58(7)
Ti2	4	0.5870(4)	0.5870(4)	0.5870(4)	0.589(16)	0.76(7)
V2	4	0.5870(4)	0.5870(4)	0.5870(4)	0.411(16)	0.76(7)
K1	4	0.2924(5)	0.2924(5)	0.2924(5)	1	3.46(18)
Na1	4	0.2924(5)	0.2924(5)	0.2924(5)	0	3.46(18)
Na2	4	0.0674(4)	0.0674(4)	0.0674(4)	0.25	3.30(16)
K2	4	0.0674(4)	0.0674(4)	0.0674(4)	0.75	3.30(16)
P1	12	0.6274(2)	0.4581(2)	0.2733(2)	1	0.69(5)
O1	12	0.6481(2)	0.5020(2)	0.4184(2)	1	1.93(7)
O2	12	0.7594(2)	0.4793(2)	0.1954(2)	1	2.28(6)
O3	12	0.5800(2)	0.3093(2)	0.2657(2)	1	1.83(5)
O4	12	0.5194(2)	0.5458(2)	0.2031(2)	1	2.14(7)

Table 37. Crystal data and structure refinement for $K_{0.5}Na_{1.5}TiV(PO_4)_3$.

Empirical formula	$Na_{2.39}O_{12}P_3Ti_{1.63}$
Formula weight	418.24
Temperature/K	100.01(10)
Crystal system	trigonal
Space group	R-3c
a/Å	8.5462(7)
b/Å	8.5462(7)
c/Å	21.4371(17)
α/°	90
β/°	90
γ/°	120
Volume/Å^3	1355.9(2)
Z	6
ρ_{calc} / g/cm^3	3.073
μ/mm^{-1}	19.476
F(000)	1220.0
Crystal size/mm^3	0.052 × 0.046 × 0.038
Radiation	CuKα (λ = 1.54184)
2Θ range for data collection/°	14.544 to 149.256
Index ranges	-7 ≤ h ≤ 8, -9 ≤ k ≤ 10, -25 ≤ l ≤ 17
Reflections collected	812
Independent reflections	307 [R_{int} = 0.0102, R_{sigma} = 0.0112]
Data/restraints/parameters	307/0/38
Goodness-of-fit on F^2	1.066
Final R indexes [I>=2σ (I)]	R_1 = 0.0265, wR_2 = 0.0729
Final R indexes [all data]	R_1 = 0.0270, wR_2 = 0.0733
Largest diff. peak/hole / eÅ^{-3}	0.47/-0.46

The low R_1 (2.65%) confirms that the model structure corresponds well to the studied sample. The difficult part of this refinement is the potential simultaneous presence of Na and K ions on the same site, where this site is not fully occupied and hence there is uncertainty in the amount of alkali ions in the cell. This introduces undefinable correlations between the total amount of alkali ions and their distribution between two crystallographic sites. Moreover, the very different nature

of these sites does not allow us to constrain values for the Na/K ratio between them. Another issue is a presence of vanadium and titanium ions with unknown charge in the crystal lattice and, therefore, regular charge balance refinement strategies cannot be applied. Therefore, in order to stabilise the refinement only one alkali metal (Na) was initially introduced and the occupancies were freely varied. In this refinement the mixed Ti/V site was refined as containing only Ti (as the scattering factors are very similar). The structural parameters obtained in this refinement are presented in tables 38-39.

Table 38. Fractional Atomic Coordinates and Equivalent Isotropic Displacement Parameters ($Å^2$×100) for $K_{0.5}Na_{1.5}TiV(PO_4)_3$. U_{eq} is defined as 1/3 of the trace of the orthogonalised U_{IJ} tensor.

Atom	x	y	z	Occupancy	U(eq)
Ti1	0.6667	0.3333	0.6873(1)	0.818(5)	1.12(4)
P1	0.3773(1)	0.3333	0.5833(1)	1	1.34(4)
Na1	0	0	0.5	0.960(17)	6.6(2)
Na2	0.3023(3)	-0.0310(3)	0.5833(1)	0.478(10)	2.42(14)
O1	0.1898(2)	0.1654(2)	0.5886(1)	1	1.70(5)
O2	0.4920(3)	0.3602(3)	0.6411(1)	1	2.36(5)

Table 39. Anisotropic Displacement Parameters ($Å^2$×100) for $K_{0.5}Na_{1.5}TiV(PO_4)_3$. The Anisotropic displacement factor exponent takes the form: $-2\pi^2[h^2a^{*2}U_{11}+2hka^*b^*U_{12}+...]$.

Atom	U_{11}	U_{22}	U_{33}	U_{23}	U_{13}	U_{12}
Ti1	1.21(4)	1.21(4)	0.94(6)	0	0	0.61(2)
P1	1.26(4)	1.34(5)	1.44(5)	0.19(3)	0.093(15)	0.67(3)
Na1	9.3(3)	9.3(3)	1.14(18)	0	0	4.64(14)
Na2	1.37(15)	1.37(15)	4.4(2)	-0.49(7)	0.49(7)	0.62(14)
O1	1.50(9)	1.55(9)	1.83(9)	0.05(7)	0.04(7)	0.61(7)
O2	2.21(10)	2.23(10)	2.60(10)	-0.04(8)	-0.83(8)	1.08(8)

The total refined Na content was larger than 2 most likely indicating the partial substitution of Na with K, which has higher X-ray scattering factor (around 2

times). However, the interesting observation was that the Ti site demonstrated some evidence of cation vacancies (around 20%). Since the V and Ti have very similar scattering factors, this cannot be explained by simply the presence of both V and Ti on this site. The potential partial substitution of Ti/V with Na/K also does not seem to be feasible as this would entail significant enlargement of the enlarge Ti-O octahedral bond length (Table 40), or at least generate significant increase in oxygen thermal ellipsoids indicating the increased disorder. Both are not observed. Also the attempt to introduce some Na onto the titanium site in the refinement did not give any sensible solution.

Table 40. Bond Lengths for $K_{0.5}Na_{1.5}TiV(PO_4)_3$.

Atom	Atom	Length/Å	Atom	Atom	Length/Å
Ti1	Na1[1]	3.1315(9)	Na1	Na2[10]	3.2590(11)
Ti1	Na2[2]	3.0396(12)	Na1	Na2[11]	3.2590(11)
Ti1	Na2[3]	3.0396(13)	Na1	Na2	3.2590(11)
Ti1	Na2[4]	3.0397(12)	Na1	O1[9]	2.4376(17)
Ti1	O1[2]	1.9641(19)	Na1	O1	2.4375(17)
Ti1	O1[3]	1.9641(19)	Na1	O1[12]	2.4376(17)
Ti1	O1[4]	1.9641(19)	Na1	O1[10]	2.4376(17)
Ti1	O2	1.8981(19)	Na1	O1[11]	2.4376(17)
Ti1	O2[5]	1.8980(19)	Na1	O1[7]	2.4376(17)
Ti1	O2[6]	1.898(2)	Na2	O1[13]	2.421(3)
P1	Na2[7]	2.959(3)	Na2	O1[9]	2.421(3)
P1	Na2[6]	2.848(2)	Na2	O1	2.3171(19)
P1	Na2	2.848(2)	Na2	O1[14]	2.3171(19)
P1	O1[8]	1.5293(19)	Na2	O2[15]	2.584(2)
P1	O1	1.5293(19)	Na2	O2[5]	2.789(3)
P1	O2[8]	1.5242(19)	Na2	O2[4]	2.584(2)
P1	O2	1.5241(19)	Na2	O2[8]	2.789(3)
Na1	Na2[9]	3.2590(11)			

[1]2/3+X,1/3+Y,1/3+Z; [2]2/3+Y,1/3-X+Y,4/3-Z; [3]2/3-Y+X,1/3+X,4/3-Z; [4]2/3-X,1/3-Y,4/3-Z; [5]1-Y,+X-Y,+Z; [6]1+Y-X,1-X,+Z; [7]-Y,+X-Y,+Z; [8]1/3-Y+X,2/3-Y,7/6-Z; [9]+Y-X,-X,+Z; [10]-Y+X,+X,1-Z; [11]-X,-Y,1-Z; [12]+Y,-X+Y,1-Z; [13]1/3-X,-1/3-X+Y,7/6-Z; [14]1/3+Y,-1/3+X,7/6-Z; [15]2/3-Y,1/3-X,-1/6+Z

Therefore we believe that there is a Ti deficiency and hence the generation of vacancies on the octahedral site, which requires further study by investigating more single crystals with similar composition.

Overall, the range of $K_{2-x}Na_xTiV(PO_4)_3$ $0 \leq x \leq 1$ appears to be rather complex. The XRD patterns suggest the formation of a solid solution with a transition from langbeinite into NASICON and indeed there is some evidence for this happening near the limits of the range. However, the crystallographic data suggests partitioning of ions between phases in the transition region. This causes formation of phases with different stoichiometry but with the same structure. These phases can have interesting properties related to the ionic conduction/electrode performance. Further work to investigate these properties is required.

Conclusion

In this chapter were presented preliminary findings on the investigation of V/Ti containing langbeinite systems. The transition of the langbeinite structure into NASICON was shown to occur as the Na content was increased above a certain value. As expected, the K rich samples exhibit langbeinite structure, while the Na rich samples lead to a NASICON structure. There appeared to be lower solubility of Na in the langbeinite phase for systems containing only Ti on the octahedral site.

Chapter Nine

Conclusions and future work

The work described in this thesis was performed to investigate a range of materials of relevance to Li/Na ion batteries. With further advances being sought in Li-ion technology, the scientific community is looking for new materials to provide further battery development. For Li-ion batteries, there is considerable research focused on ceramic electrolytes as a safer and more stable alternative to conventional liquid electrolytes. For Na-ion batteries, research is aimed at finding the best materials to use in both electrode and electrolyte areas. This work combined the modification of known materials with the discovery of new structural frameworks.

In Chapter Three, an attempt was made to improve the total conductivity of lithium lanthanum titanate perovskite (LLTO) with the addition of boron or silicon. However, the crystallography study did not provide conclusive confirmation of

incorporation of boron or silicon into LLTO lattice. Small changes of the cell parameters were observed and most likely attributed to a small change of the Li/La ratio. There was no significant change of the ionic conductivity, even though the sinterability of the pellets with these additions increased noticeably. The absence of the resulting higher density having a positive effect on the conductivity is most likely related to the formation of a thin lithium silicate/borate layer, with higher resistivity, on the surface of the grain.

In Chapter Four, sodium doped garnet materials with general formula $Li_{5+2x}La_{3-x}Na_x(Nb/Ta)_2O_{12}$ (x = 0, 0.2, 0.4) were successfully synthesized. However, Rietveld refinement suggested that only a limited amount of Na can be incorporated onto the La site. Furthermore, the conductivity of the obtained materials was found to be lower than that of the undoped phase, attributed to the partial incorporation of Na onto the Li site, where it blocks the channels. A similar experiment on mixed Ta/Zr and Nb/Zr garnets suggests that the presence of Zr suppresses the accommodation of Na in the structure. However, these systems showed some evidence of having stable La deficient sites. To investigate Li rich garnets, a new compound $Li_7LaSr_2Nb_2O_{12}$ was synthesized. This showed tetragonal symmetry with Li ordering. The by-product of this synthesis, $Li_{6.63}La_{1.35}Sr_{1.65}Nb_2O_{12}$ with cubic symmetry showed partially occupied Li sites with Li being evenly distributed over these sites. The tetragonal phase has a lower conductivity than the cubic as a result of the ordering of the Li ions.

The Na-doped samples are currently being studied by the Karen Johnston group (based at Durham University) in order to investigate the local Na

environment via multinuclear solid-state NMR spectroscopy. The ^{23}Na EXSY NMR confirmed a lack of Na-ion mobility therefore confirming that there is only one ionic charge carrier within the system – the Li-ion. Further, preliminary experiments suggest that Na is occupying multiple sites within the structure including octahedral sites, providing support for the conclusion that Na-ions block the Li-ion pathways.

In Chapter Five, a detailed VTXRD, single crystal and Raman spectroscopy study was performed to investigate the very complex phase transitions of a novel $Na_2Mg_2(SO_4)_3$ system. It was shown that a single phase can be only prepared by quenching the sample from high temperature, as otherwise the system decomposes into a mixture of $Na_2Mg(SO_4)_2$ and $Na_2Mg_3(SO_4)_4$(both phases previously unknown). Slow heating a sample of quenched $Na_2Mg_2(SO_4)_3$ leads to several phase transformations revealed on variable temperature XRD:

Monoclinic $P2_1$, $Na_2Mg_2(SO_4)_3 \xrightarrow{250°C}$ Langbeinite $P2_13$, $Na_2Mg_2(SO_4)_3 \xrightarrow{350°C}$ Mixture $Na_2Mg(SO_4)_2$ and $Na_2Mg_3(SO_4)_4 \xrightarrow{575°C}$ Langbeinite $P2_13$, $Na_2Mg_2(SO_4)_3$

Interestingly, the Raman data proposes an additional phase transition, near 100°C to a distorted orthorhombic langbeinite-type phase (similar to the one described in the Chapter Six). The final cubic langbeinite structural framework observed at high temperatures is unusual for Na as the langbeinite structure is normally only formed with larger alkali ions only. The phases observed in this study also have very interesting structural features. The orthorhombic $Na_2Mg_3(SO_4)_4$ phase was shown to contain three different types of coordination for magnesium ion

and, therefore, has a very interesting polarisation profile. The triclinic $Na_2Mg(SO_4)_2$ was found to have a hybrid structure with both NASICON and vantgoffite regions.

Some structural features related to the conductivity change near 700°C for the cubic langbeinite phase $Na_2Mg_2(SO_4)_3$ formed at high temperature are still unclear and would require a variable temperature single crystal study to be able to investigate further. Furthermore, to investigate the optic and dielectric properties of the samples, larger single crystals are required. If these studies show interesting properties it would be very interesting to further investigate polarisation features in related systems. For example it is possible that similar structures and phase transitions may be formed for other divalent cations, therefore further synthesis work is required.

In Chapter Six, the solid solution range $K_{2-x}Na_xMg_2(SO_4)_3$, where $1.9 \geq x \geq 0$, was studied in detail. Single crystals of the samples were grown to obtain accurate and complete crystallographic information. It was shown that up to x = 1.77 a stable cubic langbeinite structure is formed. At higher values of x a new orthorhombic phase is formed, which can be described with a heavily distorted langbeinite 1x3x3 supercell. In all systems there is evidence for rotational disorder of the SO_4 units, which was modelled with three split-site tetrahedrons. The orthorhombic phase at room temperature forms a polar structure with very interesting vortex clusters formed of square pyramids of MgO_5 units. An extra phase transition, near 700°C, was revealed in the conductivity experiment, and is suggested to be related to the SO_4 units being more distorted in this higher temperature region. As for $Na_2Mg_2(SO_4)_3$

at higher temperatures, the orthorhombic $K_{2-x}Na_xMg_2(SO_4)_3$ phases transformes into a cubic langbeinite with properties similar to the rest of the solid solution range.

Further investigation of these systems requires the study of their optic and dielectric properties. For such measurement large single crystals need to be grown. Also some initial work on continuing this range with further replacing Na with Li was performed (not included, due to being incomplete). Preliminary results show that for the general formula $Li_{2-x}Na_xMg_2(SO_4)_3$ with x up to 1.5 there is a mixture formed, which consists of $Li_2Mg_2(SO_4)_3$ ($Sc_2(WO_4)_3$ structure) and $Na_{1.5}Li_{0.5}Mg_2(SO_4)_3$ (NASICON framework). Further increase in Na content leads to a formation of phases whose structures is so far unknown, and is a subject of further study. The extension of this work to the incorporation of Na in phosphate langbeinite systems in $K_{2-x}Na_x\ M^{III}M^{IV}(PO_4)_3$ would also be of interest.

In Chapter Seven, an investigation was reported into the effect on the structure and properties of SeO_4^{2-}, HPO_4^{2-} and PO_3F^{2-} substitution in $NaFe(SO_4)_2$. The Raman spectroscopy results suggested that the PO_3F^{2-} anion undergoes hydrolysis during the synthesis. In this case, further synthesis work is needed to try to prevent this. The neutron diffraction and the Raman spectroscopy studies confirmed the successful incorporation of SeO_4^{2-} and HPO_4^{2-}, into the structure. The structural study suggests a slight contraction of ionic diffusion pathways, however, the conductivity study showed no significant difference in ionic mobility. The electrochemical behaviour of these samples in Na-ion cells is currently being evaluated in Almaty, Kazakhstan.

In Chapter Eight, the preliminary findings of an investigation into V/Ti phosphate containing langbeinite systems were presented. The increase of the Na content above a critical value was shown to cause the conversion of the langbeinite structure into a NASICON structure. It appears that K rich samples form the langbeinite framework, while Na rich compounds prefer to form NASICON-type structures. The solubility limit of Na in these langbeinite phases appears to be higher for Ti/V mixed systems. These mixed Ti/V systems also indicate some evidence of Ti/V partitioning between langbeinite and NASICON phases, where a mixture is formed. A single crystal study of one of the obtained NASICON phases suggests transition metal deficiency. This requires further investigation into related compositions in this region. These preliminary results need to be confirmed and the structural features of these systems clarified. Furthermore, an electrochemical study of the behaviour of these materials in a Na-cell is required in order to evaluate their performance.

Overall this study has shown a range of interesting structural features of Li/Na containing materials of relevance to Li/Na ion batteries. The work on $Na_2Mg_2(SO_4)_3$, in particular, shows that even in simple compositions, complex structural chemistry can be observed, which warrants further studies in these areas.

Publications based on thesis results

I.A. Trussov, L.L. Male, M.L. Sanjuan, A. Orera, P.R. Slater. Understanding the complex structural features and phase changes in $Na_2Mg_2(SO_4)_3$: a combined single crystal and variable temperature powder diffraction and Raman spectroscopy study.

Published *in J Solid State Chem* 2019. doi:10.1016/j.jssc.2019.02.014.

I.A. Trussov, L.L. Driscoll, M.L. Sanjuan, L.L. Male, A. Orera, P.R. Slater. Synthesis and structures of sodium containing $K_{2-x}Na_xMg_2(SO_4)_3$ langbeinite phases

Published *in J Solid State Chem* 2019. doi:10.1016/j.jssc.2019.04.036

I.A. Trussov, A.R. Haworth, K. Jonston, P.R. Slater. Synthesis and characterisation of new battery materials $Li_{5+y}La_3M_2O_{12}$ ($0<y<2$, M=Nb/Ta/Zr) garnet doping with Na^+

In preparation

I.A. Trussov, P.R. Slater. Single crystal study of Li rich cubic and tetragonal garnet $Li_{7-2\delta}La_{1+\delta}Sr_{2-\delta}Nb_2O_{12}$

In preparation

I.A. Trussov, L.L. Driscoll, R. Smith, F. Berry, P.R. Slater. Synthesis and study of Eldfellite based materials doped with SeO_4, HPO_4 and PO_3F

In preparation

References

1 Thomas M, Bruce P, Goodenough J. Lithium mobility in the layered oxide $Li_{1-x}CoO_2$. *Solid State Ionics* 1985; **17**: 13–19.

2 Lache R, Nolan P, Crane J. Electric Cars : Plugged In Batteries must be included. *Dtsch Bank Secur* 2008.

3 Hocking M, Kan J, Terry C, Begleiter D. Welcome to the Lithium-ion Age. *Dtsch Bank Mark Res* 2016; **1**: 1–179.

4 Wadia C, Albertus P, Srinivasan V. Resource constraints on the battery energy storage potential for grid and transportation applications. *J Power Sources* 2011; **196**: 1593–1598.

5 Nayak PK, Yang L, Brehm W, Adelhelm P. From Lithium-Ion to Sodium-Ion Batteries: Advantages, Challenges, and Surprises. *Angew Chemie - Int Ed* 2018; **57**: 102–120.

6 Abraham KM. Intercalation positive electrodes for rechargeable sodium cells. *Solid State Ionics* 1982; **7**: 199–212.

7 Okoshi M, Yamada Y, Yamada A, Nakai H. Theoretical Analysis on De-Solvation of Lithium, Sodium, and Magnesium Cations to Organic Electrolyte Solvents. *J Electrochem Soc* 2013; **160**: A2160–A2165.

8 Komaba S, Takei C, Nakayama T, Ogata A, Yabuuchi N. Electrochemical intercalation activity of layered $NaCrO_2$ vs. $LiCrO_2$. *Electrochem commun* 2010; **12**: 355–358.

9 Medenbach L, Adelhelm P. Cell Concepts of Metal–Sulfur Batteries (Metal = Li, Na, K, Mg): Strategies for Using Sulfur in Energy Storage Applications. *Top Curr Chem* 2017; **375**: 81.

10 Adelhelm P, Hartmann P, Bender CL, Busche M, Eufinger C, Janek J. From lithium to sodium: cell chemistry of room temperature sodium–air and sodium–sulfur batteries. *Beilstein J Nanotechnol* 2015; **6**: 1016–1055.

11 Balogun MS, Luo Y, Qiu W, Liu P, Tong Y. A review of carbon materials and their composites with alloy metals for sodium ion battery anodes. Carbon N. Y. 2016. doi:10.1016/j.carbon.2015.09.091.

12 Mizushima K, Jones PC, Wiseman PJ, Goodenough JB. Li_xCoO_2 ($0<x<1$): A new cathode material for batteries of high energy density. *Mater Res Bull* 1980; **15**: 783–789.

13 Rozier P, Tarascon JM. Review—Li-Rich Layered Oxide Cathodes for Next-Generation Li-Ion Batteries: Chances and Challenges. *J Electrochem Soc* 2015; **162**: A2490–A2499.

14 Luo K, Roberts MR, Hao R, Guerrini N, Pickup DM, Liu YS *et al.* Charge-compensation in 3d-transition-metal-oxide intercalation cathodes through the generation of localized electron holes on oxygen. *Nat Chem* 2016; **8**: 684–691.

15 Thackeray MM, Johnson PJ, de Picciotto LA, Bruce PG, Goodenough JB. Electrochemical extraction of lithium from $LiMn_2O_4$. *Mater Res Bull* 1984; **19**:

179–187.
16 Thackeray MM. Spinel Electrodes from the Li-Mn-O System for Rechargeable Lithium Battery Applications. *J Electrochem Soc* 1992; **139**: 363.
17 Tarascon JM. Li Metal-Free Rechargeable Batteries Based on $Li_{(1+x)}Mn_2O_4$ Cathodes ($0 \leq x \leq 1$) and Carbon Anodes. *J Electrochem Soc* 1991; **138**: 2864.
18 Tarascon JM. Synthesis Conditions and Oxygen Stoichiometry Effects on Li Insertion into the Spinel $LiMn_2O_4$. *J Electrochem Soc* 1994; **141**: 1421.
19 Xia Y. Capacity Fading on Cycling of 4V Li/$LiMn_2O_4$ Cells. *J Electrochem Soc* 1997; **144**: 2593.
20 Padhi AK, Nanjundaswamy KS, Goodenough JBD. Phospho-olivines as Positive-Electrode Materials for Rechargeable Lithium Batteries. *J Electrochem Soc* 1997; **144**: 1188.
21 Shukla A, Kumar T. Materials for next-generation lithium batteries. *Curr Sci* 2008; **94**: 314.
22 Yuan LX, Wang ZH, Zhang WX, Hu XL, Chen JT, Huang YH *et al.* Development and challenges of $LiFePO_4$ cathode material for lithium-ion batteries. Energy Environ. Sci. 2011; **4**: 269–284.
23 Yang S, Song Y, Ngala K, Zavalij PY, Stanley Whittingham M. Performance of $LiFePO_4$ as lithium battery cathode and comparison with manganese and vanadium oxides. In: *Journal of Power Sources*. 2003, pp 239–246.
24 Kosova NV, Devyatkina ET, Ancharov AI, Markov AV, Karnaushenko DD, Makukha VK. Structural studies of nanosized $LiFe_{0.5}Mn_{0.5}PO_4$ under cycling by in situ synchrotron diffraction. *Solid State Ionics* 2012; **225**: 564–569.
25 Islam MS, Driscoll DJ, Fisher CAJ, Slater PR. Atomic-Scale Investigation of Defects, Dopants, and Lithium Transport in the $LiFePO_4$ Olivine-Type Battery Material. *Chem Mater* 2005; **17**: 5085–5092.
26 Zeng H, Gu Y, Teng G, Liu Y, Zheng J, Pan F. Ab initio identification of the Li-rich phase in $LiFePO_4$. *Phys Chem Chem Phys* 2018; **20**: 17497–17503.
27 Park K-Y, Park I, Kim H, Yoon G, Gwon H, Cho Y *et al.* Lithium-excess olivine electrode for lithium rechargeable batteries. *Energy Environ Sci* 2016; **9**: 2902–2915.
28 Kang H, Liu Y, Cao K, Zhao Y, Jiao L, Wang Y *et al.* Update on anode materials for Na-ion batteries. J. Mater. Chem. A. 2015; **3**: 17899–17913.
29 Pang WK, Peterson VK, Sharma N, Shiu JJ, Wu SH. Lithium migration in $Li_4Ti_5O_{12}$ studied using in situ neutron powder diffraction. *Chem Mater* 2014; **26**: 2318–2326.
30 Zaghib K, Simoneau M, Armand M, Gauthier M. Electrochemical study of $Li_4Ti_5O_{12}$ as negative electrode for Li-ion polymer rechargeable batteries. *J Power Sources* 1999; **81–82**: 300–305.
31 Han MH, Gonzalo E, Singh G, Rojo T. A comprehensive review of sodium layered oxides: Powerful cathodes for Na-ion batteries. Energy Environ. Sci. 2015; **8**: 81–102.
32 Kuze S, Kageura J, Matsumoto S, Nakayama T, Makidera M, Saka M *et al.* Development of a Sodium Ion Secondary Battery, Sumitomo Chemical Co., Ltd. 2013; **2013**: 1–13.

33 Casas-Cabanas M, Roddatis V V., Saurel D, Kubiak P, Carretero-González J, Palomares V *et al.* Crystal chemistry of Na insertion/deinsertion in $FePO_4$ - $NaFePO_4$. *J Mater Chem* 2012; **22**: 17421–17423.

34 Cao JL, Ni L, Qin CC, Tang YF, Chen YF. Synthesis of hierarchical $Na_2FeP_2O_7$ spheres with high electrochemical performance via spray drying. *Ionics (Kiel)* 2017; **23**: 1783–1791.

35 He G, Huq A, Kan WH, Manthiram A. β-$NaVOPO_4$ Obtained by a Low-Temperature Synthesis Process: A New 3.3V Cathode for Sodium-Ion Batteries. *Chem Mater* 2016; **28**: 1503–1512.

36 Lander L, Tarascon J-M, Yamada A. Sulfate-Based Cathode Materials for Li- and Na-Ion Batteries. *Chem Rec* 2018; **18**: 1394–1408.

37 Mason CW, Gocheva I, Hoster HE, Yu DYW. Iron(III) sulfate: a stable, cost effective electrode material for sodium ion batteries. *Chem Commun* 2014; **50**: 2249–2251.

38 Goodenough JB, Hong H.-P, Kafalas JA. Fast Na+-ion transport in skeleton structures. *Mater Res Bull* 1976; **11**: 203–220.

39 Porkodi P, Yegnaraman V, Kamaraj P, Kalyanavalli V, Jeyakumar D. Synthesis of NASICON · A Molecular Precursor-Based Approach. *Chem Mater* 2008; **20**: 6410–6419.

40 Perret R, Thierrsorel A, Peter JP, Masse R. Triple Sulfates $MIMIIMIII(SO_4)_3$. Rhombohedral Sulfate $NaMIIMII(SO_4)_3$ (MII=Mg, Mn, Co, Ni, Zn, MIII = Al, Ga, In, Cr, Fe). *Bull La Soc Fr Mineral Cristallogr* 1975; **98**: 103–106.

41 Perret R, Bartil N, Thierrsorel A. Rhombohedral Sulfates $AgMIICr(SO_4)_3$, $NaKMII_2Cr_2(SO_4)_6$ and $AgKMII_2Cr_2(SO_4)_6$, MII - Mg, Mn, Co, Ni, Zn. *Comptes Rendus Hebd Des Seances L'Academie Des Sci Ser C* 1976; **282**: 173–174.

42 Slater PR, Greaves C. Neutron diffraction structural study of the nasicon-related phases $Li_xMII_xMIII_{2-x}(SO_4)_{3-y}(SeO_4)_y$ (MII = Mg, Ni, Zn; MIII = Al, Cr). *J Mater Chem* 1994; **4**: 1463–1467.

43 Slater PR, Greaves C. Powder neutron diffraction study of the nasicon-related phases $Na_xMII_xMIII_{2-x}(SO_4)_{3-y}(SeO_4)_y$: MII = Mg, MIII = Fe, In. *J Mater Chem* 1994; **4**: 1469–1473.

44 Slater PR, Greaves C. Synthesis and Conductivities of Sulfate/Selenate Phases Related to Nasicon: $Na_xM'(II)_xM''(III)_{2-x}(SO_4)_{3-y}(SeO_4)_y$. *J Solid State Chem* 1993; **107**: 12–18.

45 Chung S-CC, Ming J, Lander L, Lu J, Yamada A. Rhombohedral NASICON-type $Na_xFe_2(SO_4)_3$ for sodium ion batteries: comparison with phosphate and alluaudite phases. *J Mater Chem A* 2018; **6**: 3919–3925.

46 Barpanda P, Oyama G, Nishimura S, Chung S-C, Yamada A. A 3.8-V earth-abundant sodium battery electrode. *Nat Commun* 2014; **5**: 1–8.

47 Araujo RB, Chakraborty S, Barpanda P, Ahuja R. $Na_2M_2(SO_4)_3$ (M = Fe, Mn, Co and Ni): towards high-voltage sodium battery applications. *Phys Chem Chem Phys* 2016; **18**: 9658–9665.

48 Lu J, Yamada A. Ionic and Electronic Transport in Alluaudite $Na_{2+2x}Fe_{2-x}(SO_4)_3$. *ChemElectroChem* 2016; **3**: 902–905.

49 Dwibedi D, Gond R, Dayamani A, Araujo RB, Chakraborty S, Ahuja R *et al.*

$Na_{2.32}Co_{1.84}(SO_4)_3$ as a new member of the alluaudite family of high-voltage sodium battery cathodes. *Dalt Trans* 2017; **46**: 55–63.

50 Dwibedi D, Araujo RB, Chakraborty S, Shanbogh PP, Sundaram NG, Ahuja R *et al.* $Na_{2.44}Mn_{1.79}(SO_4)_3$: a new member of the alluaudite family of insertion compounds for sodium ion batteries. *J Mater Chem A* 2015; **3**: 18564–18571.

51 Dwibedi D, Barpanda P. Alluaudite class of high voltage sodium insertion materials: An interplay of polymorphism and magnetism. In: *AIP Conference Proceedings*. American Institute of Physics, 2017, p 130041.

52 Barpanda P, Oyama G, Ling CD, Yamada A. Kröhnkite-Type $Na_2Fe(SO_4)_2{\cdot}2H_2O$ as a Novel 3.25V Insertion Compound for Na-Ion Batteries. *Chem Mater* 2014; **26**: 1297–1299.

53 Reynaud M, Rousse G, Abakumov AM, Sougrati MT, Van Tendeloo G, Chotard J-N *et al.* Design of new electrode materials for Li-ion and Na-ion batteries from the bloedite mineral Na2Mg(SO4)2·4H2O. *J Mater Chem A* 2014; **2**: 2671–2680.

54 Singh P, Shiva K, Celio H, Goodenough JB. Eldfellite, $NaFe(SO_4)_2$: an intercalation cathode host for low-cost Na-ion batteries. *Energy Environ Sci* 2015; **8**: 3000–3005.

55 Yu C-J, Choe S-H, Ri G-C, Kim S-C, Ryo H-S, Kim Y-J. Ionic Diffusion and Electronic Transport in Eldfellite $Na_xFe(SO_4)_2$. *Phys Rev Appl* 2017; **8**: 024029.

56 Banerjee A, Araujo RB, Ahuja R. Unveiling the thermodynamic and kinetic properties of $Na_xFe(SO_4)_2$(x=0–2): toward a high-capacity and low-cost cathode material. *J Mater Chem A* 2016; **4**: 17960–17969.

57 Scrosati B, Garche J. Lithium batteries: Status, prospects and future. *J Power Sources* 2010; **195**: 2419–2430.

58 Takada K. Progress and prospective of solid-state lithium batteries. *Acta Mater* 2013; **61**: 759–770.

59 Thokchom JS, Gupta N, Kumar B. Superionic Conductivity in a Lithium Aluminum Germanium Phosphate Glass–Ceramic. *J Electrochem Soc* 2008; **155**: A915.

60 Feng LM, Jiang LQ, Zhu M, Liu HB, Zhou X, Li CH. Formability of ABO_3 cubic perovskites. *J Phys Chem Solids* 2008; **69**: 967–974.

61 Stramare S, Thangadurai V, Weppner W. Lithium Lanthanum Titanates: A Review. Chem. Mater. 2003; **15**: 3974–3990.

62 Mei A, Wang X, Feng Y, Zhao S, Li G, Geng H *et al.* Enhanced ionic transport in lithium lanthanum titanium oxide solid state electrolyte by introducing silica. *Solid State Ionics* 2008; **179**: 2255–2259.

63 Mei A, Jiang Q-H, Lin Y-H, Nan C-W. Lithium lanthanum titanium oxide solid-state electrolyte by spark plasma sintering. *J Alloys Compd* 2009; **486**: 871–875.

64 Inaguma Y, Chen L, Itoh M, Nakamura T. Candidate compounds with perovskite structure for high lithium ionic conductivity. *Solid State Ionics* 1994; **70–71**: 196–202.

65 Jimenez R, Rivera A, Varez A, Sanz J. Li mobility in $Li_{0.5-x}Na_xLa_{0.5}TiO_3$ perovskites (0≤x≤0.5)Influence of structural and compositional parameters.

Solid State Ionics 2009; **180**: 1362–1371.

66 Ibarra J, Várez A, León C, Santamaría J, Torres-Martínez L., Sanz J. Influence of composition on the structure and conductivity of the fast ionic conductors $La_{2/3-x}Li_{3x}TiO_3$ ($0.03 \leq x \leq 0.167$). *Solid State Ionics* 2000; **134**: 219–228.

67 Inaguma Y, Itoh M. Influences of carrier concentration and site percolation on lithium ion conductivity in perovskite-type oxides. *Solid State Ionics* 1996; **86–88**: 257–260.

68 Zou Y, Inoue N. Calculation of 7Li MAS NMR chemical shift in $La_{4/3-y}Li_{3y}Ti_2O_6$. *Ionics (Kiel)* 2006; **12**: 185–189.

69 Zheng F, Kotobuki M, Song S, Lai MO, Lu L. Review on solid electrolytes for all-solid-state lithium-ion batteries. *J Power Sources* 2018; **389**: 198–213.

70 Zhang Y, Chen Y. Al,F-doped new perovskite lithium fast ion conductor $Li_{3x}La_{2/3-x}\square_{1/3-2x}Ti_{1-y}Al_yO_{3-y}F_y$ (x=0.11). *Ionics (Kiel)* 2006; **12**: 63–67.

71 Zou Y, Inoue N, Ohara K, Thangaduri V, Weppner W. Structure and lithium ionic conduction of B-site Al-ion substitution in $La_{4/3-y}Li_{3y}Ti_2O_6$. *Ionics (Kiel)* 2004; **10**: 463–468.

72 Thangadurai V, Weppner W. Effect of B-site substitution of $(Li,La)TiO_3$ perovskites by di-, tri-, tetra- and hexavalent metal ions on the lithium ion conductivity. *Ionics (Kiel)* 2000; **6**: 70–77.

73 Rogez J, Knauth P, Garnier A, Ghobarkar H, Schäf O. Determination of the crystallization enthalpies of lithium ion conducting alumino–silicate glasses. *J Non Cryst Solids* 2000; **262**: 177–182.

74 Kuhn A, Wilkening M, Heitjans P. Mechanically induced decrease of the Li conductivity in an alumosilicate glass. *Solid State Ionics* 2009; **180**: 302–307.

75 Kim JM, Park GB, Lee KC, Park HY, Nam SC, Song SW. Li–B–O–N electrolytes for all-solid-state thin film batteries. *J Power Sources* 2009; **189**: 211–216.

76 Berkemeier F, Shoar Abouzari MR, Schmitz G. Sputter-deposited network glasses : SStructural and electrical properties. *Ionics (Kiel)* 2009; **15**: 241–248.

77 Heitjans P, Tobschall E, Wilkening M. Ion transport and diffusion in nanocrystalline and glassy ceramics. *Eur Phys J Spec Top* 2008; **161**: 97–108.

78 Wells AF. *Structural inorganic chemistry*. 5th edn. C. Clarendon Press: Oxford, 1984.

79 Thangadurai V, Kaack H, Weppner WJF. Novel fast lithium ion conduction in garnet-type $Li_5La_3M_2O_{12}$ (M = Nb, Ta). *J Am Ceram Soc* 2003; **86**: 437–440.

80 O'Callaghan MP, Lynham DR, Cussen EJ, Chen GZ. Structure and ionic-transport properties of lithium-containing garnets $Li_3Ln_3Te_2O_{12}$ (Ln = Y, Pr, Nd, Sm-Lu). *Chem Mater* 2006; **18**: 4681–4689.

81 Howard MA, Clemens O, Parvathy AS, Anderson PA, Slater PR. Synthesis and ionic conductivity of new high Li ion content garnets, $LnSr_2Ta_2Li_7O_{12}$ (Ln = La, Pr, Nd, Sm, Gd). *J Alloys Compd* 2016; **670**: 78–84.

82 Ramakumar S, Deviannapoorani C, Dhivya L, Shankar LS, Murugan R. Lithium garnets: Synthesis, structure, Li + conductivity, Li + dynamics and applications. *Prog Mater Sci* 2017; **88**: 325–411.

83 Murugan R, Thangadurai V, Weppner W. Fast lithium ion conduction in garnet-type $Li_7La_3Zr_2O_{12}$. *Angew Chem Int Ed Engl* 2007; **46**: 7778–81.

84 Howard MA, Clemens O, Kendrick E, Knight KS, Apperley DC, Anderson PA *et al.* Effect of Ga incorporation on the structure and Li ion conductivity of $La_3Zr_2Li_7O_{12}$. *Dalt Trans* 2012; **41**: 12048.

85 Rangasamy E, Wolfenstine J, Allen J, Sakamoto J. The effect of 24c-site (A) cation substitution on the tetragonal–cubic phase transition in $Li_{7-x}La_{3-x}A_xZr_2O_{12}$ garnet-based ceramic electrolyte. *J Power Sources* 2013; **230**: 261–266.

86 Rangasamy E, Wolfenstine J, Sakamoto J. The role of Al and Li concentration on the formation of cubic garnet solid electrolyte of nominal composition $Li_7La_3Zr_2O_{12}$. *Solid State Ionics* 2012; **206**: 28–32.

87 Percival J, Apperley D, Slater PR. Synthesis and structural characterisation of the Li ion conducting garnet-related systems, $Li_6ALa_2Nb_2O_{12}$ (A = Ca, Sr). *Solid State Ionics* 2008; **179**: 1693–1696.

88 Murugan R, Thangadurai V, Weppner W. Lithium ion conductivity of $Li_{5+x}Ba_xLa_{3-x}Ta_2O_{12}$ (x=0-2) with garnet-related structure in dependence of the barium content. *Ionics (Kiel)* 2007; **13**: 195–203.

89 Thangadurai V, Weppner W. $Li_6ALa_2Ta_2O_{12}$ (A = Sr, Ba): Novel Garnet-Like Oxides for Fast Lithium Ion Conduction. *Adv Funct Mater* 2005; **15**: 107–112.

90 Awaka J, Kijima N, Takahashi Y, Hayakawa H, Akimoto J. Synthesis and crystallographic studies of garnet-related lithium-ion conductors $Li_6CaLa_2Ta_2O_{12}$ and $Li_6BaLa_2Ta_2O_{12}$. *Solid State Ionics* 2009; **180**: 602–606.

91 Percival J, Slater PR. Identification of the Li sites in the Li ion conductor, $Li_6SrLa_2Nb_2O_{12}$, through neutron powder diffraction studies. 2007 doi:10.1016/j.ssc.2007.02.036.

92 Thangadurai V, Weppner W. Effect of sintering on the ionic conductivity of garnet-related structure $Li_5La_3Nb_2O_{12}$ and In- and K-doped $Li_5La_3Nb_2O_{12}$. *J Solid State Chem* 2006; **179**: 974–984.

93 Ohta S, Kobayashi T, Asaoka T. High lithium ionic conductivity in the garnet-type oxide $Li_{7-X}La_3(Zr_{2-X}, Nb_X)O_{12}$ (X = 0-2). *J Power Sources* 2011; **196**: 3342–3345.

94 Kennedy JH, Sammells AF. Conductivity of Beta-Alumina and Its Dependence on Sodium and Magnesium Content. *J Electrochem Soc* 1972; **119**: 1609.

95 Fergus JW. Ion transport in sodium ion conducting solid electrolytes. *Solid State Ionics* 2012; **227**: 102–112.

96 Anantharamulu N, Koteswara Rao K, Rambabu G, Vijaya Kumar B, Radha V, Vithal M. A wide-ranging review on Nasicon type materials. *J Mater Sci* 2011; **46**: 2821–2837.

97 Hancock CA, Porras-Vazquez JM, Keenan PJ, Slater PR. Oxyanions in perovskites: from superconductors to solid oxide fuel cells. *Dalt Trans* 2015; **44**: 10559–10569.

98 Driscoll LL, Kendrick E, Wright AJ, Slater PR. Investigation into the effect on structure of oxoanion doping in $Na_2M(SO_4)_2{\cdot}2H_2O$. *J Solid State Chem* 2016; **242**: 103–111.

99 Bohr A, Mottelson BR. *Nuclear structure Vol.2, Nuclear deformations.* Reading, Mass.: London, 1975.

100 Rietveld HM. Line profiles of neutron powder-diffraction peaks for structure refinement. *Acta Crystallogr* 1967; **22**: 151–152.

101 Prince E (ed.). Volume C: Mathematical, physical and chemical tables. In: *International Tables for Crystallography*. International Union of Crystallography: London, England, 2004, p 711.

102 Toby BH. R factors in Rietveld analysis: How good is good enough? *Powder Diffr* 2006; **21**: 67–70.

103 Toby BH, Von Dreele RB. GSAS-II: The genesis of a modern open-source all purpose crystallography software package. *J Appl Crystallogr* 2013; **46**: 544–549.

104 Coelho AA. TOPAS and TOPAS-Academic: An optimization program integrating computer algebra and crystallographic objects written in C++: An. *J Appl Crystallogr* 2018; **51**: 210–218.

105 Johnson D. ZView: A Software Program for IES Analysis, Version 3.1c. *Scribner Assoc Inc* 2009; : 1990–2005.

106 Irvine JTS, Sinclair DC, West AR. Electroceramics : Characterization by impedance spectroscopy. *Adv Mater* 1990; **2**: 132–138.

107 Tobergte DR, Curtis S. *Labview for Engineers*. 2013 doi:10.1017/CBO9781107415324.004.

108 Dokko K, Akutagawa N, Isshiki Y, Hoshina K, Kanamura K. Preparation of three dimensionally ordered macroporous $Li_{0.35}La_{0.55}TiO_3$ by colloidal crystal templating process. *Solid State Ionics* 2005; **176**: 2345–2348.

109 Rosero-Navarro NC, Yamashita T, Miura A, Higuchi M, Tadanaga K. Preparation of $Li_7La_3(Zr_{2-x},Nb_x)O_{12}$ (x=0–1.5) and $Li_3BO_3/LiBO_2$ composites at low temperatures using a sol–gel process. *Solid State Ionics* 2015. doi:10.1016/j.ssi.2015.06.015.

110 Tadanaga K, Takano R, Ichinose T, Mori S, Hayashi A, Tatsumisago M. Low temperature synthesis of highly ion conductive $Li_7La_3Zr_2O_{12}$–Li_3BO_3 composites. *Electrochem commun* 2013; **33**: 51–54.

111 Wang XL, Mei A, Li M, Lin Y, Nan CW. Effect of silane-functionalized mesoporous silica SBA-15 on performance of PEO-based composite polymer electrolytes. *Solid State Ionics* 2006; **177**: 1287–1291.

112 Porras-Vazquez JM, Smith RI, Slater PR. Investigation into the effect of Si doping on the cell symmetry and performance of $Sr_{1-y}Ca_yFeO_{3-\delta}$ SOFC cathode materials. *J Solid State Chem* 2014; **213**: 132–137.

113 Sanjuán ML, Laguna MA, Belous AG, V'yunov OI. On the Local Structure and Lithium Dynamics of $La_{0.5}(Li,Na)_{0.5}TiO_3$ Ionic Conductors. A Raman Study. *Chem Mater* 2005; **17**: 5862–5866.

114 Ibarra J. Influence of composition on the structure and conductivity of the fast ionic conductors $La_{2/3-x}Li_{3x}TiO_3$ ($0.03 \leq x \leq 0.167$). *Solid State Ionics* 2000; **134**: 219–228.

115 Cussen EJ. The structure of lithium garnets: cation disorder and clustering in a new family of fast Li^+ conductors. *Chem Commun* 2006; : 412–413.

116 O'Callaghan MP, Cussen EJ. Lithium dimer formation in the Li-conducting garnets $Li_{5+x}Ba_xLa_{3-x}Ta_2O_{12}$ ($0 < x \leq 1.6$). *Chem Commun* 2007; : 2048–2050.

117 Percival J, Kendrick E, Smith RI, Slater PR. Cation ordering in Li containing garnets: synthesis and structural characterisation of the tetragonal system, $Li_7La_3Sn_2O_{12}$. *Dalt Trans* 2009; : 5177.

118 Awaka J, Kijima N, Kataoka K, Hayakawa H, Ohshima K, Akimoto J. Neutron powder diffraction study of tetragonal $Li_7La_3Hf_2O_{12}$ with the garnet-related type structure. *J Solid State Chem* 2010; **183**: 180–185.

119 Rettenwander D, Geiger CA, Tribus M, Tropper P, Amthauer G. A Synthesis and Crystal Chemical Study of the Fast Ion Conductor $Li_{7-3x}Ga_xLa_3Zr_2O_{12}$ with x = 0.08 to 0.84. *Inorg Chem* 2014; **53**: 6264–6269.

120 Geiger CA, Alekseev E, Lazic B, Fisch M, Armbruster T, Langner R *et al.* Crystal Chemistry and Stability of "$Li_7La_3Zr_2O_{12}$" Garnet: A Fast Lithium-Ion Conductor. *Inorg Chem* 2011; **50**: 1089–1097.

121 Wang Y, Lai W. High Ionic Conductivity Lithium Garnet Oxides of $Li_{7-x}La_3Zr_{2-x}Ta_xO_{12}$ Compositions. *Electrochem Solid-State Lett* 2012; **15**: A68.

122 Peng H, Li L, Feng L, Zhang Y, Zou Y. Effect of Na substitution for La on Li ion conductivity of $Li_5La_3Nb_2O_{12}$ garnets by sol–gel process. *Mater Res Bull* 2018; **99**: 414–418.

123 Dolomanov O V., Bourhis LJ, Gildea RJ, Howard JAK, Puschmann H. OLEX2 : a complete structure solution, refinement and analysis program. *J Appl Crystallogr* 2009; **42**: 339–341.

124 Sheldrick GM. SHELXT – Integrated space-group and crystal-structure determination. *Acta Crystallogr Sect A Found Adv* 2015; **71**: 3–8.

125 Sheldrick GM. Crystal structure refinement with SHELXL. *Acta Crystallogr Sect C Struct Chem* 2015; **71**: 3–8.

126 Sato H. Some theoretical aspects of solid electrolytes. In: Geller S (ed). *Solid Electrolytes*. Springer Berlin Heidelberg: Berlin, Heidelberg, 1977, pp 3–39.

127 Zeier WG, Zhou S, Lopez-Bermudez B, Page K, Melot BC. Dependence of the li-ion conductivity and activation energies on the crystal structure and ionic radii in $Li_6MLa_2Ta_2O_{12}$. *ACS Appl Mater Interfaces* 2014; **6**: 10900–10907.

128 Nalbandyan VB, Shukaev IL. New Lithium Tantalates and Niobates. *Russ J Inorg Chem* 1989; **34**: 444–445.

129 Nemori H, Matsuda Y, Mitsuoka S, Matsui M, Yamamoto O, Takeda Y *et al.* Stability of garnet-type solid electrolyte $Li_xLa_3A_{2-y}B_yO_{12}$ (A=Nb or Ta, B=Sc or Zr). *Solid State Ionics* 2015; **282**: 7–12.

130 Thangadurai V, Huggins RA, Weppner W. Use of simple ac technique to determine the ionic and electronic conductivities in pure and Fe-substituted $SrSnO_3$ perovskites. *J Power Sources* 2002; **108**: 64–69.

131 Peng H, Wu Q, Xiao L. Low temperature synthesis of $Li_5La_3Nb_2O_{12}$ with cubic garnet-type structure by sol–gel process. *J Sol-Gel Sci Technol* 2013; **66**: 175–179.

132 Percival J, Kendrick E, Slater PR. Synthesis and conductivities of the garnet-related Li ion conductors, $Li_5Ln_3Sb_2O_{12}$ (Ln = La, Pr, Nd, Sm, Eu). *Solid State Ionics* 2008; **179**: 1666–1669.

133 Narayanan S, Epp V, Wilkening M, Thangadurai V. Macroscopic and microscopic Li+ transport parameters in cubic garnet-type

"$Li_{6.5}La_{2.5}Ba_{0.5}ZrTaO_{12}$" as probed by impedance spectroscopy and NMR. *RSC Adv* 2012; **2**: 2553.

134 Goodenough JB, Kim Y. Challenges for rechargeable Li batteries. Chem. Mater. 2010; **22**: 587–603.

135 Sun M, Rousse G, Saubanère M, Doublet ML, Dalla Corte D, Tarascon JM. $A_2VO(SO_4)_2$ (A = Li, Na) as electrodes for Li-Ion and Na-ion batteries. *Chem Mater* 2016; **28**: 6637–6643.

136 Oyama G, Nishimura S, Suzuki Y, Okubo M, Yamada A. Off-Stoichiometry in Alluaudite-Type Sodium Iron Sulfate $Na_{2+2x}Fe_{2-x}(SO_4)_3$ as an Advanced Sodium Battery Cathode Material. *ChemElectroChem* 2015; **2**: 1019–1023.

137 Driscoll LL, Wright AJ, Slater PR. Designing a facile low cost synthesis strategy for the Na–V–S–O systems, $NaV(SO_4)_2$, $Na_3V(SO_4)_3$ and $Na_2VO(SO_4)_2$. *Dalt Trans* 2018; **47**: 13535–13542.

138 Jakobsson SP, Leonardsen ES, Jakobsson SP, Leonardsen ES, Balić-Žunić T. Encrustations from three recent volcanic eruptions in Iceland: the 1963–1967 Surtsey, the 1973 Eldfell and the 1991 Hekla eruptions. *Fjölrit Náttúrufræðistofnunar* 2008; **52**: 65.

139 Balić-Žunić T, Birkedal R, Katerinopoulou A, Comodi P. Dehydration of blödite, $Na_2Mg(SO_4)2(H_2O)_4$, and leonite, $K_2Mg(SO_4)2(H_2O)4$. *Eur J Mineral* 2016; **28**: 33–42.

140 Zemann A, Zemann J. Die Kristallstruktur von Langbeinit, $K_2Mg_2(SO_4)_3$. *Acta Crystallogr* 1957; **10**: 409–413.

141 Gattw G, Zemann J. Über Doppelsulfate vom Langbeinit-Typ, $A_2B_2(SO_4)_3$. *Zeitschrift für Anorg und Allg Chemie* 1958; **293**: 233–240.

142 Zatovsky I V., Strutynska NY, Hizhnyi YA, Nedilko SG, Slobodyanik NS, Klyui NI. Partial Substitution of Potassium with Sodium in the $K_2Ti_2(PO_4)_3$ Langbeinite-Type Framework: Synthesis and Crystalline Structure of $K_{1.75}Na_{0.25}Ti_2(PO_4)_3$. *ChemistryOpen* 2018; **7**: 504–512.

143 Hidouri M, Jerbi H, Ben Amara M. The iron phosphate $NaBaFe_2(PO_4)_3$. *Acta Crystallogr Sect E Struct Reports Online* 2008; **64**: i51–i51.

144 Coles SJ, Gale PA. Changing and challenging times for service crystallography. Chem. Sci. 2012; **3**: 683–689.

145 Hatert F. $Na_4Fe^{2+}Fe^{3+}(PO_4)_3$, a new synthetic NASICON-type phosphate. *Acta Crystallogr Sect E Struct Reports Online* 2009; **65**: i30–i30.

146 Hamilton A, Menzies RI. Raman spectra of mirabilite, $Na_2SO_4{\cdot}10H_2O$ and the rediscovered metastable heptahydrate, Na2SO4·7H2O. *J Raman Spectrosc* 2010; **41**: 1014–1020.

147 Alpers CN, Jambor JL, Nordstrom DK, Ribbe PH. *Sulfate minerals : crystallography, geochemistry, and environmental significance*. Mineralogical Society of America: Washington, DC, 2000https://copac.jisc.ac.uk/id/8111937?style=html&title=Sulfate mineralscrystallography%2C geochemistry%2C and.

148 Léost I, Féraud G, Blanc-Valleron MM, Rouchy JM. First absolute dating of Miocene Langbeinite evaporites by $^{40}Ar/^{39}Ar$ laser step-heating: $[K_2Mg_2(SO_4)_3]$ Stebnyk Mine (Carpathian Foredeep Basin). *Geophys Res Lett*

2001; **28**: 4347–4350.
149 Kher RS, Panigrahi AK, Dhoble SJ, Khokhar MSK. Correlation between thermoluminescence and mechanoluminescence of gamma–irradiated Dy activated potassium and magnesium mixed sulphate. *Radiat Prot Dosimetry* 2006; **119**: 66–70.
150 Mandlik N, Sahare PD, Kulkarni MS, Bhatt BC, Bhoraskar VN, Dhole SD. Study of TL and optically stimulated luminescence of $K_2Ca_2(SO_4)_3$:Cu nanophosphor for radiation dosimetry. *J Lumin* 2014; **146**: 128–132.
151 Abrahams SC, Bernstein JL. Piezoelectric langbeinite-type $K_2Cd_2(SO_4)_3$: Room temperature crystal structure and ferroelastic transformation. *J Chem Phys* 1977; **67**: 2146.
152 Březina B, Glogarová M. New ferroelectric langbeinite $Tl_2Cd_2(SO_4)_3$. *Phys Status Solidi* 1972; **11**: K39–K42.
153 Devarajan V, Salje E. Phase transitions in langbeinites II: Raman spectroscopic investigations of $K_2Cd_2(SO_4)_3$. *Phys Chem Miner* 1986; **13**: 25–30.
154 Sakai A, Inagaki T, Moriyoshi C, Itoh K. Micro-Raman mapping study of the phase transition in $K_2Mn_2(SO_4)_3$. In: *Ferroelectrics*. 2002, pp 27–32.
155 Souamti A, Kahlaoui M, Mohammed B, Diego Lozano-Gorrín A, Chehimi DBH. Synthesis, structural and electrochemical properties of new ytterbium-doped langbeinite ceramics. *Ceram Int* 2017; **43**: 10939–10947.
156 Lander L, Rousse G, Batuk D, Colin C V, Dalla Corte DA, Tarascon J-M. Synthesis, Structure, and Electrochemical Properties of K-Based Sulfates $K_2M_2(SO_4)_3$ with M = Fe and Cu. *Inorg Chem* 2017; **56**: 2013–2021.
157 Trussov IA, Male LL, Sanjuan ML, Orera A, Slater PR. Understanding the complex structural features and phase changes in $Na_2Mg_2(SO_4)_3$: a combined single crystal and variable temperature powder diffraction and Raman spectroscopy study. *J Solid State Chem* 2019; **272**: 157–165.
158 Driscoll LL, Kendrick E, Knight KS, Wright AJ, Slater PR. Investigation into the dehydration of selenate doped $Na_2M(SO_4)_2{\cdot}2H_2O$ (M = Mn, Fe, Co and Ni): Stabilisation of the high Na content alluaudite phases $Na_3M_{1.5}(SO_4)_{3-1.5x}(SeO_4)_{1.5x}$(M = Mn, Co and Ni) through selenate incorporation. *J Solid State Chem* 2018; **258**: 64–71.
159 Speer D, Salje E. Phase transitions in langbeinites I: Crystal chemistry and structures of K-double sulfates of the langbeinite type $M^{2+}{}_2K_2(SO_4)_3$, M2+ = Mg, Ni, Co, Zn, Ca. *Phys Chem Miner* 1986; **13**: 17–24.
160 Cumby J, Attfield JP. Ellipsoidal analysis of coordination polyhedra. *Nat Commun* 2017; **8**: 14235.
161 Zhou D, Huang W, Kang X, Zhao F, Zhao L, Deng Z *et al.* Titanium-doped P2-type $Na_{0.67}Co_{0.67}Mn_{0.33-x}Ti_xO_2$($0 \le x \le 0.2$) as Novel Cathodes for sodium ion batteries with superior-rate. *Int J Electrochem Sci* 2018; **13**: 2010–2021.
162 Kumakura S, Tahara Y, Kubota K, Chihara K, Komaba S. Sodium and Manganese Stoichiometry of P2-Type $Na_{2/3}MnO_2$. *Angew Chemie - Int Ed* 2016; **55**: 12760–12763.
163 Wang L, Wang J, Zhang X, Ren Y, Zuo P, Yin G *et al.* Unravelling the origin of irreversible capacity loss in $NaNiO_2$ for high voltage sodium ion batteries.

Nano Energy 2017; **34**: 215–223.

164 Sun X, Jin Y, Zhang CY, Wen JW, Shao Y, Zang Y *et al.* $Na[Ni_{0.4}Fe_{0.2}Mn_{0.4-x}Ti_x]O_2$: A cathode of high capacity and superior cyclability for Na-ion batteries. *J Mater Chem A* 2014; **2**: 17268–17271.

165 Fang Y, Xiao L, Ai X, Cao Y, Yang H. Hierarchical Carbon Framework Wrapped $Na_3V_2(PO_4)_3$ as a Superior High-Rate and Extended Lifespan Cathode for Sodium-Ion Batteries. *Adv Mater* 2015; **27**: 5895–5900.

166 Jian Z, Han W, Lu X, Yang H, Hu Y-S, Zhou J *et al.* Superior Electrochemical Performance and Storage Mechanism of $Na_3V_2(PO_4)_3$ Cathode for Room-Temperature Sodium-Ion Batteries. *Adv Energy Mater* 2013; **3**: 156–160.

167 Lim SY, Kim H, Shakoor RA, Jung Y, Choi JW. Electrochemical and Thermal Properties of NASICON Structured $Na_3V_2(PO_4)_3$ as a Sodium Rechargeable Battery Cathode: A Combined Experimental and Theoretical Study. *J Electrochem Soc* 2012; **159**: A1393–A1397.

168 Jian Z, Zhao L, Pan H, Hu Y-S, Li H, Chen W *et al.* Carbon coated $Na_3V_2(PO_4)_3$ as novel electrode material for sodium ion batteries. *Electrochem commun* 2012; **14**: 86–89.

169 Fang Y, Liu Q, Xiao L, Ai X, Yang H, Cao Y. High-Performance Olivine $NaFePO_4$ Microsphere Cathode Synthesized by Aqueous Electrochemical Displacement Method for Sodium Ion Batteries. *ACS Appl Mater Interfaces* 2015; **7**: 17977–17984.

170 Kim J, Seo D-H, Kim H, Park I, Yoo J-K, Jung S-K *et al.* Unexpected discovery of low-cost maricite $NaFePO_4$ as a high-performance electrode for Na-ion batteries. *Energy Environ Sci* 2015; **8**: 540–545.

171 Park CS, Kim H, Shakoor RA, Yang E, Lim SY, Kahraman R *et al.* Anomalous manganese activation of a pyrophosphate cathode in sodium ion batteries: a combined experimental and theoretical study. *J Am Chem Soc* 2013; **135**: 2787–92.

172 Nose M, Nakayama H, Nobuhara K, Yamaguchi H, Nakanishi S, Iba H. $Na_4Co_3(PO_4)_2P_2O_7$: A novel storage material for sodium-ion batteries. *J Power Sources* 2013; **234**: 175–179.

173 Jin H, Dong J, Uchaker E, Zhang Q, Zhou X, Hou S *et al.* Three dimensional architecture of carbon wrapped multilayer $Na_3V_2O_2(PO_4)_2F$ nanocubes embedded in graphene for improved sodium ion batteries. *J Mater Chem A* 2015; **3**: 17563–17568.

174 Gover RKB, Burns P, Bryan A, Saidi MY, Swoyer JL, Barker J. $LiVPO_4F$: A new active material for safe lithium-ion batteries. *Solid State Ionics* 2006; **177**: 2635–2638.

175 Broux T, Bamine T, Fauth F, Simonelli L, Olszewski W, Marini C *et al.* Strong Impact of the Oxygen Content in $Na_3V_2(PO_4)_2F_{3-y}O_y$ ($0 \le y \le 0.5$) on Its Structural and Electrochemical Properties. *Chem Mater* 2016; **28**: 7683–7692.

176 Kawabe Y, Yabuuchi N, Kajiyama M, Fukuhara N, Inamasu T, Okuyama R *et al.* A Comparison of Crystal Structures and Electrode Performance between Na_2FePO_4F and $Na_2Fe_{0.5}Mn_{0.5}PO_4F$ Synthesized by Solid-State Method for Rechargeable Na-Ion Batteries. *Electrochemistry* 2012; **80**: 80–84.

177 Li S, Guo J, Ye Z, Zhao X, Wu S, Mi JX *et al.* Zero-Strain Na_2FeSiO_4 as Novel Cathode Material for Sodium-Ion Batteries. *ACS Appl Mater Interfaces* 2016; **8**: 17233–17238.

178 Balić-Žunić T, Garavelli A, Acquafredda P, Leonardsen E, Jakobsson SP. Eldfellite, $NaFe(SO_4)_2$, a new fumarolic mineral from Eldfell volcano, Iceland. *Mineral Mag* 2009; **73**: 51–57.

179 Nisar U, Gulied MH, Shakoor RA, Essehli R, Ahmad Z, Alashraf A *et al.* Synthesis and performance evaluation of nanostructured $NaFe_xCr_{1-x}(SO_4)_2$ cathode materials in sodium ion batteries (SIBs). *RSC Adv* 2018; **8**: 32985–32991.

180 Nanjundaswamya K, Padhi A, Goodenough J, Okada S, Ohtsukab H, Arai H *et al.* Synthesis, redox potential evaluation and electrochemical characteristics of NASICON-related-3D framework compounds. *Solid State Ionics* 1996; **92**: 1–10.

181 Nyquist RA. *The handbook of infrared and Raman spectra of inorganic compounds and organic salts*. Academic Press: San Diego, 1997.

182 Weil M, Puchberger M, Füglein E, Baran EJ, Vannahme J, Jakobsen HJ *et al.* Single-Crystal Growth and Characterization of Disilver(I) Monofluorophosphate(V), Ag_2PO_3F: Crystal Structure, Thermal Behavior, Vibrational Spectroscopy, and Solid-State ^{19}F, ^{31}P, and ^{109}Ag MAS NMR Spectroscopy. *Inorg Chem* 2007; **46**: 801–808.

183 Frost RL, Palmer SJ, Xi Y. A Raman spectroscopic study of the mono-hydrogen phosphate mineral dorfmanite $Na_2(PO_3OH)\cdot 2H_2O$ and in comparison with brushite. *Spectrochim Acta Part A Mol Biomol Spectrosc* 2011; **82**: 132–136.

184 Long GJ, Longworth G, Battle P, Cheetham AK, Thundathil R V., Beveridge D. A study of anhydrous iron(III) sulfate by magnetic susceptibility, Moessbauer, and neutron diffraction techniques. *Inorg Chem* 1979; **18**: 624–632.

185 Masse R, Tordjman I, Durif A, Guitel JC. Crystal-structure of lacunary monophosphate $KTi_2(PO_4)_3$. Lacunary monophosphates $NbGe(PO_4)_3$ and $M^{+5}Ti(PO_4)_3$, where M^{+5} = Sb, Nb, Ta. *Bull la sosiete Fr Mineral Cristallogr* 1972; **95**: 47.

186 Orlova AI, Koryttseva AK, Loginova EE. A family of phosphates of langbeinite structure. Crystal-chemical aspect of radioactive waste immobilization. *Radiochemistry* 2011; **53**: 51–62.

187 Hazen RM, Palmer DC, Finger LW, Stucky GD, Harrison WTA, Gier TE. High-pressure crystal chemistry and phase transition of $RbTi_2(PO_4)_3$. *J Phys Condens Matter* 1994; **6**: 1333–1344.

188 Sysoeva TS, Asabina EA, Pet'kov VI, Kurazhkovskaya VS. Alkali (alkaline-earth) metal, aluminum, and titanium complex orthophosphates: Synthesis and characterization. *Russ J Inorg Chem* 2009; **54**: 829–839.

189 Leclaire A, Benmoussa A, Borel MM, Grandin A, Raveau B. $K_{2-x}Ti_2(PO_4)_3$ with $0 \leq x \leq 0.5$: A mixed-valence nonstoichiometric titanophosphate with the langbeinite structure. *J Solid State Chem* 1989; **78**: 227–231.

190 Niu LF, Liang W, Wu CZ, Wang YH. Cooperative Energy Transfer of Er-Gd-Tb System in Tb^{3+}, Er^{3+} Co-Doped $K_2GdZr(PO_4)_3$ as a Potential Visible Quantum Cutting Phosphor. *Adv Mater Res* 2014; **936**: 585–590.

191 Hu Q, Liao J-Y, Li C-T, He X-D, Ding X, Chen C-H. Synthesis of porous carbon-coated $NaTi_2(PO_4)_3$ nanocubes with a high-yield and superior rate properties. *J Mater Chem A* 2018; **6**: 24503–24508.
192 Xu Y, Cao W, Yin Y, Sheng J, An Q, Wei Q *et al.* Novel $NaTi_2(PO_4)_3$ nanowire clusters as high performance cathodes for Mg-Na hybrid-ion batteries. *Nano Energy* 2019; **55**: 526–533.
193 Liu Z, An Y, Pang G, Dong S, Xu C, Mi C *et al.* TiN modified $NaTi_2(PO_4)_3$ as an anode material for aqueous sodium ion batteries. *Chem Eng J* 2018; **353**: 814–823.
194 Vaalma C, Buchholz D, Passerini S. Non-aqueous potassium-ion batteries: a review. *Curr Opin Electrochem* 2018; **9**: 41–48.
195 Hwang J-Y, Myung S-T, Sun Y-K. Recent Progress in Rechargeable Potassium Batteries. *Adv Funct Mater* 2018; **28**: 1802938.
196 Strutynska N, Bondarenko M, Slobodyanik N, Baumer V, Zatovsky I, Bychkov K *et al.* Phase formation in molten system $(Na/K)_2O$-TiO_2-P_2O_5 . Crystal structures of NASICON and langbeinite-related phosphates $(K/Na)_{1+x}Ti_2(PO_4)_3$ (x = 0 and 0.357). *Cryst Res Technol* 2016; **51**: 627–633.
197 Mary TA, Evans JSO, Vogt T, Sleight AW. Negative Thermal Expansion from 0.3 to 1050 Kelvin in ZrW_2O_8. *Science (80-)* 1996; **272**: 90–92.
198 Fergus JW. Ceramic and polymeric solid electrolytes for lithium-ion batteries. *J Power Sources* 2010; **195**: 4554–4569.
199 Farlab. Elaborate: Diffraction. 2013. https://www.farlabs.edu.au/structure/elaborate-diffraction/.

Appendix

Table A1. Fractional Atomic Coordinates (×10^4) and Equivalent Isotropic Displacement Parameters (Å^2×10^3) for $Na_2Mg_2(SO_4)_3$_P21. U_{eq} is defined as 1/3 of the trace of the orthogonalised U_{IJ} tensor.

Atom	Wyckoff Symbol	x	y	z	Atomic Occupancy	U(eq)
S1	2a	45.5(7)	4879.9(10)	4473.4(5)	1	3.47(18)
S2	2a	4347.0(7)	3982.1(11)	8316.9(5)	1	3.32(18)
S3	2a	2614.8(7)	-964.0(10)	5121.1(5)	1	3.19(17)
S4	2a	8859.2(7)	-931.4(10)	8228.2(5)	1	3.90(18)
S5	2a	698.4(7)	5540.7(10)	8709.2(5)	1	3.20(18)
S6	2a	6597.6(7)	140.9(10)	9068.2(5)	1	3.44(19)
S7	2a	3264.2(7)	193.1(10)	2382.1(5)	1	3.53(19)
S8	2a	5799.1(7)	2784.5(11)	10617.1(5)	1	3.40(19)
S9	2a	2433.5(7)	10423.6(10)	8107.4(5)	1	3.26(18)
S10	2a	9201.0(7)	2921.6(10)	7201.3(5)	1	3.02(18)
S11	2a	1028.0(7)	6471.2(11)	6899.0(5)	1	3.62(18)
S12	2a	7614.8(7)	-1938.7(10)	6067.4(5)	1	3.21(19)
S13	2a	5813.4(8)	426.0(11)	4706.5(5)	1	3.15(18)
S14	2a	4348.0(7)	-2226.0(11)	7057.8(5)	1	3.13(18)
S15	2a	2202.6(7)	2739.8(11)	6417.7(5)	1	3.89(19)
S16	2a	1160.3(7)	7702.5(11)	10449.0(5)	1	3.41(18)
S17	2a	4130.7(7)	-3366.9(10)	3446.3(5)	1	3.64(19)
S18	2a	2413.1(8)	11511.5(11)	9914.8(5)	1	4.00(19)
Mg1	2a	2006.4(10)	8310.2(14)	9245.6(7)	1	4.8(3)
Mg2	2a	-1036.7(11)	9354.9(15)	9766.4(7)	1	4.3(3)
Mg3	2a	7865.1(11)	1347.6(15)	5920.1(7)	1	4.3(3)
Mg4	2a	5144.5(10)	-1561.4(15)	5724.6(7)	1	4.3(3)
Mg5	2a	1650.8(10)	3571.6(14)	7800.6(7)	1	5.4(3)
Mg6	2a	2163.0(11)	9415.6(15)	6545.8(7)	1	4.2(3)
Mg7	2a	8980.7(11)	-3763.4(15)	7307.3(7)	1	4.2(3)
Mg8	2a	5599.2(11)	-540.8(15)	3156.2(7)	1	4.6(3)
Mg9	2a	7503.8(11)	2038.7(15)	8052.1(7)	1	6.4(3)
Mg10	2a	4334.6(11)	1168.8(15)	9281.0(7)	1	4.5(3)
Mg11	2a	1305.7(10)	1981.7(14)	4912.7(7)	1	5.0(3)
Mg12	2a	5744.1(10)	-2908.9(15)	8540.9(7)	1	5.2(3)
Na1	2a	8597.4(14)	-4023.7(19)	8923.6(9)	1	9.8(4)
Na2	2a	2113.8(15)	-4098(2)	5775.3(10)	1	14.1(4)
Na3	2a	4566.2(17)	891(2)	7581.2(11)	1	21.9(5)
Na4	2a	506.5(13)	1741.2(19)	8764.5(9)	1	8.7(4)
Na5	2a	-77.2(14)	4756(2)	2864.0(9)	1	11.7(4)
Na6	2a	2901.1(13)	-3054(2)	7988.2(9)	1	9.8(4)
Na7	2a	6055.4(13)	-3092.2(19)	4548.9(9)	1	8.4(4)
Na8	2a	-193.1(13)	3667(2)	5929.1(9)	1	8.8(4)
Na9	2a	6727.0(14)	-1368(2)	7398.2(10)	1	10.5(4)
Na10	2a	3203(2)	-136(2)	3808.9(11)	1	33.9(6)
Na11	2a	6529.8(14)	3712(2)	9141.1(9)	1	9.7(4)
Na12	2a	6901.5(14)	-429.5(19)	10575.8(9)	1	9.3(4)
O1	2a	10205.8(19)	2707(3)	7641.9(13)	1	6.1(5)
O2	2a	1404(2)	4407(3)	8634.0(13)	1	5.9(6)

Atom	Wyckoff Symbol	x	y	z	Atomic Occupancy	U(eq)
O3	2a	2211(2)	9166(3)	8442.2(13)	1	6.2(5)
O4	2a	5525(2)	2892(3)	11239.3(13)	1	5.7(5)
O5	2a	5531(2)	-941(3)	4923.8(13)	1	5.8(5)
O6	2a	8904(2)	-1554(3)	8868.3(15)	1	6.0(6)
O7	2a	187(2)	7192(3)	7080.8(15)	1	6.8(6)
O8	2a	-427.1(19)	5326(3)	4989.8(12)	1	6.0(5)
O9	2a	1921(2)	11665(3)	8282.2(13)	1	5.9(5)
O10	2a	1987.9(19)	7595(3)	10126.3(12)	1	5.2(5)
O11	2a	3093(2)	12100(3)	9551.0(14)	1	5.5(6)
O12	2a	781(2)	6315(3)	10583.9(14)	1	6.2(6)
O13	2a	3287(2)	-2730(3)	3663.4(15)	1	6.7(6)
O14	2a	1159(2)	6906(3)	8674.4(13)	1	6.6(6)
O15	2a	3706.9(19)	-1130(3)	5213.1(13)	1	7.1(5)
O16	2a	2422.9(19)	557(3)	5048.7(12)	1	5.7(5)
O17	2a	3297(2)	4378(3)	8287.6(14)	1	7.1(6)
O18	2a	4407(2)	3383(3)	7690.8(15)	1	5.2(6)
O19	2a	7589.5(19)	-1919(3)	5371.2(13)	1	5.0(5)
O20	2a	4994.7(19)	1434(3)	4704.7(13)	1	6.7(5)
O21	2a	1663(2)	2818(3)	6922.8(13)	1	8.7(6)
O22	2a	5163(2)	-1949(3)	7643.4(14)	1	8.4(6)
O23	2a	7477(2)	-80(3)	9621.3(14)	1	6.2(6)
O24	2a	4767(2)	-2187(3)	6501.4(14)	1	9.7(6)
O25	2a	5984(2)	4189(3)	10373.2(13)	1	6.0(5)
O26	2a	975.3(19)	5706(3)	4541.0(13)	1	6.1(5)
O27	2a	9139(2)	4324(3)	6900.3(13)	1	5.9(6)
O28	2a	9820(2)	-288(3)	8210.6(14)	1	7.2(6)
O29	2a	484(2)	5350(3)	9345.2(13)	1	6.4(5)
O30	2a	1569(2)	8390(3)	11084.9(13)	1	8.0(6)
O31	2a	6602.5(19)	-2176(3)	6166.7(13)	1	8.5(6)
O32	2a	8437.4(19)	2715(3)	7552.6(13)	1	7.5(5)
O33	2a	8261(2)	-3120(3)	6365.4(13)	1	6.1(6)
O34	2a	2984(2)	11168(3)	10588.1(14)	1	8.3(6)
O35	2a	2049(2)	10165(3)	7412.8(12)	1	6.0(5)
O36	2a	2055(2)	-1668(3)	4520.7(14)	1	5.8(6)
O37	2a	5023(2)	5203(3)	8471.0(13)	1	6.8(6)
O38	2a	4193(2)	308(3)	2910.8(14)	1	5.4(6)
O39	2a	1450(2)	2900(3)	5777.4(13)	1	6.9(6)
O40	2a	8570(2)	-2047(3)	7730.5(14)	1	6.4(6)
O41	2a	9067.8(19)	1894(3)	6664.7(12)	1	5.5(5)
O42	2a	6475(2)	-1079(3)	8639.4(14)	1	7.6(6)
O43	2a	-666(2)	5110(3)	3828.2(14)	1	5.2(6)
O44	2a	3872(2)	-3588(3)	7114.2(13)	1	5.4(6)
O45	2a	8031(2)	103(3)	8066.5(13)	1	7.0(6)
O46	2a	5010(2)	2034(3)	10158.4(13)	1	8.2(6)
O47	2a	254(2)	3367(3)	4549.4(14)	1	7.4(6)
O48	2a	356(2)	8519(3)	10027.1(14)	1	7.4(6)
O49	2a	2739(2)	1397(3)	6429.0(13)	1	5.6(6)
O50	2a	695(2)	5688(3)	6292.4(13)	1	8.6(6)
O51	2a	2291(2)	-1522(3)	5678.4(15)	1	6.4(6)
O52	2a	3762(2)	-3864(3)	2766.1(13)	1	6.6(6)
O53	2a	3610(2)	-1084(3)	7014.9(14)	1	8.9(6)
O54	2a	1589(2)	12501(3)	9913.9(15)	1	6.7(6)

Atom	Wyckoff Symbol	x	y	z	Atomic Occupancy	U(eq)
O55	2a	1527(2)	5530(3)	7439.6(13)	1	6.3(5)
O56	2a	1922(2)	10242(3)	9592.5(14)	1	8.2(6)
O57	2a	5936(2)	273(3)	4052.8(13)	1	8.2(6)
O58	2a	-267(2)	5456(3)	8207.0(13)	1	4.7(6)
O59	2a	6706(2)	1411(3)	8691.6(13)	1	4.8(5)
O60	2a	2411(2)	352(3)	2676.3(13)	1	5.8(5)
O61	2a	5716(2)	323(3)	9333.6(13)	1	6.8(6)
O62	2a	3200(2)	1329(3)	1902.6(13)	1	6.7(6)
O63	2a	1786(2)	7522(3)	6838.6(16)	1	6.8(6)
O64	2a	4946(2)	-2326(3)	3486.8(15)	1	7.4(6)
O65	2a	6782(2)	905(3)	5119.2(14)	1	7.4(6)
O66	2a	3541(2)	10679(3)	8300.6(14)	1	6.2(6)
O67	2a	4716(2)	2957(3)	8839.9(15)	1	6.1(6)
O68	2a	2925(2)	3899(3)	6488.1(14)	1	9.6(6)
O69	2a	6771(2)	2006(3)	10735.2(13)	1	6.3(5)
O70	2a	4571(2)	-4542(3)	3868.7(13)	1	7.3(6)
O71	2a	8011(2)	-592(3)	6369.1(13)	1	8.4(6)
O72	2a	3256(2)	-1155(3)	2046.7(14)	1	6.7(6)

Table A2. Bond Lengths for $Na_2Mg_2(SO4)_3$_P21.

Atom	Atom	Length/Å	Atom	Atom	Length/Å
S1	O8	1.477(3)	Mg5	O55	2.010(3)
S1	O26	1.472(3)	Mg6	$Na2^{7}$	3.723(2)
S1	O43	1.480(3)	Mg6	$Na3^{7}$	3.728(3)
S1	O47	1.471(3)	Mg6	$Na5^{13}$	3.424(2)
S2	Na3	3.388(2)	Mg6	$Na6^{7}$	3.794(2)
S2	Na11	3.059(2)	Mg6	O35	2.025(3)
S2	$Na12^{1}$	3.304(2)	Mg6	$O43^{13}$	2.104(3)
S2	O17	1.473(3)	Mg6	$O49^{7}$	2.087(3)
S2	O18	1.473(3)	Mg6	$O51^{7}$	2.102(3)
S2	O37	1.470(3)	Mg6	$O53^{7}$	2.030(3)
S2	O67	1.469(3)	Mg6	O63	2.021(3)
S3	$Na7^{2}$	3.262(2)	Mg7	Na1	3.627(2)
S3	Na10	3.205(2)	Mg7	$Na5^{3}$	3.733(3)
S3	O15	1.466(3)	Mg7	Na9	3.885(2)
S3	O16	1.474(3)	Mg7	$Na10^{3}$	3.551(3)
S3	O36	1.472(3)	Mg7	$O7^{14}$	2.052(3)
S3	O51	1.471(3)	Mg7	$O27^{12}$	2.054(3)
S4	Na1	3.360(2)	Mg7	O33	2.085(3)
S4	$Na5^{3}$	3.265(2)	Mg7	O40	2.018(3)
S4	Na9	3.023(2)	Mg7	$O58^{14}$	2.065(3)
S4	O6	1.474(3)	Mg7	$O60^{3}$	2.093(3)
S4	O28	1.461(3)	Mg8	$Na2^{2}$	3.630(3)
S4	O40	1.481(3)	Mg8	$Na3^{3}$	3.729(3)
S4	O45	1.474(3)	Mg8	Na7	3.762(2)
S5	$Na1^{4}$	3.058(2)	Mg8	Na10	3.904(3)
S5	$Na12^{1}$	3.373(2)	Mg8	$O18^{3}$	2.075(3)
S5	O2	1.486(3)	Mg8	O38	2.028(3)
S5	O14	1.456(3)	Mg8	$O44^{2}$	2.131(3)
S5	O29	1.471(3)	Mg8	O57	2.002(3)
S5	O58	1.471(3)	Mg8	O64	2.126(3)

Atom	Atom	Length/Å	Atom	Atom	Length/Å
S6	Na12	3.178(2)	Mg8	O68^{3}	2.037(3)
S6	O23	1.464(3)	Mg9	Na9	3.584(2)
S6	O42	1.462(3)	Mg9	Na11	3.366(2)
S6	O59	1.482(3)	Mg9	O30^{5}	2.332(3)
S6	O61	1.471(3)	Mg9	O32	1.973(3)
S7	Na1^{2}	3.333(2)	Mg9	O45	1.979(3)
S7	Na9^{2}	3.311(2)	Mg9	O52^{2}	2.283(3)
S7	Na10	3.080(2)	Mg9	O59	2.047(3)
S7	O38	1.467(3)	Mg9	O72^{2}	1.995(3)
S7	O60	1.471(3)	Mg10	Na3	3.728(3)
S7	O62	1.476(3)	Mg10	Na11	3.934(2)
S7	O72	1.469(3)	Mg10	Na12^{1}	3.707(2)
S8	Mg1^{5}	2.9858(17)	Mg10	O11^{12}	2.127(3)
S8	Na6^{1}	3.144(2)	Mg10	O25^{5}	2.113(3)
S8	O4	1.473(3)	Mg10	O46	2.033(3)
S8	O25	1.482(3)	Mg10	O61	2.033(3)
S8	O46	1.444(3)	Mg10	O66^{12}	2.140(3)
S8	O69	1.487(3)	Mg10	O67	2.078(3)
S9	O3	1.467(3)	Mg11	Na7^{2}	3.497(2)
S9	O9	1.473(3)	Mg11	Na8	3.716(2)
S9	O35	1.457(3)	Mg11	Na8^{15}	3.755(2)
S9	O66	1.485(3)	Mg11	O8^{15}	2.028(3)
S10	Na5^{3}	3.264(2)	Mg11	O16	2.010(3)
S10	Na8^{6}	3.118(2)	Mg11	O19^{2}	2.057(3)
S10	O1	1.464(3)	Mg11	O39	2.003(3)
S10	O27	1.476(3)	Mg11	O47	1.958(3)
S10	O32	1.450(3)	Mg12	Na1	3.925(2)
S10	O41	1.481(3)	Mg12	Na6	3.766(2)
S11	Na2^{7}	3.178(2)	Mg12	Na9	3.408(2)
S11	Na6^{7}	3.012(2)	Mg12	Na11^{12}	3.529(2)
S11	O7	1.478(3)	Mg12	O4^{5}	2.062(3)
S11	O50	1.459(3)	Mg12	O22	2.082(3)
S11	O55	1.480(3)	Mg12	O34^{16}	2.360(3)
S11	O63	1.472(3)	Mg12	O37^{12}	2.040(3)
S12	Mg11^{3}	3.0368(17)	Mg12	O42	1.995(3)
S12	Na10^{3}	3.281(2)	Mg12	O62^{3}	2.056(3)
S12	O19	1.476(3)	Na1	O6	2.400(4)
S12	O31	1.474(3)	Na1	O29^{14}	2.575(3)
S12	O33	1.470(3)	Na1	O30^{16}	2.476(3)
S12	O71	1.474(3)	Na1	O34^{16}	2.643(3)
S13	Na2^{2}	3.293(2)	Na1	O54^{16}	2.940(4)
S13	O5	1.468(3)	Na1	O58^{14}	2.497(3)
S13	O20	1.476(3)	Na1	O62^{3}	2.648(3)
S13	O57	1.454(3)	Na2	O26^{12}	2.693(3)
S13	O65	1.461(3)	Na2	O39^{12}	3.003(4)
S14	Na3	3.160(2)	Na2	O50^{12}	2.480(3)
S14	Na6	3.246(2)	Na2	O51	2.482(4)
S14	Na9	3.253(2)	Na2	O57^{3}	2.668(3)
S14	O22	1.465(3)	Na2	O63^{12}	2.873(4)
S14	O24	1.447(3)	Na2	O65^{3}	2.726(4)
S14	O44	1.472(3)	Na2	O68^{12}	2.511(4)
S14	O53	1.472(3)	Na3	Na9	3.762(3)
S15	Na2^{7}	3.300(2)	Na3	O18	2.403(4)

Atom	Atom	Length/Å	Atom	Atom	Length/Å
S15	Na8	3.294(2)	Na3	O22	2.821(4)
S15	O21	1.458(3)	Na3	O52^{2}	2.594(4)
S15	O39	1.489(3)	Na3	O53	2.427(3)
S15	O49	1.473(3)	Na3	O66^{12}	2.342(4)
S15	O68	1.465(3)	Na4	Na5^{15}	3.862(3)
S16	Na1^{8}	3.377(2)	Na4	O1^{11}	2.496(3)
S16	Na4^{9}	3.295(2)	Na4	O2	2.868(3)
S16	Na11^{1}	3.203(2)	Na4	O9^{12}	2.420(3)
S16	O10	1.475(3)	Na4	O12^{10}	2.546(3)
S16	O12	1.477(3)	Na4	O28^{11}	2.332(3)
S16	O30	1.478(3)	Na4	O54^{12}	2.614(4)
S16	O48	1.453(3)	Na4	O56^{12}	2.671(3)
S17	Na3^{3}	3.244(2)	Na5	O1^{2}	3.001(4)
S17	Na7	3.052(2)	Na5	O7^{15}	2.453(4)
S17	O13	1.483(3)	Na5	O28^{2}	2.407(3)
S17	O52	1.483(3)	Na5	O35^{15}	2.640(3)
S17	O64	1.480(3)	Na5	O41^{2}	2.519(3)
S17	O70	1.465(3)	Na5	O43	2.420(3)
S18	Na1^{8}	3.177(2)	Na5	O71^{2}	2.895(4)
S18	Na4^{7}	3.089(2)	Na6	O3^{12}	2.605(3)
S18	Na12^{8}	3.315(2)	Na6	O4^{5}	2.514(3)
S18	O11	1.470(3)	Na6	O17^{12}	2.552(3)
S18	O34	1.481(3)	Na6	O44	2.606(3)
S18	O54	1.471(3)	Na6	O55^{12}	2.363(3)
S18	O56	1.466(3)	Na6	O63^{12}	2.586(4)
Mg1	Na4^{7}	3.856(2)	Na6	O69^{5}	2.641(3)
Mg1	Na6^{7}	3.477(2)	Na7	O5	2.379(3)
Mg1	Na11^{1}	3.521(2)	Na7	O15^{3}	2.943(3)
Mg1	Na12^{1}	3.846(2)	Na7	O16^{3}	2.410(3)
Mg1	O3	1.982(3)	Na7	O19	2.611(3)
Mg1	O10	2.004(3)	Na7	O20^{3}	2.449(3)
Mg1	O14	1.971(3)	Na7	O49^{3}	3.017(3)
Mg1	O56	1.999(3)	Na7	O64	2.485(4)
Mg1	O69^{1}	2.077(3)	Na7	O70	2.571(3)
Mg2	Na1^{4}	3.658(2)	Na8	O8	2.505(3)
Mg2	Na4^{9}	3.919(2)	Na8	O21	2.967(3)
Mg2	Na12^{4}	3.679(2)	Na8	O27^{11}	2.550(3)
Mg2	O6^{4}	2.083(3)	Na8	O36^{13}	2.500(3)
Mg2	O12^{9}	2.075(3)	Na8	O39	2.466(3)
Mg2	O23^{4}	2.050(3)	Na8	O41^{11}	2.677(3)
Mg2	O29^{9}	2.077(3)	Na8	O50	2.302(3)
Mg2	O48	2.007(3)	Na9	O22	2.399(3)
Mg2	O54^{10}	2.104(3)	Na9	O24	2.966(3)
Mg3	Na2^{2}	3.647(2)	Na9	O31	2.699(3)
Mg3	Na5^{3}	3.756(2)	Na9	O40	2.523(3)
Mg3	Na8^{6}	3.455(2)	Na9	O42	2.770(4)
Mg3	Na10^{2}	3.762(3)	Na9	O45	2.420(3)
Mg3	O13^{2}	2.187(3)	Na9	O52^{2}	2.478(3)
Mg3	O26^{3}	2.163(3)	Na9	O62^{3}	2.641(3)
Mg3	O36^{2}	2.128(3)	Na10	O13	2.498(4)
Mg3	O41	2.035(3)	Na10	O31^{2}	2.833(4)
Mg3	O65	1.994(3)	Na10	O33^{2}	2.732(4)
Mg3	O71	2.068(3)	Na10	O36	2.856(4)

Atom	Atom	Length/Å	Atom	Atom	Length/Å
Mg4	Na7	3.406(2)	Na10	O38	2.652(4)
Mg4	Na7[2]	3.671(2)	Na10	O60	2.420(3)
Mg4	Na9	3.664(2)	Na11	O10[5]	2.458(3)
Mg4	O5	2.004(3)	Na11	O25	2.948(3)
Mg4	O15	2.029(3)	Na11	O30[5]	2.786(3)
Mg4	O20[3]	2.106(3)	Na11	O34[5]	2.461(3)
Mg4	O24	1.952(3)	Na11	O37	2.605(3)
Mg4	O31	2.059(3)	Na11	O59	2.430(3)
Mg4	O70[2]	2.106(3)	Na11	O67	2.504(3)
Mg5	Na4	3.377(2)	Na11	O72[2]	2.627(3)
Mg5	Na6[7]	3.617(2)	Na12	O2[5]	2.492(3)
Mg5	Na12[1]	3.638(2)	Na12	O11[16]	2.370(4)
Mg5	O1[11]	2.089(3)	Na12	O17[5]	2.514(3)
Mg5	O2	2.054(3)	Na12	O23	2.389(3)
Mg5	O9[12]	2.073(3)	Na12	O61	2.814(3)
Mg5	O17	2.352(3)	Na12	O69	2.360(3)
Mg5	O21	2.009(3)			

[1]1-X,1/2+Y,2-Z; [2]1-X,1/2+Y,1-Z; [3]1-X,-1/2+Y,1-Z; [4]-1+X,1+Y,+Z; [5]1-X,-1/2+Y,2-Z; [6]1+X,+Y,+Z; [7]+X,1+Y,+Z; [8]1-X,3/2+Y,2-Z; [9]-X,1/2+Y,2-Z; [10]-X,-1/2+Y,2-Z; [11]-1+X,+Y,+Z; [12]+X,-1+Y,+Z; [13]-X,1/2+Y,1-Z; [14]1+X,-1+Y,+Z; [15]-X,-1/2+Y,1-Z; [16]1-X,-3/2+Y,2-Z

Table A3. Fractional Atomic Coordinates (×10⁴) and Equivalent Isotropic Displacement Parameters (Å²×10³) for $Na_2Mg_3(SO_4)_3$_Pbca. U_{eq} is defined as 1/3 of of the trace of the orthogonalised U_{IJ} tensor.

Atom	Wyckoff Symbol	x	y	z	Atomic Occupancy	U(eq)
S1	8c	3821.7(5)	1022.2(6)	6308.8(2)	1	4.74(13)
S2	8c	9467.3(5)	709.9(6)	6204.5(2)	1	4.84(13)
S3	8c	3648.0(5)	-2952.1(6)	7649.6(2)	1	4.56(13)
S4	8c	6026.1(5)	2701.8(6)	5151.5(2)	1	4.78(13)
Mg1	8c	11496.9(7)	-942.6(8)	6967.8(2)	1	5.12(16)
Mg2	8c	6775.0(7)	2332.7(8)	6269.8(2)	1	6.60(17)
Mg3	8c	8082.6(7)	559.2(8)	4537.1(2)	1	5.97(16)
Na1	8c	5914.9(9)	-798.1(10)	5581.8(3)	1	11.1(2)
Na2	8c	5403.5(9)	-1458.5(10)	6915.4(3)	1	8.85(19)
O1	8c	6876.4(16)	4097.8(17)	5081.5(5)	1	7.3(3)
O2	8c	10155.6(16)	581.3(17)	6650.8(5)	1	8.5(3)
O3	8c	5092.5(16)	-2413.0(18)	7728.3(5)	1	7.7(3)
O4	8c	2771.4(16)	-2598.7(17)	8056.0(5)	1	7.5(3)
O5	8c	8258.8(15)	-362.9(18)	6181.3(5)	1	8.7(3)
O6	8c	8880.5(15)	2292.7(17)	6163.4(5)	1	7.2(3)
O7	8c	10421.0(16)	449.9(18)	5822.4(5)	1	9.3(3)
O8	8c	3112.0(16)	193.2(18)	6673.2(5)	1	8.8(3)
O9	8c	4513.5(16)	3024.6(18)	5152.5(5)	1	7.5(3)
O10	8c	3658.3(15)	-4624.3(17)	7569.0(5)	1	6.4(3)

Atom	Wyckoff Symbol	x	y	z	Atomic Occupancy	U(eq)
O11	8c	3370.6(16)	513.6(18)	5851.7(5)	1	9.4(3)
O12	8c	5351.6(16)	664.9(18)	6351.7(5)	1	8.5(3)
O13	8c	6452.8(16)	1968.8(18)	5585.7(5)	1	8.9(3)
O14	8c	6298.2(15)	1594.2(18)	4775.9(5)	1	7.5(3)
O15	8c	3095.1(15)	-2167.6(17)	7243.4(5)	1	6.6(3)
O16	8c	3638.6(17)	2701.0(18)	6348.5(6)	1	10.5(3)

Table A4. Bond Lengths for $Na_2Mg_3(SO_4)_3$_Pbca.

Atom	Atom	Length/Å	Atom	Atom	Length/Å
S1	O8	1.4497(16)	Mg2	O5^{3}	2.0226(18)
S1	O11	1.4667(16)	Mg2	O5	2.7507(18)
S1	O12	1.4942(16)	Mg2	O6	2.0281(17)
S1	O16	1.4763(16)	Mg2	O12	1.9999(17)
S2	O2	1.4593(16)	Mg2	O13	2.0397(17)
S2	O5	1.4831(16)	Mg3	Na1^{6}	3.8261(11)
S2	O6	1.4915(15)	Mg3	Na1	3.8602(11)
S2	O7	1.4534(16)	Mg3	O1^{4}	2.0324(17)
S3	O3	1.4706(15)	Mg3	O7^{7}	1.9734(17)
S3	O4	1.4798(15)	Mg3	O9^{8}	2.0471(17)
S3	O10	1.4745(15)	Mg3	O11^{6}	2.0163(17)
S3	O15	1.4633(15)	Mg3	O14	2.0444(17)
S4	O1	1.4742(16)	Na1	O1^{4}	2.5591(18)
S4	O9	1.4667(15)	Na1	O5	2.8575(18)
S4	O13	1.4728(16)	Na1	O6^{4}	2.3803(17)
S4	O14	1.4806(16)	Na1	O9^{6}	2.9141(18)
Mg1	Na2^{1}	3.7483(11)	Na1	O11	2.7901(18)
Mg1	Na2^{2}	3.4427(11)	Na1	O12	2.6326(18)
Mg1	O2	2.0592(17)	Na1	O13	2.4623(18)
Mg1	O3^{2}	2.0514(17)	Na1	O14^{6}	2.4498(17)
Mg1	O8^{1}	2.0189(17)	Na2	O2^{4}	2.7416(18)
Mg1	O10^{3}	2.0978(17)	Na2	O3	2.5253(17)
Mg1	O15^{1}	2.0236(16)	Na2	O4^{2}	2.4640(17)
Mg1	O16^{4}	2.1588(18)	Na2	O6^{4}	2.5373(18)
Mg2	Na1^{3}	3.3900(11)	Na2	O8	2.7058(18)
Mg2	Na1	3.4796(11)	Na2	O10^{5}	2.3662(17)
Mg2	Na2^{3}	3.4425(11)	Na2	O12	2.4722(18)
Mg2	O4^{5}	2.0104(16)	Na2	O15	2.4738(17)

^{1}1+X,+Y,+Z; ^{2}1/2+X,+Y,3/2-Z; ^{3}3/2-X,1/2+Y,+Z; ^{4}3/2-X,-1/2+Y,+Z; ^{5}1-X,1/2+Y,3/2-Z; ^{6}1-X,-Y,1-Z; ^{7}2-X,-Y,1-Z; ^{8}1/2+X,1/2-Y,1-Z

Table A5. Fractional Atomic Coordinates (×10⁴) and Equivalent Isotropic Displacement Parameters (Å²×10³) for $Na_2Mg(SO_4)_2$ P-1. U_{eq} is defined as 1/3 of the trace of the orthogonalised U_{IJ} tensor.

Atom	Wyckoff Symbol	x	y	z	Atomic Occupancy	U(eq)
S1	2i	8233.4(5)	5398.7(4)	4312.9(3)	1	4.64(8)
S2	2i	7713.1(5)	2335.6(4)	5197.9(3)	1	4.91(8)
S3	2i	7039.3(5)	3057.9(4)	9699.3(3)	1	4.86(8)
S4	2i	7856.8(5)	6187.4(4)	9068.1(3)	1	4.05(8)
S5	2i	6054.3(5)	4721.3(4)	6167.2(3)	1	4.30(8)
S6	2i	3799.2(5)	4097.7(4)	8582.7(3)	1	6.62(9)
S7	2i	4707.2(5)	2314.6(4)	2048.2(3)	1	6.82(9)
S8	2i	6763.5(5)	9429.3(4)	10604.4(3)	1	6.99(9)
S9	2i	-950.0(5)	2496.4(4)	2471.0(3)	1	7.86(9)
S10	2i	9169.0(5)	3836.0(4)	7874.2(3)	1	4.50(8)
S11	2i	2583.3(5)	1384.2(4)	3887.1(3)	1	6.40(8)
S12	2i	921.4(7)	-633.9(4)	1284.6(3)	1	17.11(12)
S13	2i	4838.6(5)	-1102.0(4)	3039.0(4)	1	15.27(11)
S14	2i	-972.8(17)	-1126.4(13)	3318.4(11)	0.4833(16)	7.8(2)
S15	2i	-790.3(16)	-849.8(12)	3591.0(10)	0.5167(16)	7.8(2)
Mg1	2i	6101.2(7)	3734.5(5)	7816.0(4)	1	4.92(12)
Mg2	2i	9258.6(7)	4981.5(5)	6274.9(4)	1	5.12(12)
Mg3	2i	1841.3(7)	-1257.7(6)	3154.9(4)	1	5.90(12)
Mg4	1c	10000	5000	10000	1	4.95(17)
Mg5	2i	5464.4(7)	6693.8(6)	9652.5(4)	1	5.96(12)
Mg6	2i	5420.9(7)	3436.2(5)	4170.7(4)	1	5.12(12)
Mg7	2i	4062.6(9)	-364.1(7)	1235.0(8)	1	26.0(2)
Na1	2i	-3634.7(12)	-1750.9(10)	1985.1(8)	1	27.3(3)
Na2	2i	1720.5(10)	1353.0(8)	516.8(6)	1	16.37(19)
Na3	2i	7946.4(9)	7077.7(7)	7388.9(6)	1	10.38(16)
Na4	2i	3404.7(9)	2700.1(7)	6021.0(6)	1	10.41(16)
Na5	2i	5397.9(9)	4621.9(7)	2671.0(6)	1	9.46(16)
Na6	2i	-3454.0(9)	1393.2(7)	3244.4(6)	1	11.29(16)
Na7	2i	9190.8(9)	6740.2(7)	3200.9(6)	1	10.48(16)
Na8	2i	8015.5(9)	32.7(7)	4908.2(6)	1	14.03(18)
Na9	2i	4990(4)	646(4)	4750(3)	1	19.0(9)
Na10	2i	-3862.2(10)	1659.1(9)	851.0(6)	1	15.93(19)
Na11	2i	959.5(10)	-1967.4(11)	-533.7(7)	1	24.9(2)
Na12	2i	-1186.3(11)	-2883.6(10)	1106.2(8)	1	29.8(3)
Na13	2i	11762.7(13)	5610.4(10)	8489.3(9)	0.782(3)	13.6(3)
Mg15	2i	10255(6)	2340(3)	4373(4)	0.5	20.7(7)
Na14	2i	5061(5)	-128(5)	5118(3)	0.25	19.0(9)
Na15	2i	12100(5)	5706(4)	8216(4)	0.218(3)	13.6(3)
O1	2i	4225.7(14)	3771.4(12)	7858.3(9)	1	7.0(3)
O2	2i	5055.6(15)	-2146.6(12)	2912.1(10)	1	8.4(3)
O3	2i	8249.5(15)	1742.5(12)	4653.1(10)	1	9.1(3)
O4	2i	8814.9(14)	4965.4(12)	3709.8(9)	1	7.5(3)
O5	2i	5311.6(16)	4145.2(12)	5272.2(9)	1	9.1(3)
O6	2i	7312.4(14)	6810.0(11)	9602.9(9)	1	6.8(3)
O7	2i	6761.6(14)	5398.7(11)	8323.2(9)	1	7.3(3)
O8	2i	8241.7(16)	6480.0(12)	4230.3(10)	1	9.6(3)
O9	2i	6422.6(15)	3428.9(12)	10305.1(9)	1	8.6(3)
O10	2i	9335.0(14)	2789.7(11)	7589.2(9)	1	7.4(3)
O11	2i	675.9(16)	-839.9(12)	2074.7(10)	1	11.6(3)

Atom	Wyckoff Symbol	x	y	z	Atomic Occupancy	U(eq)
O12	2i	6378.2(16)	3168.7(13)	8855.6(10)	1	10.9(3)
O13	2i	5909.7(14)	5793.5(11)	6387.1(9)	1	6.6(2)
O14	2i	4999.8(16)	1327.6(12)	1781.8(10)	1	10.1(3)
O15	2i	5452.3(14)	4090.5(11)	6680.6(9)	1	5.9(2)
O16	2i	7239.7(15)	1651.2(12)	5719.9(10)	1	8.9(3)
O17	2i	5460.6(16)	2783.3(14)	2971.5(10)	1	12.7(3)
O18	2i	9799.1(14)	4579.0(12)	7447.1(9)	1	7.1(3)
O19	2i	7462.6(15)	4866.6(13)	6396.3(10)	1	9.9(3)
O20	2i	7778.2(15)	3710.1(13)	7676.8(10)	1	9.4(3)
O21	2i	5226.6(15)	3099.9(12)	1598.1(10)	1	9.2(3)
O22	2i	6578.3(15)	2550.9(13)	4638.1(10)	1	10.3(3)
O23	2i	-495.7(17)	1747.3(12)	1964.2(10)	1	11.9(3)
O24	2i	8748.9(15)	6937.9(12)	8786.9(9)	1	7.7(3)
O25	2i	9929.6(15)	4253.7(12)	8800.3(9)	1	7.8(3)
O26	2i	8995.1(16)	5489.4(13)	5202.0(10)	1	10.9(3)
O27	2i	8470.6(15)	3665.4(12)	10051.6(10)	1	9.7(3)
O28	2i	8583.3(15)	5639.2(12)	9607.5(10)	1	9.4(3)
O29	2i	8753.1(15)	3338.9(12)	5757.0(10)	1	8.7(3)
O30	2i	3439.6(16)	-1246.3(13)	2847.4(10)	1	11.3(3)
O31	2i	228.6(15)	3433.9(12)	3001.0(10)	1	9.9(3)
O32	2i	6844.5(15)	4714.1(13)	4075.3(10)	1	10.9(3)
O33	2i	3736.6(15)	3266.3(13)	9059.4(10)	1	10.2(3)
O34	2i	5996.2(17)	8331.0(13)	10064.5(11)	1	15.0(3)
O35	2i	2742.0(17)	318.9(12)	3842.4(10)	1	12.5(3)
O36	2i	6875.2(17)	1920.0(12)	9658.5(10)	1	11.9(3)
O37	2i	3293.4(16)	2113.9(13)	1858.9(10)	1	11.5(3)
O38	2i	4750.7(17)	5117.8(13)	9145.9(10)	1	11.9(3)
O39	2i	1508.9(17)	1357.8(14)	3118.6(10)	1	15.5(3)
O40	2i	2459.3(16)	4165.1(15)	8233.8(11)	1	14.5(3)
O41	2i	-1520.9(18)	1953.8(14)	3015.1(11)	1	16.1(3)
O42	2i	-1909.6(17)	2806.2(15)	1850.9(12)	1	20.6(4)
O43	2i	2241.7(19)	1685.1(14)	4642.3(11)	1	17.2(3)
O44	2i	3813.5(17)	2147.9(14)	3936.1(14)	1	20.7(4)
O45	2i	446(2)	280.7(14)	1151.0(11)	1	26.1(5)
O46	2i	7263(2)	10085.6(17)	10099.7(14)	1	31.2(5)
O47	2i	108(2)	-1583.4(14)	560.7(11)	1	27.6(5)
O48	2i	2316(2)	-368.3(15)	1411.4(13)	1	28.6(5)
O49	2i	-792(3)	-37(2)	3197.8(19)	0.610(3)	7.6(4)
O50	2i	5127(3)	-661(2)	2268(2)	0.577(4)	10.9(4)
O51	2i	5668(3)	-324(2)	3786.5(19)	0.576(4)	12.6(5)
O52	2i	6178(6)	9796(4)	11143(4)	0.375(5)	18.4(6)
O53	2i	8070(4)	9308(3)	11104(3)	0.375(5)	16.3(5)
O54	2i	-2002(3)	-1729(3)	3407(3)	0.4833(16)	15.6(5)
O55	2i	360(20)	-1202(17)	3699(12)	0.4833(16)	8.0(14)
O56	2i	-399(4)	-71(4)	4396(3)	0.4833(16)	28.7(7)
O57	2i	-1054(11)	-252(9)	2938(7)	0.197(3)	7.6(4)
O65	2i	-1198(9)	-485(7)	2737(6)	0.193(3)	7.6(4)
O58	2i	-1702(3)	-1266(3)	3901(2)	0.5167(16)	15.6(5)
O59	2i	290(20)	-1312(16)	3579(11)	0.5167(16)	8.0(14)
O60	2i	-1693(4)	-1958(3)	2509(3)	0.5167(16)	28.7(7)
O61	2i	5732(3)	9894(2)	10792(2)	0.625(5)	18.4(6)
O62	2i	7679(3)	9461(2)	11439(2)	0.580(4)	16.3(5)

Atom	Wyckoff Symbol	x	y	z	Atomic Occupancy	U(eq)
O63	2i	5561(4)	-430(3)	2696(3)	0.423(4)	10.9(4)
O64	2i	5604(4)	-656(3)	4076(3)	0.424(4)	12.6(5)
Na17	2i	10230(8)	2051(4)	4442(5)	0.5	20.7(7)
Na18	2i	-279.0(8)	377.3(7)	2193.0(5)	1	6.87(15)

Table A6. Bond Lengths for $Na_2Mg(SO_4)_2$ P-1.

Atom	Atom	Length/Å	Atom	Atom	Length/Å
S1	Na5	3.3109(10)	Mg5	O38	1.9862(17)
S1	Na7	3.0408(10)	Mg6	Na3^{6}	3.7112(11)
S1	O4	1.4795(15)	Mg6	Na5	3.2169(11)
S1	O8	1.4797(15)	Mg6	Na6^{2}	3.6155(11)
S1	O26	1.4636(15)	Mg6	O5	1.9999(16)
S1	O32	1.4710(15)	Mg6	O13^{6}	2.1177(16)
S1	Na17^{1}	3.385(7)	Mg6	O17	2.0909(17)
S2	Na6^{2}	3.0745(10)	Mg6	O22	2.0581(16)
S2	Na8	3.1697(11)	Mg6	O32	2.0727(16)
S2	Na9	3.061(5)	Mg6	O44	2.0191(18)
S2	O3	1.4730(15)	Mg7	Na1^{2}	3.6179(14)
S2	O16	1.4825(15)	Mg7	Na6^{2}	3.6268(13)
S2	O22	1.4726(15)	Mg7	Na10^{2}	3.3640(14)
S2	O29	1.4692(15)	Mg7	Na10^{11}	3.5816(15)
S3	Na10^{3}	3.1207(11)	Mg7	O14	2.1397(18)
S3	Na11^{4}	3.1146(13)	Mg7	O36^{4}	2.1452(18)
S3	Na13^{5}	2.9820(14)	Mg7	O46^{6}	2.463(3)
S3	Na15^{5}	3.370(6)	Mg7	O48	2.053(2)
S3	O9	1.4817(15)	Mg7	O50	1.975(3)
S3	O12	1.4576(15)	Mg7	O52^{14}	2.365(5)
S3	O27	1.4696(16)	Mg7	O61^{14}	2.171(3)
S3	O36	1.4769(16)	Mg7	O63	2.582(5)
S4	Na2^{6}	3.1337(11)	Na1	O1^{8}	2.6955(18)
S4	Na3	3.2855(10)	Na1	O2^{9}	2.4694(18)
S4	Na12^{7}	3.2114(14)	Na1	O12^{8}	2.911(2)
S4	O6	1.4906(15)	Na1	O33^{8}	2.414(2)
S4	O7	1.4732(15)	Na1	O50^{9}	2.344(3)
S4	O24	1.4638(15)	Na1	O52^{15}	2.729(6)
S4	O28	1.4639(15)	Na1	O54	2.551(4)
S5	Na3	3.2334(10)	Na1	O65	2.589(9)
S5	Na4	3.3565(10)	Na1	O60	2.198(4)
S5	Na5^{6}	3.0507(10)	Na1	O62^{15}	2.387(3)
S5	O5	1.4546(15)	Na1	O63^{9}	2.480(4)
S5	O13	1.4876(15)	Na2	Na11^{11}	3.3095(16)
S5	O15	1.4886(14)	Na2	O6^{6}	2.4859(17)
S5	O19	1.4528(15)	Na2	O24^{6}	2.6477(18)
S6	Na1^{8}	3.0746(13)	Na2	O34^{6}	2.944(2)
S6	Na5^{6}	3.1318(10)	Na2	O37	2.2870(19)
S6	Na12^{8}	3.1788(12)	Na2	O45	2.363(2)
S6	Na15^{9}	3.250(5)	Na2	O46^{6}	2.696(3)
S6	O1	1.4815(15)	Na2	O47^{11}	2.436(2)
S6	O33	1.4834(15)	Na2	O53^{6}	2.837(5)
S6	O38	1.4529(17)	Na3	O13	2.3879(17)
S6	O40	1.4706(16)	Na3	O19	2.9780(19)

Atom	Atom	Length/Å	Atom	Atom	Length/Å
S7	Na2	3.3224(12)	Na3	O23^{6}	2.6451(19)
S7	Na5	2.9091(10)	Na3	O24	2.3346(17)
S7	Na6^{2}	3.0986(10)	Na3	O31^{6}	2.5336(18)
S7	Na10^{2}	3.0765(11)	Na3	O37^{6}	2.4634(18)
S7	O14	1.4757(16)	Na3	O39^{6}	2.401(2)
S7	O17	1.4731(16)	Na3	Na18^{6}	3.5149(12)
S7	O21	1.4958(15)	Na4	Na5^{6}	3.5587(12)
S7	O37	1.4530(16)	Na4	Na8^{4}	3.4598(13)
S8	Na1^{7}	3.1104(11)	Na4	O1	2.9544(17)
S8	Na2^{6}	3.1163(11)	Na4	O2^{4}	2.4662(17)
S8	Na10^{7}	3.2360(12)	Na4	O8^{6}	2.3518(18)
S8	Na10^{10}	3.2103(11)	Na4	O15	2.3451(17)
S8	O34	1.4710(16)	Na4	O43	2.284(2)
S8	O46	1.4469(19)	Na4	O54^{8}	2.307(4)
S8	O52	1.366(5)	Na4	O58^{8}	2.374(3)
S8	O53	1.523(4)	Na4	Na17^{9}	3.535(8)
S8	O61	1.529(3)	Na5	O1^{6}	2.4558(17)
S8	O62	1.468(3)	Na5	O7^{6}	2.4930(17)
S8	Na18^{7}	3.3434(10)	Na5	O13^{6}	2.4936(17)
S9	Na3^{6}	3.1744(10)	Na5	O15^{6}	2.4342(17)
S9	Na10	3.3412(11)	Na5	O17	2.6178(19)
S9	Na11^{11}	3.2364(12)	Na5	O21	2.4192(18)
S9	Na15^{6}	3.246(5)	Na5	O32	2.4151(18)
S9	O23	1.4956(17)	Na6	Na9^{9}	3.614(4)
S9	O31	1.4739(16)	Na6	O3^{9}	2.4552(18)
S9	O41	1.4534(16)	Na6	O14^{9}	2.5443(18)
S9	O42	1.4656(17)	Na6	O17^{9}	2.5136(19)
S9	Na18	3.1226(10)	Na6	O22^{9}	2.5838(18)
S10	Na7^{1}	3.0791(10)	Na6	O41	2.2572(19)
S10	Na12^{4}	3.1101(12)	Na6	O50^{9}	2.733(3)
S10	Na13	2.9811(14)	Na6	O51^{9}	2.678(3)
S10	Na15	3.376(6)	Na6	O63^{9}	2.297(4)
S10	O10	1.4834(15)	Na7	O4	2.6414(17)
S10	O18	1.4780(15)	Na7	O8	2.3188(17)
S10	O20	1.4437(15)	Na7	O10^{1}	2.4327(17)
S10	O25	1.4732(15)	Na7	O18^{1}	2.5940(17)
S11	Na3^{6}	3.2707(10)	Na7	O29^{1}	2.4922(18)
S11	Na8^{4}	3.1104(10)	Na7	O40^{6}	2.4455(19)
S11	Na9	3.150(5)	Na7	O54^{16}	2.754(4)
S11	O35	1.4789(16)	Na7	O55^{16}	2.59(2)
S11	O39	1.4774(17)	Na7	O59^{16}	2.457(19)
S11	O43	1.4623(17)	Na7	O60^{16}	2.516(5)
S11	O44	1.4497(17)	Na8	O3	2.3686(18)
S11	Na17^{9}	3.311(8)	Na8	O16	2.8353(18)
S11	Na18	3.3631(9)	Na8	O35^{4}	2.5679(19)
S12	Na2	3.1939(11)	Na8	O43^{4}	2.521(2)
S12	Na2^{11}	3.3429(12)	Na8	O51	2.611(3)
S12	Na11	3.3098(14)	Na8	O55^{4}	2.461(17)
S12	Na12	3.2042(12)	Na8	O56^{4}	2.556(4)
S12	O11	1.4983(16)	Na8	O56^{2}	2.210(4)
S12	O45	1.486(2)	Na8	O58^{2}	2.378(4)
S12	O47	1.4707(18)	Na8	O59^{4}	2.656(16)
S12	O48	1.442(2)	Na8	O64	2.471(4)

Atom	Atom	Length/Å	Atom	Atom	Length/Å
S12	Na18	2.7316(11)	Na9	Na9^{4}	2.059(10)
S13	Na1^{2}	2.9801(12)	Na9	Na14	1.308(8)
S13	Na6^{2}	3.2893(11)	Na9	Na14^{4}	0.760(6)
S13	Na9	3.338(4)	Na9	O16	2.422(5)
S13	Na14^{4}	3.232(5)	Na9	O22	2.771(5)
S13	O2	1.4762(15)	Na9	O35	2.404(5)
S13	O30	1.4489(16)	Na9	O44	2.994(5)
S13	O50	1.603(3)	Na9	O51	2.335(5)
S13	O51	1.381(3)	Na9	O51^{4}	2.854(5)
S13	O63	1.367(4)	Na9	O64	2.290(6)
S13	O64	1.635(4)	Na9	O64^{4}	2.274(6)
S14	Na1	2.957(2)	Na10	O9^{17}	2.6684(18)
S14	Na7^{12}	2.8949(19)	Na10	O14^{9}	2.3252(18)
S14	O49	1.481(3)	Na10	O21^{9}	2.7088(18)
S14	O54	1.283(4)	Na10	O34^{10}	2.436(2)
S14	O55	1.48(2)	Na10	O36^{17}	2.4379(18)
S14	O56	1.927(4)	Na10	O42	2.275(2)
S14	O57	1.442(11)	Na10	O46^{15}	3.014(3)
S14	O65	1.425(9)	Na10	O52^{15}	2.640(6)
S14	O58	1.456(4)	Na10	O61^{10}	2.966(4)
S14	O59	1.45(2)	Na10	O61^{15}	2.271(3)
S14	O60	1.463(4)	Na11	O23^{11}	2.4133(18)
S14	Na18	3.1071(19)	Na11	O24^{15}	2.3276(18)
S15	Na7^{12}	3.1841(18)	Na11	O27^{4}	2.713(2)
S15	Na8^{9}	3.1363(18)	Na11	O36^{4}	2.414(2)
S15	Na8^{4}	3.1480(18)	Na11	O42^{11}	2.922(2)
S15	O49	1.372(3)	Na11	O46^{6}	2.594(2)
S15	O54	1.450(4)	Na11	O47	2.360(2)
S15	O55	1.46(3)	Na12	O6^{15}	2.5005(18)
S15	O56	1.440(4)	Na12	O10^{4}	2.5032(18)
S15	O57	1.479(11)	Na12	O11	2.830(2)
S15	O65	1.585(9)	Na12	O25^{4}	2.589(2)
S15	O58	1.316(4)	Na12	O28^{15}	2.846(2)
S15	O59	1.50(2)	Na12	O33^{8}	2.672(2)
S15	O60	1.949(4)	Na12	O40^{8}	2.553(2)
Mg1	Na1^{8}	3.4278(13)	Na12	O47	2.446(2)
Mg1	Na4	3.3532(11)	Na12	O60	2.769(4)
Mg1	Na5^{6}	3.1781(11)	Na13	Na15	0.686(6)
Mg1	O1	2.1264(16)	Na13	O9^{5}	2.2907(19)
Mg1	O2^{4}	2.1118(16)	Na13	O18	2.2677(19)
Mg1	O7	2.0941(16)	Na13	O25	2.601(2)
Mg1	O12	2.0088(16)	Na13	O27^{5}	2.613(2)
Mg1	O15	2.0335(15)	Na13	O40^{2}	2.294(2)
Mg1	O20	1.9597(16)	Na13	O42^{6}	2.273(2)
Mg2	Na3	3.9517(11)	Mg15	O3	2.382(6)
Mg2	Na7^{1}	3.3207(11)	Mg15	O8^{1}	2.436(7)
Mg2	Na13	3.7621(14)	Mg15	O26^{1}	2.713(4)
Mg2	Na15	3.606(5)	Mg15	O41^{2}	2.424(7)
Mg2	O4^{1}	2.1227(16)	Mg15	O43^{2}	2.542(6)
Mg2	O18	2.1067(15)	Na14	Na14^{4}	0.579(9)
Mg2	O19	2.0407(16)	Na14	O16	2.704(6)
Mg2	O26	2.0177(16)	Na14	O16^{4}	2.627(6)
Mg2	O29	2.0860(16)	Na14	O35^{4}	2.671(5)

Atom	Atom	Length/Å	Atom	Atom	Length/Å
Mg2	O31[6]	2.1032(16)	Na14	O51	2.531(5)
Mg3	Na7[12]	3.4608(11)	Na14	O51[4]	2.288(5)
Mg3	Na8[4]	3.3521(12)	Na14	O64[4]	2.010(7)
Mg3	Na9	3.680(5)	Na14	O64	2.103(6)
Mg3	Na14	3.834(5)	Na15	O4[1]	3.013(6)
Mg3	Na14[4]	3.580(5)	Na15	O9[5]	2.437(5)
Mg3	O10[4]	2.0671(16)	Na15	O18	2.429(5)
Mg3	O11	2.1671(17)	Na15	O21[1]	2.882(6)
Mg3	O16[4]	2.1097(16)	Na15	O40[2]	2.212(5)
Mg3	O30	1.9947(17)	Na15	O42[6]	2.082(5)
Mg3	O35	2.0510(17)	O3	Na17	2.282(8)
Mg3	O55	2.12(2)	O8	Na17[1]	2.518(8)
Mg3	O59	2.04(2)	O11	Na18	2.1855(19)
Mg4	Na12[7]	3.8690(15)	O23	Na18	2.0031(18)
Mg4	Na12[4]	3.8690(15)	O39	Na18	2.0631(18)
Mg4	Na13[5]	3.7274(17)	O41	Na17[9]	2.584(8)
Mg4	Na13	3.7274(17)	O43	Na17[9]	2.362(8)
Mg4	O25	2.0787(14)	O45	Na18	2.145(2)
Mg4	O25[5]	2.0788(14)	O49	O65	0.817(9)
Mg4	O27[5]	2.1573(15)	O49	Na17[9]	2.917(8)
Mg4	O27	2.1573(15)	O49	Na18	2.064(3)
Mg4	O28[5]	1.9920(15)	O50	O63	0.705(4)
Mg4	O28	1.9920(15)	O51	O63	1.796(5)
Mg5	Na2[6]	3.6398(12)	O51	O64	0.722(5)
Mg5	Na5[6]	3.7537(11)	O52	O61	0.713(6)
Mg5	Na10[10]	3.2621(12)	O52	O62	1.798(7)
Mg5	Na12[7]	3.6563(13)	O53	O62	0.841(5)
Mg5	Na13[9]	3.7605(15)	O53	Na18[7]	2.140(4)
Mg5	Na15[9]	3.564(5)	O54	O58	0.865(5)
Mg5	O6	2.0525(16)	O54	O60	1.654(5)
Mg5	O9[13]	2.0901(16)	O56	O58	1.729(5)
Mg5	O21[6]	2.1260(16)	O56	Na17[9]	2.730(7)
Mg5	O33[13]	2.0885(16)	O65	Na18	1.878(9)
Mg5	O34	2.0547(17)	O62	Na18[7]	2.149(3)

[1]2-X,1-Y,1-Z; [2]1+X,+Y,+Z; [3]1+X,+Y,1+Z; [4]1-X,-Y,1-Z; [5]2-X,1-Y,2-Z; [6]1-X,1-Y,1-Z; [7]1+X,1+Y,1+Z; [8]-X,-Y,1-Z; [9]-1+X,+Y,+Z; [10]-X,1-Y,1-Z; [11]-X,-Y,-Z; [12]-1+X,-1+Y,+Z; [13]1-X,1-Y,2-Z; [14]+X,-1+Y,-1+Z; [15]-1+X,-1+Y,-1+Z; [16]1+X,1+Y,+Z;[17]-1+X,+Y,-1+Z

Table A7. Fractional Atomic Coordinates (×10⁴) and Equivalent Isotropic Displacement Parameters (Å²×10³) for $K_{0.1}Na_{1.9}Mg_2(SO_4)_3$. U_{eq} is defined as 1/3 of the trace of the orthogonalised U_{IJ} tensor.

Atom	x	y	z	U(eq)
K1	8005.1(19)	10617.9(6)	9310.3(8)	33.8(8)
K2	1877.0(16)	8932.8(5)	9115.2(6)	18.0(6)
K4	-1827.7(16)	7237.5(5)	9177.8(5)	16.2(6)
K6	7046.6(18)	6035.7(6)	7580.1(6)	24.7(7)
K9	7977.8(18)	7256.0(6)	5950.7(6)	25.5(7)
K12	6844.2(16)	6017.6(5)	4294.2(5)	16.6(6)
K13	3085.9(17)	4406.7(5)	4093.8(6)	20.3(6)
K15	1900.7(15)	5633.8(5)	2425.5(5)	14.4(6)
K18	8011.6(18)	7243.8(6)	2594.0(7)	28.3(7)

Atom	x	y	z	U(eq)
S1	7674.8(9)	9585.1(3)	9797.8(3)	7.43(17)
S2	2718.2(9)	8613.8(3)	10201.8(3)	7.44(17)
S3	4977.6(10)	9281.8(3)	8802.9(3)	10.57(18)
S4	8805.3(9)	8375.1(3)	9198.8(3)	6.71(16)
S5	2386.6(9)	7943.8(3)	8526.6(3)	8.07(17)
S6	4923.1(10)	7599.2(3)	9496.6(3)	8.44(17)
S7	1277.4(9)	6697.8(3)	9062.8(3)	10.31(17)
S8	7412.4(9)	6951.4(3)	8122.1(3)	6.64(16)
S9	5126.1(9)	5873.9(3)	8829.4(3)	6.37(17)
S10	258.0(9)	5691.1(3)	7878.1(3)	6.33(16)
S11	9874.9(9)	7457.2(3)	7110.4(3)	5.79(16)
S12	7552.0(9)	6332.0(3)	6503.6(3)	6.54(16)
S13	13796.4(9)	6589.6(3)	7483.2(3)	8.08(17)
S14	6266.6(9)	8256.7(3)	4138.4(3)	6.53(16)
S15	7371.3(9)	7061.6(3)	4851.1(3)	6.57(17)
S16	12625.5(9)	5382.0(3)	6846.1(3)	6.07(16)
S17	14764.8(9)	7660.6(3)	6222.6(3)	6.72(17)
S18	8808.8(9)	5076.0(3)	5892.3(3)	6.43(16)
S19	10065.8(9)	5683.6(3)	4558.1(3)	8.07(17)
S20	6286.6(9)	4914.5(3)	4317.7(3)	8.11(17)
S21	1291.8(9)	6754.3(3)	2362.6(3)	7.39(16)
S22	7884.5(9)	6197.2(3)	3178.7(3)	6.62(17)
S23	13731.7(10)	6616.1(3)	4254.5(3)	7.17(16)
S24	8772.1(9)	5041.7(3)	2451.6(3)	6.51(16)
S25	5026.9(9)	6001.0(3)	2146.0(3)	6.98(17)
S26	9843.9(9)	4080.8(3)	441.7(3)	6.82(17)
S27	2899.6(9)	5443.1(3)	3508.4(3)	7.69(17)
Mg1	5626.1(15)	8669.1(5)	9656.0(5)	17.7(3)
Mg2	6593.4(14)	7282.7(4)	10438.8(4)	9.2(2)
Mg3	3372.4(13)	8882.5(4)	7892.3(4)	6.5(2)
Mg4	4279.2(14)	6988.2(5)	8539.4(5)	16.3(3)
Mg5	3532.3(13)	5507.8(4)	7921.7(4)	8.2(2)
Mg6	6544.0(13)	7284.5(4)	7109.1(4)	7.2(2)
Mg7	10693.1(13)	6308.9(4)	6929.0(4)	8.0(2)
Mg8	11481.6(13)	7856.2(4)	6210.9(4)	7.7(2)
Mg9	11655.9(13)	4420.6(4)	6244.6(4)	8.6(2)
Mg10	8469.6(13)	6098.0(4)	5437.7(4)	8.6(2)
Mg11	9414.0(13)	7968.3(4)	4682.1(4)	8.3(2)
Mg12	9165.2(13)	4557.1(4)	4846.3(4)	9.7(2)
Mg13	10822.9(13)	6322.2(4)	3723.4(4)	8.8(2)
Mg14	6579.4(13)	3969.0(4)	3762.7(4)	6.5(2)
Mg15	5773.9(13)	5318.7(4)	2942.5(4)	7.4(2)
Mg16	9375.5(13)	4594.4(4)	1405.6(4)	6.8(2)
Mg17	11639.6(13)	4469.7(4)	-428.3(4)	7.2(2)
Mg18	4287.3(13)	7110.2(4)	1864.2(4)	8.3(2)
Na1	8005.1(19)	10617.9(6)	9310.3(8)	33.8(8)
Na2	1877.0(16)	8932.8(5)	9115.2(6)	18.0(6)
Na3	4076.8(17)	6482.9(5)	9755.7(5)	13.4(3)
Na4	-1827.7(16)	7237.5(5)	9177.8(5)	16.2(6)
Na5	893.7(16)	6842.6(5)	8059.3(5)	12.6(3)
Na6	7046.6(18)	6035.7(6)	7580.1(6)	24.7(7)
Na7	9143.1(17)	5183.0(6)	6894.4(5)	13.6(3)
Na8	14084.4(16)	6500.1(5)	6424.7(5)	13.3(3)

Atom	x	y	z	U(eq)
Na9	7977.8(18)	7256.0(6)	5950.7(6)	25.5(7)
Na10	5789.2(17)	8171.3(5)	5207.3(5)	13.1(3)
Na11	5784.8(17)	4814.5(6)	5308.9(5)	14.0(3)
Na12	6844.2(16)	6017.6(5)	4294.2(5)	16.6(6)
Na13	3085.9(17)	4406.7(5)	4093.8(6)	20.3(6)
Na14	4091.2(16)	6507.1(5)	3102.0(5)	11.8(3)
Na15	1900.7(15)	5633.8(5)	2425.5(5)	14.4(6)
Na16	9084.9(17)	5166.5(5)	3580.2(5)	11.8(3)
Na17	894.5(17)	6918.2(6)	1387.2(5)	16.8(3)
Na18	8011.6(18)	7243.8(6)	2594.0(7)	28.3(7)
O1	7844(15)	9801(5)	9359(5)	11.7(19)
O2	6418(12)	9271(4)	9797(4)	9.8(15)
O3	8986(3)	9332.6(11)	9885.3(10)	19.1(6)
O4	4101(3)	8786.0(10)	10078.5(9)	14.6(6)
O5	2598(3)	8619.1(9)	10690.4(8)	9.4(5)
O6	1624(3)	8902.1(9)	9988.6(9)	13.6(6)
O7	4345(10)	9055(4)	9198(4)	11.7(16)
O8	6371(3)	9089.9(10)	8700.5(11)	19.0(6)
O9	2518(3)	8123.4(9)	10052.3(9)	12.1(5)
O10	5015(8)	9817(2)	8928(2)	11.1(11)
O11	4052(6)	9245.1(19)	8428.5(17)	13.2(9)
O12	2110(3)	8099.2(10)	8985.0(10)	17.3(6)
O13	2608(8)	8413(3)	8317(2)	13.2(11)
O14	7509(3)	8452.7(10)	9447.8(10)	17.9(6)
O15	9340(3)	8828.0(9)	9025.4(9)	11.1(5)
O16	9807(3)	8164.1(9)	9511.8(9)	11.5(5)
O17	8535(3)	8047.5(9)	8825.6(9)	15.3(6)
O18	5716(3)	7606.1(10)	9910.2(9)	17.1(6)
O19	4810(3)	8094.9(9)	9341.8(9)	13.0(5)
O20	3532(3)	7385.7(9)	9562.6(9)	13.9(6)
O21	5647(3)	7321.5(10)	9149.5(10)	19.4(6)
O22	3673(3)	7659.7(10)	8509.6(9)	13.3(5)
O23	1193(3)	7670.6(10)	8366.8(9)	16.1(6)
O24	689(3)	7141.7(9)	9232.5(9)	12.7(5)
O25	178(3)	6440.5(10)	8819.6(10)	14.4(6)
O26	2363(3)	6800.7(10)	8733.4(11)	22.4(7)
O27	1855(3)	6403.7(11)	9416.0(13)	29.8(8)
O28	6105(3)	7162.4(9)	8268.3(9)	13.2(5)
O29	5014(3)	6375.6(9)	8742.1(10)	15.9(6)
O30	4864(3)	5783.5(10)	9304.2(9)	13.5(5)
O31	6511(3)	5686.2(9)	8705.5(9)	10.2(5)
O32	4061(3)	5608.9(9)	8573.2(9)	13.0(5)
O33	8592(3)	7227.8(9)	8303.4(9)	10.6(5)
O34	7573(3)	6462.2(9)	8280.2(9)	10.4(5)
O35	7456(3)	6935.2(9)	7631.2(8)	9.1(5)
O36	1624(3)	5781.2(10)	8089.6(9)	13.5(6)
O37	-70(3)	6081.0(9)	7569.9(9)	13.0(5)
O38	-850(3)	5659.7(9)	8215.4(9)	11.7(5)
O39	286(3)	5233.6(8)	7643.4(9)	8.2(5)
O40	8458(3)	7632.3(9)	7008.9(9)	9.8(5)
O41	10187(3)	7517.7(9)	7585.3(8)	11.7(5)
O42	10030(3)	6964.1(9)	6991.4(9)	13.4(6)
O43	10886(3)	7751.8(9)	6859.6(8)	10.7(5)

Atom	x	y	z	U(eq)
O44	8687(3)	6110.0(10)	6754.3(11)	22.7(7)
O45	12567(3)	6474.7(10)	7216.7(10)	19.0(6)
O46	13376(3)	6903.5(10)	7856.6(10)	17.5(6)
O47	14435(3)	6156.2(10)	7664.7(9)	12.9(5)
O48	14790(3)	6837.9(10)	7189.7(9)	13.5(5)
O49	11279(3)	5635.8(8)	6820.5(9)	8.9(5)
O50	13007(3)	5275.9(11)	7307.1(9)	15.9(6)
O51	13706(3)	5671.2(11)	6635.9(12)	23.5(7)
O52	12487(3)	4940.5(11)	6608.1(11)	22.6(7)
O53	13359(3)	7542.8(9)	6391.2(9)	12.6(5)
O54	15778(3)	7686.5(10)	6586.0(9)	13.8(5)
O55	15232(3)	7286.8(10)	5914.2(9)	14.2(6)
O56	14719(3)	8125.2(9)	6000.3(9)	11.1(5)
O57	7305(3)	6822.9(9)	6644.3(9)	12.5(5)
O58	6282(3)	6061.4(10)	6585.4(13)	29.0(8)
O59	7885(4)	6351.3(10)	6030.4(9)	21.5(7)
O60	7653(3)	5227.5(9)	6179.5(9)	11.2(5)
O61	9827(3)	4830.7(9)	6178.2(9)	11.1(5)
O62	9463(3)	5497.0(9)	5684.3(9)	10.0(5)
O63	8314(3)	4751.9(9)	5539.6(9)	12.1(5)
O64	7700(3)	6697.0(11)	5175.3(10)	24.1(7)
O65	8658(3)	7330.6(10)	4784.7(9)	16.2(6)
O66	6262(3)	7354.3(9)	5041.7(9)	15.1(6)
O67	5381(3)	8515.8(10)	4456.6(9)	13.9(6)
O68	7614(3)	8178.8(11)	4354.7(11)	24.0(7)
O69	6496(3)	8544.6(9)	3734.8(9)	15.8(6)
O70	5613(3)	7801.3(9)	4023.1(9)	11.2(5)
O71	6933(3)	6859.9(10)	4422.7(9)	14.4(6)
O72	8996(3)	5965.1(11)	4793.4(10)	20.8(7)
O73	5190(3)	5186.8(10)	4546.4(9)	14.7(6)
O74	7217(3)	4729.8(9)	4669.7(9)	11.5(5)
O75	9837(3)	5181.2(10)	4619.0(11)	19.1(6)
O76	11448(3)	5834.9(9)	4721.1(9)	12.9(5)
O77	7051(3)	5219.9(10)	4013.8(10)	18.0(6)
O78	5627(3)	4513.2(9)	4088.9(9)	10.2(5)
O79	2634(3)	5259.6(9)	3963.1(8)	8.3(5)
O80	2471(3)	5946.3(9)	3479.3(8)	10.0(5)
O81	2095(3)	5180.5(9)	3176.3(9)	12.0(5)
O82	4403(3)	5414.5(9)	3423.3(9)	12.2(5)
O83	7136(3)	6474.7(9)	3516.5(9)	10.4(5)
O84	7372(3)	5705.4(9)	3197.3(9)	12.4(5)
O85	9397(3)	6188.8(10)	3267.7(9)	15.1(6)
O86	12240(3)	6621.5(9)	4135.9(9)	11.0(5)
O87	13853(3)	6874.4(12)	4673.7(10)	22.5(7)
O88	14262(3)	6132.3(10)	4293.5(10)	16.3(6)
O89	14500(3)	6859.6(10)	3893.8(9)	11.8(5)
O90	9933(3)	5797.1(9)	4077.0(9)	12.4(5)
O91	1973(3)	6468.9(10)	2700.0(10)	15.7(6)
O92	591(3)	7174.3(9)	2551.1(9)	10.0(5)
O93	2317(3)	6919.2(9)	2026.4(9)	10.5(5)
O94	4775(3)	5837.8(9)	2610.7(8)	12.6(5)
O95	7677(3)	6396.9(9)	2728.0(8)	8.9(5)
O96	4996(3)	6516.8(9)	2149.7(11)	17.5(6)

Atom	x	y	z	U(eq)
O97	3903(3)	5812.1(12)	1869.6(10)	20.6(6)
O98	6383(3)	5816.4(9)	1996.1(9)	12.4(5)
O99	7265(3)	5025.6(9)	2549.9(9)	11.4(5)
O100	9283(3)	5528.7(10)	2407.8(11)	18.8(6)
O101	9517(3)	4807.5(9)	2819.3(9)	9.4(5)
O102	8957(3)	4777.1(11)	2037.7(9)	20.9(7)
O103	10058(7)	4423.9(19)	786.7(17)	18.0(9)
O104	8479(7)	4274(3)	326(3)	11.9(14)
O105	9858(5)	3588.6(17)	621.5(18)	11.8(8)
O106	10981(6)	4122(2)	118.8(17)	12.2(9)
O107	246(3)	6468.3(9)	2124.4(9)	11.8(5)
O108	9909(6)	3597.0(19)	325(2)	11.8(8)
O109	10991(7)	4355(2)	218(2)	12.2(9)
O110	10152(7)	4149(2)	925.7(19)	18.0(9)
O111	3856(8)	9028(3)	8530(2)	13.2(9)
O112	4969(12)	9753(4)	8753(3)	11.1(11)
O113	4717(16)	9124(6)	9265(6)	11.7(16)
O114	8465(14)	4142(5)	194(4)	11.9(14)
O115	2582(9)	8275(3)	8155(3)	13.2(11)
O116	7457(8)	9905(2)	10174(2)	12.2(11)
O117	7529(9)	10046(3)	10020(3)	12.2(11)
O118	7526(19)	9693(6)	9311(7)	11.7(19)
O119	6565(17)	9286(5)	9946(4)	9.8(15)

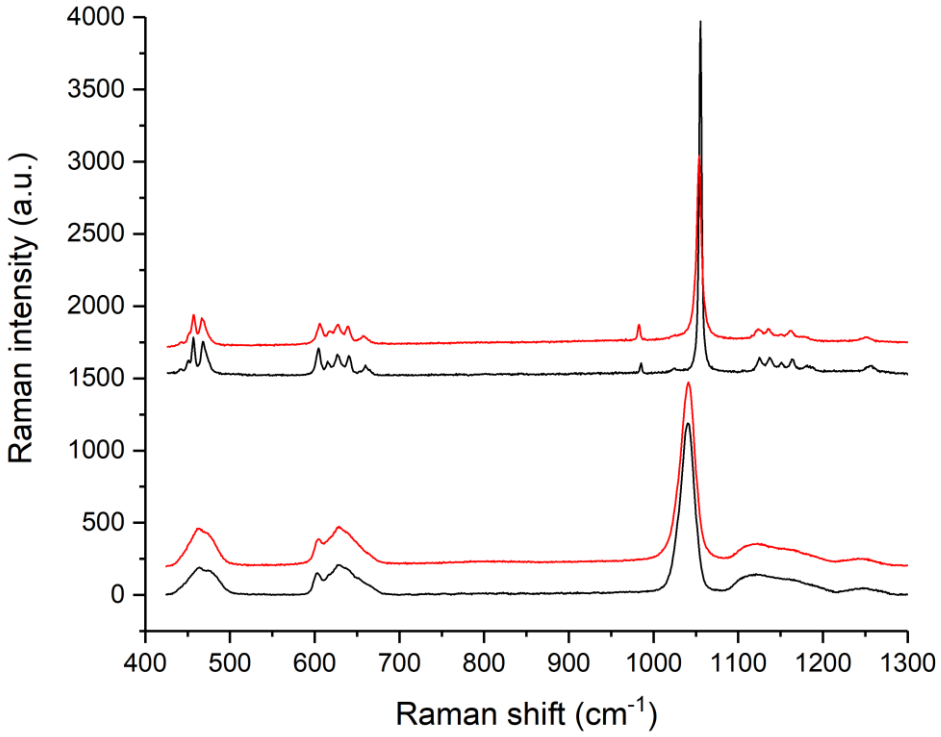

Figure A1. spectra of $K_{0.2}Na_{1.8}Mg_2(SO_4)_3$ (lower graphs) and of $K_2Mg_2(SO_4)_3$ (upper graphs) at RT (in red) and 77K (in black) displaying ν_2, ν_4, ν_1 and ν_3 internal bands of sulphate tetrahedra around 460, 630, 1040 and 1100-1200 cm^{-1}, respectively.

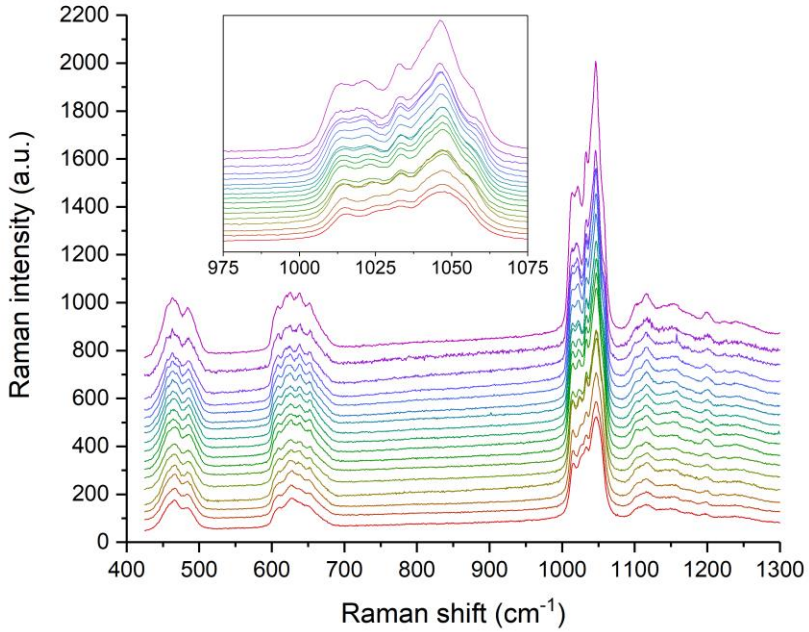

Figure A2. Raman spectra of monoclinic $K_{0.1}Na_{1.9}Mg_2(SO_4)_3$ between 77 K (top spectrum) and RT (bottom spectrum). The inset shows an expanded view of the ν_1 region.

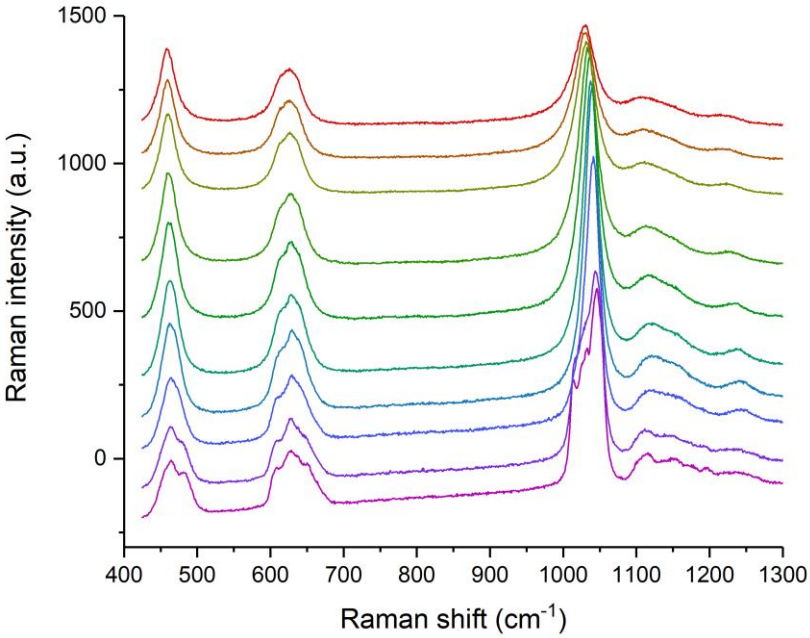

Figure A3. Raman spectra of $K_{0.1}Na_{1.9}Mg_2(SO_4)_3$ between RT (bottom spectrum) and 700 °C (top spectrum) displaying the phase transition from monoclinic to cubic symmetry at ~200 °C.

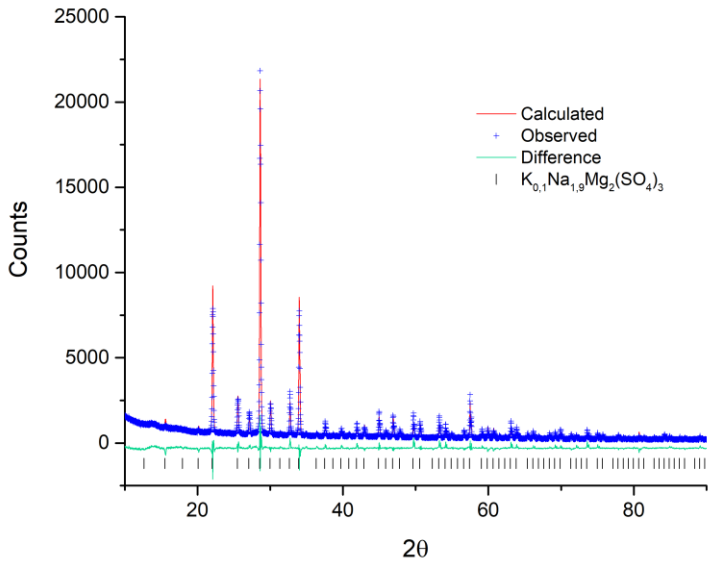

Figure A4. Observed, calculated and difference plot for structural refinement of $K_{0.1}Na_{1.9}Mg_2(SO_4)_3$ at 750°C R_{wp} = 9.9% GOF = 2.39

Table A8. Fractional Atomic Coordinates, Occupancies and U_{iso}(x100) Å^2 for $K_{0.1}Na_{1.9}Mg_2(SO_4)_3$ at 750^{o}C.

Atom	x	y	z	Fractional occupancy	U_{iso}(x100) Å^2
Na1	0.6577(12)	0.6577(12)	0.6577(12)	1.00(2)	10.48(42)
Na2	0.9465(11)	0.9465(11)	0.9465(11)	0.90(2)	10.48(42)
K1	0.6577(12)	0.6577(12)	0.6577(12)	0.00(2)	10.48(42)
K2	0.9465(11)	0.9465(11)	0.9465(11)	0.10(2)	10.48(42)
Mg1	0.1834(10)	0.1834(10)	0.1834(10)	1.0	3.86(26)
Mg2	0.3916(7)	0.3916(7)	0.3916(7)	1.0	3.86(26)
S	0.1186(3)	0.5166(2)	0.2315(3)	1.0	8.60(26)
O1	0.1495(23)	0.4746(24)	0.3888(9)	0.3333	0.77(21)
O2	0.2593(13)	0.5104(22)	0.1440(2)	0.3333	0.77(21)
O3	0.0086(19)	0.4110(21)	0.1666(22)	0.3333	0.77(21)
O4	0.0571(23)	0.6704(11)	0.2264(23)	0.3333	0.77(21)
O5	0.2415(30)	0.4325(46)	0.3043(15)	0.3333	0.77(21)
O6	0.1449(17)	0.5222(14)	0.0679(6)	0.3333	0.77(21)
O7	-0.0257(27)	0.4409(46)	0.2617(17)	0.3333	0.77(21)
O8	0.1138(50)	0.6708(7)	0.2920(16)	0.3333	0.77(21)
O9	0.1772(22)	0.5085(26)	0.3863(9)	0.3333	0.77(21)
O10	0.2429(15)	0.5504(18)	0.1271(18)	0.3333	0.77(21)
O11	0.0502(21)	0.3713(13)	0.1906(23)	0.3333	0.77(21)
O12	0.0042(16)	0.6362(16)	0.2218(23)	0.3333	0.77(21)

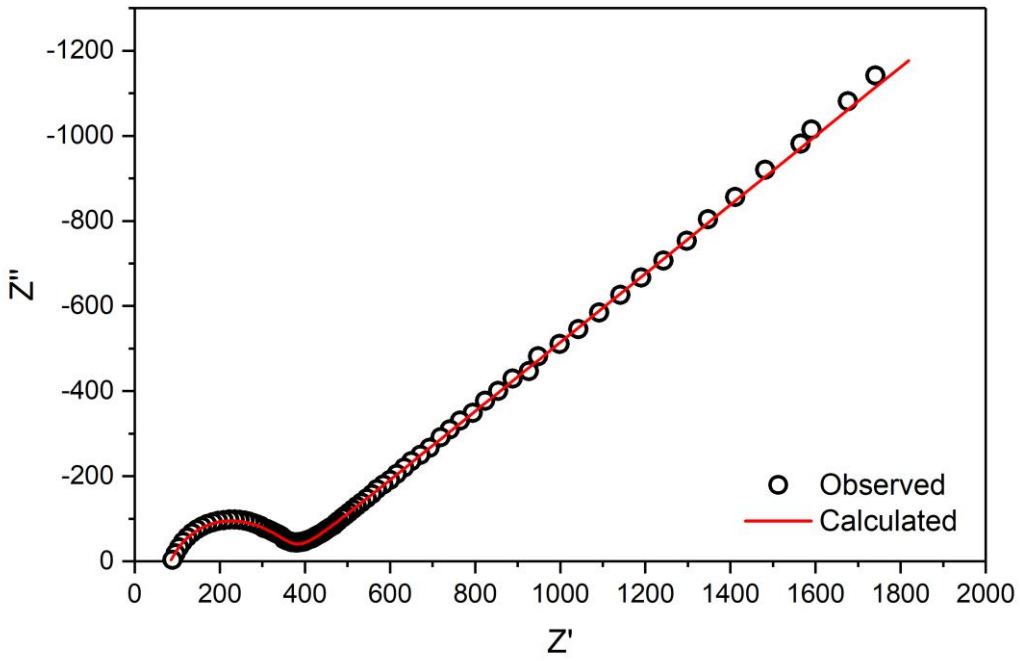

Figure A5. Observed and modelled imdedance spectrum of $La_{2.63}Na_{0.38}Li_{5.75}Nb_2O_{12}$ at 285°C.

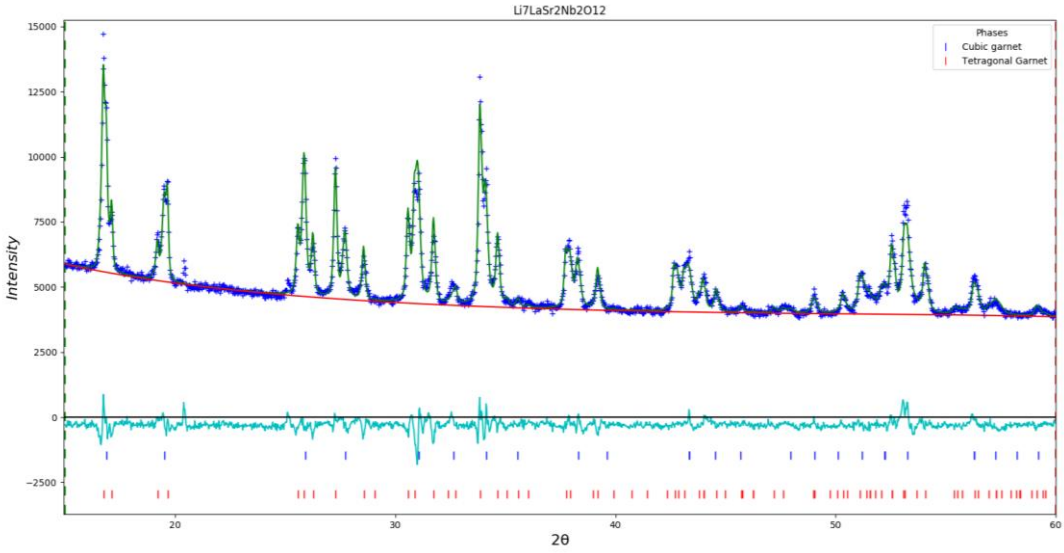

Figure A6. Observed, calculated and difference plot for structural refinement of sample with nominal composition $Li_7LaSr_2Nb_2O_{12}$. Impurity phase is not identified. R_{wp} = 3.186%, GOF = 2.27.

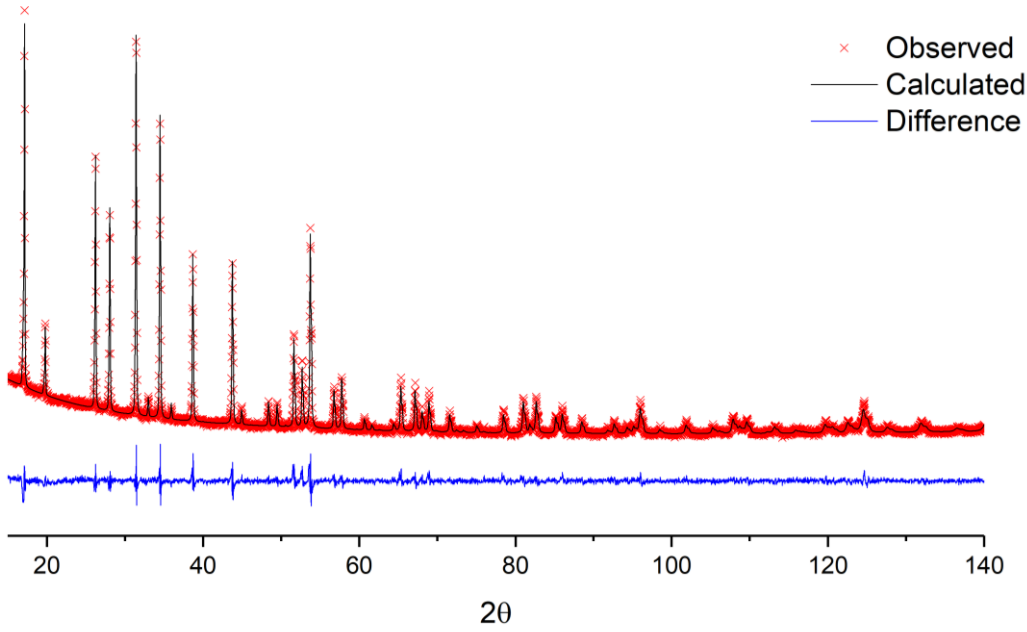

Figure A7. Observed, calculated and difference plot for structural refinement of sample with nominal composition $Li_{5.4}La_{2.8}Na_{0.2}Nb_2O_{12}$. R_{wp} = 3.424%, GOF = 1.61.

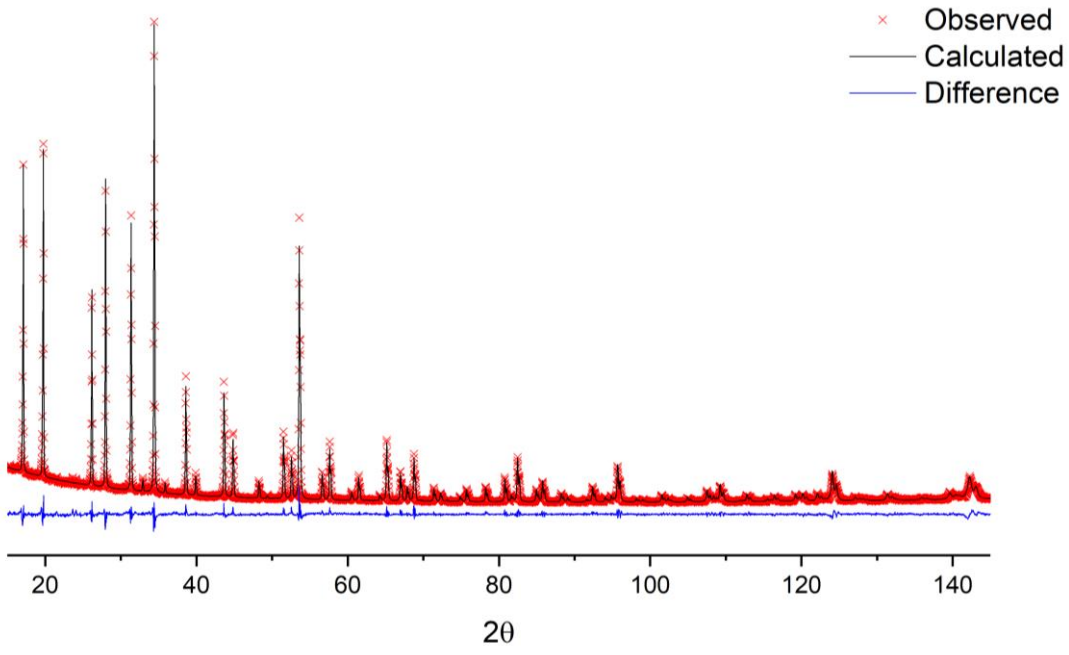

Figure A8. Observed, calculated and difference plot for structural refinement of sample with nominal composition $Li_{5.4}La_{2.8}Na_{0.2}Ta_2O_{12}$. R_{wp} = 4.214%, GOF = 1.55.

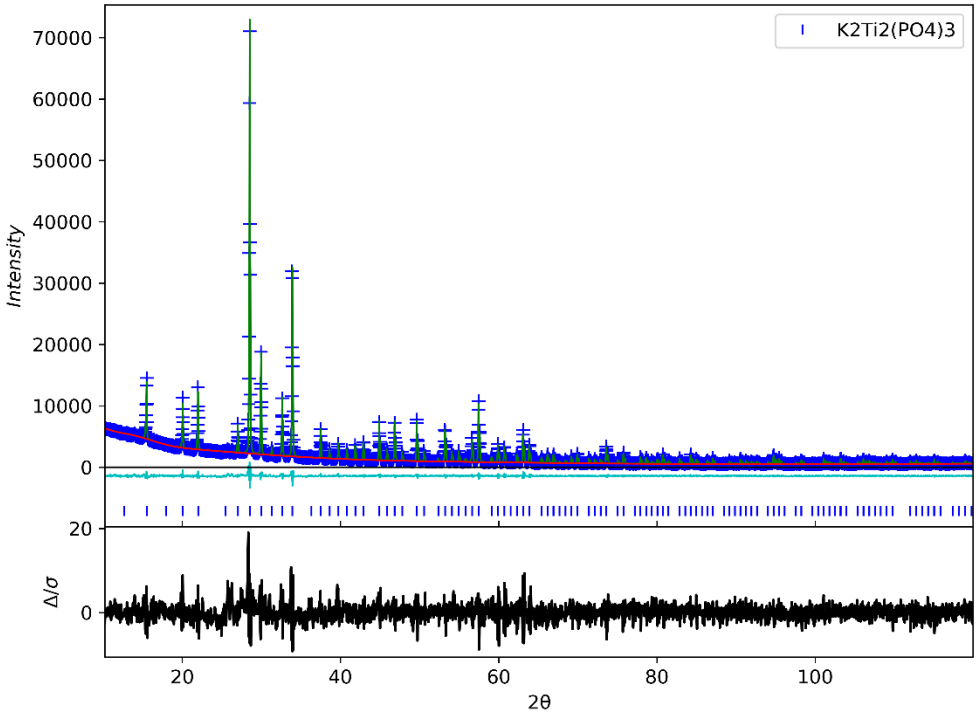

Figure A9. Observed, calculated and difference plot for structural refinement of sample with nominal composition $K_2Ti_2(PO_4)_3$. R_{wp} = 4.427%, GOF = 1.84.

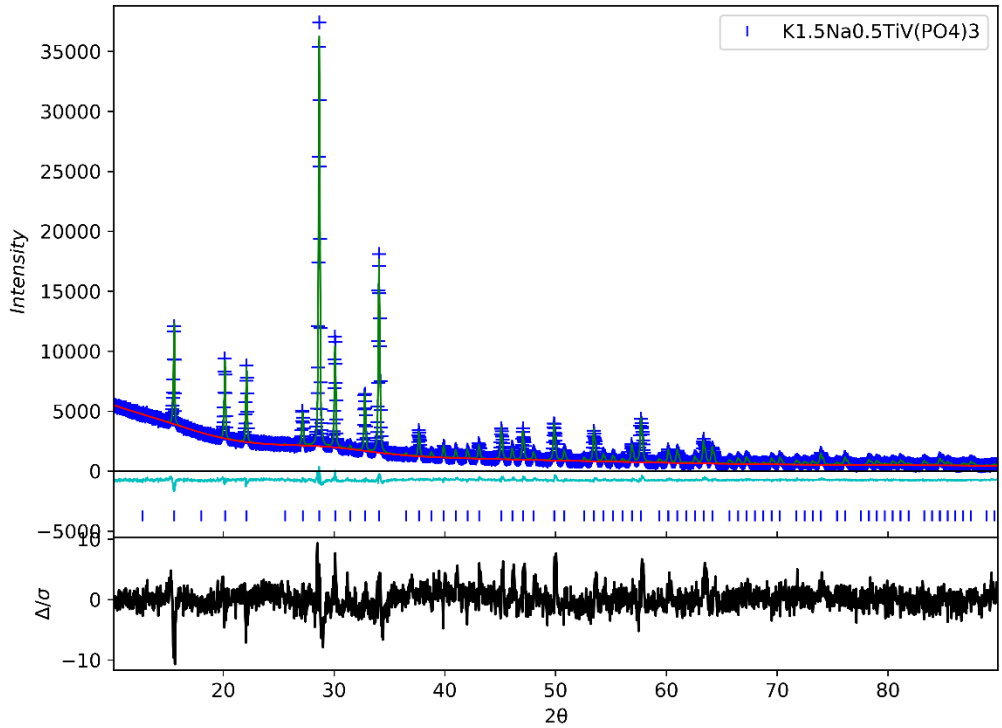

Figure A10. Observed, calculated and difference plot for structural refinement of sample with nominal composition $K_{1.5}Na_{0.5}TiV(PO_4)_3$. R_{wp} = 3.825%, GOF = 1.58.